Development of a Dual-Pressure Air Receiver System for the SUNDISC Cycle

by

Lukas Heller

Dissertation presented for the degree of Doctor of Philosophy in Mechanical Engineering in the Faculty of Engineering at Stellenbosch University

Supervisor: Dr. Jaap Hoffmann

March 2017

Declaration

By submitting this dissertation electronically, I declare that the entirety of the work contained therein is my own, original work, that I am the sole author thereof (save to the extent explicitly otherwise stated), that reproduction and publication thereof by Stellenbosch University will not infringe any third party rights and that I have not previously in its entirety or in part submitted it for obtaining any qualification.

Date: March 2017

Abstract

Development of a Dual-Pressure Air Receiver System for the SUNDISC Cycle

L. Heller

Department of Mechanical and Mechatronic Engineering,
Stellenbosch University,
Private Bag X1, Matieland 7602, South Africa.

Dissertation: PhD (Eng)

November 2016

Combined cycle CSP plants with solarized gas turbines have the potential to generate dispatchable electricity at a high efficiency and with the option to integrate cost-effective rock bed thermal energy storage. However, as only the energy downstream of the gas turbine can be dispatched in such a setup, solar-derived electricity generation is only possible for a few hours after sunset or at a low rating. The novel SUNDISC cycle is proposed to overcome this shortcoming by adding an additional, non-pressurized air receiver that directly charges the storage.

A techno-economical model of a SUNDISC cycle plant was created based on efficiency estimates for the solar field and receivers, empirical correlations for the heat transfer in the rock bed storage, a part-load model for the Brayton cycle as well as a simplification of the steam cycle. A parametric study with this model suggests that electricity can be generated at an almost constant rating at a levelized cost of 0.143 USD/kW$_e$ h (24 % lower than the reference single-receiver cycle) during more than 8200 h per year. A learning-curve scenario predicts the levelized costs of such plants to drop to less than 0.075 USD/kW$_e$ h by the year 2035.

Heating of the non-pressurized air for charging the storage system and of the pressurized air in the Brayton cycle can be done in a dedicated receiver at each respective pressure level or in a hybrid receiver. Based on the previously proposed HPAR concept, the potential of a metallic tubular hybrid receiver to fulfill the requirements of a SUNDISC cycle plant was investigated. Models of the main heat transfer mechanisms (solar and thermal radiation as well as internal and external convection of the absorber tubes) were merged to estimate

the optical and thermal efficiency of the receiver as well as the two air streams' respective achievable outlet temperature.

It was found that the desired temperature increase in the non-pressurized air stream cannot be achieved for sensible flow velocities with a basic HPAR receiver design. Additionally, the thermal efficiency was calculated to be lower than in competing pressurized air receiver technologies and temperature gradients in the absorber tubes were high. The potential of three enhancements was investigated: (1) Externally finned absorber tubes can be designed to increase the convective heat transfer to reach the desired outlet temperatures but the energy input into the pressurized air stream is lowered and the assemblies' durability is unproven. (2) Quartz glass elements can be used to minimize the effect of wind on the receiver and to increase mixing in the tube bundle. (3) A volumetric absorber behind the absorber tubes can help achieve the nominal outlet temperature of the flow. While the results suggest that these enhancements have the potential to improve the receiver performance (combined optical and thermal efficiencies greater than 73 % were calculated), the level of detail of the model has to be increased to validate the findings and their durability is critical.

As further steps in the development of the SUNDISC cycle, improvements in models of the receivers, the steam generator and Rankine cycle as well as of component costs are recommended. Utilization of an HPAR concept receiver in the cycle depends on manufacturability, durability and cost of enhancements to the basic design.

Uittreksel

Ontwikkeling van 'n Twee-Druk Lugverkoelde Ontvanger Stelsel vir die SUNDISC Kringloop

("Development of a Dual-Pressure Air Receiver System for the SUNDISC Cycle")

L. Heller

Departement Meganiese en Megatroniese Ingenieurswese,
Universiteit van Stellenbosch,
Privaatsak X1, Matieland 7602, Suid Afrika.

Proefskrif: PhD (Ing)

November 2016

Gekonsentreerde sonkragstasies met 'n gekombineerde gas- en stoomturbien kringloop het die potensiaal om elektrisiteit op aanvraag te lewer indien dit termiese energie in 'n lae koste rotsbed gestoor kan word. Die gekombineerde siklus maak 'n hoë termiese benuttingsgraad moontlik. In bestaande kringlope word warm uitlaatgas van die gasturbien in die rotsbed gestoor, wat opwekking in die stoomturbien beperk tot 'n paar ure na sononder. Hierdie werk beskryf die ontwikkeling van die SUNDISC kringloop. Dié kringloop maak gebruik van 'n addisionele laedruk ontvanger wat son energie direk in die rotsbed stoor. Sodoende kan die elektriese uitset van die stoomturbien, asook die duur van opwekking na sononder verleng word.

'n Model van die hele kragstasie, wat die heliostate, ontvanger, rots bed, en gas- en stoomturbiene insluit, is ontwikkel vanuit emperiesie vergelykings vir hierdie komponente. Die gemiddelde jaarlikse bedryfskoste, verwerk na 'n huidige waarde, is ook bereken. Hierdie model is in 'n parametriese studie gebruik, wat aandui dat elektrisiteit teen feitlik konstante tempo opgewek kan word vir meer as 8200 ure per jaar, teen 'n koste van 0.143 USD/kW$_e$ h. Die koste is sowat 24 % laer as wat met vergelykbare kringlope behaal kan word. Daar word voorspel dat 'n steil leerkurwe die koste van opwekking teen 2035 tot sowat 0.075 USD/kW$_e$ h kan verlaag.

Dit is moontlik om die lae- en hoëdruk ontvangers onafhanklik te bedryf. Deur hulle saam te voeg, hou egter beduidende voordele in. In 'n buis-tipe ontvanger, word die buitekant van die buise deur die laedruk lugstroom verkoel, wat lei tot laer termiese spannings, stralingsverliese en geen konveksieverliese vir

die hoëdruk ontvanger. Hierdie sogenaamde HPAR konsep is verder ondersoek, om te sien of dit aan die vereistes van die SUNDISC kringloop kan voldoen. Son en termiese straling, sowel as konveksie warmteoordrag oor en deur die buise is in 'n enkele model saamgevat. Die model is gebruik om die vermoë van die onvanger om son energie in warmte om te skakel, sowel as die uitlaat temperature van beide lugstrome vooruit te skat.

'n Basiese twee-druk ontvanger ontwerp wat van gladde buise gebruik maak, kon nie die gewensde temperature teen sinvolle vloeitempos haal nie. Die benuttingsgraad was ook aansienlik laer as wat in bestaande ontvangers aangeteken is. Temperatuur gradiënte was hoog en kan lei tot faling as gevolg van termiese spannings. Drie aanpassings van die ontwerp is ondersoek, naamlik (1) die gebruik van vinbuise om konveksie warmteoordrag aan die laedruk kant te verhoog, (2) kwarts vensters en balke om windeffekte te verlaag, en vermenging aan te help, en (3) 'n volumetriese onvanger aan die uitlaat kant van die laedruk ontvanger. Resultate dui daarop dat 'n kombinasie van die aanpassings die benuttingsgraad van die ontvanger tot 73 % kan opstoot, en dat die gewensde temperature behaal kan word. Daar bestaan egter twyfel oor die langtermyn betroubaarheid van veral die vinbuise by hoë temperatuur. Die model was slegs daarop gemik om die potensiële voordele van die konsep uit te lig, en sal in die toekoms verfyn moet word om betroubare antwoorde te gee.

Die studie het bevestig dat die SUNDISC kringloop tasbare voordel inhou, en stel verdere komponent ontwikkeling op alle vlakke voor om die koste te verlaag. Die gebruik van 'n HPAR konsep ontvanger sal daarvan afhang of probleme rondom die vervaardigbaarheid, betroubaarheid en koste daaraan verbonde suksesvol oorkom kan word.

Acknowledgements

I would like to express my sincere gratitude to the following people and organizations:

My supervisor, Dr. Jaap Hoffmann, for his support throughout the project,

Dr. Paul Gauché for his ideas and guidance,

Prof. Johan van der Spuy and Dr. Stephan Heide for help with modeling of the gas turbine,

Prof. Hanno Reuter for advice during development of the SUNDISC cycle,

Prof. Thomas Harms for his feedback on the heat transfer modeling of the HPAR,

Dr. Reiner Buck for feedback on the HPAR concept,

Dr. Kenny Allen for support with modeling the rock bed storage system,

Mr. Jean Pitot for sharing his knowledge on open volumetric air receivers,

Mr. Matti Lubkoll and Dr. Stefan Hess for discussions, questions and sometimes solutions,

the Department of Mechanical and Mechatronic Engineering, the Centre for Renewable and Sustainable Energy Studies as well as the Postgraduate and International Office at Stellenbosch University for funding and

my family for everything more important.

Contents

List of Figures

List of Tables

Nomenclature

Abbreviations

BC	Brayton cycle
CC	Combined cycle
CPC	Compound parabolic concentrator
CSP	Concentrating solar power
DNI	Direct normal irradiance
DSG	Direct steam generation
GT(U)	Gas turbine (unit)
HPRS	High-pressure receiver system
HTE	Heat transfer enhancement
HTF	Heat transfer fluid
HTRe	High-temperature receiver
LCOE	Levelized cost of electricity
LPRS	Low-pressure receiver system
NPA	Non-pressurized air
O&M	Operation and maintenance
OVAR	Open volumetric air receiver
PA	Pressurized air
RC	Rankine cycle
SAM	System Advisor Model
SG	Steam generator
TES	Thermal energy storage
TNPG	Time of no power generation
VA	Volumetric absorber

Constants

R_{air}	$= 287.0\,J/(kg\,K)$
π	$= 3.142$

σ_{SB}	$= 5.670 \times 10^{-8}\,\mathrm{W/(m^2\,K^4)}$

Variables

A	Area	$[\mathrm{m^2}]$
$CAPEX$	Capital expenditure	[USD]
$c_{(\mathrm{p})}$	Specific (isobaric) heat capacity	$[\mathrm{J/(kg\,K)}]$
cf	Capacity factor	[-]
d	Diameter	[m]
E_{a}	Annual electricity yield	$[\mathrm{W_e\,h}]$
f_{defocus}	Fraction of defocused solar energy	[-]
f_{NPA}	Fraction of thermal input to NPA stream	[-]
$f_{\mathrm{sol,aper,pl}}$	Part-load solar influx fraction	[-]
k	Thermal conductivity	$[\mathrm{W_t/(m\,K)}]$
$LCOE$	Levelized cost of electricity	$[\mathrm{USD/(kW_e\,h)}]$
$\dot{m}$	Mass flow rate	[kg/s]
Nu	Nusselt number	[-]
Pr	Prandtl number	[-]
p	Pressure	[Pa]
Q	Thermal energy	$[\mathrm{W_t\,h}]$
$\dot{Q}$	Heat rate	$[\mathrm{W_t}]$
Q_{TES}	Thermal energy storage capacity	$[\mathrm{W_t\,h}]$
$\dot{q}$	Heat flux	$[\mathrm{W_t/m^2}]$
$\dot{q}_{\mathrm{cond}\to\mathrm{i}}$	Conductive heat flux into the tube	$[\mathrm{W/m^2}]$
Re	Reynolds number	[-]
s	Axial distance between fins	[m]
SM	Solar multiple	[-]
T	Temperature (absolute)	[K]
t	Temperature	[°C]
$TNPG_{\mathrm{a}}$	Annual time of no power generation	[h]
Δr	Distance between tube rows	[m]
$\Delta\phi_{\mathrm{columns}}$	Angular distance between columns of tubes	[°]
$\Delta\phi_i$	Angular offset between rows i and $i+1$	[°]
δ	Fin thickness	[m]
ϵ	Packed bed void fraction	[-]
ε	Emittance	[-]
μ	Dynamic viscosity	[Pa s]

ρ	Density	$[\mathrm{kg/m^3}]$

Subscripts

amb	Ambient
cond	Conduction
conv	Convection
dp	Design point
e	Electric
emit	Emitted
f	Fluid
i	Inside
in	Inlet/incoming
nom	Nominal
o	Outside
opt+t	Optical and thermal
out	Outlet/outgoing
p	Particle
Re	Receiver
rad	Radiation (thermal)
SF	Solar field
sol, abs	Absorbed solar radiation
t	Thermal

Chapter 1

Introduction

1.1 Background

World electricity demand is projected to increase by 69 % until 2040 compared to 2012 levels (U.S. Energy Information Administration, 2016, p. 81). While currently approximately 80 % of electricity is generated from fossil fuels and nuclear (the rest is mostly from hydropower), the share of renewable energy carriers is planned to grow considerably in the upcoming decades. The reasoning for this is (a) ecological, (b) related to resource scarcity and security as well as (c) economic, in light of an expected long-term fuel price increase and cost reductions in renewable energy technology. Since 2011 more than half of all new installed power generation capacity has been by renewable energy projects (IRENA, 2015, Figure 3.3).

Solar energy is the primary energy source with the largest potential by far. Yet, due to their high cost, solar-to-electric technologies have had an insignificant share in the renewable electricity generation capacity until recently (IRENA, 2015, Figure 3.1). This only changed in the last decade when prices for photovoltaic (PV) modules decreased rapidly and national incentive schemes supported their installation.

The biggest downside of PV, as well as wind power, is the intermittency of their sources and the lack of viable electricity storage systems. In this regard, concentrating solar power (CSP) offers the unique possibility of cost-effective thermal energy storage (TES). While the levelized cost of electricity (LCOE) of PV and wind power is generally lower than that of CSP, if a sizable storage capacity is added to the respective systems CSP becomes more viable (Allen and von Backström, 2016).

The Northern Cape Province in South Africa has one of the best solar resources in terms of cumulative annual direct normal irradiance (DNI) in the world. South Africa also has a high share of electricity generated from dated coal power plants, which are CO_2-emission extensive, and an electric grid in need of additional capacity (Department of Energy, 2013). The South

African demand profile shows distinct morning and — even more so — evening peaks which are higher in winter. Added generating capacity should, therefore, provide dispatchable power at times of no solar irradiation.

Using spacial-temporal modeling, Gauché *et al.* (2015) showed that the addition of electricity generation capacity from renewable sources to the South African grid will have economic benefits already in the short term. Although the investigated scenarios allocated larger capacities to wind power and PV, CSP was identified as a key component for grid stability.

1.2 CSP technology

Most CSP plants in operation today are of the parabolic trough type with synthetic oil as the heat transfer fluid (HTF) in the collector and, if applicable, molten salt as the thermal energy storage medium (IRENA, 2015, p. 100). However, the second commercially available technology, the central receiver, has higher potential in terms of efficiency and cost-effectiveness (Behar *et al.*, 2013). In this section, the subsystems of a central receiver plant are defined and selected central receiver cycles are presented.

1.2.1 Layout of a central receiver plant

In central receiver systems, as depicted in Figure 1.1, radiation is concentrated by a field of individual collectors, called heliostats, that track the sun in two axes and reflect solar radiation onto a target. The target is normally a thermal receiver on top of a tower in the center, for a surrounding field, or on the side of the field that is closest to the equator, for a so-called polar field.

The absorber is the part of the receiver system in which concentrated solar radiation, which is focused by the solar field (and potentially further by a secondary concentrator), is absorbed. The thermal energy is then passed on to an HTF to either charge the thermal energy storage (potentially via a heat exchanger), feed the heat exchanger of the thermal-to-electric cycle or directly run the turbine (if the used HTF is also the working fluid of the power cycle).

1.2.2 Central receiver cycles

In this section, selected central receiver technologies are distinguished by the utilized HTF as this choice greatly influences the designs of most subsystems.

Direct Steam Generation

Direct steam generation (DSG) plants have a simple general layout, depicted in Figure 1.2, as the HTF can be used as the storage medium and is also the working fluid of the power cycle (two of the heat exchangers in Figure 1.1 are

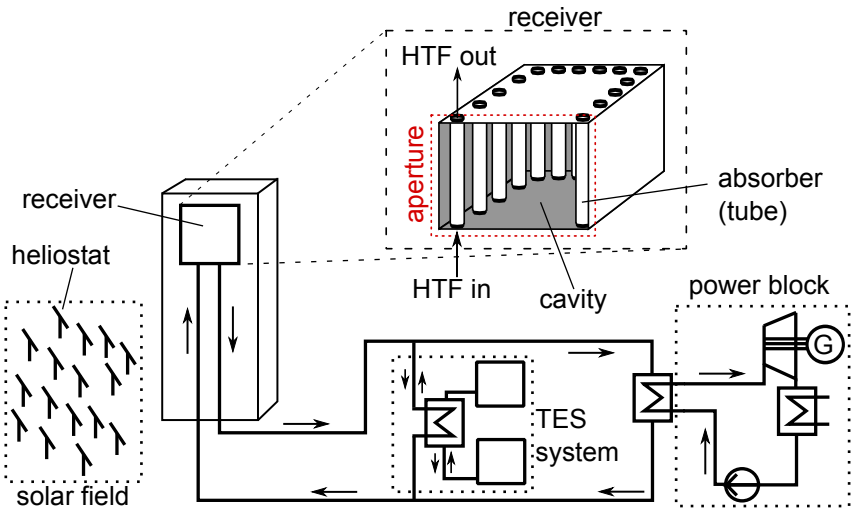

Figure 1.1: Subsystems of a generic central receiver CSP plant and receiver components

not necessary). This also means that the steam temperature is not limited by temperature restrictions of the HTF and the power block can reach a high solar-to-electric efficiency (for example, 42 % predicted by Kolb *et al.*, 2011, for the Ivanpah Solar Electric Generating System). Additionally, the fluid (water/steam) is common in engineering applications and has a low freezing point. These are the reasons why DSG towers are the most commonly constructed tower technology at the moment.

However, since the storage medium is a highly pressurized fluid the storage tanks are expensive and the TES system cost becomes prohibitively high for larger capacities (Pitz-Paal *et al.*, 2005). Additional problems arise from the high-pressure of the HTF in the receiver and the need for a reheating flow path

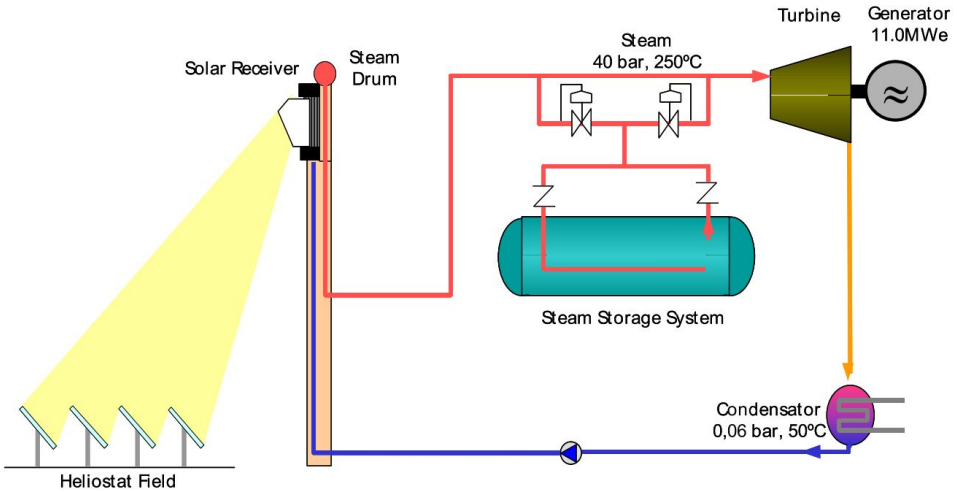

Figure 1.2: Schematic of a DSG CSP plant (Osuna *et al.*, 2006)

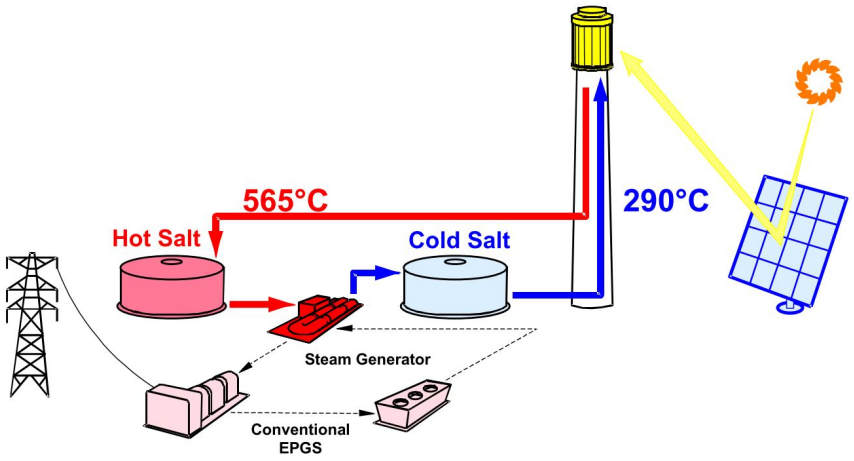

Figure 1.3: Schematic of a molten salt CSP plant (Pacheco, 2002); EPGS: electric power generation system

in order to reach a high thermal-to-electric conversion efficiency.

Direct molten salt

Due to its high heat capacity and low cost, molten salt (mostly so-called Solar Salt with a composition of 60 % $NaNO_3$ and 40 % KNO_3 by mass) is used as the storage medium in all commercial CSP plants with large storage capacities. In some central receiver plants, molten salt is also used as the HTF in an active direct storage configuration (that is, the TES consists of tanks containing the hot or cold HTF, the HTF-to-TES heat exchanger in Figure 1.1 is omitted, see Figure 1.3). The salt is heated to approximately 565 °C (its operating limit with typical components) in the receiver and directed towards the steam generator (SG) or into the hot storage tank. Due to the favorable heat transfer properties of solar salt, this setup allows for high solar fluxes on the absorber and therefore a high thermal efficiency of the receiver above 90 % (Kolb, 2011). The high upper temperature of the fluid also allows for efficient power cycles and, due to the large temperature increase, a low specific cost of the TES system.

Although the technology has only been implemented in few projects, it can be considered state of the art and is generally seen as one of the most promising configurations for future CSP power plants. Nevertheless, there are shortcomings of these systems: Firstly, the upper temperature limit of the fluid prevents the use of the highest-efficiency power cycles (Kolb, 2011). The power block is the subsystem with by far the lowest efficiency in central receiver systems with common values between 25 % and 42 % (Pitz-Paal *et al.*, 2005; Kolb *et al.*, 2011). Secondly, the HTF's solidification temperature of 222 °C requires special care to avoid clogging of receiver pipes and pumps which can lead to their destruction. Thirdly, despite the low cost of molten salt compared

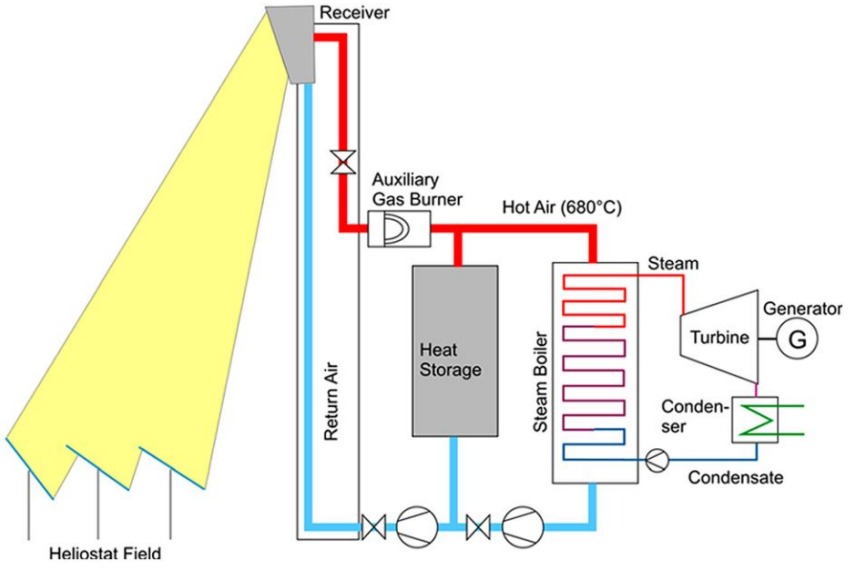

Figure 1.4: Schematic of an open air receiver-powered steam cycle CSP plant (PHOEBUS type; Zunft *et al.*, 2011)

to most other candidate TES media (for example, synthetic oil or liquid metals), depending on storage capacity the cost for the TES subsystem typically still accounts for more than 10 % of a plant's investment cost (IRENA, 2015). Lower cost storage appears feasible.

Open air receiver with Rankine steam cycle

Non-pressurized air as an HTF has the potential to address all three mentioned shortcomings of molten salt. The fluid has no practical upper temperature limit, which means that higher-efficiency steam cycles can be powered by it given suitable piping and containment. Furthermore, operation is simplified as freezing does not occur and the fluid is inert. Finally, while it is not feasible to directly store thermal energy in heated air, low cost passive storage systems (that is, a solid storage medium in direct contact with the HTF) are possible and the fluid itself is freely available. Figure 1.4 shows the typical layout of an open air receiver powered Rankine steam cycle plant (also referred to as PHOEBUS type).

To date, no commercial plants of this technology have been constructed, however, the design for at least two projects has been pursued to advanced stages (Grasse, 1991; Romero *et al.*, 2000) and a demonstration plant has been operating since 2009 (Ávila-Marín, 2011). The current manifestation of the technology features a ceramic absorber with volumetric geometry providing air at a nominal outlet temperature of 680 °C and a thermal efficiency above 80 % (Hoffschmidt *et al.*, 2003*a*). Detailed information on the technology can be found in Section 6.2.

The TES of the pre-commercial demonstration plant mentioned above consists of a packed bed of ceramic particles that is charged by the outlet flow of the receiver and discharged with the exhaust air of the steam generator (SG) at a temperature of 120 °C (Zunft *et al.*, 2011). Pitz-Paal *et al.* (2005) predicted the specific cost for a 94 $MW_t h$ TES system of this type at approximately 88 USD/($kW_t h$) (inflation adjusted to 2015) for a first-of-a-kind plant. For this specific plant, this capacity translates to only 3 h of energy supply to the steam generator when running at full load. Nevertheless, the subsystem cost accounts for 15 % of the total direct investment cost of the plant.

An alternative packed bed storage medium that could cut this cost considerably is rock. Although rock bed storage systems have been proposed for CSP for decades, the first demonstration system with a rating of 100 $MW_t h$ has only been constructed recently (Zanganeh *et al.*, 2013). Allen and von Backström (2016) predicted specific costs for three different proposed designs of packed bed TES systems at ratings above 200 $MW_t h$. For rock that is abundantly available in the Northern Cape province of South Africa, system costs in the range of 3 USD/($kW_t h$) to 11 USD/($kW_t h$) were found.

The major disadvantage of the PHOEBUS-type CSP cycle is the low solar-to-electric efficiency, predicted at a gross annual mean of 15 % by Pitz-Paal *et al.* (2005). Firstly, this is caused by the lower annual thermal efficiency of the receiver (77 %) compared to DSG or molten salt receivers. Due to the poor heat transfer properties of air, absorber surfaces are at considerably higher temperatures (up to 1000 °C) than, for example, in a molten salt receiver (less than 600 °C). Secondly, despite the high HTF temperature, the power block only reaches a low thermal-to-electric efficiency because of (a) the high superheater approach temperature and (b) the amount of lost energy in the exhaust gas stream (Buck *et al.*, 2006).

The heat-exchanger temperature diagram in Figure 1.5 shows that for an investigated plant with a receiver that heats air to 700 °C the live steam temperature only reaches 460 °C. At the same time, the outlet air of the steam generator still has considerable energy content at a temperature of 110 °C. While up to 50 % of this energy can be recovered by reintroducing it into the receiver (through an air return loop), the lost energy still significantly penalizes the overall performance (Pitot de la Beaujardiere *et al.*, 2016).

Dual air/steam receiver cycle

To alleviate the issue of required high air temperatures at the receiver outlet Buck *et al.* (2006) proposed a dual receiver in which steam is evaporated directly in addition to air being heated for use in the steam generator. In Figure 1.6 the schematic of this plant layout (left) alongside the $\dot{Q}$-T diagram for the updated steam generator (right) are shown. Compared to Figure 1.5 the lower required air inlet temperature — 500 °C instead of 700 °C — and the lowered preheater outlet temperature — from 110 °C to 80 °C — are apparent. This is

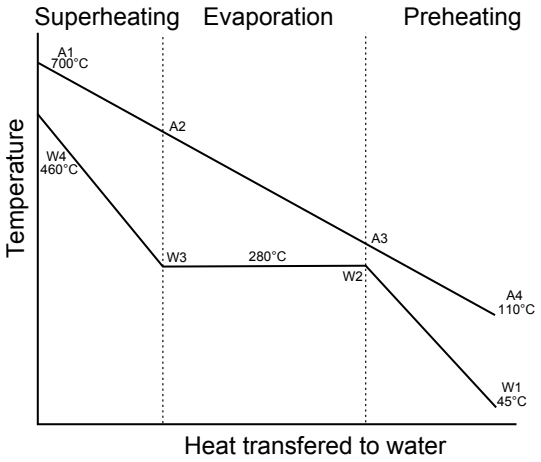

Figure 1.5: Heat rate-temperature diagram of an air-steam heat exchanger (Buck *et al.*, 2006)

achieved by using the heated air only for preheating and superheating of the water/steam and therefore lowering the temperature difference at the cold side of the superheater (difference between points A2 and W3 in Figure 1.5, b).

A comparison of the yearly performance of a 100 MW_e plant of this type with a PHOEBUS-type plant of the same rating yielded an increase of the average net efficiency by more than 20 %, which was mainly attributed to the higher receiver efficiency, the decreased losses in the exhaust air stream as well as a decreased parasitic power consumption (Eck *et al.*, 2006). A TES system was not foreseen in the setup, however, a dual system featuring a passive storage for the air cycle and a direct or another passive storage for the steam cycle are conceivable. Due to the system's increased complexity and the lack of a simple TES solution, the technology was not further developed (Buck, 2016).

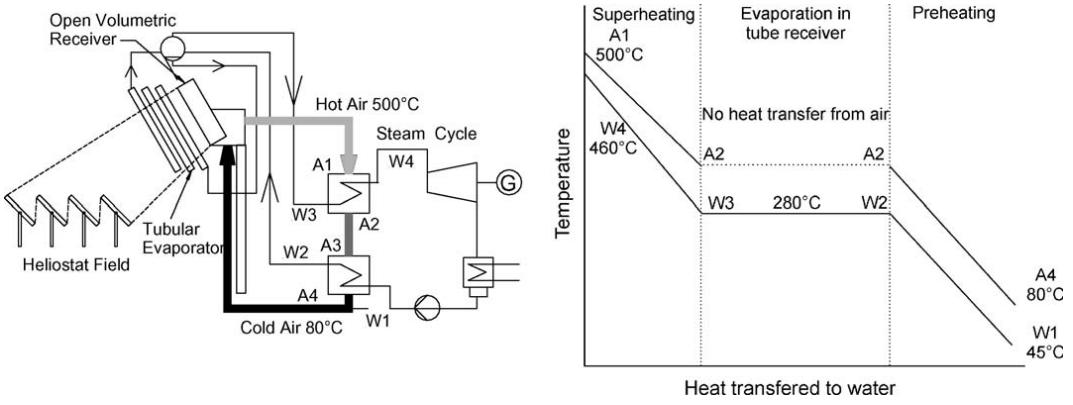

Figure 1.6: Schematic of a dual air-steam receiver cycle (left) and $\dot{Q}$-T diagram of the air-steam heat exchanger (Buck *et al.*, 2006)

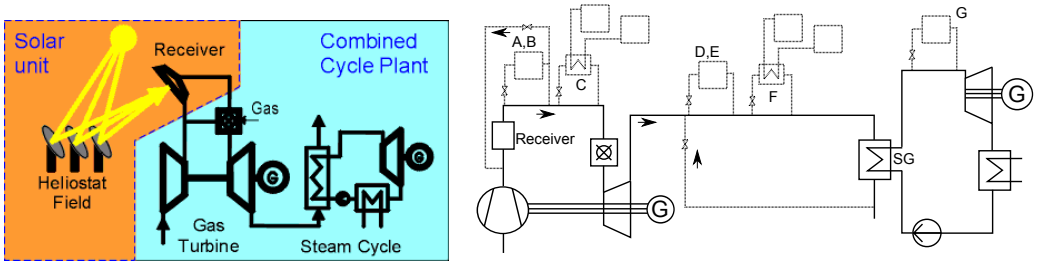

(a) (b)

Figure 1.7: (a) Schematics of a CC CSP plant without TES (Pitz-Paal *et al.*, 2005) and (b) TES system locations in a CC cycle with solarized gas turbine (derived from Heller and Gauché, 2014)

Combined cycle with solarized gas turbine[1]

At a proven thermal-to-electric efficiency above 50 % (Kribus *et al.*, 1999), a combined air-steam cycle (in the following referred to as "combined cycle" or "CC") is the most efficient conventional power cycle. To convert solar thermal energy to electricity at such high efficiencies a pressurized air stream has to be heated downstream the compressor of the gas turbine (GT). The schematic of a simplified CC CSP plant with a pressurized air receiver and a combustion chamber for co-firing is depicted in Figure 1.7(a). While indirect heating of the air via an additional HTF cycle has been proposed — for example, with non-pressurized air (Wilson Solarpower, 2015) or particles (see review by Ho and Iverson, 2014) as the HTF — these technologies (especially the heat exchangers) have not been proven yet and are, therefore, not considered further.

The CC CSP concept with a pressurized air receiver has three major challenges:

1. A receiver has to be designed that effectively absorbs concentrated solar radiation, has minimal thermal losses and achieves sufficiently high air outlet temperatures at a tolerable pressure drop. An overview of proposed and experimentally tested designs is given in Section 6.3.

2. The receiver has to be implemented into a (usually internally fired) gas turbine unit and the combustion chamber has to be adapted to cope with increased air inlet temperatures.

3. The implementation of a TES system into the cycle is considered challenging but necessary unless the plant is to rely on fuel co-firing for generating electricity. Schwarzbözl *et al.* (2006), for example, compared different solarized gas turbine cycles which reached an annual solar share of 70 % only if the power plant is exclusively operated during the day. Many national feed-in tariffs for renewable energy allow only much lower co-firing

[1] parts of this section have previously been published (see Heller and Gauché, 2014)

rates and other locations with favorable solar irradiation, including in South Africa, have no access to gaseous fuel at a competitive cost.

Conceivable locations of the TES system in a CC with a solarized gas turbine are depicted in Figure 1.7(b). Direct storage of pressurized or non-pressurized gas (A and D, respectively, in Figure 1.7, b) is not feasible because of its low volumetric heat capacity. Indirect storage in a separate high-temperature (HT) storage medium upstream the GT (C) does not appear viable as this would require a pressurized heat exchanger and a low-cost fluid that can be used at high temperatures. In the near future, the remaining option to store thermal energy on the HT side of the cycle is a passive TES system (B). However, due to the gas being pressurized, the TES tank(s) will have to withstand elevated pressures at high temperatures which appears uneconomical (Fraidenraich *et al.*, 1992).

Another option is to only store the thermal energy downstream of the GT. At this lower temperature (LT), lower cost active storage media and containment materials are available and non-pressurized air can be used to charge/discharge the TES. An indirect active (F) storage medium in the appropriate temperature range is, for example, molten salt. The most promising concept, however, seems to be a passive TES system upstream the SG in the gas cycle (E). This is mainly due to available low cost storage media, like for example, high temperature concrete (Laing *et al.*, 2011; Selvam and Strasser, 2012), ceramics (Dreißigacker *et al.*, 2013) and especially rock (Allen and von Backström, 2016). When thermal energy is stored directly in the steam cycle (G), as done in DSG plants described in Section 1.2.2, the TES system has to provide sensible and latent heat. This leads to more complex set-ups as well as operation and is, therefore, not considered a desirable solution.

The SUNSPOT cycle[2]

One concept of a combined cycle CSP plant with passive low-temperature TES system is the SUNSPOT (Stellenbosch University Solar Power Thermodynamic) cycle, as proposed by Kröger (2011). Figure 1.8 shows a schematic of the basic concept employing a packed bed of rocks as the TES.

An important aspect of the SUNSPOT cycle is that its gas and steam cycles are operationally decoupled. This allows for continuous (baseload) electricity generation in an asynchronous operation, where the gas turbine runs during daytime and charges the TES system while the Rankine steam cycle operates at night. The latter is powered by storage discharging. A positive side-effect is that the condenser, which is intended to use dry-cooling, operates at higher efficiencies during night-time.

However, there are inherent limitations to the concept. Namely, all available solar energy has to be captured in a receiver system that is directly linked

[2]parts of this section have previously been published (see Heller and Gauché, 2014)

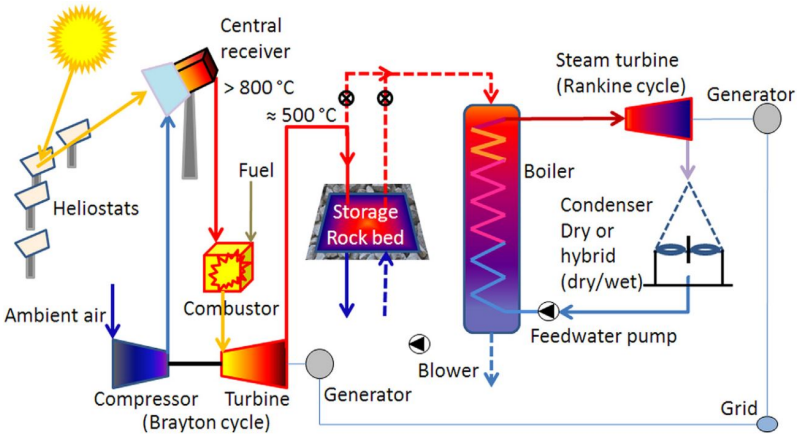

Figure 1.8: Schematic of the SUNSPOT cycle (Allen *et al.*, 2014)

to the gas turbine (GT). This in turn means that, as the solar input changes constantly, the GT has to run in part-load conditions for most hours of the day unless the difference to full-load is made up by extensive co-firing or large quantities of solar radiation remain unused. Even if this is acceptable, the amount of thermal energy that can be dispatched to hours of no solar input is limited to the energy content in the GT's exhaust gas.

Comparison of cycles

A concise evaluation of the respective strengths and weaknesses of the presented cycles is presented in Table 1.1. Therein, the asynchronous SUNSPOT cycle is shown instead of a generic CC with a solarized gas turbine (that is, a rock bed TES is assumed to be implemented).

The demand on solar field accuracy and concentration ratio is high for pressurized air receivers as required by solarized gas turbines because they commonly require a secondary concentrator with a limited acceptance angle (see Section 6.3). The demand on these receivers is also high as they experience the highest temperatures and utilize a heat transfer fluid with poor heat transfer

Table 1.1: Qualitative evaluation of presented cycles (+: positive, –: negative, o: neutral)

Technology	Demand on			efficiency	dispatchability
	SF	Receiver	TES		
DSG	+	o	–	o	–
Molten salt	+	o	o	o	+
PHOEBUS	+	o	o	–	+
Dual air/steam	+	o	–	o	–
SUNSPOT	–	–	+	+	o

characteristics. The PHOEBUS type receiver has the considerable advantage of being part of an open air loop and, therefore, working with a non-pressurized, non-corrosive fluid. However, its operating temperature and the poor heat transfer also require high material temperatures.

TES systems are challenging if they need to store pressurized fluids. Molten salt storage system costs are higher than that of proposed passive TES systems (Allen and von Backström, 2016). The PHOEBUS cycle is predicted to have a lower overall thermal-to-electric efficiency than other cycles, while combined cycles reach the highest values. The amount of dispatchable electricity generation is limited by the specific TES cost of the cycles and, in case of the SUNSPOT cycle, by the location downstream the primary heat engine.

1.3 Scope of this work

The SUNSPOT cycle has the potential to enable high solar-to-electric efficiencies and the implemented non-pressurized rock bed TES system could provide a cost-effective way of dispatching electricity generation to hours of no solar irradiation. However, the amount of energy that can be dispatched is limited to the energy available to the bottoming cycle, which typically only has below 40 % of the total plant rating for applicable gas turbines (Kehlhofer, 1999, Table 4-1). Baseload characteristics of a plant, which could be enabled by the low-cost rock bed technology, can therefore not be achieved without considerable amounts of fuel co-firing.

In Part I of this work, it is investigated if a modification of the basic SUNSPOT cycle can alleviate the identified problems with it. Firstly, a techno-economic model of a SUNSPOT cycle plant is created which is then used for annual hourly simulations to quantify the cycle's limitations. Furthermore, the model is extended for simulations of plants featuring the novel cycle. A parametric study is performed to identify sensible plant setups in terms of annual output, dispatchability and LCOE and compare these performance indicators to the original cycle.

The enhanced cycle enables the use of a dual-pressure air receiver system. In Part II, one concept of this technology is adapted for the enhanced cycle and its performance evaluated. A review of existing air receivers is presented to define the technology's state of the art. Thereafter, the heat transfer mechanisms of a manifestation of the proposed dual-receiver system concept are modeled to determine its optical and thermal efficiency, the achievable outlet temperatures as well as identify shortcomings of the design. Furthermore, the potential of adaptations of the original design that address identified difficulties is investigated.

Conclusions on the potential of the novel cycle and recommendations on how to improve confidence into the model are provided in Chapter 5. Results of the modeling of the designed dual-pressure air receiver system are given in

Chapter 10 and general conclusions on the potential of such a receiver as part of a SUNDISC cycle plant finalize the work in Part III.

Part I

The SUNDISC Cycle

Chapter 2

Simulation of a SUNSPOT cycle plant[1]

In the following sections, a model of a SUNSPOT cycle plant is developed and used for annual simulations. The aim is to quantify the expected energetic limitations of the cycle — that is, how much energy can be dispatched for "on-demand" electricity generation and how much solar radiation has to be defocused — as well as its economic performance in terms of the LCOE.

2.1 Model of the SUNSPOT cycle

The plant is modeled in the MATLAB® R2015a numerical computing environment in hourly time steps with quasi-steady states. As the time steps of the solar input data are greater (hourly) than the response time of the power cycles, a transient model is not deemed necessary. The simplified flow diagram of the model is depicted in Figure 2.1. Descriptions of the main components are presented in this section.

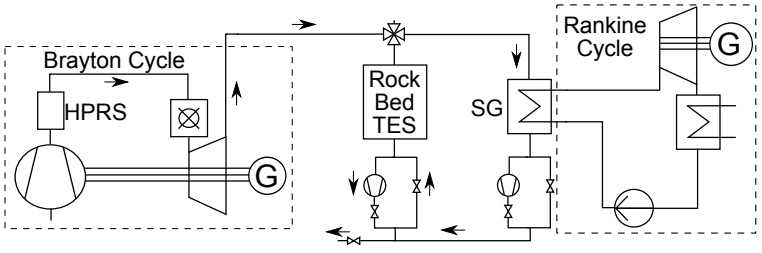

Figure 2.1: Schematic of the SUNSPOT cycle model

[1]parts of this section have previously been published (see Heller and Gauché, 2014) or are under preparation for publishing (see Heller *et al.*, 2016*a*)

2.1.1 Rock bed TES

A model for the rock bed TES in a SUNSPOT cycle plant has previously been developed and validated (Heller and Gauché, 2014). Here, an updated version of it is presented briefly while the reader is referred to the original publication for details on the basic approach.

Thermal model

The basis of the thermal model is the effectiveness-number of transfer units (E-NTU) method of Hughes (1975) as a solution to the so-called Schumann equations (Schumann, 1929) with a correction term proposed by Sagara and Nakahara (1991)

$$NTU^* = \frac{h_\mathrm{v} L}{G\, c_\mathrm{p,f}} \frac{20}{3h_\mathrm{v}\, d_\mathrm{p}^2 / \left[4k_\mathrm{f}\,(1-\epsilon)\right] + 20}. \tag{2.1.1}$$

Therein, L represents the bed length, $G = \dot{m}_\mathrm{f}/A_\mathrm{cs}$ the air mass flux (the quotient of the mass flow rate of the fluid divided by the cross-sectional area of the storage), $c_\mathrm{p,f}$ the specific heat capacity of the fluid (air), d_p the diameter of the particles (rocks), k_f the thermal conductivity of air and ϵ the bed void fraction. All air properties in the model are calculated according to the equations in Appendix A.1.

The volumetric heat transfer coefficient, h_v, can be derived from the surface area-specific heat transfer coefficient, h, and the specific surface area per unit volume of the bed, a:

$$h_\mathrm{v} = h\, a = h \frac{6\,(1-\epsilon)}{d_\mathrm{p}}. \tag{2.1.2}$$

This equation is technically only valid for spheres but is assumed to be sufficiently accurate for crushed rock as well (Allen *et al.*, 2015).

Finding the correct correlation for this surface area-specific heat transfer coefficient is the fundamental challenge of the method. Out of the many different approaches in the literature, the correlation of Wakao and Funazkri (1979), was chosen as it is well established and compares favorably to experiments by Allen *et al.* (2015) with applicable rocks

$$Nu = h\, k_\mathrm{f}/d_\mathrm{p} = 2 + 1.1 Pr_\mathrm{f}^{1/3}\, Re_\mathrm{p}^{0.6}. \tag{2.1.3}$$

Therein, Pr_f is the Prandtl number of the air and $Re_\mathrm{p} = G d_\mathrm{p}/\mu_\mathrm{f}$ is the particle Reynolds number of the flow (Allen, 2014, Eq. 3); μ_f represents the dynamic viscosity of the air.

The model is only valid if the temperature difference within the individual rocks is negligible compared to the difference to the air stream temperature. This is generally the case if the Biot number, $Bi = h\, d_\mathrm{v}/(2k_\mathrm{p})$, has a value of less than 0.3, or more conservatively 0.1 (Allen *et al.*, 2016). In the conducted simulations the maximum Biot number is kept at a value below 0.2 by applying

sufficiently low air mass fluxes through increasing the cross-sectional flow area of the storage.

Allen *et al.* (2014) found dolerite rock to survive thermal cycling well and be available throughout most of central South Africa. Due to this general suitability, dolerite is utilized in the modeled TES as well.

The thermal capacity of rock material, c_s, strongly depends on its temperature, t_s (in degree Celsius). Based on a generalized correlation for rock (Waples and Waples, 2004), Allen *et al.* (2015) propose the dependency for South African dolerite as

$$c_\mathrm{s} = \left[748 + 1.518\frac{t_\mathrm{s}}{^\circ\mathrm{C}} - 0.00129\left(\frac{t_\mathrm{s}}{^\circ\mathrm{C}}\right)^2\right] \mathrm{J/(kg\,K)}. \tag{2.1.4}$$

Further used properties for this type of rock are the thermal conductivity, $k_\mathrm{p} = 3\,\mathrm{W/(m\,K)}$ and density, $\rho_\mathrm{p} = 2657\,\mathrm{kg/m^3}$ (both derived from Allen, 2010), as well as the bed void fraction, $\epsilon = 0.45$ (Allen, 2014).

Pressure drop

Allen *et al.* (2015) present a curve-fit to experimental data for the friction factor of the bed

$$f_\mathrm{v} = 620/Re_\mathrm{v} + 13.7/Re_\mathrm{v}^{0.08} \tag{2.1.5}$$

depending on the volume-equivalent Ergun Reynolds number, $Re_\mathrm{v} = Re_\mathrm{p}/(1-\epsilon)$. The pressure drop can then be derived through

$$\Delta p = f_\mathrm{corr}\, f_\mathrm{v} \frac{L\,\rho_\mathrm{f}\,U_\mathrm{sf}^2}{2\,d_\mathrm{v}} \frac{1-\epsilon}{\epsilon^3} \tag{2.1.6}$$

with $f_\mathrm{corr} = 1.3$ being a correction factor that was added by the author for the degradation of rock due to thermal cycling based on findings by Allen (2014) and U_sf being the superficial approach flow velocity. The volume-equivalent sphere diameter, d_v, is an approximation of the average rock diameter (for more information see Allen, 2014, p. 83).

Discretization

The length of time steps and the size of axial segments have to be chosen so that the error compared with a very high resolution is acceptable (grid independence). Allen *et al.* (2016) found low aberrations of the bed temperature profile after charging-discharging cycles for spacial and temporal resolutions at least up to 2 cm and 30 s, respectively. For annual simulations, this spacial resolution was confirmed, while larger time steps greater than 120 s appear acceptable (see Figure 2.2). All further TES simulations were conducted with a temporal and axial resolution of 60 s and 2 cm (or at least 200 segments for short beds), respectively.

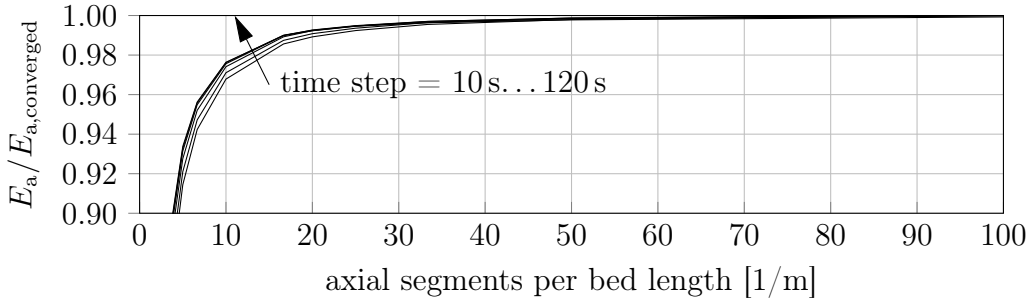

Figure 2.2: Accuracy of annual electricity yield over number of grid cells per meter axial length for different time step lengths

2.1.2 Solar field

The hourly solar field efficiency, η_{SF}, is defined (for example by Wagner, 2008) as the quotient of impinging concentrated solar radiation on the receiver, $\dot{I}_{Re,in}$, divided by the product of the incoming radiation (direct normal irradiance, DNI, $\dot{I}_{DNI}$) and the solar field aperture area

$$\eta_{SF} = \frac{\dot{I}_{Re,in}}{\dot{I}_{DNI} A_{SF}} = \eta_{cbs}\, \eta_{spill}\, \eta_{atm}\, \eta_{HS,refl}\, \eta_{HS,clean}\, \eta_{HS,avail}. \tag{2.1.7}$$

Individual efficiencies are calculated for the loss mechanisms: Losses due to the finite reflectivity and cleanliness of the heliostats (Kolb *et al.*, 2011, Table 8), $\eta_{HS,refl} = 0.95$ and $\eta_{clean} = 0.95$, respectively, as well as the average availability of the solar field, $\eta_{HS,avail} = 0.99$ (Kolb, 2011, Table 7), are implemented as annual averages. Cosine, blocking and shading losses, η_{cbs}, spillage losses, η_{spill}, and atmospheric attenuation losses, η_{atm}, are calculated with the techno-economic simulation tool System Advisor Model (SAM) V.2015.6.30 for every hour of the year.

The solar field geometry is based on eSolar's 1.14 m^2 heliostats in the same layout as utilized in their Sierra SunTower demonstration facility (Schell, 2011). The main parameters of this rectangular, densely-packed solar field are provided in Table 2.1. Details on the model and its validation can be found in Appendix B.

To simulate the hourly solar field efficiency at different solar field aperture areas, the size of the field in the model is expanded while keeping the identical distances between heliostats. At the same time, the tower height (to minimize losses through blocking and shading) and the receiver aperture area (to accommodate for the higher solar field rating) are adjusted to the respective field sizes. Figure 2.3 depicts the simulated annual solar field efficiency for fields up to 8 times the size of the original 13 600 m^2 at the locations Upington, South Africa, and Lancaster, California. The efficiency for a field in either location remains almost constant within this range, which is achieved by the increases in tower height and receiver size (see Appendix B). The field in Upington is

Table 2.1: Parameters of the eSolar field (Schell, 2011)

Parameter	Value
Mirror size	1.14 m^2
North-South field size	190 m
East-West field size	175 m
Number of heliostats	12 180
Image error	1.4 mrad
Tower height	50 m

approximately 4 % more efficient than the one in Lancaster (apart from a higher cumulative annual DNI) due to the closer proximity to the equator.

2.1.3 Pressurized air receiver system

Several receiver systems have been proposed for utilization in solarized gas turbines. A review of them, presented in Section 6.3, shows that the most developed, tested and published on technology is the one utilized in the SOLGATE project (SOLGATE Project Report, 2005) and the follow-up HST project (Buck, 2005). Data from this system is used as the basis of the pressurized air receiver model of the SUNSPOT cycle.

The goal of the HST project was to reach a receiver system air outlet temperature of 1100 °C. However, due to technical problems during testing, a conservative window cooling mechanisms had to be fitted. This increased the thermal energy lost to ambient and therefore limited the energy available to heating up the pressurized air stream. The maximum air outlet temperature achieved in the HST project was approximately 1030 °C (Buck, 2005).

In the present study, it is assumed that these problems can be solved so that the high-pressure receiver system (HPRS) can be operated at a nominal air

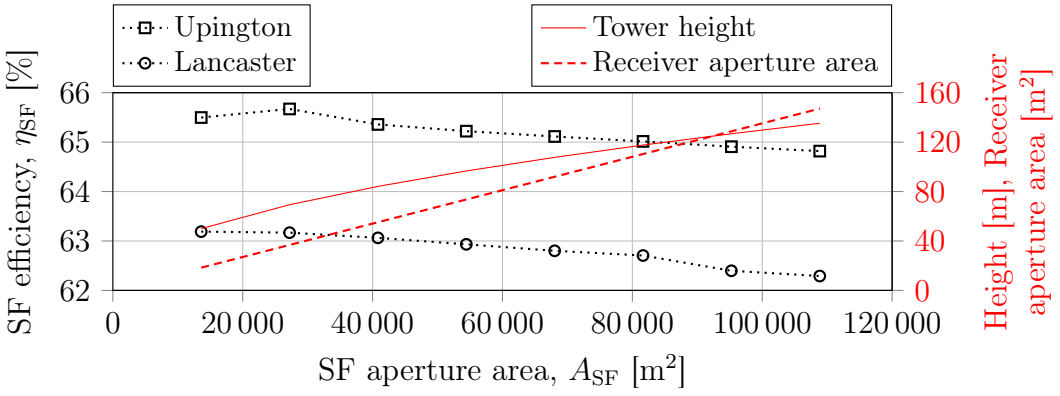

Figure 2.3: Solar field (SF) efficiency for Upington and Lancaster, respectively, as well as tower height and receiver aperture area over solar field aperture area

outlet temperature of approximately $t_{\mathrm{HPRS,out}} = 1100\,^{\circ}\mathrm{C}$. The thermal efficiency of the HPRS, $\eta_{\mathrm{HPRS,t}}$, is based on experimental values from the HST project. However, this data contains obviously unrealistic values of up to 105 % which Buck (2005, p. 50) assumes to stem from imprecise measurements of air mass flow rates or incoming flux. Although Buck (2005, p. 52) excludes all values above 90 % for his linear fit to thermal efficiency data, there is still uncertainty in the validity of the remaining data. To achieve a more conservative receiver system model, the thermal efficiency curve fit was lowered by 5 % (absolute) by the author. The resulting correlation in dependence of the HPRS air outlet temperature, $T_{\mathrm{HPRS,out}}$ (in kelvin), is then defined as

$$\eta_{\mathrm{HPRS,t}} = 0.956 - 1.70 \times 10^{-4} \frac{T_{\mathrm{HPRS,out}}}{\mathrm{K}}. \tag{2.1.8}$$

The most developed HPRS designs necessitate a secondary concentrator, also called compound parabolic concentrator (CPC, see Section 6.1.2). This optical component introduces additional losses from the incoming concentrated solar radiation due to absorption and reflection to ambient. The magnitude of these losses depends strongly on the angle at which the incoming radiation reaches the CPC aperture area (incidence angle). As the solar field model is not sufficiently detailed to provide this information, an annual average CPC efficiency, $\eta_{\mathrm{CPC}} = 0.86$, is assumed. Buck *et al.* (2002) state this as the CPC's design value for an incidence angle of 21° and a CPC reflectivity of 90 %.

In accordance with the SOLGATE system the pressure drop of the HPRS is set to 120 mbar (SOLGATE Project Report, 2005, p. 14). As the receiver system is modular, the individual modules are (mostly) operated in parallel. The flow velocity in them, and the pressure drop caused by them, is therefore expected to be independent of the receiver system load.

2.1.4 Brayton cycle

The Brayton cycle (BC) model assumes a simple cycle without inter-cooling or recuperation (see Figure 2.4). In this section, a gas turbine model is developed and validated.

Design-point conditions

The gas turbine unit (GTU) model is based on the SGT-100 industrial gas turbine by SIEMENS AG (2005) with an ISO rating of 5.25 $\mathrm{MW_e}$. This rating was found to be a likely size for modular medium-scale CSP plants. The single-shaft SGT-100 model was chosen because it fits the desired rating well and has a relatively high design outlet temperature of 534 °C which is needed for an efficient bottoming cycle.

Like most industrial gas turbines on the market, the SGT-100 is not designed for external (solar) firing but for internal combustion of gaseous fuel. In

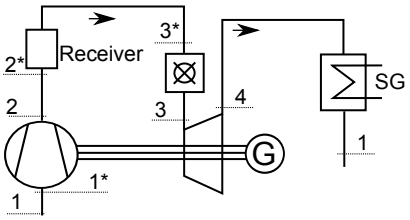

Figure 2.4: Schematic of the Brayton cycle

this work it is assumed that a suitable solarized gas turbine with similar characteristics as the SGT-100 is available. The most important fluid temperatures and pressures at design point of the GTU are given in Table 2.2.

To simulate the GTU's performance under off-design conditions, that is in terms of ambient temperature and load, a simple model was developed. Firstly, the total pressure drop in the diffuser (between points 2 and $2^\star$ in Figure 2.4) is calculated from the GTU's compression ratio of $\pi_{\mathrm{Comp}} = 14.9$ as stated by SIEMENS AG (2005). The pressure drop in the combustion chamber can be calculated from the information given in Table 2.2 as $\Delta p_{\mathrm{Comb}} = p_3 - p_{3^*} = 78\,\mathrm{kPa}$.

Since the respective design-point pressure and temperature at the inlet and outlet of the compressor and turbine are known, the isentropic efficiency of them can be calculated (see for example Boyce, 2006, p. 121) assuming perfect gas behavior

$$\eta_{\mathrm{Comp,is}} = \left[\pi_{\mathrm{Comp}}^{(\gamma_{\mathrm{Comp}}-1)/\gamma_{\mathrm{Comp}}} - 1\right] / \left(T_2/T_{1^\star} - 1\right) = 0.843, \tag{2.1.9}$$

$$\eta_{\mathrm{GT,is}} = \left(1 - T_4/T_3\right) / \left[1 - \pi_{\mathrm{GTp}}^{(\gamma_{\mathrm{GT}}-1)/\gamma_{\mathrm{GT}}}\right] = 0.858. \tag{2.1.10}$$

Therein, γ_{Comp} and γ_{GT} represent the mean heat capacity ratio at the compressor and the gas turbine, respectively. They are calculated from the gas constant of air, $R_{\mathrm{air}} = 287.0\,\mathrm{J/(kg\,K)}$, and the specific heat capacity of air according to Appendix A.1

Table 2.2: Design (single-cycle) parameters of the SGT-100 GTU by SIEMENS AG (2005); "Location" refers to Figure 2.4

Location	Temperature [°C]	Static Pressure [kPa]
1	15	101.3
1*	15	100.3
3*	396	1476
3	1102	1398
4	534	101.3

$$\begin{aligned} \gamma_{\text{Comp}} &= (\gamma_{1^\star} + \gamma_2)/2 \\ &= \left[c_{\text{p},1^\star}/\left(c_{\text{p},1^\star} - R_{\text{air}}\right) + c_{\text{p},2}/\left(c_{\text{p},2} - R_{\text{air}}\right)\right]/2, \qquad (2.1.11) \\ \gamma_{\text{GT}} &= (\gamma_3 + \gamma_4)/2 \\ &= \left[c_{\text{p},3}/\left(c_{\text{p},3} - R_{\text{air}}\right) + c_{\text{p},4}/\left(c_{\text{p},4} - R_{\text{air}}\right)\right]/2. \qquad (2.1.12) \end{aligned}$$

Finally, the GTU's design-point electric power output can be calculated from its design-point air mass flow rate, $\dot{m}_{\text{GTU,air,dp}} = 20.5\,\text{kg/s}$, and the specific work of the compressor, $\Delta h_{1^\star\to 2}$, and the turbine, $\Delta h_{3\to 4}$

$$P_{\text{GTU,dp}} = \eta_{\text{gear}}\,\eta_{\text{Gen}}\,\dot{m}_{\text{GTU,air,dp}}\left(\Delta h_{1^\star\to 2} + \Delta h_{3\to 4}\right). \qquad (2.1.13)$$

With the provided data from SIEMENS AG (2005) for the gear box efficiency, $\eta_{\text{gear}} = 0.99$ and the generator efficiency, $\eta_{\text{Gen}} = 0.965$, a design-point capacity of $5.16\,\text{MW}_\text{e}$ results. This deviates only by 1.7 % from the stated design capacity of $5.25\,\text{MW}_\text{e}$.

Influence of pressure drops, inlet conditions and part-load

In GTUs that are optimized for combined cycle operation, the turbine outlet temperature can be kept within a range of approximately ±10 % for loads above 50 % via variable inlet guide vanes (see for example Muñoz de Escalona *et al.*, 2012, Figure 1). As a simplification, a constant GT outlet temperature is assumed in the developed model. The isentropic efficiency of the compressor and turbine are modeled as being constant in the given range of loads as well (compare with Boyce, 2006, Figure 3-16).

The desired power output is achieved by adjusting the pressure ratio of the compressor, which furthermore influences the air mass flow rate through the turbine. At the high pressure ratio over the single turbine stage of the SGT-100, choking conditions are reached (Mallinson and Lewis, 1948, Figure 10). Therefore, the flow velocity, $U_{\text{air},3}$, reaches the speed of sound, c_3, at the turbine inlet

$$\dot{m}_{\text{GT,air}} = \rho_{\text{air},3}\,A_{\text{cs},3}\,U_{\text{air},3} = \rho_{\text{air},3}\,A_{\text{cs},3}\,c_3 = \rho_{\text{air},3}\,A_{\text{cs},3}\,\sqrt{\gamma_3\,R_{\text{air}}T_3}. \qquad (2.1.14)$$

The cross-sectional area at the turbine inlet, $A_{\text{cs},3}$, is derived by solving Equation (2.1.14) for it with design-point pressure, temperature and mass flow rate input data.

SIEMENS AG (2005) presents performance data for an SGT-100 turbine in a CC configuration with a heat recovery steam generator downstream. The SG system causes a pressure drop of 2.0 kPa so that the turbine outlet pressure is increased to $p_4 = 103.3\,\text{kPa}$. This lowers the power output to $P_{\text{GT}} = 5.13\,\text{MW}_\text{e}$ at a fuel-to-electric efficiency of 30.2 %. The simulation of this case with the

developed model predicts a power output of 5.05 MW_e (−1.5 %) and a thermal-to-electric efficiency of 32.2 %. Adding an estimated combustor efficiency of 99 %, the deviation in fuel-to-electric efficiency is 5.5 %.

The GT model is, therefore, seen as sufficiently accurate for simulating the effect of changing pressures upstream the compressor (ambient air pressure), upstream the turbine (receiver pressure drop) and downstream the turbine (rock bed or steam generator) on power generation and the required turbine inlet temperature.

2.1.5 Rankine cycle and steam generator

The Rankine cycle (RC) model is based on a simple overall thermal-to-electric efficiency $\eta_{RC} = 1 - \sqrt{T_{sink}/T_{source}}$ (Curzon and Ahlborn, 1975). Deviating from the original definition, T_{sink} is here defined as the condensate temperature and T_{source} as the live-steam temperature (both in kelvin) to account for the poor heat transfer of non-pressurized air as the heat sink (for dry cooling) and source. The superheater approach temperature is estimated at 40 K (Li and Priddy, 1985, p. 545) resulting in a design-point live steam temperature of approximately 500 °C. This results in common hourly RC efficiencies between 37 % and 40 % for the ambient temperatures at the location Upington.

Additional losses result from the elevated exhaust air temperature of the steam generator, which is estimated at a value of 140 °C — in accordance with SIEMENS AG (2005); compare also with PHOEBUS-type plants (Section 1.2.2). For the defined design-point temperatures and an ambient temperature of 25 °C, approximately 22 % of the energy contained in the air entering the steam generator is thus lost. The pressure drop in the SG is estimated at 2.0 kPa (see Section 2.1.4).

A heat transfer model of the steam generator and RC would result in more detailed information on the properties in the bottoming cycle and, potentially, more realistic results for the annual power generation. However, such a model requires a detailed design of the steam cycle including, for example, the number and pressure levels of the turbine stages, the utilization of reheating and the number of extraction points (see Pitot de la Beaujardiere *et al.*, 2016). This level of detail seems unjustified at the current state as it would have to be adjusted to individual set-ups of the plant and, therefore, limit comparability.

2.1.6 Economic model

The economic model is based on specific costs for the major components of the plant. In this section, first costs for the rock bed TES system as well as the local fossil fuel and land cost are specified. Afterwards the remaining components' costs are presented as derived from the SOLGATE Project Report (2005) and the ECOSTAR Roadmap Document (Pitz-Paal *et al.*, 2005).

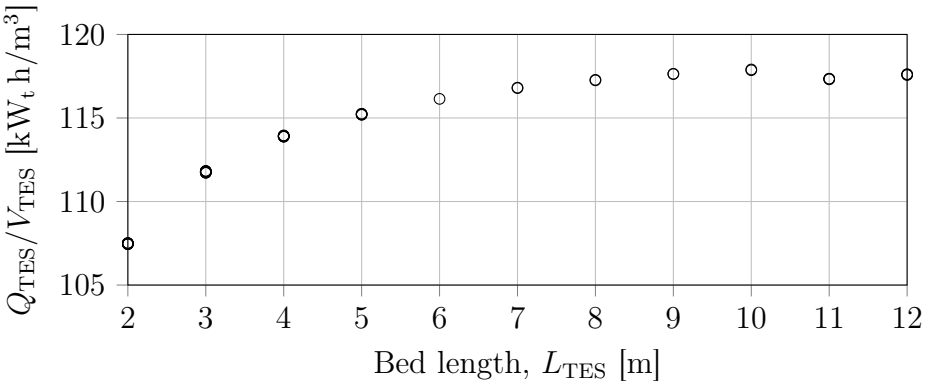

Figure 2.5: Storage capacity per volume of rock bed over bed length

Specific TES system cost

The specific capital cost of the TES system is estimated at 11.5 USD/(kW$_t$ h). This value was derived for a conservative design in a rock bed concept comparison by Allen and von Backström (2016). Two other investigated concepts are predicted by the authors to lower this price below 5 USD/(kW$_t$ h). All of these values compare very favorably to cost forecasts of two-tank molten salt storage systems (for example by Kolb, 2011) which predict a specific cost of 25 USD/(kW$_t$ h).

The TES capacity used as the reference for the specific cost by Allen and von Backström (2016) is the amount of retrievable energy once cyclic thermocline stability has been reached. To calculate costs of TES systems implemented into the plants of this study (*not* for operating the TES), the procedure by Allen and von Backström (2016) is repeated: The storage is charged with hot air at 600 °C until the air outlet temperature increases to 45 °C. Discharging is done with cold air at a temperature of 20 °C until the air outlet temperature drops below 550 °C. The air mass flux during charging and discharging is 0.1 kg/m^2 s and 0.2 kg/m^2 s, respectively. The charging-discharging cycle is repeated 80 times, at which time thermocline stability was achieved.

The calculated specific storage capacity per volume of rock for storage diameters between 17 m and 32 m and bed length between 2 m and 12 m over the storage length is depicted in Figure 2.5. There is no dependence of the capacity on the storage diameter as the mass flux is kept constant. The capacity per volume increases slightly from approximately 108 kW$_t$ h/m^3 to 118 kW$_t$ h/m^3 for longer bed length, which is caused by the decreasing fraction of unused bed length due to the thermocline region. To decrease the computational time of simulations, the specific capacity is universally set to a value of 118 kW$_t$ h/m^3 in the economic model.

The found capacities are approximately half of the amount of thermal energy that could be retrieved from a bed completely heated to 600 °C. The charging methodology used in the annual simulations (see Section 2.1.7) — that

is, continued charging when the outlet air temperature rises — can thus double the effective capacity of the TES system.

Location-dependent costs

The fuel cost is based on a forecast by the South African Department of Energy (2013, p. 34) on which an annual cost increase equal to the South African inflation rate (6 %) was superimposed. As this price is based on the world market price for liquefied natural gas (LNG), it can be seen as an upper limit appropriate for countries without access to natural gas through pipelines.

The cost of land generally does not make up a large fraction of the investment cost of a CSP plant. The specific land cost of property located in proximity to Upington, as advertised on online property search engines, averages at below 0.02 USD/m^2 which is two orders of magnitude lower than as defined in the ECOSTAR report for locations in southern Spain. Even if a considerable cost increase is applicable for property with good access to infrastructure (water, roads, electrical grid), the impact on the total cost will remain small.

Cost model for 2005

As most cost figures are derived from sources that are more than ten years old, the specific costs should be adjusted (a) for inflation and (b) for cost decreases due to innovation and increasing operating experience. The former can easily be calculated with the inflation data of the years since publication. However, technology cost decline prediction is disproportionately more difficult and associated with large uncertainty, especially because the core components of the technology are still in the development stage. The system comparison is, thus, based on non-adjusted cost information in 2005 United States dollar. All costs are converted to United States dollar at the time of their publication (where necessary) and those of the TES system, land, fuel and for operation and maintenance (O&M, derived from Kolb, 2011, Section 3.5) are adjusted for inflation to the year 2005 with data of the United States Department of Labor (2016). The used values for specific component costs are stated in Table 2.3. An adjusted cost model that takes technology cost decrease through learning rates into account is presented in Appendix C. A surcharge of 20 % of the total investment cost is added for indirect costs (see Pitz-Paal *et al.*, 2005).

The correlation given by Pitz-Paal *et al.* (2005, Figure 1-3) is used for calculating the LCOE

$$LCOE = (crf \times CAPEX + OPEX) / E_{\mathrm{a}}, \tag{2.1.15}$$

wherein $CAPEX$ and $OPEX$ represent the capital and operational expenditure (including insurance), respectively, and the fixed charge rate is calculated as

$$crf = k_{\mathrm{d}} (1 + k_{\mathrm{d}})^n / [(1 + k_{\mathrm{d}})^n - 1]. \tag{2.1.16}$$

Table 2.3: Specific costs (in 2005-USD) of components (SOLGATE Project Report, 2005, tables 8 and 9; Pitz-Paal *et al.*, 2005, tables 5-19–5-22); the constant for the cost calculation of the tower is part of an exponential equation dependent on its height

Component	Cost	Unit	Relative to
TES system	9.50	USD/kW$_t$h	TES capacity
HPRS	191	USD/kW$_t$	HPRS nominal rating
Brayton cycle	519	USD/kW$_e$	GTU nominal rating
Adaption of GT	1090	10^3 USD	absolute
Rankine cycle	729	USD/kW$_e$	cycle nominal rating
Solar field	160	USD/m^2	mirror surface area
Tower	484	10^3 USD	constant in equation
Control	605	10^3 USD	absolute
Annual O&M	58.6	USD/kW$_e$	installed total rating

The remaining input parameters include the annual interest rate $k_d = 8\,\%$, the plant lifetime of $n = 30$ years, and the annual insurance cost of 1.5 % (real) of the total plant investment cost (derived from Pitz-Paal *et al.*, 2005, p. 13, and the SOLGATE Project Report, 2005, Section 4.5.4.1, respectively). A lower annual interest rate, as currently realistic for developed countries, would improve the viability of any CSP plant considerably. The used value is chosen for the South African economic environment.

2.1.7 Operating strategy

The operating strategy has a determining influence on power generation, plant lifetime, LCOE and co-firing rates. In this model, continuous electricity generation was sought without taking a demand profile or differing feed-in tariffs into account. The resulting primary operating rules used are the following:

- The gas turbine is operated at loads between 55 % and 100 % when a threshold solar radiation will be exceeded for at least two consecutive hours. The GT is therefore not started for an isolated hour of good solar irradiation and a drop in GT outlet temperature is avoided.
- Co-firing is only employed to complement incoming concentrated radiation when the latter accounts for more than 80 % of the GT threshold. This is intended to keep the co-firing rate at below approximately 1 % while allowing to utilize most incoming solar radiation.
- The steam turbine is operated whenever the GT will not run for at least two consecutive hours to avoid starting up the turbine for a short duration. The RC only runs at full load or no load to achieve a constant supply of electricity and a high thermal-to-electric efficiency.

- The start-up time of the Brayton cycle including pressurized air receiver is estimated at 30 minutes. Although this value is derived from experiments with a different pressurized air receiver technology (Quero *et al.*, 2014), it is assumed to be valid for the SOLGATE receiver.

- The start-up time of the Rankine cycle including SG is estimated at 30 minutes. Kehlhofer (1999, p. 199) state typical start-up times of 40 min to 50 min for 50 MW_e to 400 MW_e CC plants after 8 h of standstill. The reasons for the shorter start-up time are that (1) the implemented SG and RC are several-fold smaller in rating and therefore have less thermal inertia as well as (2) the bottoming cycle is decoupled from the GT and thus does not depend (directly) on its operational limitations.

- Storage charging continues even when the air outlet temperature of the TES increases. While this highly increases the thermal capacity of the TES system, the additional costs due to increased pumping power consumption and the need for a high-temperature fan have to be evaluated at a later stage. A promising option is to run the Rankine cycle directly from the LPRS outlet air once the TES air outlet temperature surpasses a pre-defined threshold.

- Storage discharging continues until the air outlet temperature reaches 480 °C. This is assumed to be the limit at which the SG can operate (compare to Allen and von Backström, 2016).

2.2 Parametric study on SUNSPOT cycle plants[2]

The developed model is used to conduct simulations of the annual electricity yield and LCOE of SUNSPOT cycle plants. Selected component ratings are varied to investigate the potential and shortcomings of the cycle.

2.2.1 Component rating ranges

While the GT is kept constant at a value of 5.25 MW_e (see Section 2.1.4), the nominal rating of the RC is varied between 1 MW_e and 5 MW_e. A steam turbine with a small rating requires less thermal energy from the TES and, therefore, allows for (almost) uninterrupted electricity generation of the plant, however, at a much lower level than during gas turbine operation. A steam turbine with a comparable rating to the gas turbine's, on the other hand, can

[2]This section presents updated results, which were derived with the refined model of Section 2.1, to previously published studies (Heller and Gauché, 2014; Heller and Hoffmann, 2014)

only be operated for a few hours per night due to the large required amount of thermal energy in the steam generator.

The storage volume is defined by the length and cross-sectional area of the storage. While the bed length is varied between 2 m and 5 m, the cross-sectional area is found iteratively with the boundary condition of a maximum Biot number of 0.2 (see Section 2.1.1). Note that here the *maximum* Biot number is set to 0.2 while Allen and von Backström (2016) adjusted the flow so that the *average* Biot number during charging reached approximately 0.2. Resulting from this, the air mass flux in this study is only approximately 40 % of the value used by Allen and von Backström and the cross-sectional area, therefore, considerably larger. For the defined RC ratings, the cross-sectional area varied between 227 m^2 and 346 m^2. The resulting storage capacity was calculated according to the methodology presented in Section 2.1.6 to be between 49 MW_t h and 202 MW_t h. Annual simulations are started by pre-charging the TES from ambient temperature (completely discharged) with air at nominal charging temperature and flow rate for 12 h.

The solar multiple is a widely-used figure to quantify how much thermal energy can be collected in a CSP plant compared to the amount that the power block requires to run at nominal load. A CSP plant without storage (in the HTF cycle) would commonly have a solar multiple close to unity so that little to no concentrated solar radiation has to be defocused. For example, the PS10 plant, which includes a small buffer storage for cloud transients with a capacity of 0.5 h at full turbine load, has a solar multiple of 1.3 (Osuna *et al.*, 2006). Avila-Marin *et al.* (2013) found that DSG and molten salt central receiver plants without storage reach their lowest LCOE values at a respective solar multiple of 1.4.

In an asynchronous combined cycle, like the SUNSPOT cycle, the solar field and receiver operate similarly as in a plant without a TES system because the nominal receiver rating is at most the same as the GTU nominal energy requirement. Therefore, the solar multiple in the current study is only varied between 1.0 and 2.0, which corresponds to solar field aperture areas between 27 000 m^2 and 57 000 m^2.

2.2.2 Results

Energetic results of the simulations are presented in terms of the configurations' annual electricity yield, E_a, the capacity factor of each of the two cycles (cf_{BC} and cf_{RC}, respectively) and the fraction of incoming concentrated solar radiation that is defocused due to a limited receiver rating, $f_{defocus}$. The receiver rating is dictated by the gas turbine rating as they are directly linked. The annual time of no power generation, $TNPG_a$, quantifies the cumulative number of hours per year in which no power is generated. The time of no power generation (TNPG) can be used to compare different setups in terms of their ability to provide guaranteed baseload power at the lowest part-load capacity. Unlike

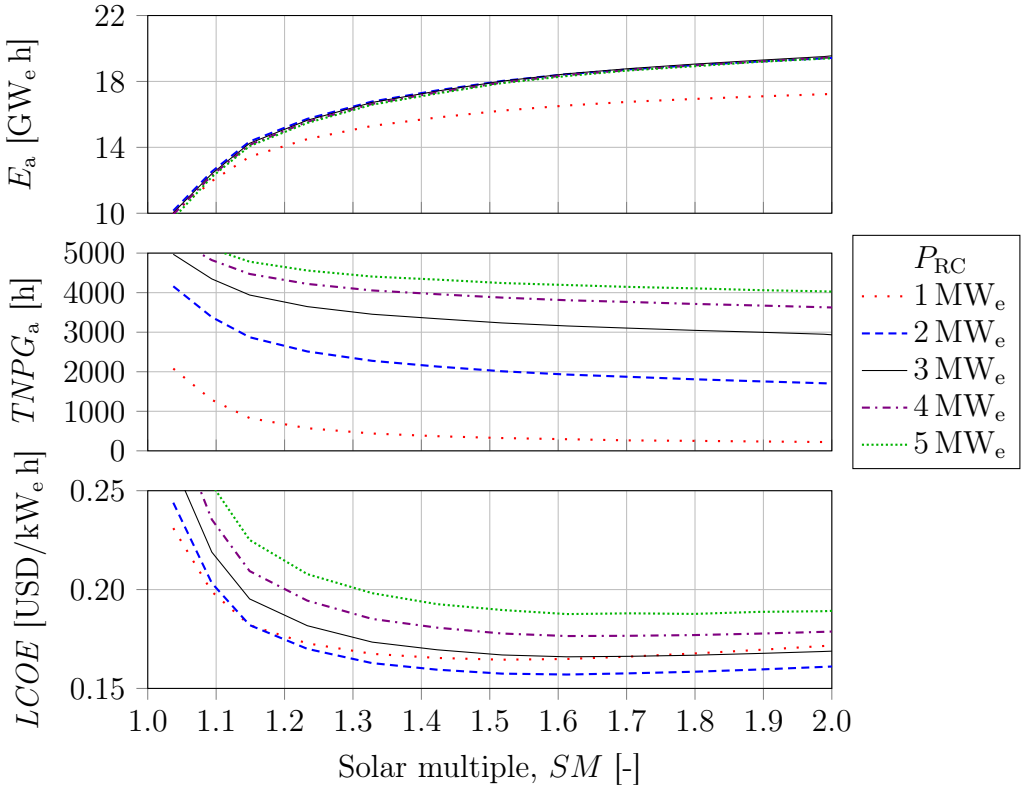

Figure 2.6: (Top) Annual electricity yield, E_a, (middle) time of no power generation, $TNPG_a$, and (bottom) $LCOE$ over solar multiple for SUNSPOT cycle plants with different RC cycle ratings, P_{RC} (bed length optimized for lowest LCOE — see text)

the annual electricity yield, the TNPG does not include the mean annual plant availability of 96 % (derived from Pitz-Paal *et al.*, 2005, p. 12) to allow easy comparison with a perfect baseload plant operating for 8760 h per year.

In the following plots, every data point represents the plant configuration with the bed length that renders the lowest LCOE (mostly 3 m). Due to its low specific cost, an oversized TES system leads to only slightly increased LCOE values.

In Figure 2.6 (top), the annual electricity yield is shown for the investigated plant configurations. The most important finding from the plot is that — for any solar multiple — increasing the RC rating above 2 MW$_e$ only results in a small increase in electricity yield. This is expected as the energy contained in the exhaust gas of the Brayton cycle is only enough to supply a steam generator for a RC of approximately half the nominal rating at design point. The curve for the annual electricity yield over the solar multiple, expectedly, flattens towards larger solar fields.

The plot in Figure 2.6 (middle) depicts the annual TNPG of the plants. The plant with the lowest RC rating operates almost throughout the year if the solar multiple is larger than 1.2. For a plant with twice that RC rating,

Table 2.4: Simulation input parameters and performance indicators for four SUNSPOT cycle plant configurations

Parameter	Unit	Configurations			
		SPOT 1	SPOT 2	SPOT 3	SPOT 4
BC rating	MW_e	5.4	5.4	5.4	5.4
RC rating	MW_e	1.0	2.0	5.0	5.0
SM	-	1.5	1.6	1.6	2.0
Q_{TES}	MW_t	80.4	80.4	111	111
$f_{defocus}$	%	17.5	20.2	20.2	31.0
$TNPG_a$	h	323	1930	4190	4030
cf_{BC}	%	23.7	24.4	24.4	25.8
cf_{RC}	%	59.3	40.8	16.1	17.0
E_a	$GW_e\,h$	16.2	18.4	18.3	19.4
LCOE	$USD/kW_e\,h$	0.165	0.157	0.188	0.189

the annual TNPG does not fall below approximately 1500 h even for very large fields. For plants with even larger RC ratings, the minimum annual TNPG increases further. If a RC with a rating of 5 MW_e is implemented, the plant only operates during roughly half of the year.

The plot in Figure 2.6 (bottom) shows that the lowest electricity generation costs occur at a RC rating of 2 MW_e and a solar multiple between 1.5 and 1.7. The LCOE increases strongly for solar multiple values below 1.2.

The quantitative results of selected plant configurations are presented in Table 2.4. Configuration SPOT 1 represents the combination of solar multiple and bed length that results in the lowest LCOE for a RC rating of 1 MW_e. Only a relatively small fraction of concentrated solar radiation is defocused due to the small solar field. In fact, most of this defocusing occurs when the solar input is not sufficient to start-up the gas turbine. Almost uninterrupted power delivery to the grid is achieved ($TNPG_a \ll 500$ h), which is made possible by the low energy demand of the SG and the large TES system capacity (approximately 30 hours of full-load operation). Configuration SPOT 2, with a higher RC rating and a slightly larger solar multiple, has an increased need for defocusing and a much higher $TNPG_a$ value. However, the annual electricity yield is also increased by 14 %.

Configurations SPOT 1 and SPOT 2 have a much lower RC rating than that of their respective Brayton cycle. SPOT 3 and SPOT 4, on the other hand, have a RC nominal rating of 5 MW_e so that power generation at night can continue at a high rate. However, due to the high thermal demand of the steam generators, power generation only occurs during approximately half of the year and the capacity factor of the RC, cf_{RC}, is low. This might be a desirable behavior for plants that mainly provide dispatchable power during a limited number of hours per day but not for delivering baseload power to the

grid. Furthermore, the LCOE of SPOT 3 is 20 % higher than that of SPOT 2.

In SPOT 4, the solar multiple is increased to a high value (for a plant without storage) of 2.0. Therefore, the fraction of defocused energy increases to 31 % while the electricity yield and the TNPG can only be improved slightly, considering the high cost of the solar field. Plant setups with Rankine cycle ratings of 3 MW_e and 4 MW_e showed the expected behavior with results between those of SPOT 2 and SPOT 3.

2.3 Conclusions on the SUNSPOT cycle

It was found that even with a high TES capacity, the basic SUNSPOT cycle is not able to achieve baseload characteristics at a high annual solar share. The bottleneck of the whole system in terms of dispatchability is the limited mass flow throughput of the gas turbine, which limits the thermal energy supply into the TES even at high solar multiples. This additional energy would most likely be available, because a solar multiple greater than unity is necessary to run the GT at full load at any time except for times of highest irradiation. An elevated solar multiple of, for example, 2.0, means that during hours of high solar irradiation potentially usable solar energy has to be discarded through heliostat defocusing. At the same time, the TES does not generally acquire enough thermal energy to power the Rankine cycle throughout the night, which results in a low capacity factor of the latter.

Chapter 3

Dual-Pressure Air Receiver Cycle[1]

To address the identified shortcomings of the basic SUNSPOT cycle in terms of dispatchability and baseload capability a novel cycle is presented. In this section, the so-called Stellenbosch University Direct Storage Charging Dual-Pressure Air Receiver (SUNDISC) cycle is first described in detail with the expected benefits compared to the SUNSPOT cycle. Furthermore, potential variations to its layout and common operating modes of a SUNDISC cycle plant are presented. Finally, the SUNSPOT cycle model of Section 2.1 is extended and simulations are conducted with the SUNDISC cycle plant model.

3.1 Description of the cycle

The SUNDISC cycle, as depicted in Figure 3.1, extends the basic SUNSPOT cycle with an additional low-pressure receiver system (LPRS). The LPRS circumvents the GTU, which has been identified as the bottleneck of the original cycle, by directly charging the TES or supplying the SG with hot, non-pressurized air. However, it not only provides additional thermal energy to the bottoming cycle, it does so by capturing concentrated solar radiation which would normally have to be discarded through defocusing (depicted in Figure 3.2). Therefore, larger solar multiples can be utilized in a cost-effective manner, especially if the specific LPRS cost is lower than that of the HPRS (which is not necessarily the case). The expected effects of the enhancement can be summarized as follows: Increased capacity factors of the GTU, steam turbine, heliostat field and HPRS are achieved at the cost of a potentially lower capacity factor of the LPRS while maintaining high solar shares.

The LPRS is expected to be of the open volumetric type (as in PHOEBUS-type plants), which enables the use of an air return loop. In such a loop the outlet air of the SG or TES is ducted back up the tower, potentially around the receiver walls and partially drawn into the receiver. The fraction of the total amount of returned air that is drawn back into the receiver is

[1] parts of this section are under preparation for publishing (see Heller *et al.*, 2016*a*)

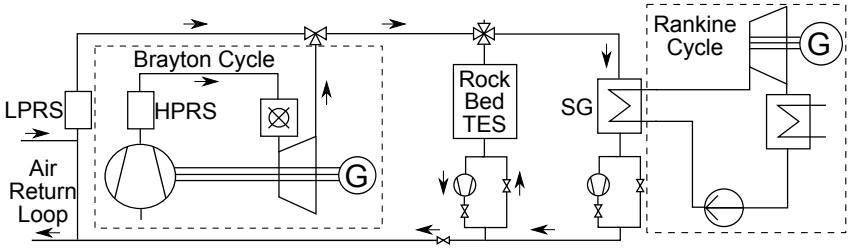

Figure 3.1: Schematic of the SUNDISC cycle

referred to as its air-return ratio. Air-return ratios of approximately 50 % have been achieved in experiments with the HiTRec technology (Ávila-Marín, 2011) while Marcos *et al.* (2004) suggested values of up to 60 % for improved designs. The incentive for reintroducing the outlet air of the SG or TES is the possibility of capturing the thermal energy that remains in the exhaust gas due to its elevated temperature. SG air outlet temperatures between 100 °C and 200 °C are common (Marcos *et al.*, 2004). However, if most of the exhaust energy is recovered, higher temperatures may be preferable to increase the mean temperature of heat supply, therefore benefiting the Rankine cycle thermal-to-electric efficiency.

3.2 Variations to the layout

So far, only general properties of a dual-pressure receiver system have been discussed. In this section, different variations of the receiver system and their respective characteristics are described.

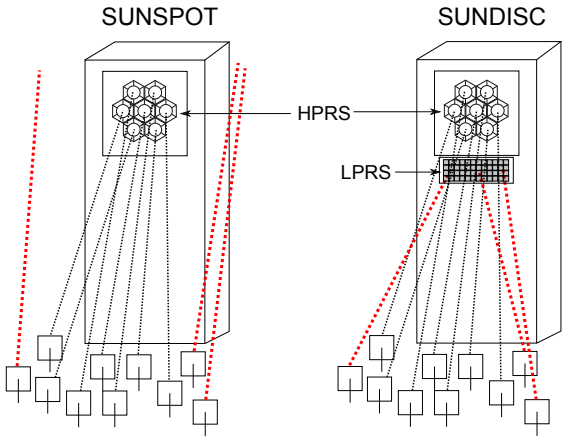

Figure 3.2: Schematic comparison of defocused concentrated radiation in the SUNSPOT cycle and its use in a SUNDISC system

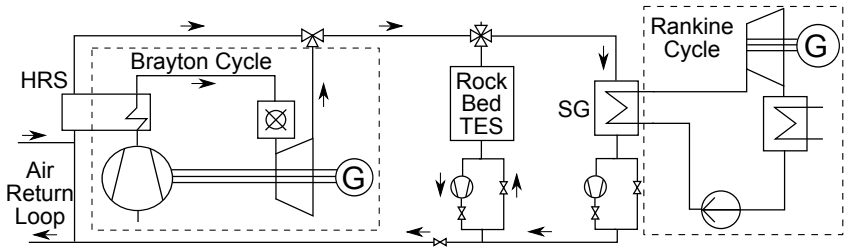

Figure 3.3: Schematic of the SUNDISC cycle with hybrid receiver system (HRS)

3.2.1 Dual receiver system

The first variation of the SUNDISC cycle employs two physically separated receiver systems, as depicted in Figure 3.1. The HPRS can consist of several pressurized air receivers in parallel — to increase the mass flow rate — and in series — to heat up the pressurized air in a cascaded manner. The latter has, among others, been proposed and tested for the two most mature high-temperature pressurized air receiver technologies, the DIAPR and the REFOS. Both technologies reached mean outlet temperatures in excess of 1000 °C (see Section 6.3).

Utilizing a dual receiver system has the advantage that the receivers can be operated independently of each other, which simplifies their design and operation. Because they are separate targets, however potentially directly adjacent, heliostat re-focusing between the two is a possible way of controlling them (see Figure 3.2). If one of the systems — typically the HPRS — requires a higher thermal flux or has a smaller acceptance angle, they can be arranged in an appropriate manner. This could mean that the HPRS is located at the heliostats' central aiming point, geometrically surrounded by a ring of low-pressure receivers. Another option is the intentional separation of both receiver systems in one or several tower(s) in order to create two targets and, therefore, decrease losses through blocking, shading and spillage throughout the day and year. The latter option could prove more advantageous in a multi-tower arrangement.

3.2.2 Hybrid receiver system

A hybrid receiver system, as depicted in Figure 3.3, heats up both air streams in one component. The high- and low-pressure absorber elements in this configuration would typically be the same, although different surfaces of them are used for the two air streams. The thermodynamic characteristics of this concept are discussed in detail in Section 6.4.

An obvious advantage of the hybrid over the dual-receiver system is that only a single receiver system is implemented. At least in some cases, this will enable lower total system costs. Compared to a purely pressurized receiver system additional thermal energy can be absorbed in the same system. Therefore,

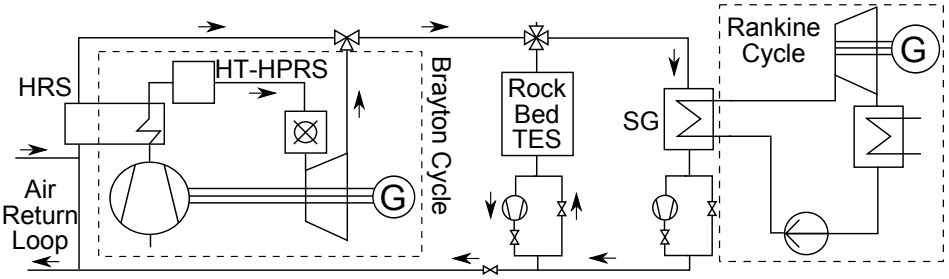

Figure 3.4: Schematic of the SUNDISC cycle with cascaded hybrid receiver system (HRS)

fluxes can be increased and the thermal efficiency as well as the cost-effectiveness of the receiver system are enhanced. However, controlling heat transfer from incoming radiation to two separate fluids that use the same absorber elements is expected to prove challenging.

3.2.3 Cascaded hybrid receiver system

The air outlet temperature of tubular receivers is limited to approximately 850 °C by the maximum allowable material temperature of the steel absorber elements. These receivers are, therefore, often designated (a) as pre-heaters for combustion chambers, (b) for high-temperature receivers with ceramic absorbers or (c) for utilization in Brayton cycles with low turbine inlet temperatures — typically micro gas turbines. The SUNDISC cycle is intended to feature higher GT inlet (and outlet) temperatures without significant co-firing in nominal conditions. This can be achieved by employing a pressurized high-temperature (HT) receiver system downstream the hybrid receiver system (see Figure 3.4). The HT-HPRS in such a cascaded hybrid receiver system is likely to be a pressurized volumetric air receiver such as the DIAPR or REFOS (see Section 6.3). In principle, the addition of the HT-HPRS to the hybrid receiver system does not have a fundamental impact on the operation or design of the components or system.

3.3 Operating modes

The increased number of independent subsystems in the SUNDISC cycle compared to synchronous CCs or the asynchronous SUNSPOT cycle allows for a large degree of flexibility in operating strategy. Depending, for example, on component ratings, demand profile and allowable co-firing rates different operating modes can be desirable. The most common modes of a SUNDISC cycle plant with a dual receiver system are depicted in Figure 3.5 and can be grouped as follows.

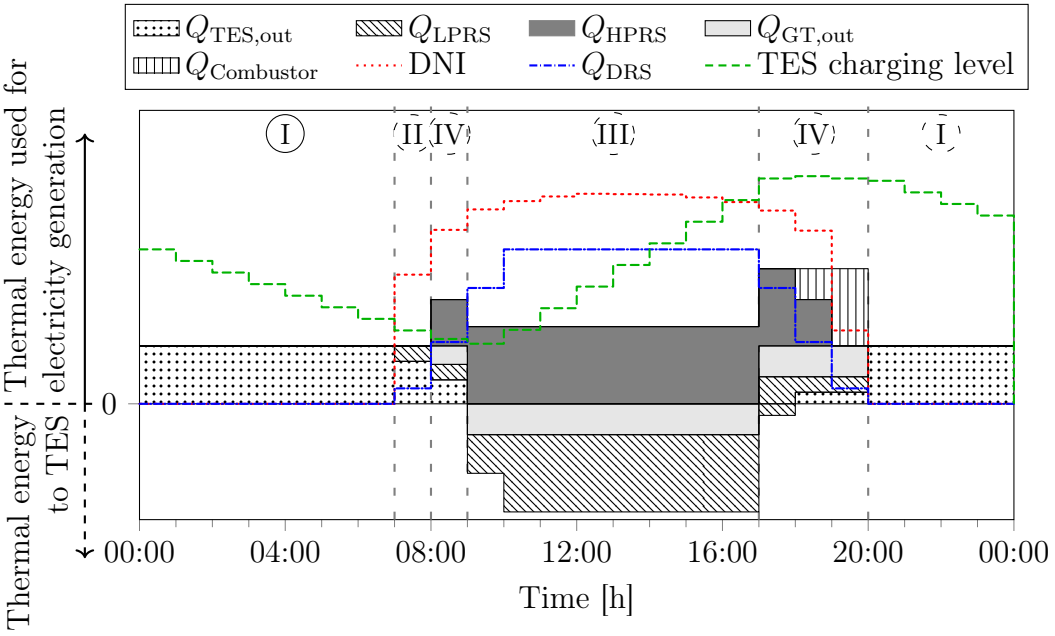

Figure 3.5: Schematic of thermal energy usage in a SUNDISC cycle plant on an generic day; $Q_{\text{GT,out}}$: thermal energy of the GT outlet air flow; $\dot{Q}_{\text{Combustor}}$: thermal input from co-firing; Q_{DRS}: combined thermal output of both receiver systems

Nominal discharge operation — nighttime (I) At night or during prolonged periods of no irradiation the SG is supplied with thermal energy by discharging the TES.

Low irradiation — morning/afternoon (II) In morning and afternoon hours, when the irradiation is not sufficient to power the gas turbine, the LPRS can assist the TES in providing hot air for use in the SG.

Nominal solar operation — daytime (III) During nominal conditions at midday the HPRS and Brayton cycle run at full load and additional concentrated solar radiation, available due to a large solar multiple, can be captured in the LPRS. The exhaust gases of both receiver systems charge the TES while the SG is not in use.

High demand — morning/evening/midday (IV) Both turbines can generate electricity simultaneously whenever the electricity demand from the grid is high. Depending on the time of the day when this occurs, they can be powered from different sources. If the available amount of solar energy is larger than the demand from the HPRS, both receiver systems provide thermal energy for their respective cycles. If need be, the SG can be powered by the LPRS and storage discharging simultaneously. If higher hybridization rates are allowed, the GT can also be powered through the combustion chamber. The

SG is supplied with hot air from the GT outlet and through TES discharging in this case. To avoid starting up the Rankine cycle for short periods of time, this mode should preferably be limited to morning or evening hours before or after periods of Mode (I) or (II), which agrees well with South African peak demand hours.

3.4 Higher LPRS outlet temperatures

Mean outlet temperatures far higher than those of common GTs can be achieved in state-of-the-art open volumetric receivers (see Section 6.2). This allows for an increase of the live steam temperature, as well as of the charging temperature of and energy density in the TES. Assuming that the TES system as well as the SG can facilitate higher temperatures, they could be supplied with hotter air from the LPRS or a mixture of LPRS and GT exhaust air.

If it proves advantageous to limit the SG inlet temperature to a lower value, the TES can still be charged with higher-temperature air — achieving higher energy densities. During discharging this hotter air would then be mixed with ambient air through a mixing valve to reach tolerable temperatures at the SG inlet.

The merit of such a setup featuring two TES charging temperature levels will have to be determined taking changes in storage cost, LPRS efficiency and Rankine cycle efficiency at higher air temperatures into consideration.

Chapter 4

Simulation of a SUNDISC cycle plant[1]

To compare the energetic and economic performance of different configurations of a SUNDISC cycle plant with each other and to other technologies, the model of the SUNSPOT cycle is expanded and a parametric study is conducted with it. The operational and economic performance of the configuration that yields the lowest levelized cost is further presented.

4.1 Additions to previous model

The model used for simulations of SUNDISC cycle plants is almost identical to the one of the SUNSPOT cycle. Only small changes had to be made to the operating strategy and a model for the LPRS was added.

4.1.1 LPRS model

The LPRS model is based on the HiTRec technology (Hoffschmidt *et al.*, 2003*a*). The combined optical and thermal efficiency of the LPRS is calculated through an adaptation of a curve fit to experimental data (Hoffschmidt *et al.*, 2003*a*, Figure 15) as

$$\eta_{\text{opt+t,LPRS}} = 1.26 - 4.82 \times 10^{-4} \frac{T_{\text{LPRS,out}}}{\text{K}}, \tag{4.1.1}$$

wherein, $T_{\text{LPRS,out}}$ is the receiver's air outlet temperature (in kelvin).

The outlet temperature of the LPRS is equal to that of the GT (534 °C) and its inlet temperature is equal to the ambient temperature, that is, no air return loop is implemented. The model additionally includes a start-up time of 30 min to account for the system's thermal inertia (Hirsch *et al.*, 2011).

[1] parts of this section are under preparation for publishing (see Heller *et al.*, 2016*a*)

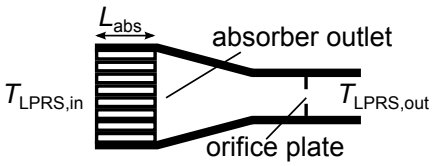

Figure 4.1: Schematic of a HiTRec absorber module

The pressure drop of the absorber of the LPRS, $\Delta p_{\text{LPRS-absorber}}$, can be calculated from an approximation of the Forchheimer-Darcy equation

$$\Delta p_{\text{LPRS-absorber}} = L_{\text{abs}} \left[\frac{\mu}{k_1} U_{\text{sf}} - \frac{\rho}{k_2} U_{\text{sf}}^2 \right]_{\text{NPA,out}} . \tag{4.1.2}$$

Therein, L_{abs} is the length of the absorber in flow direction (see Figure 4.1). Conservatively, the dynamic viscosity, μ, density, ρ, and superficial flow velocity (orthogonal to the absorbing surface), U_{sf}, of the non-pressurized air stream are evaluated at the outlet of the absorber. With values according to Becker *et al.* (2006) for the two coefficients $k_1 = 1 \times 10^{-7}\,\text{m}^2$ and $k_2 = 0.011\,\text{m}$, this results in values of less than 0.1 kPa. The pressure drops of orifice plates and connecting piping are therefore expected to dominate the total pressure drop so that a constant value for it is used instead. From design parameters for the PHOEBUS plant by Grasse (1991) this is estimated at 1.0 kPa.

The specific cost of the LPRS is defined relative to its nominal rating according to Pitz-Paal *et al.* (2005, Table 5-19) at 125 USD/kW$_\text{t}$.

4.1.2 Operating strategy

The operating strategy of the SUNDISC cycle plant model is mostly identical to the one of the SUNSPOT cycle. The major difference is that instead of being defocused, concentrated solar radiation is directed to the LPRS when the available radiation exceeds the maximum HPRS rating or cannot supply at least 80 % of the Brayton cycle's *minimum* energy demand. This means the LPRS has the lower priority of the two systems and does not operate if the available amount of radiation is within the operating limits of the Brayton cycle.

The pressure of the gas turbine's exhaust gas stream is modeled to be throttled to the outlet pressure of the LPRS. This is a conservative assumption as the gas turbine outlet could otherwise be lowered, resulting in a higher power output. The pressure difference to ambient is at all times generated by the TES charging fan.

4.2 Parametric study

A parametric study similar to the one presented in Section 2.2 is conducted for the SUNDISC cycle. The aim is to find economically optimal configurations to generate a close-to continuous electricity output (baseload) and compare their technical and economic performance to that of the SUNSPOT cycle and other CSP technologies.

4.2.1 Component rating ranges

The rating of the LPRS is added as an additional parameter and varied between 10 MW_t and 30 MW_t. The RC rating, on the other hand, is now kept at a constant value of 5 MW_e to enforce almost constant electricity generation. The ranges of solar multiple (1.9 to 3.4) and bed length (2 m to 8 m) are increased to supply the increased energy demand of the bottoming cycle and accommodate the additionally captured energy for nighttime operation, respectively.

4.2.2 Results and comparison to SUNSPOT cycle plants

The plots in Figure 4.2 show the performance of the simulated configurations in terms of the performance indicators annual electricity yield (top), TNPG (middle) and LCOE (bottom). Compared to the results of the SUNSPOT cycle plants in Figure 2.6, the annual electricity yield is increased from a maximum of approximately 20 $GW_e h$ to more than 35 $GW_e h$ for selected SUNDISC cycle configurations with LPRS ratings of at least 25 MW_t and solar multiples of more than 3.0. With even larger solar multiples, these particular plants also generate electricity almost throughout the year at less than 500 h TNPG per year. LCOE values close to 0.14 $USD/kW_e h$ were generated with plants featuring solar multiples between 2.3 and 3.2 and LPRS ratings of 15 MW_t to 25 MW_t. Steps in the curves, for example for $\dot{Q}_{LPRS} = 15\,MW_t$ between $SM = 2.8$ and $SM = 3.1$, are caused by a change of optimum bed length. As the discretization of the bed length is coarse at the lower end of the parametric range, the steps are noticeable.

In Table 4.1 the performance indicators of two SUNDISC cycle configurations are compared to two SUNSPOT cycle configurations. SPOT 2 and SPOT 3 represent the SUNSPOT cycle plant configurations previously identified to provide the lowest overall LCOE and the lowest LCOE for a RC rating of 5 MW_e, respectively (see Section 2.2). DISC 1 represents the SUNDISC cycle plant with the lowest LCOE and DISC 2 the configuration that achieves $TNPG_a < 500\,h$ at the lowest LCOE.

As depicted in Figure 4.2 (bottom), SUNDISC cycle plants with a larger solar multiple than in SUNSPOT cycle plants are economically favorable. The minimum LCOE is more than 10 % lower than in SPOT 2 and 25 % lower than in SPOT 3, which is also able to supply the plant's nominal load to the grid

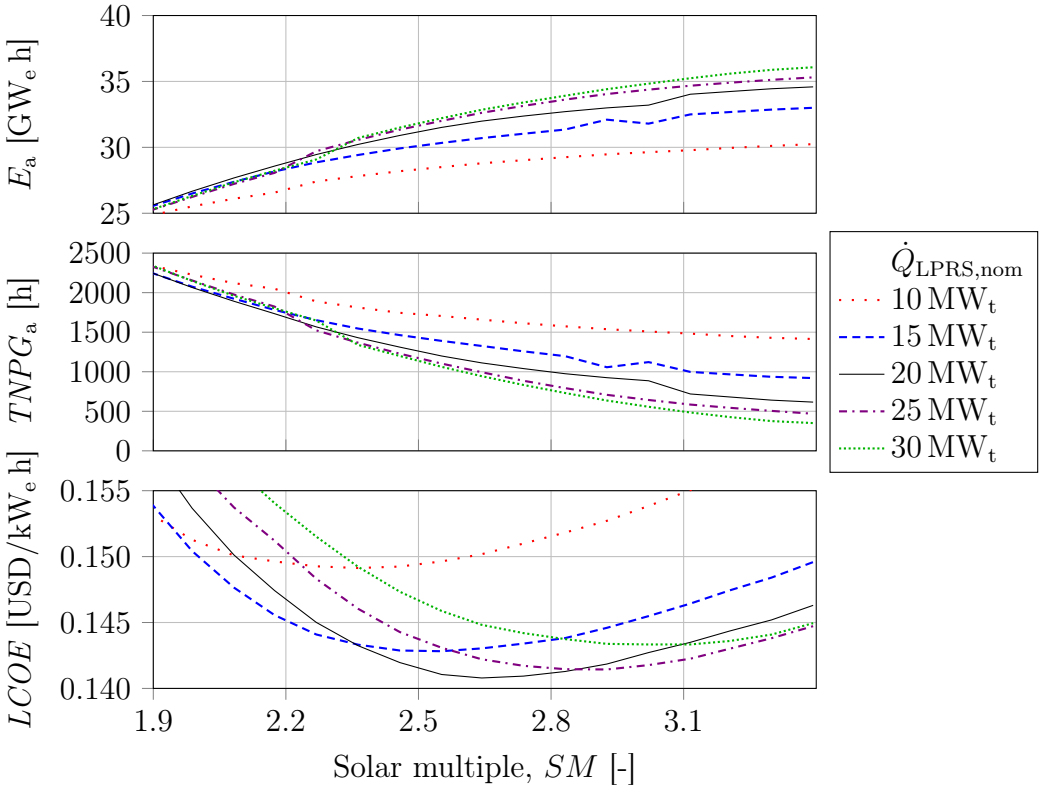

Figure 4.2: (Top) Annual electricity yield, E_a, (middle) time of no power generation, $TNPG_a$, and (bottom) $LCOE$ over solar multiple for SUNDISC cycle plants with different LPRS ratings (bed length optimized for lowest LCOE — see text)

at night. However, DISC 1 provides this baseload for 3180 h more per year, resulting in only 1110 h annual TNPG. This additional power output more than compensates for the increased capital cost for LPRS, solar field and larger TES capacity. DISC 2 demonstrates that even more continuous power generation is feasible at only marginally increases levelized costs.

4.2.3 Cost break-down

The total capital cost of the SPOT 3, DISC 1 and DISC 2 plants is broken down by subsystems in Figure 4.3. As anticipated, the comparison shows that the investment cost difference is mainly driven by the solar field as well as, to a lesser extend, the LPRS and the TES system. As indirect costs are calculated as surcharge on all other investment costs they also show a large discrepancy.

Costs for the construction of the tower are calculated as dependent on its height and, therefore, the solar field size (see Section 2.1.2). As the field of the DISC 1 plant is 65 % larger than that of SPOT 2, its tower is higher and more expensive.

As mentioned in Section 2.1.6, the estimated area-specific land cost for a

Table 4.1: Simulation input parameters and performance indicators for SUNSPOT cycle and SUNDISC cycle plant configurations

Parameter	Unit	Configurations			
		SPOT 2	SPOT 3	DISC 1	DISC 2
BC rating	MW_e	5.4	5.4	5.4	5.4
RC rating	MW_e	2.0	5.0	5.0	5.0
SM	–	1.6	1.6	2.6	3.1
HPRS rating	MW_t	16.5	16.5	16.5	16.5
LPRS rating	MW_t	0	0	20	30
Q_{TES}	$MW_t\,h$	80.4	111	218	303
CAPEX	million USD	22.7	25.8	36.3	41.6
$f_{defocus}$	%	20.2	20.2	4.74	2.92
$TNPG_a$	h	1930	4190	1110	485
cf_{BC}	%	24.4	24.4	27.3	28.4
cf_{RC}	%	40.8	16.1	45.0	51.6
E_a	$GW_e\,h$	18.4	18.3	32.0	35.2
LCOE	$USD/(kW_e\,h)$	0.157	0.188	0.141	0.143

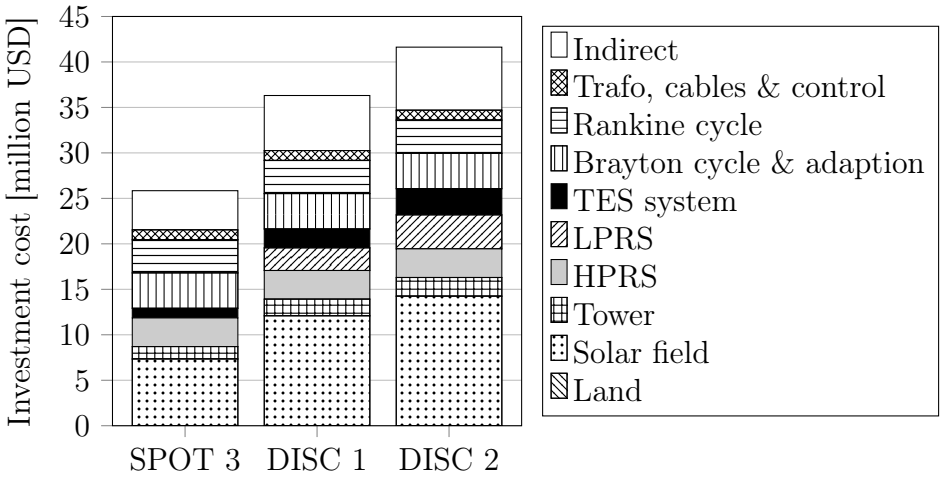

Figure 4.3: Investment cost break-downs for the SPOT 3, and DISC 2 plant configurations in 2005-USD

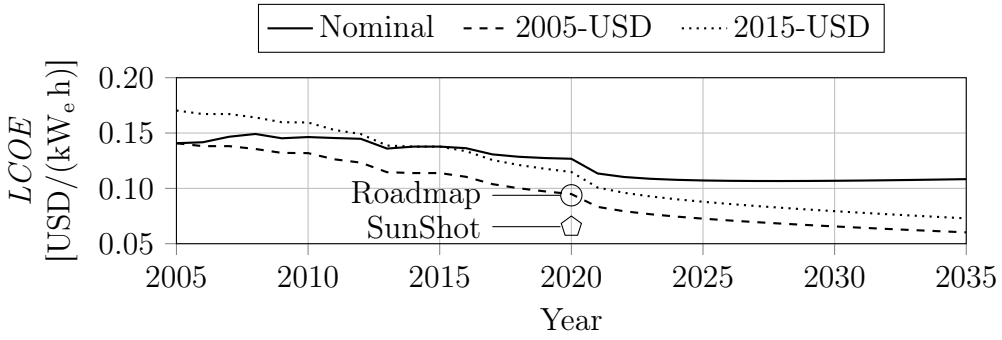

Figure 4.4: LCOE for the DISC 1 plant configuration depending on the construction year (nominal and real values) as well as the SunShot Initiative's and Roadmap cost goals (adapted to 2015-USD)

plant in the area of Upington, South Africa, is very low. The resulting absolute cost is, therefore, not visible in Figure 4.3.

4.2.4 Results with adjusted cost data

Figure 4.4 depicts the predicted LCOE for a plant with the DISC 1 layout depending on the construction year. The cost decrease in the years 2005 to 2015, based on the model presented in Appendix C, is small as most of the used technologies have not been installed on a large scale yet.

Starting after 2015, central receiver technology is assumed to reach commercial mid-scale roll-out while air receiver-related technologies follow approximately five years later. Due to this delay of air receiver technology compared to, for example, molten salt technology, the SUNDISC cycle will not be cost-competitive by 2020. This is shown in Figure 4.4, in which the ambitious cost goal of the United States Department of Energy's SunShot Initiative and predicted levelized cost for a next-generation "Roadmap" molten salt plant (both according to Kolb *et al.*, 2011, Figure 8) are additionally shown.

In the long term there is a large potential for cost-reduction due to the current infancy of the technology and the reference costs can be reached. Other advantages of the technology, mainly efficient fuel hybridization and viable large storage capacities, should be economically quantified with appropriate tariffs or penalties for non-delivery of electricity.

4.3 Operating performance of a SUNSDISC cycle plant

Figure 4.5 shows the plant performance in terms of heat rates, TES charging level and capacity factor for two consecutive days in summer and winter, respectively. The high direct normal irradiance (DNI) during most of the day

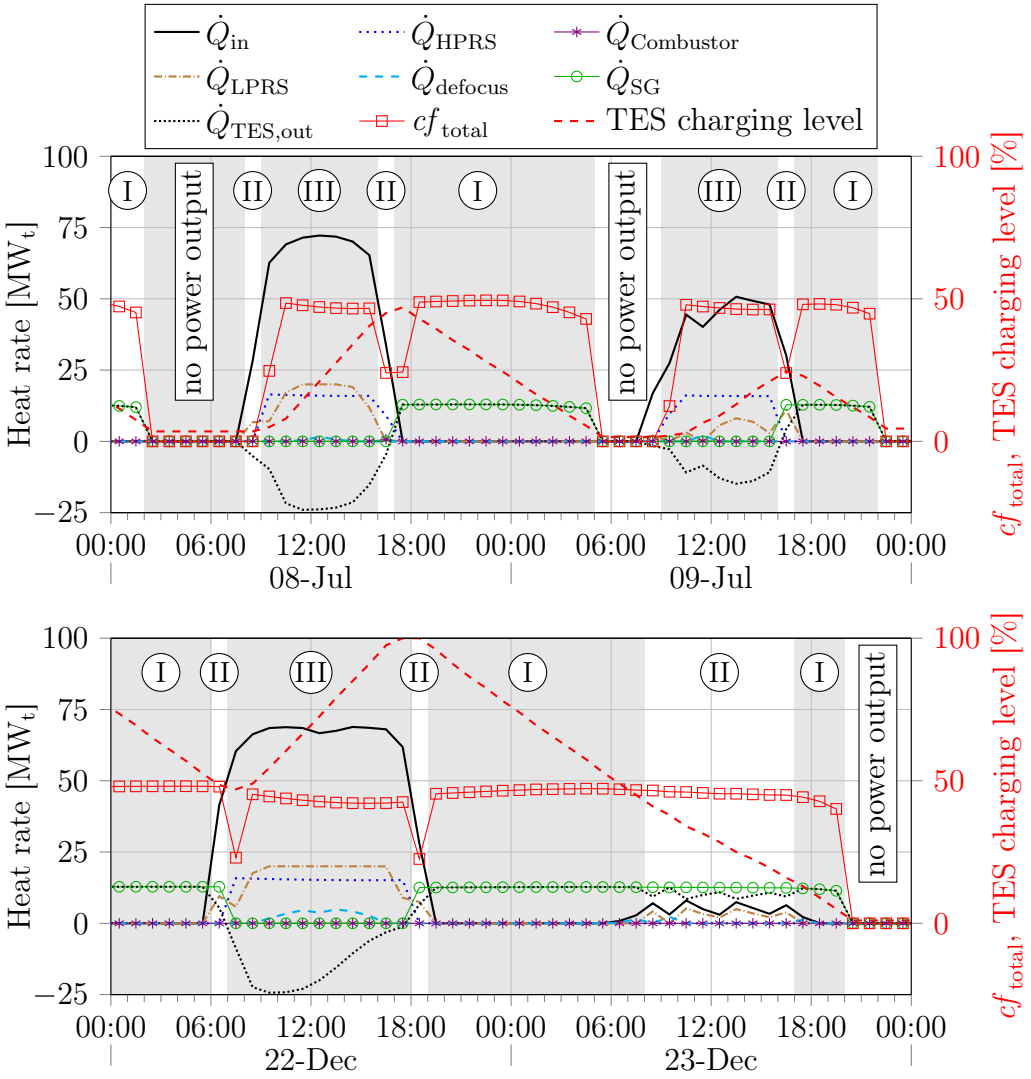

Figure 4.5: Heat rates on two consecutive winter days (top) and two consecutive summer days (bottom) for the investigated SUNDISC plant setup; negative values of $\dot{Q}_{TES,out}$ indicate storage charging; $\dot{Q}_{in} = DNI \cdot A_{SF}$; $\dot{Q}_{Combustor}$: thermal input from co-firing; $\dot{Q}_{defocus}$: lost solar radiation due to defocusing; cftotal: plant capacity factor (both cycles); encircled numbers refer to operating modes defined in Section 3.3

on 08-Jul enables running the HPRS throughout the day (except for early morning hours) and, at the same time, charging the TES additionally from the LPRS output during midday. The low output of the GT in the mornings and the RC when it starts power generation, demonstrated through the low plant capacity factor, cf_{total}, is caused by the cycles' respective start-up times. Between 16:00 and 17:00, the Brayton cycle runs in part-load and at 17:00, when the receiver system input is insufficient to operate the Brayton cycle, the Rankine cycle starts operating so that a uninterrupted plant output is achieved.

Due to the low solar field efficiency in winter, defocusing is at a very low

level despite the high DNI. The stored energy in the TES is sufficient for running the SG at full load for most of the night. However, when the TES starts depleting (after approximately 01:00), the electricity output of the cycle decreases due to the dropping live steam temperature. In the remaining hours of the night no power is generated as co-firing is only used in conjunction with solar radiation. The heat rate of the combustor is therefore nil throughout the shown days.

Although solar irradiation on 09-Jul is much lower than on the previous day, the HPRS can still be operated at full load for most of the day due to the large solar multiple ($SM \approx 2.6$ relative to the HPRS). The amount of energy directed to the LPRS, however, is much smaller than on the previous day. Therefore, the storage is charged to a lower level which only allows operating the SG until 22:00.

The first investigated summer day, 22-Dec, in Figure 4.5 (bottom) is characterized by high DNI throughout the long day. This allows for the HPRS and the LPRS to run at nominal load for a longer time than on 08-Jul. For several hours during midday, the available solar energy even exceeds the combined rating of the receiver systems so that defocusing is required. As the combined thermal energy from the outlet of the GT and of the LPRS is larger than required to run the SG throughout the night, the TES is fully charged after several days of good irradiation. The outlet temperature of the TES rises as a result in the afternoon of 22-Dec, storage charging slows even though the receiver system provides sufficient thermal energy and a portion of the thermal energy is unused (this would not occur if a long bed length was implemented, as done, for example, by Allen and von Backström, 2016).

The charging level of the storage is sufficient to run the SG continuously for more than 24 h as necessitated by the low solar irradiation on the following day, 23-Dec. On this day the LPRS contributes only a small fraction of the thermal energy demand of the SG. In reality, the plant's solar field and receiver system might not be started up under such conditions.

The large capacity of the TES is economically viable because of the low specific cost of the rock bed storage. Longer bed lengths would reduce the storage outlet temperature during charging, however, the additional costs were found to outweigh the energetic benefit. The almost constant capacity factor of the SUNDISC cycle plant, cf_{total}, illustrates the utilized TES system's ability to act as a source for reliable power output in summer. The drop in plant output at the start-up of the RC could be avoided by preheating the steam generator and turbine while the BC is still operating.

Chapter 5

Conclusions on the SUNDISC cycle

A novel CSP cycle, the SUNDISC cycle, is proposed to address identified shortcomings of asynchronous combined cycles with a solarized gas turbine. These are namely, the limitation of thermal energy available to the bottoming cycle and the low capacity factor of the gas turbine (unless high levels of defocusing or co-firing are accepted). The SUNDISC cycle is intended to overcome these constraints by adding a low-pressure receiver system (LPRS) to the existing high-pressure receiver system (HPRS) that is directly embedded in the Brayton cycle. This LPRS collects excess concentrated solar radiation — allowing for larger solar fields and higher capacity factors of the GT — and directly charges the TES — allowing for the bottoming cycle to run for prolonged periods of time.

The energy flows for winter and summer days, depicted in Figure 4.5, demonstrate the capability of a SUNDISC cycle plant to provide close to baseload capacity in clear weather. For the investigated configuration with large solar components — that is, solar field, LPRS rating and TES capacity — the plant's power output is only interrupted for a few hours per night in winter. Because of the large storage capacity, almost uninterrupted full-load power generation is possible in summer time (for approximately 24 h without charging). Prioritizing the HPRS during the day enables continuous operation of the GT during daytime while the SG is normally operated at night and powered by the stable output of the TES.

The mentioned uninterrupted electricity generation during periods of low solar input in summer is enabled by the large capacity of the modeled TES. It is noteworthy that the TES dimensions were chosen on economical grounds (at the implemented operating strategy and financial assumptions). This indicates that the rock bed storage can, due to its low cost, considerably benefit a CSP plant in terms of viability and ability to provide baseload capacity. Plant configurations with larger solar components result in an only marginally increased levelized cost while interrupting power generation for only a few hundred hours per year.

The comparison of a SUNDISC cycle plant (DISC 1) with a plant with the identical Rankine cycle rating but without the LPRS (SPOT 3) shows that the SUNDISC cycle plant provides electricity at a 25 % lower cost and a 75 % higher capacity factor (all configurations have a solar share of approximately 99 %). For the comparison with the SunShot cost goal, a learning-curve scenario for the upcoming two decades was developed. It shows that the investigated SUNDISC plant will not reach the ambitious goals by the year 2020 due to a lack of installed capacity. Once the medium-scale roll-out has commenced, however, the levelized cost is expected to drop to less than 0.075 USD by the year 2035 (2015-USD).

A non-quantifiable advantage of the cycle is its adaptability. Depending on local demand and project-dependent requirements, the rating of the receiver systems, the turbines, the TES capacity and the operating mode of co-firing and the bottoming cycle can be adjusted, allowing for a high degree of flexibility. However, the greater number of targets and receivers also increases the complexity of the plant. This is in addition to challenges that affect other solarized combined cycles, for example, the storage system, the solarization of the gas turbine and development of pressurized air receivers.

Overall, it could be shown that the SUNDISC cycle can solve the identified shortcomings of combined cycle CSP plants with solarized gas turbines in terms of dispatchable power generation. It has the potential to provide (close to) baseload capacity with a high solar share at competitive prices in the mid-term.

In a follow-up project the modeling of the solar receivers, the steam generator (including air return loop), Rankine cycle and cost assumptions should be improved to increase confidence in the results. Furthermore, the operating strategy of an asynchronous cycle has a large influence on its economic performance. The current strategy prioritizes maximum generation time at constant load, however, certain applications (for example, off-grid consumers) can benefit from different priorities. The economic potential of a plant under differing conditions should be investigated.

An alternative possibility to the presented system with two separated receivers is the utilization of a hybrid receiver that provides pressurized and non-pressurized heated air. Combining both receivers in one assembly has the potential to increase the overall receiver efficiency and lower its cost but means a higher complexity than the dual receiver system. The feasibility of such a hybrid receiver system is investigated in the second part of this work.

Part II

Dual-Pressure Air Receiver System

Chapter 6

State of the art of solar air receivers

The SUNDISC cycle requires two air streams to be heated at different parameters. Firstly, the pressurized air stream enters the receiver system at an elevated pressure and temperature of approximately 5 bar to 15 bar and 200 °C to 400 °C, respectively. This stream should ideally be heated up to the turbine inlet temperature (1102 °C for the chosen turbine). Secondly, the non-pressurized air stream is drawn into the receiver system at (close to) ambient pressure. Depending on the use of an air-return loop, its inlet temperature is expected to be between 20 °C and 200 °C. The air outlet of the LPRS should be at or above (see Section 3.4) the temperature of the GT outlet air (534 °C for the given turbine).

To identify possible designs of a dual-pressure air receiver system, existing pressurized and non-pressurized air receiver technologies have to be examined. While reviews of air receiver technologies with differing scopes can be found in literature — for example by Ávila-Marín (2011), Lubkoll *et al.* (2014) or Ho and Iverson (2014) — a study with specific focus on technologies that provide the identified operating parameters is deemed necessary. In the following section, tested and proposed air receiver technologies that operate in the given ranges are presented. Particular attention is paid to proposed and used enhancements to overcome the limitations of heat transfer to air streams.

6.1 Receiver performance indicators

The most important performance criteria for all solar receiver systems are energetic efficiency and cost (including lifetime) as well as the influence on other subsystems' efficiency and cost. The different loss mechanisms and the resulting efficiencies are in the following defined. The influence of the receiver system on the solar field and the power block/TES system is furthermore discussed.

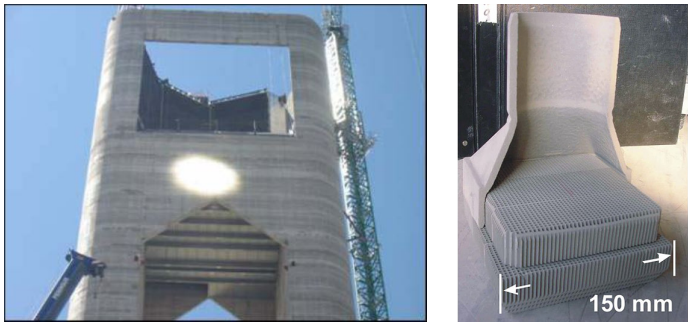

(a) (b)

Figure 6.1: (a) Photo of the PS10 tubular cavity receiver during construction (Solúcar, 2006) and (b) of a volumetric absorber module of the Jülich Solar Tower (Fend *et al.*, 2013)

6.1.1 Optical efficiency

The optical efficiency of a receiver, $\eta_{\mathrm{Re,opt}}$, is defined as the amount of radiation that is absorbed in it, $\dot{Q}_{\mathrm{Re,in}}$, divided by the amount of concentrated solar radiation that reaches the aperture of the receiver, $\dot{I}_{\mathrm{Re,in}}$:

$$\eta_{\mathrm{Re,opt}} = \dot{Q}_{\mathrm{Re,in}}/\dot{I}_{\mathrm{Re,in}} = 1 - \dot{I}_{\mathrm{Re,refl}}/\dot{I}_{\mathrm{Re,in}}. \tag{6.1.1}$$

The losses are caused by reflections from the receiver, $\dot{I}_{\mathrm{Re,refl}}$. These can be lowered by applying a highly absorptive coating on the absorber or by trapping the reflected rays so that they eventually hit the absorber again. This light-trapping can be achieved on a macro-level by employing a cavity receiver, depicted in Figure 6.1(a), or on a micro-level by utilizing a volumetric absorber in which the radiation penetrates into the absorber structure, shown in Figure 6.1(b) and described in detail in Section 6.2.1.

Both approaches have, however, limitations: Cavity receivers dictate the positioning of the heliostats, as they have an opening only on one side (compared to a 360° external receiver). This negatively influences the annual solar field efficiency. Volumetric absorbers require geometries that are impractical for closed (pressurized) receivers unless a window closes the system (see Section 6.3.1). More detailed information on volumetric absorbers can be found in Section 6.2.

6.1.2 CPC

The optical efficiency of the receiver *system*, $\eta_{\mathrm{ReS,opt}}$, additionally includes the efficiency of a potential compound parabolic concentrator (CPC), $\eta_{\mathrm{CPC,opt}}$:

$$\eta_{\mathrm{ReS,opt}} = \eta_{\mathrm{CPC,opt}}\,\eta_{\mathrm{Re,opt}}. \tag{6.1.2}$$

CPCs are intended to lead to an increase in thermal efficiency of the receiver as they increase the flux on it and form a further cavity. However, they have

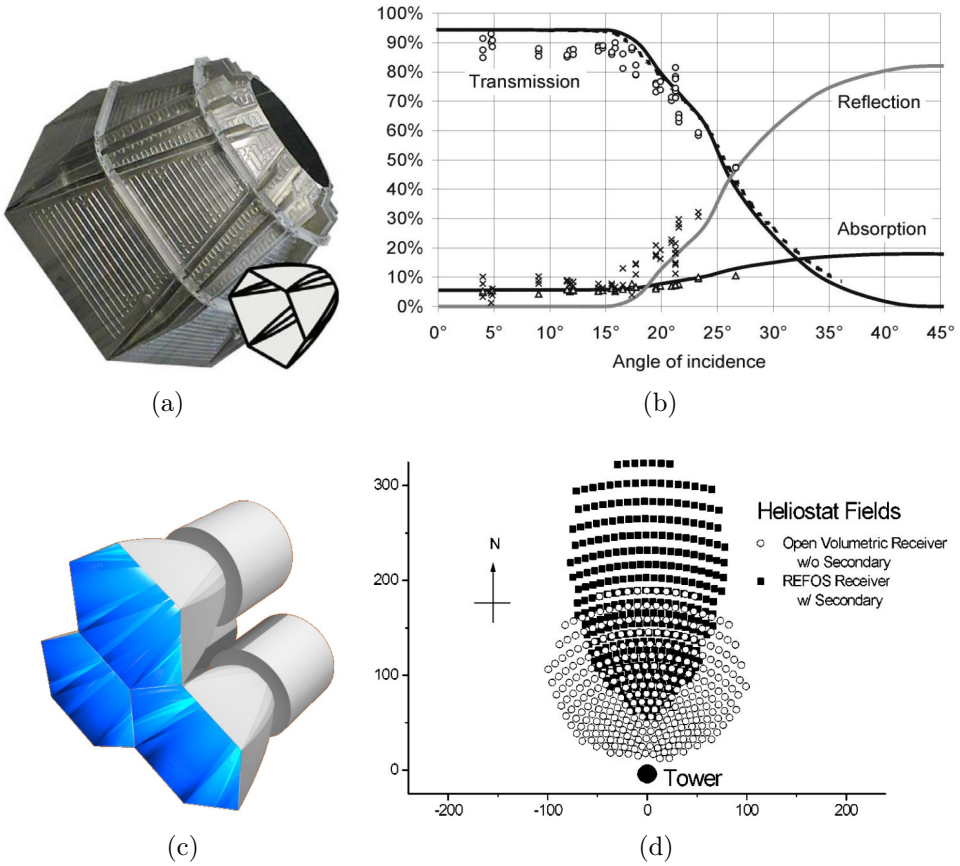

Figure 6.2: (a) Photo of a CPC from the back, (b) plot of optical performance of a CPC over solar radiation incidence angle, (c) rendering of a cluster of CPCs with connected receivers in a honeycomb arrangement and (d) effect of CPCs on a solar field layout (derived from SOLGATE Project Report, 2005, and Buck *et al.*, 2002)

relatively high costs, a limited acceptance angle for incoming solar radiation and induce optical losses. The influence of the angle of incidence on the optical performance of the German Aerospace Center's (DLR) so-called "second generation" CPC, depicted in Figure 6.2(a), can be seen in Figure 6.2(b). The low optical performance at incidence angles larger than 15° favors an otherwise non-optimal field configuration with a lower annual optical solar field efficiency. The change in solar field configuration between a receiver system without a CPC and a system with a cluster of CPCs, depicted in Figure 6.2(c), is shown in Figure 6.2(d). CPCs have mainly been proposed for pressurized air receivers, where high absorber temperatures necessitate small cavity openings to limit thermal losses.

6.1.3 Thermal efficiency

The thermal efficiency of a receiver, $\eta_{\mathrm{Re,t}}$, is calculated as the quotient of the thermal energy that is passed on to the heat transfer fluid divided by the thermal energy absorbed in the receiver:

$$\begin{aligned} \eta_{\mathrm{Re,t}} &= \dot{Q}_{\mathrm{Re,t}}/\dot{Q}_{\mathrm{Re,in}} \\ &= 1 - \left(\dot{Q}_{\mathrm{Re,loss,rad}} + \dot{Q}_{\mathrm{Re,loss,conv}} + \dot{Q}_{\mathrm{Re,loss,cond}}\right)/\dot{Q}_{\mathrm{Re,in}} \end{aligned} \tag{6.1.3}$$

The losses associated with the thermal efficiency are due to thermal radiation, $\dot{Q}_{\mathrm{Re,loss,rad}}$, convection to ambient air, $\dot{Q}_{\mathrm{Re,loss,conv}}$, and conduction to the receiver structure, $\dot{Q}_{\mathrm{Re,loss,cond}}$. Since as per the Stefan-Boltzmann law, radiation emittance is a function of surface temperature, T_{surf}, to the fourth power

$$\dot{Q}_{\mathrm{rad}} = A_{\mathrm{surf}}\varepsilon_{\mathrm{surf}}\sigma_{\mathrm{SB}}T_{\mathrm{surf}}^4, \tag{6.1.4}$$

these losses become increasingly relevant for higher-temperature receivers. Besides lowering the temperature of the receiver surfaces, radiation losses can be lowered by (a) lowering the emissivity of the surfaces, $\varepsilon_{\mathrm{surf}}$, (through coating with low-emissivity paint, which are, to the author's best knowledge, not available for the specifications of high-temperature central receiver technology) or (b) by capturing the emitted radiation within the receiver (for example, in a macro/micro cavity). Convective losses can be lowered by limiting flow along hot surfaces of the receiver, for example by means of a window or an air-curtain. Conductive losses of a receiver can normally be limited by design to a low percentage so that they are commonly neglected in thermal models of high-temperature receivers (for example by Uhlig *et al.*, 2013).

6.1.4 Pressure drop

The pressure drop induced by a receiver system can have a significant influence on the efficiency of the whole CSP plant. In plants with a heat transfer fluid loop that is separated from the power block, the pressure drop of the receiver system has to be overcome by pumps or fans which leads to parasitic losses. If the heat transfer fluid is part of the power cycle, for example in a DSG plant or a solarized Brayton cycle, the pressure drop in the receiver directly lowers the power output of the turbine generator.

The allowable pressure drop in pressurized air receiver systems, that is between compressor outlet and combustion chamber inlet, is commonly given a value of 200 mbar to 300 mbar (Grange *et al.*, 2011; Uhlig *et al.*, 2013). As enhancements in the convective heat transfer to a fluid usually also induce higher pressure drops, the optimum flow conditions in a receiver should be defined as a balance between thermal efficiency and pressure drop.

6.2 Non-pressurized air receivers

Receivers that are used to heat a non-pressurized air flow have the advantage over any other CSP technology that they can operate in an open, non-pressurized setup by drawing in air from ambient. Due to the poor heat transfer properties of non-pressurized air, however, they need a large surface area to effectively transfer the collected heat to the air flow. To the author's knowledge, all non-pressurized air receivers that have been tested at least on a pilot scale are of the open volumetric kind. This is why this section focuses exclusively on this technology.

6.2.1 Volumetric absorber concept

Volumetric absorbers were developed with the goal of creating a device that (a) absorbs solar radiation effectively inside the absorber volume (as opposed to at its surface) as the small channels in it act as micro cavities and (b) has a large absorber surface area that is directly cooled by the fluid. Naturally, this means that the fluid is not contained in the absorber but rather flows past the absorbing surfaces. Volumetric absorbers in pressurized air receivers work by the same principle as in open volumetric air receivers (OVAR), however, the air flow is pressurized and contained by a window in front of the absorber (more details are given in Section 6.3.1).

The *volumetric effect* describes a situation when an absorber that absorbs heat in its volume and is cooled with cold air from the irradiated front has its highest temperature in the depth instead of at its front surface (see Figure 6.3). Kribus *et al.* (2014) report, however, that OVARs tested to date have not achieved the volumetric effect as they show a higher absorber front than back temperature, resulting in considerably lower thermal efficiencies than aspired (around 85 % at an air outlet temperature around 700 °C). They further report that some pressurized air receivers with pressurized windows have achieved higher efficiencies, however, mostly under very high incidence fluxes which are difficult to attain without high penalties on the solar field efficiency (see Section 6.3.1).

Kribus *et al.* (1996) predict local fluid channel choking which can cause thermal hot spots in volumetric receivers and, therefore, receiver failure. The occurrence of these flow instabilities depends on the absorber geometry, material and solar flux (see Becker *et al.*, 2006) and can therefore be avoided in the design of the systems.

6.2.2 State of open volumetric absorber technologies

Ávila-Marín (2011) presents an elaborate chronological review of developed receivers with volumetric absorbers. It is not intended to repeat this study

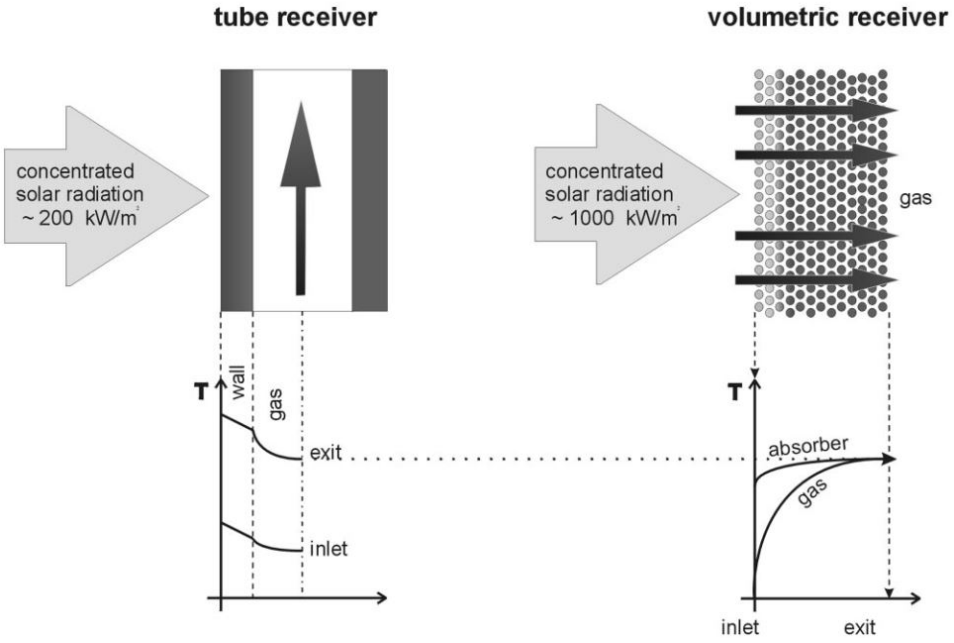

Figure 6.3: Schematic comparison of external absorption with the idealized volumetric effect (Romero *et al.*, 2002, based on Hoffschmidt, 1996)

here, however, key findings on OVARs and a description of the state-of-the-art technology are presented.

Early development for OVARs was focused on meshes of metallic wire as the absorber material. However, since the early 2000s mainly work on ceramic absorbers has been reported. This is due to the high absorber temperatures experienced when heating air to the temperature necessary to supply the steam generator of an efficient Rankine steam cycle (approximately 700 °C). Ceramic absorbers can achieve higher temperatures, have a higher durability and lower thermal expansion than metallic ones (Ávila-Marín, 2011).

In recent years the HiTRec (High-Temperature Receiver) technology has been developed most actively. It is based on individual receiver cups, each holding a porous ceramic block as the absorber, which are then assembled to create OVARs of scalable size and rating (see Figure 6.4, a and b). This principle design has been kept throughout evolutionary cycles although the geometry of the cups (from hexagonal to square) and their material (from steel to ceramic) has seen changes. The HiTRec technology's main positive characteristics are

- a highly scalable design and economies of scale,
- the easy replacement of modules,
- the possibility of (limited) movement during thermal expansion,
- cup cooling with return air from the SG/TES (see Figure 6.4, c) and

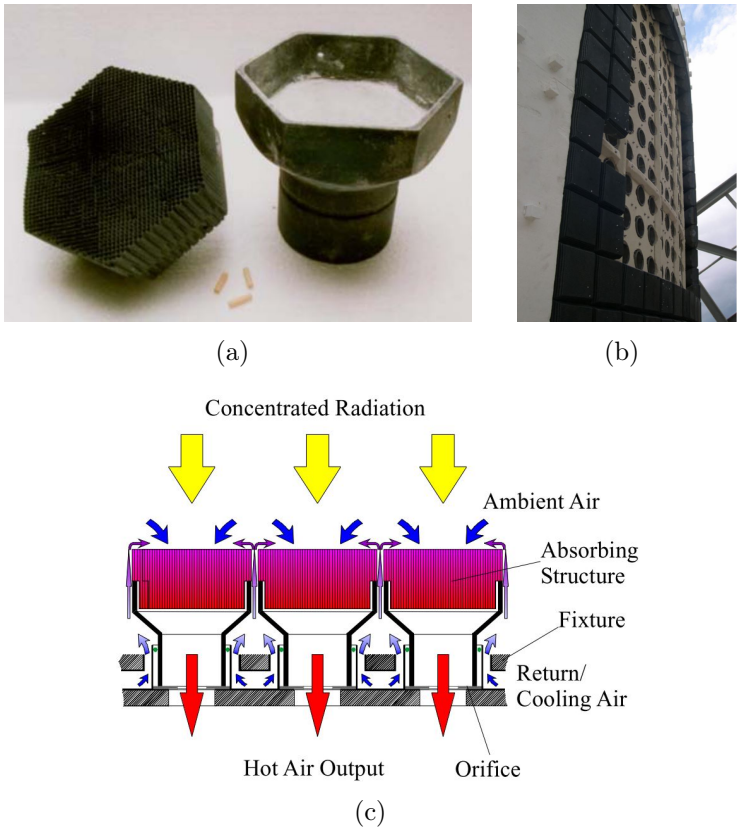

Figure 6.4: (a) Photo of an early HiTRec absorber and cup, (b) of a 3 MW_t HiTRec receiver (both from Hoffschmidt *et al.*, 2001) and (c) schematic of the HiTRec principle (Hoffschmidt *et al.*, 2003*a*)

- return air introduction between absorbers instead of exclusively from the edges of the receiver.

Early versions of the HiTRec were tested up to air outlet temperatures of 980 °C, however, nominal operation is between 680 °C and 800 °C (Ávila-Marín, 2011). The change of the ceramic absorber material at a later stage brought about an increase in efficiency of approximately 5 %. A thermal efficiency of the receiver between 81 % and 83 % at an air outlet temperature of 700 °C was reported for some of the latest tests with published results (Hoffschmidt *et al.*, 2003*a*). Air return ratios of approximately 50 % were accomplished. This was limited by the test setup; higher values appear technically feasible in an optimally designed system.

As a result of the positive results, a pre-commercial demonstration plant using the HiTRec technology was constructed in Jülich, Germany in 2008. This plant features a 1.5 MW_e steam turbine, a packed bed storage system and an OVAR with an aperture area of approximately 22 m^2 (Hennecke *et al.*, 2008).

6.3 Pressurized air receivers

Pressurized air receivers can, most generally, be categorized in two groups: Designs in which a transparent window separates the absorbing surface as well as the pressurized air stream from ambient and those in which the absorber itself separates the two pressure levels. Examples of tested technologies of both groups are presented in this section.

6.3.1 Designs with pressurized windows

Pressurized air receiver designs with pressurized windows allow for the direct cooling of the absorber surfaces with pressurized air, similar to an open volumetric air receiver. This has two main advantages: Firstly, there is no thermal resistance caused by conduction through the absorber material. The pressurized air is, therefore, in direct contact with the hottest surface of the receiver. Secondly, the absorber does not have to sustain the pressure difference between the air flow and ambient because the window creates a pressurized chamber. This allows, for example, for the use of porous, high temperature-resistant ceramics as the (volumetric) absorber material. To the author's knowledge, only two designs of pressurized air receivers with pressurized windows have been developed to a pilot scale. In this section, firstly the general characteristics of pressurized windows for pressurized air receivers are described, followed by a presentation of these two designs and findings on them.

Quartz glass windows

Fused silica (commonly called quartz glass) is well suited as the material of pressurized air receiver windows as it has a high transmissivity for radiation in the solar spectrum, a low thermal expansion coefficient and a relatively high tensile strength at temperatures up to 800 °C (Röger *et al.*, 2009). However, it has a high absorptivity for radiation in the infrared/thermal spectrum, which leads to elevated window temperatures. Furthermore, analyses of quartz glass windows showed defects, namely devitrification spots (crystal formation) and burnt-in contaminations, already after short-term experiments in pressurized air receivers (Hofmann *et al.*, 2009).

To increase the reflectance of thermal radiation, Röger *et al.* (2009) applied coatings to the pressurized side of a quartz glass window. They found temperature decreases of the window up to 78 K compared to the uncoated window, leading to higher achievable thermal efficiencies and air outlet temperatures within the tolerated operating temperature range of the quartz glass.

Hertel *et al.* (2016) experimentally determined the failure stress of quartz glass samples with detrifications and after treating their surfaces, respectively, at ambient temperature and at 800 °C. While they measured a lowered transmissivity of contaminated glass, the contaminations did not grow during or

after heat treatment of the samples. They also found all samples to have survival probabilities of more than 99.99 % at the design stress level for a specific pressurized air receiver.

In conclusion, quartz glass is a potentially suitable material of pressurized windows in volumetric air receivers. However, besides such windows' high costs, their long-term performance under solar conditions has yet to be proven.

DIAPR

The Directly Irradiated Annular Pressurized Receiver (DIAPR) was developed in the 1990s by the Israeli Weizmann Institute of Science. The concept is build around a volumetric ceramic absorber structure called the Porcupine which is depicted in Figure 6.5(a). The ceramic quills of the absorber allow for the penetration of concentrated solar radiation into the depth of the structure and form a large surface area for the heat transfer to the pressurized air stream passing through. This stream is separated from ambient by use of a Frustum-Like High-Pressure (FLHiP) window, manufactured from quartz glass. Due to the load on the window, its poorer high-temperature material strength and its exposed position, it is designed to be cooled by the coldest available air directly from the flow inlet as depicted in Figure 6.5(b).

A prototype of the DIAPR technology was successfully tested at air outlet temperatures of up to 1300 °C and an absolute pressure of up to 30 bar at solar fluxes up to 10 MW_t/m^2 (Karni *et al.*, 1997). The thermal efficiency of a later manifestation of the receiver was calculated at 70 % to 90 %, however, direct measurement of the solar energy input was not conducted (Kribus *et al.*, 2001). While absorber temperatures of up to 1600 °C were measured, the window temperature could be kept below 600 °C.

In further experiments, Kribus *et al.* (1999) tested a multistage receiver system consisting of a high-temperature DIAPR receiver and several metallic tubular pre-heaters as depicted in Figure 6.5(c). Due to deteriorated optical equipment during tests, namely the heliostat field and the CPC, the thermal input into the receiver was lower than the design value. Its thermal output (30 kW_t to 60 kW_t), outlet temperature (1000 °C) and efficiency, therefore, also did not reach the previously achieved values.

The very high flux required to operate the DIAPR at temperatures above 1000 °C and at a high thermal efficiency, approximately 5 MW_t/m^2 to 10 MW_t/m^2, necessitates secondary or even tertiary (beam-down) concentration devices with high concentration ratios. These systems have a negative impact on the optical performance of the solar field and receiver system besides imposing high costs.

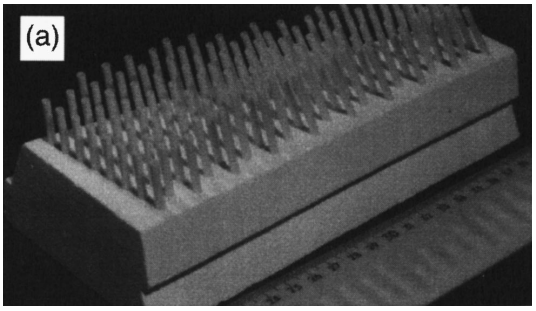

(a)

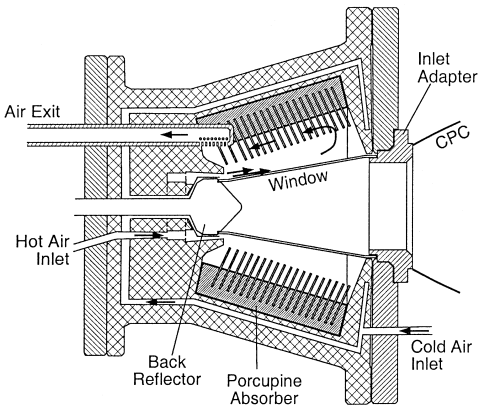

(b)

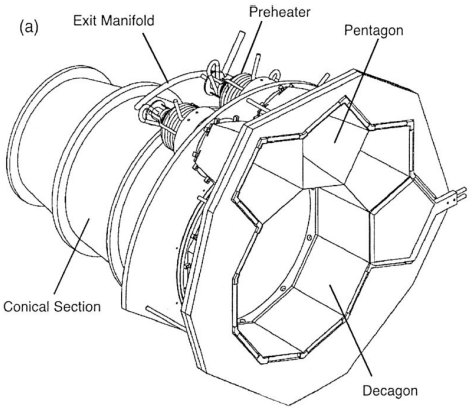

(c)

Figure 6.5: (a) Photo of the Porcupine ceramic absorber (Kribus *et al.*, 2001), (b) half-section drawing of the DIAPR assembly (Kribus *et al.*, 1999) and (c) drawing of the multi-stage DIAPR receiver cluster (Kribus *et al.*, 1999)

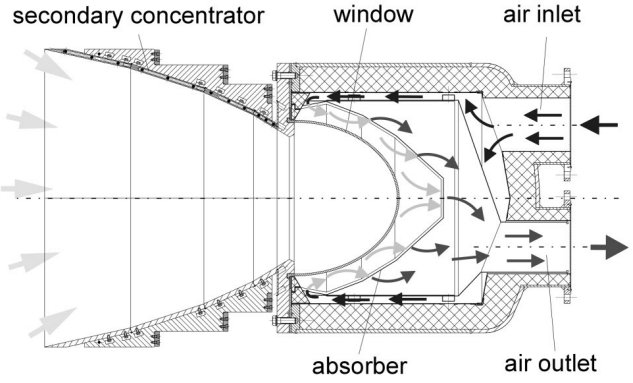

Figure 6.6: Half-section drawing of the REFOS receiver (Buck *et al.*, 2002)

REFOS

The design of the REFOS receiver of the German Aerospace Center (DLR) is similar to that of the DIAPR in many ways: It utilizes a ceramic volumetric absorber (although there were also manifestations with an Inconel wire absorber) behind a pressurized quartz glass window and features a CPC for further concentration as well as to enable clusters of receiver modules with minimized spillage (see Section 6.1.2). Some differences between the two concepts can be seen in the drawing in Figure 6.6: The volumetric absorber is a mesh or porous medium instead of a defined structure and the window is dome- instead of frustum-shaped.

REFOS receivers with an Inconel wire absorber were tested for more than a hundred hours reaching a maximum air outlet temperature of 815 °C and absolute pressures up to 15 bar (Buck, 2003, p. 3). Higher temperatures and efficiencies could be achieved by replacing the metallic absorber with silicone carbide (SiC) foams. These are available with high porosities, generating a micro-cavity effect, and have higher allowable operating temperatures.

In the SOLGATE and HST projects, a cluster consisting of a metallic tubular pre-heater (presented in Section 6.3.2) and two REFOS receivers was connected to a gas turbine. The air outlet temperature of the high-temperature REFOS module with ceramic absorber could be increased to 1030 °C (Buck, 2005, p. 55). Problems with the mounting of a quartz glass window prevented reaching the originally declared goal of an air outlet temperature above 1100 °C. The thermal efficiency of the cluster was calculated at approximately 80 % to 85 % at air outlet temperatures between 650 °C and 1000 °C, however, there was doubt regarding the validity of these values (see Section 2.1.3).

Conclusions

Air receivers with pressurized glass windows have shown remarkable performance in terms of air outlet temperatures and thermal efficiencies. However, the two tested concepts both suffer from similar problems, namely their complexity and high cost. Both of these issues are directly related to the quartz glass window, which enables the technology but has undesirable side-effects. Additionally, the optical performance is greatly lowered by the necessary CPCs, which also increase the cost further. To replace these complex receiver systems, or at least supplement them, more robust options are sought after.

6.3.2 Tubular absorbers

Arguably the most simple absorber design for pressurized air receivers is the tubular one. In tubular air receivers the pressurized air flows through the inside of tubes that are exposed to concentrated solar radiation. However, due to the poor heat transfer properties of air, the solar heat flux on the tubes has to be

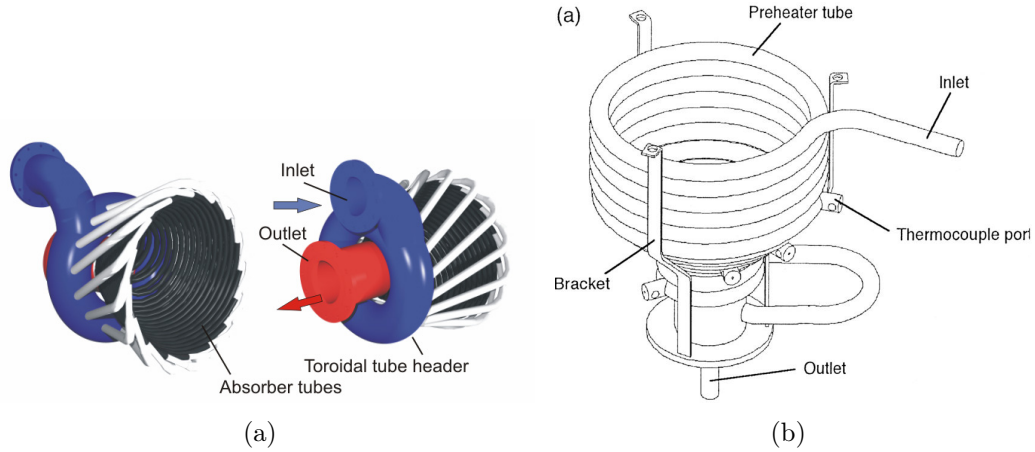

Figure 6.7: (a) Renderings of the low-temperature module of the SOLGATE receiver cluster (SOLGATE Project Report, 2005) and (b) drawing of the DIAPR multi-stage tubular preheater (Kribus *et al.*, 1999)

lower than for other HTFs (for example, molten salt) to avoid high absorber temperatures and, therefore, high thermal losses. The allowable flux is further limited by the maximum operating temperature of the material (metals) and temperature gradient-induced stresses. The latter is largely caused by high flux differences between front and back of tubes. Selected designs that attempt to alleviate one or several of these shortcomings are presented here.

SOLGATE and DIAPR pre-heater

The SOLGATE receiver consisted of three individual solar receivers connected in series to heat up pressurized air upstream of a gas turbine from 300 °C to 1000 °C (SOLGATE Project Report, 2005). While the intermediate- and high-temperature stages were of the REFOS-type (see Section 6.3.1), the low-temperature stage was an attempt to pre-heat the pressurized air to approximately 550 °C in a more cost-effective manner.

The design of the low-temperature stage is similar to the pre-heater stage of the DIAPR, depicted in Figure 6.7(a) and (b), respectively. It consists of 16 parallel tubes of 2.3 m length each that are spiraled (improving heat transfer) and coated with a highly absorptive paint to form a light-trapping cavity (SOLGATE Project Report, 2005, pp. 9–10). The production cost of the stage could be halved compared to the REFOS stages, however, during on-sun testing it experienced high material temperatures up to 950 °C and temperature differences of up to 220 K in the tube walls (Heller, 2010, p. 5), potentially negatively influencing thermal efficiency and longevity. Furthermore, the module caused a pressure drop of approximately 85 mbar — 70 % of the whole cluster's.

Similar experiences were made with the DIAPR tubular preheaters: They

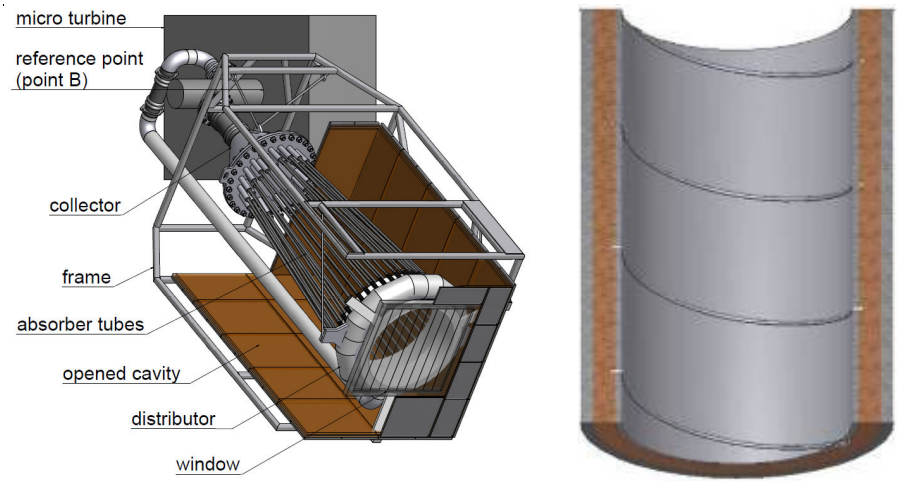

(a) (b)

Figure 6.8: (a) Rendering of the SOLHYCO tubular cavity receiver with window (Amsbeck *et al.*, 2009) and (b) of a PML tube half-section (Heller, 2010)

supplied air at temperatures of approximately 650 °C to 750 °C to the DIAPR and had a similar combined rating to it. Their pressure drop varied between approximately 200 mbar and 600 mbar depending on flow rates.

Another disadvantage of both tested designs is that they required a CPC, as do the REFOS and DIAPR receivers. As mentioned in Section 6.1.2, these concentrators enforce non-optimal field shapes and have non-negligible optical losses of approximately 14 % at design operation (Buck *et al.*, 2002).

SOLHYCO

In a follow-up project to SOLGATE, a new metallic tubular pressurized air receiver was developed in the SOLHYCO project. This receiver, depicted in Figure 6.8(a), features straight absorber tubes that are arranged almost perpendicular to the main direction of incoming concentrated solar radiation. This geometry creates a deep cavity — without requiring a CPC — with lowered heat fluxes on the absorber surfaces and potentially low (reflection, convection and radiation) losses through the small cavity opening. Gaps were intentionally created between the tubes to allow solar radiation to reach the insulated cavity walls. From there it is reflected to irradiate the back surface of the tubes to lower flux and temperature gradients in the absorber material.

The receiver was designed to preheat an air flow of 0.8 kg/s from 600 °C to 800 °C with a total pressure drop of less than 150 mbar to feed the combustor of a micro gas turbine (Amsbeck *et al.*, 2009). The thermal efficiency of the receiver was calculated at 67.7 % with large losses due to thermal radiation (16.5 %) and convection (12.2 %). To reduce these losses, a non-pressurized quartz glass window (shown in Figure 6.8, a) with anti-reflective coating was

designed and manufactured. Simulations predicted a minimal increase in reflection losses (from 3.6 % to 5.6 %) but much lower losses due to thermal radiation (12.2 %) and, especially, convection (1.1 %). The combined optical and thermal efficiency of the windowed design was predicted at 80.8 %.

Unfortunately, the experimental validation of these values was not successful as other unaccounted for problems led to significant losses (see Heller, 2010, pp. 48–49). Namely, the nominal air mass flow rate was not reached and conductive losses through the cavity insulation were high. Additionally, an inhomogeneous flux distribution inside the cavity and wind effects (for the windowless design) caused large temperature differences between sections of the receiver. The experimentally derived thermal efficiency of the SOLHYCO receiver without and with the quartz glass window were 37.8 % and 43.0 %, respectively.

A further part of the SOLHYCO project was the development and laboratory testing of so-called profiled multi layer (PML) tubes, depicted in Figure 6.8(b). These tubes feature a wire-coil insert to disrupt the boundary layer of the air flow along the tube surface and thus increase the heat transfer. "Multi layer" refers to the tube being manufactured by co-axially joining three individual tubes of different diameters via hydro-forming. The inside and outside tubes are made of Inconel steel alloy for high-temperature material strength and corrosion resistance while the central tube is made of copper for its superior heat conduction to alleviate radial and circumferential temperature gradients.

To evaluate the effectiveness of the two enhancements compared with a plain tube, Heller (2010) conducted thermo-hydraulic tests with a multi-layered tube (without wire-coil), a PML tube and a reference plain Inconel tube. The three tubes were heated from one half of their outside circumference only and an internal air-flow was heated from 550 °C to approximately 660 °C. The experiments were repeated at two different flow velocities, resulting in Reynolds numbers of 1.7×10^4 and 3.4×10^4, respectively. For both flow cases the maximum tube temperature as well as the temperature difference between irradiated and non-irradiated part could be lowered considerably for multi-layered and PML tubes. The average reduction of both flow cases from plain tube to PML was 5.30 % in maximum temperature and 80.9 % in maximum temperature difference.

Despite these promising results, the technology has not been developed further, to the author's knowledge. This is expected to be due to issues identified during thermal cycling tests between 600 °C and 900 °C. The contact area between the inner Inconel tube and the copper section showed cracks which likely increase thermal conduction resistance and shorten the assembly's lifetime.

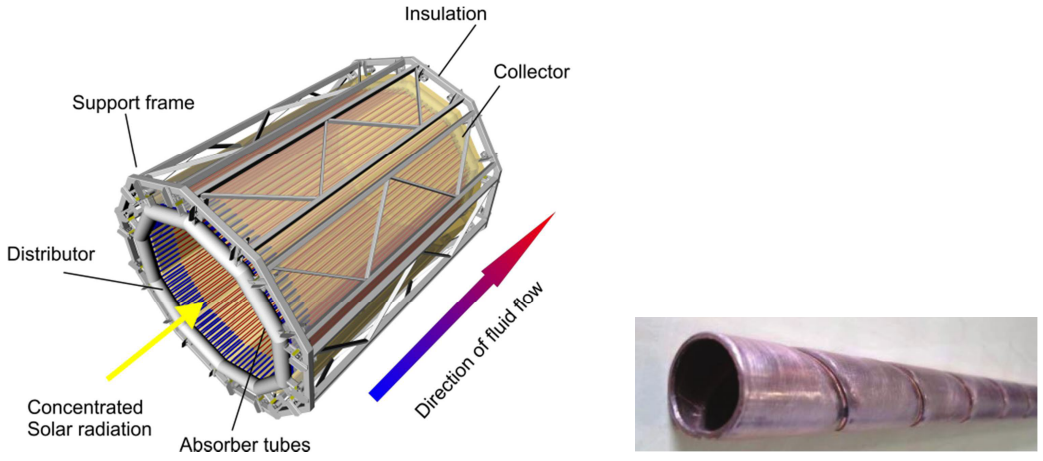

(a) (b)

Figure 6.9: (a) Rendering of the SOLUGAS receiver (Korzynietz *et al.*, 2012) and (b) photo of a corrugated tube (Uhlig *et al.*, 2015)

SOLUGAS

The SOLUGAS receiver, depicted in Figure 6.9(a), is in essence a scale-up of the SOLHYCO receiver. The 3.1 MW_t receiver was designed to pre-heat air at an absolute pressure of 10 bar from 330 °C to 800 °C (Quero *et al.*, 2014; Uhlig *et al.*, 2015). A combustion chamber downstream the receiver is used to further elevate the air temperature to 1150 °C as required by the installed gas turbine. The absorber consists of 170 parallel, 5 m-long Inconel tubes with an inner diameter of 19.6 mm in a cylindrical cavity with an aperture diameter of 2.7 m (Uhlig, 2009; Quero *et al.*, 2014). The design pressure drop of the system is 250 mbar (Uhlig *et al.*, 2015).

Experimental results on the thermal efficiency of the tested system could not be retrieved. However, Uhlig *et al.* (2013) predict the thermal efficiency of a scaled-up manifestation of the concept at 80 % with additional optical losses through reflections of 6 %. When equipped with a window similar to the one investigated in the SOLHYCO project, the combined optical-thermal efficiency is predicted to increase from 75 % to 83 %. In a further study, Uhlig *et al.* (2015) found considerable potential in thermal efficiency improvement (from 71.9 % to 83.5 %) by using (a) a larger number of tubes than necessary to comply with the pressure drop requirements and (b) corrugated tubes, depicted in Figure 6.9(b), instead of smooth tubes. According to Uhlig *et al.*, these corrugated tubes, which are manufactured by plastically deforming a plain tube by applying force from its outside, are potentially superior to the wire-coil inserts used in the SOLHYCO project in terms of manufacturability and heat transfer.

In an extension to the project named SOLTREC, an enlarged version of the REFOS receiver was added downstream the SOLUGAS receiver to further

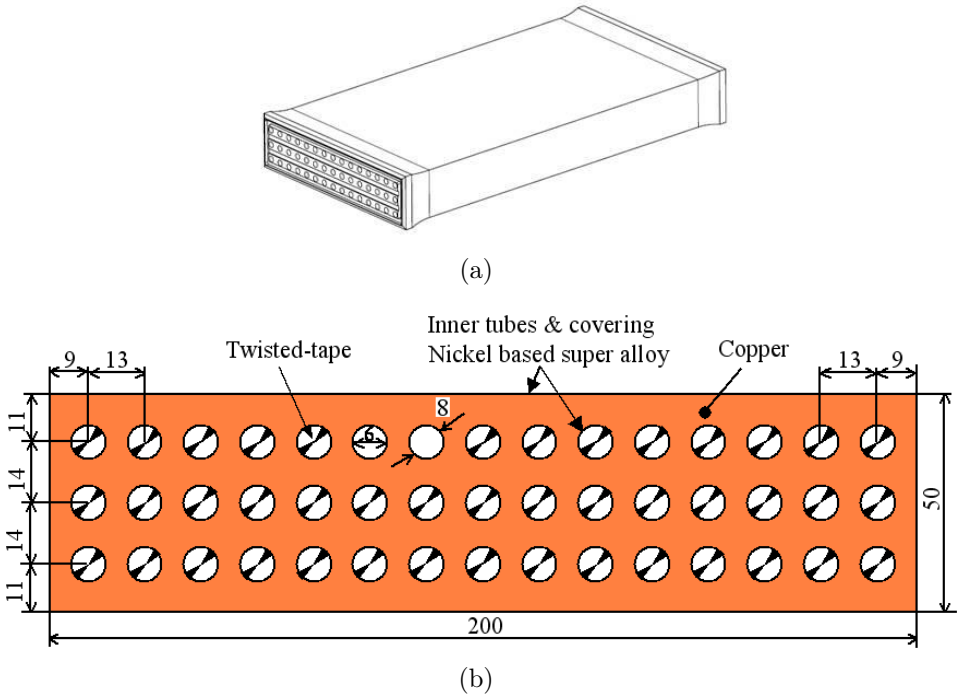

Figure 6.10: (a) Drawing and (b) cross-section of a PEGASE absorber module (Bellard *et al.*, 2012)

heat up the pressurized air to 1000 °C (del Río *et al.*, 2015).

PEGASE

The receiver developed by the French CNRS in the PEGASE project does not have a tubular absorber, however, it can be seen as a related concept that attempts to mitigate problems of these. A PEGASE absorber module, depicted in Figure 6.10(a), absorbs solar radiation on one of the flat steel alloy surface covers of a rectangular block of copper. The block is cooled by pressurized air flowing through Inconel tubes (enhanced with twisted tape inserts) that are embedded into the copper (see Figure 6.10, b). The copper block is intended to conduct heat to all tubes, therefore minimizing temperature differences within the absorber and around the tube circumferences. Several of these modules, which are 40 cm long and 20 cm wide, are connected in series to successively raise the air temperature and in parallel to increase the total receiver rating (Grange *et al.*, 2011).

Bellard *et al.* (2012) define the design conditions of the PEGASE receiver as follows: The air stream is heated up from 300 °C to 550 °C in the first module and further to 750 °C in the second one at a maximum allowable total pressure drop of 300 mbar. In experiments with a 300 kW_t pilot receiver, air outlet temperatures close to 800 °C could be achieved when the inlet air was

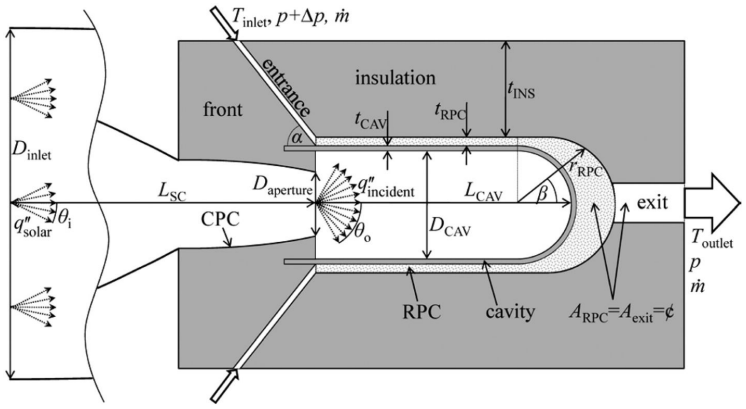

Figure 6.11: Schematic half-section of the ETH Zurich's pressurized air receiver concept showing relevant heat transfer mechanisms (Hischier *et al.*, 2015)

preheated. However, the pressure drop exceeded 250 mbar for a single absorber at high air temperatures.

ETH

The absorbing surface in the ETH Zurich's pressurized air receiver is not the outside of a metallic tube but the inside of a ceramic one (see Figure 6.3.2). The concentrated solar radiation penetrates into the aperture of the cavity (after being concentrated further in a CPC) and heats it up. The thermal energy is conducted through the tube wall and further into an annular reticulate porous ceramic (RPC) foam. The outer tube surface and the RPC are cooled by pressurized air, which is contained by an insulation on the inside of a pressure vessel. Advantages of the concept compared to other receivers with tubular absorbers are (a) the intrinsic cavity to increase optical and thermal efficiency, (b) a homogeneous heat flux on the inside of the tube and pressure on the outside, (c) an increasing temperature towards the depth of the cavity (due to the air flow direction) and higher sustainable temperatures due to the ceramic absorber material as well as (d) the large heat transfer area of the RPC foam to the air flow (Hischier *et al.*, 2009). The disadvantages are the optical penalties associated with CPCs and cavities, the thermal resistance associated with the conductive heat transfer through the absorber tube wall, into and through the RPC foam as well as durability concerns under thermal stress.

Laboratory tests of a single receiver unit in a high-flux solar simulator resulted in a maximum air outlet temperature of approximately 1060 °C at a thermal efficiency of 36 % (Hischier *et al.*, 2012). The maximum thermal efficiency of 77 % was achieved at a much lower outlet temperature of close to 550 °C. At the design outlet temperature of the previously mentioned tubular receivers (around 800 °C), the pilot receiver had a thermal efficiency of approximately 65 %. The measured pressure drop in the conducted experiments

was below 10 mbar for all air mass flow rates.

In simulations with optimized geometries, Hischier *et al.* (2012) predict much higher efficiencies between 75 % and 90 % for air outlet temperature above 1000 °C, however at much higher pressure drops and absorber temperatures. The optical efficiency of the optimized cavity geometry is calculated to be 99 %, however optical losses caused by the CPC are expected to be high.

Conclusions

Tubular metallic pressurized air receivers have been proposed as more cost-effective alternatives to receivers with pressurized windows for air outlet temperatures up to approximately 800 °C. The major challenge is to achieve effective heat transfer to the air stream while not exceeding the allowable pressure drop. Low heat transfer coefficients cause high absorber temperatures and, in combination with the generally inhomogeneous influx on the absorber, also large temperature gradients. This, furthermore, leads to high thermal losses and material stresses.

Convective losses were found to significantly penalize the thermal efficiency of the respective tubular cavity receivers of the SOLHYCO and SOLUGAS projects. A non-pressurized quartz glass window was proposed to lower convection and, to a lesser degree, radiation losses. However, this additional component also results in an increased system cost and complexity.

The ETH Zurich's receiver is more complex than the previously mentioned tubular receivers as it has a ceramic absorber and requires a CPC. It is, therefore, rather directed at high-temperature applications where it competes with the (to date) more extensively tested DIAPR and REFOS concepts. The PEGASE receiver has, so far, not reached the milestones in terms of pressure drop and is less extensively tested than the other presented pre-heaters.

6.4 The Hybrid Pressurized Air Receiver (HPAR) concept[1]

In the Hybrid Pressurized Air Receiver (HPAR) concept, first introduced by Kretzschmar and Gauché (2012), the insufficient heat removal from absorber tubes through the internal, pressurized air stream is supported by additionally cooling the tubes with an external, non-pressurized air flow. The concept's potential advantages compared to other metallic tubular receivers are described in this section. Furthermore, an adaptation of the concept is proposed for implementation as part of the cascaded hybrid receiver system of a SUNDISC cycle plant.

[1] parts of this section have previously been published (see Heller *et al.*, 2016*b*)

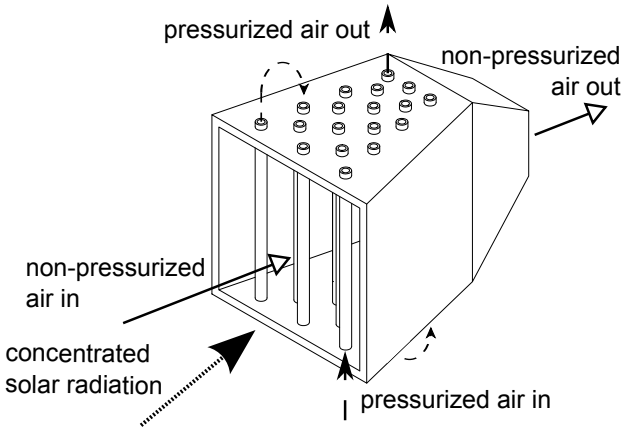

Figure 6.12: Sketch of the HPAR concept (adapted from Heller *et al.*, 2016*b*)

6.4.1 Concept description

The absorber tubes in the HPAR concept are arranged as a staggered bundle to create a macro-volumetric absorber with a small surface area exposed to ambient but a large heat transfer area to the heat transfer fluids (see Figure 6.12). Thermal radiation and reflected concentrated solar radiation from the tubes are partially absorbed by other tubes instead of being lost to the surroundings. Ideally, the highest absorber temperature in such a receiver is apparent at tubes inside the cavity as opposed to external receivers where the outermost surfaces have the highest temperature. Heating up of the pressurized air stream should advantageously start at the highly irradiated and exposed front before flowing through a serpentine path towards the shielded back, supporting the volumetric effect (see Section 6.2.1).

The second defining feature of the HPAR is a non-pressurized air flow around the tubes of the bundle. This forced flow cools the tube surfaces by means of convection and evens out the circumferential temperature gradients on the tubes, therefore decreasing thermal stresses. The coldest air is in contact with the most exposed surfaces of the bundle, enabling a strong cooling effect (depending on flow conditions) and further minimizing losses due to thermal radiation from the exposed frontal rows.

In a single-pressure receiver system, thermal energy transferred to ambient air via natural convection would be discarded. This convection loss can account for approximately 10 % of the incoming concentrated radiation in a cavity receiver (see sections 6.3.2 and 6.3.2). In the HPAR concept, the thermal energy is not lost but used as a source of lower-temperature thermal energy to the cycle. However, as the convection heat transfer to the non-pressurized air stream is enforced, the maximum energy input to the pressurized air stream decreases. The value of the receiver concept, therefore, largely depends on a beneficial introduction of this lower-grade heat into the cycle.

6.4.2 Adaptation of the HPAR concept to the SUNDISC cycle

The potential of utilizing a (cascaded) hybrid receiver system to heat up the pressurized and non-pressurized air streams in the SUNDISC cycle is discussed in brief in Section 3.2.2. In this section, a specific manifestation of the HPAR concept that was adapted for implementation in the SUNDISC cycle is presented.

The high-temperature part in a cascaded pressurized receiver system (HT-HPRS) is expected to feature receivers of the volumetric type with pressurized quartz glass windows that increase the air temperature to above 1000 °C while the low-temperature part could feature a metallic tubular absorber and preheat the pressurized air to approximately 800 °C. The non-pressurized air stream should ideally be heated to the same temperature as the gas turbine outlet flow so that both streams can simultaneously charge the thermal energy storage system or power the steam generator without further loss of exergy. A return loop of the exhaust gas from the TES system and SG to the non-pressurized inlet stream of the hybrid receiver system is a likely option if found feasible and viable.

A rendering of a possible manifestation of the two receiver systems and the connecting piping can be seen in Figure 6.13. The HT-HPRS could be located on the northern side of the tower (for a Northern Hemisphere plant) to benefit from the highest annual solar field efficiency, lowered spillage losses and shorter piping at the highest temperature while the 360° HPAR receiver allows for the utilization of a surrounding field.

6.4.3 Conclusions

A manifestation of the HPAR system is a promising alternative to other proposed pre-heaters for high-temperature pressurized air receivers if the non-pressurized air stream can be utilized efficiently. It is expected that such a receiver has the following benefits:

- A high annual overall optical efficiency (including the solar field's) due to the option of utilizing a surround field and a relatively large aperture (compared to cavity receivers) as well as the light-trapping effect of the tube bundle,
- a high thermal efficiency due to (a) the elimination (ideally) of convection losses, (b) dual-cooling of the most exposed surfaces and (c) an absorber temperature increase towards the center of the receiver, enforced by the flow direction of both air streams (volumetric effect),
- lowered temperature gradients around the tubes' circumference due to the dual-cooling of the absorbers compared to air receivers whose absorbers

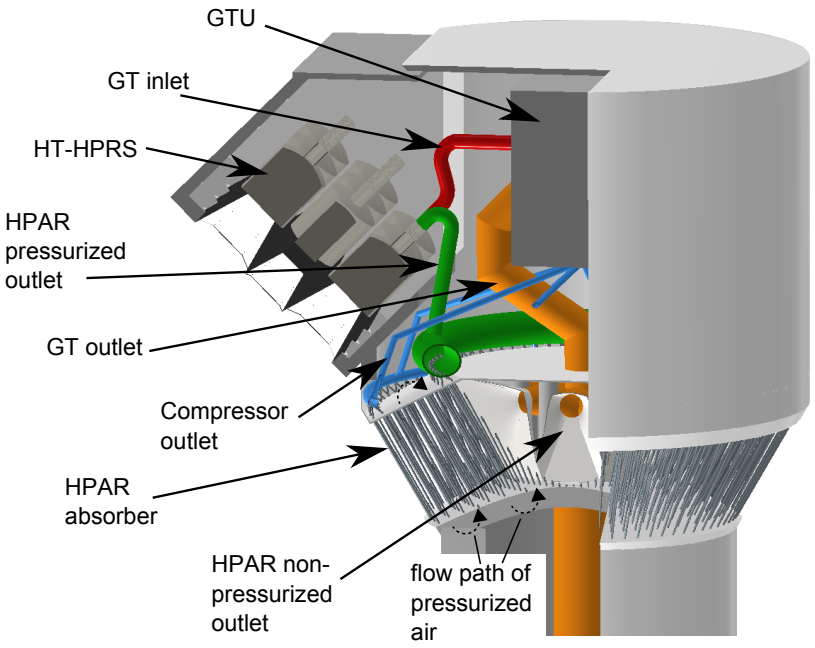

Figure 6.13: Rendering of a manifestation of a cascaded hybrid receiver system (Heller *et al.*, 2016*b*)

are only internally cooled and that are also arranged perpendicular to incoming radiation,

- a relatively simple design because of the use of well-known materials (high temperature-resistant steel) for the absorbers, which have a simple tubular geometry as well as
- advantageous part-load behavior as the number of operational parameters is increased compared to a single-fluid receiver system (two air streams).

Challenges, on the other hand, are mainly expected due to

- a high solar flux on the front surfaces of exposed tubes that are operated at their material limit in terms of temperature,
- insufficient heat transfer to the non-pressurized fluid resulting in low outlet temperatures,
- convective losses due to wind effects,
- the complexity in operation of a hybrid system under different load situations and
- manufacturing of the absorber tubes and construction (welding) of the receiver.

To quantify the expected benefits and challenges in terms of optical and thermal efficiency of the receiver system, a thermal model of it is developed in the upcoming section.

Chapter 7

Modeling of an HPAR system[1]

The overall performance of an HPAR receiver is dictated by its effectiveness in absorbing incoming concentrated solar radiation and the ability to transfer the absorbed thermal energy to the air streams. For an overall energy balance of the receiver, detailed modeling is therefore necessary for the following heat transfer areas:

- Absorption and reflection of incoming solar radiation,
- internal forced convection to the pressurized air (PA) stream,
- radiation heat transfer between tubes, walls and ambient as well as
- external forced/mixed convection to the non-pressurized air (NPA) stream.

In this section, models of different levels of detail are presented for these mechanisms. These models are primarily intended to provide insights into the interaction of the energy flows at design point and help identify sensible geometrical parameters for later, more in-depth simulations. Boundary conditions and performance indicators are derived from the chosen implementation of the HPAR in a SUNDISC cycle plant with a cascaded hybrid receiver system.

7.1 Boundary conditions and design assumptions

The conducted simulations and parametric study on the SUNDISC cycle (see Chapter 4) allow for the definition of requirements for a potential hybrid receiver system in the cycle. It should be noted that these definitions are strongly affected by the operating strategy and the choice of gas turbine parameters. The boundary conditions and geometric parameters of Table 7.1 are chosen for a plant in which the previously described SGT-100 gas turbine and a metallic

[1] parts of this section have previously been published (see Heller *et al.*, 2016*b*)

Table 7.1: Boundary conditions of the investigated receiver system

Parameter	Value	Reference
GTU rating	5.25 MW_e	SIEMENS AG (2005)
PA mass flow rate	20.5 kg/s	SIEMENS AG (2005)
Operating pressure	14.7 bar	SIEMENS AG (2005)
Compressor outlet temperature	400 °C	SIEMENS AG (2005)
GT outlet/desired HPAR NPA outlet temperature	534 °C	SIEMENS AG (2005)
HPAR PA outlet temperature	800 °C	Uhlig *et al.* (2015)
Absorber tube max. temperature	900 °C	Heller (2010)
Absorber tube d_i/d_o	25 mm/30 mm	Uhlig *et al.* (2015)
Maximum pressure drop	100 mbar	see paragraph

tubular receiver are used in a cascaded hybrid receiver system setup. The absorber tube diameters are an initial guess in accordance with Uhlig *et al.* (2013) and might be revised as a result of a detailed simulation of the HPAR and system design. The tubes are coated with Pyromark 2500 absorptive paint as it is the standard for state-of-the-art tubular solar absorbers and resists temperatures above 1000 °C (Ho *et al.*, 2013).

The maximum allowable pressure drop was deduced from an allowable system pressure drop between compressor outlet and turbine inlet of 250 mbar (Uhlig *et al.*, 2015) and estimates on the pressure drops of the HT-HPRS, connecting piping and fittings (presented in Appendix D).

The parametric study in Section 4.2 shows the lowest LCOE value for plants with an LPRS rating of 20 MW_t. Ratings between approximately 15 MW_t and 30 MW_t appear to still give close-to-optimal results. At an HPRS rating of 16.5 MW_t, the ratio of LPRS to HPRS rating should, therefore, be between 0.9 and 1.8. As the HPAR is foreseen to only preheat the PA stream from approximately 400 °C to 800 °C, instead of to the final 1102 °C, only approximately 55 % of the thermal energy demand into the PA stream is supplied by the HPAR. This means that between 23 % and 38 % of the thermal output of the HPAR should be transferred to the PA flow. However, the parametric study was conducted with specific thermal and economic models of the receiver systems. If other systems are implemented, for example a hybrid one, the economic optimum is likely to change. This ratio should, therefore, rather be seen as a first approximation.

7.2 Solar radiation

One of the aims of the HPAR concept's staggered tube bundle design is to imitate the effect of a cavity by absorbing incoming radiation on surfaces that

are at least partially shielded from the environment. The deeper the radiation penetrates, the more thermal energy can be transferred from surfaces that have reduced view factors to the environment and the more even the thermal input to the tubes, the better the utilization of all absorber tubes. As the geometric tube bundle layout that generates the deepest penetration or most uniform flux distribution on the absorbers is not obviously identifiable, a ray-tracing study with varying geometrical parameters has been conducted in SolTrace V. 2012.7.9 (NREL, 2012).

7.2.1 Ray tracing

In ray tracing simulations, rays of light are shot in random directions from the location of the sun towards the location of optical elements. These rays interact with the modeled system by transmission, absorption and reflection depending on pre-defined properties of the surfaces. In a CSP system, the rays would typically arrive on the concentrating mirrors at the angle of the sun's position, be (mainly) reflected towards the receiver and absorbed there. Due to mirror absorptivity, the sun half-angle, slope errors, blocking, shading and other factors, not all rays will arrive at the receiver. When tracing a large number of rays, the probable radiation onto the receiver and its origin in terms of angle and specific mirror can be predicted.

According to Bode and Gauché (2012), two ray tracing software suites for CSP are freely available: SolTrace and Tonatiuh, maintained by NREL and CENER, respectively. Due to the more complete help files and experience in usage of the software within the research group, SolTrace is used in this project. Additional MATLAB and SolTrace code was developed for the following four purposes:

- Automatically define geometrical input data for SolTrace (sun shape, location, field layout, absorber surfaces),
- define the sun position and calculate the respective aim point of each heliostat for any point in time,
- run several iterations in SolTrace and write results in output files as well as
- combine results of iterations and plot data for interpretation (post-processing).

SolTrace has an inherent limitation in terms of the numbers of rays that can be cast in a single simulation. This limit depends on the number of surfaces involved and can cause unacceptably coarse flux maps on the absorbers. In this study, multiple simulation runs are conducted for each layout. The hit points of these iterations are then combined until sufficient convergence is reached. Figure 7.1 shows the fraction of absorbed rays per angular section of all tubes

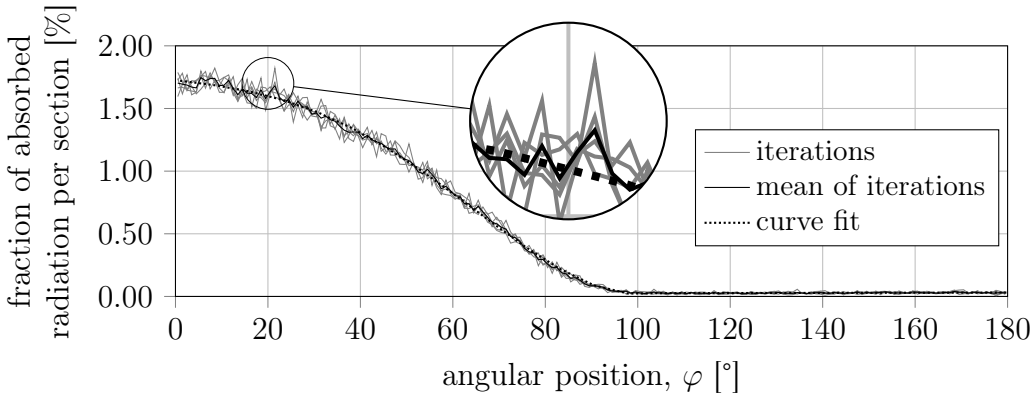

Figure 7.1: Ray tracing iterations: Multiple iterations' results, mean and curve fit for angular distribution (measured from front of tube) of absorbed radiation on first tube row

in the front row (Row 1) for 5 iterations with 5×10^5 rays each, the mean of all iterations and a piece-wise curve fit. The exact number of necessary iterations varies depending on the complexity of the optical system and which information is sought after.

7.2.2 Solar field optical model

To simulate the influx on absorber tubes realistically, the heliostat field is modeled based on an existing layout, namely the field of eSolar's Sierra SunTower. The geometry, depicted in Figure 7.2(a), is identical to the one generated for the SAM model presented in Appendix B.

The receiver is assumed to be tilted 45° to horizontal, as depicted in figures 6.13 and 7.2(b). The receiver aperture (and target) is therefore a truncated cone with an initially estimated upper diameter of 5.7 m and, at a tube length of 2.0 m, a lower diameter of 2.8 m. The total image error of the flat mirrors was set to 1.4 mrad as given for eSolar's heliostats by Schell (2011). Each heliostat aims at a target circle, which is described as the center of the conical aperture area. In other words, each heliostat aims at the axial center of the absorber tube closest to it.

At this stage of the receiver development, the ray-tracing model is only used to determine the flux distribution on receiver and absorber elements at design point (summer solstice) but not for determining the solar field efficiency or flux distribution throughout the year. The model is therefore only validated against the design-point solar field efficiency as determined by Tyner and Pacheco (2009) through their own ray-tracing model ($\eta_{SF} = 78\,\%$). This includes losses due to availability, mirror reflectivity, cleanliness, cosine effect, blocking, shading, spillage and atmospheric attenuation. As the values calculated by SolTrace do not include losses due to availability and atmospheric attenuation, these were

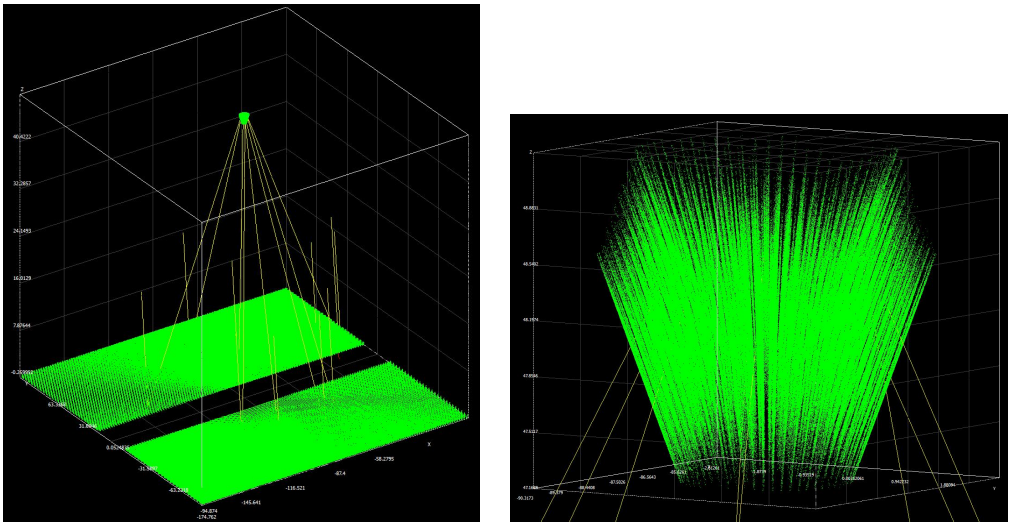

(a) (b)

Figure 7.2: Screenshots from SolTrace showing ray hit points (a) on solar field and receiver as well as 10 random rays and (b) on one receiver configuration (5×10^6 rays; note that the three dimensions are scaled differently)

estimated. Heliostat availability was set to a value of 99 % (see Section 2.1.2) and atmospheric attenuation to 98.4 %, which was determined as the annual average in the SAM model (see Appendix B). The overall efficiency of the developed model for summer solstice at the location of the Sierra SunTower facility in Lancaster, California, is then (compare with Equation 2.1.7):

$$\begin{aligned} \eta_{\text{SF}} &= \eta_{\text{cbs}}\,\eta_{\text{spill}}\,\eta_{\text{atm}}\,\eta_{\text{HS,refl}}\,\eta_{\text{HS,clean}}\,\eta_{\text{HS,avail}} \\ &= \eta_{\text{SolTrace}}\,\eta_{\text{atm}}\,\eta_{\text{HS,avail}} \\ &= 0.859 \times 0.984 \times 0.950 \times 0.980 \times 0.99 = 0.779. \end{aligned} \tag{7.2.1}$$

Although there are uncertainties regarding spillage losses due to the different receiver designs, the agreement is considered sufficient for investigating flux profiles on the absorber surfaces.

7.2.3 Receiver optical model

The absorber tubes are modeled with the incidence angle-dependent reflectance of Pyromark 2500 paint on Inconel (Ho *et al.*, 2013, Table 1). The input into SolTrace is a look-up table of angle-reflectance pairs which were generated with Equation (A.3.1). As the software does not interpolate between angles, a higher resolution was chosen at large incidence angles where the absorptance values decrease rapidly. The top, bottom and back wall are given an absorption coefficient of 0.3 in the solar spectrum (Ebert *et al.*, 2015). A large slope error was chosen for all absorber and wall surfaces to simulate diffuse reflection.

Assumptions for the geometrical layout that were not varied in the parametric studies include that

- the receiver is tilted by a non-optimized angle of 45°,
- the number of tubes per row is identical and
- the radial distance between each neighboring row (Δr in Figure 7.3) is identical.

At the investigated design point, the influx on the receiver from all directions is almost identical in magnitude. This greatly simplifies the interpretation of results as the receiver can be modeled as circumferentially periodic. Therefore, the flux distribution for each column of tubes — that is, one tube of every row — is identical.

The hit point location of all absorbed rays is saved in an output file, which is interpreted by a MATLAB code. The code is used to determine the distribution of hit points in terms of (a) row number, (b) axial height and (c) circumferential position on the tube. These distribution data sets are used to create piece-wise curve fits (see Figure 7.1) for the axial and circumferential flux distribution for each row. The order of the polynomial fits and the threshold of the piece-wise functions were decided on after individual comparison of the fitted curves, created with the "polyfit" function in MATLAB, with the original data curves. Additionally, the maximum absolute and relative difference between data and fitted curve was kept below approximately 0.1 %, respectively.

The top and bottom wall are each divided into as many sections as there are rows (each having the shape of a truncated cone). For these, the individual hit points are counted to obtain the radial distribution (from the central vertical axis of the receiver) of influx on them.

7.2.4 Initial findings of ray-tracing simulations

Simulations with the standalone optical model generated results that lead to findings regarding the penetration of concentrated solar radiation into the depth of the receiver as well as axial and circumferential flux distributions on the absorber tubes. These findings are used to limit the ranges of geometrical parameters for further studies that include heat transfer models.

Penetration of radiation

In successive design point simulations the angle between the tubes in a row, $\Delta\phi_{\text{columns}}$, and the tangential offset of each tube row to the next, $\Delta\phi_i$, was varied. The absorbed radiation in the front row is almost exclusively dictated by the fraction of blocked aperture area, which depends on the angle between the tubes, the distance from the center of the receiver and the tube diameter.

Therefore, if more tube rows are to be implemented, for example to increase the flow path length of the pressurized air stream or lower the flux reaching the back wall, the tubes have to be located farther apart to still achieve penetration of radiation into the depth of the receiver. This, however, means that there are less tube columns in parallel to heat up the pressurized air stream.

The absorption in rows further inside the cavity is strongly influenced by the tangential offset. The distribution of the absorbed flux per row for layouts with identical offsets between all rows is depicted in Figure 7.3. Additionally, the distribution for one layout with varying offsets between the rows is shown. The latter was chosen as a configuration providing a compromise between constant influx per row, low influx on the second and third row (to lower their thermal losses) and low reflection to ambient. It can be seen that considerable penetration into the tube bundle is feasible and the angular offset between tube rows has a major influence on the absorption distribution. It has to be kept in mind, however, that this distribution is bound to change over the course of a day and year as blocking, shading and cosine efficiencies change. Reflection losses and the amount of solar radiation that reaches the back wall are relatively low. Radiation absorbed in the top and bottom wall is even lower (not shown in plot).

Axial distribution of flux on tubes

The simple utilized aim point strategy, described in Section 7.2.2, leads to a high flux maximum at the center of the tubes, which is most pronounced in the first row (see Figure 7.4, left, for a setup with 10 rows and $\Delta\phi_{\text{columns}} = 6°$) as this is where the focus point of all heliostats is located. This leads to high temperature gradients and maximum temperatures of the tubes, resulting in high material stresses and thermal losses. As a dedicated aim point strategy is out of scope for this study, a simple assumption is implemented: The absorbed solar radiation, $\dot{Q}_{\text{sol,abs}}$, is calculated as the average of the derived value, $\dot{Q}_{\text{sol,abs,SolTrace}}$, and its mean value. The absorbed thermal energy in section i_{ax} of row n_{row} can then be calculated through

$$\dot{Q}_{\text{sol,abs},n_{\text{row}},i_{\text{ax}}} = \left[\dot{Q}_{\text{sol,abs},n_{\text{row}},i_{\text{ax}},\text{SolTrace}} + \sum_{i_{\text{ax}}=1}^{n_{\text{ax}}} \left(\dot{Q}_{\text{sol,abs},n_{\text{row}},i_{\text{ax}},\text{SolTrace}}\right)/n_{\text{ax}}\right]/2, \quad (7.2.2)$$

wherein n_{ax} represents the number of axial sections of a tube.

Circumferential distribution of flux on tubes

The circumferential distribution of the incoming radiation, which was averaged over the length of each tube, is depicted in Figure 7.4 (right). The expected

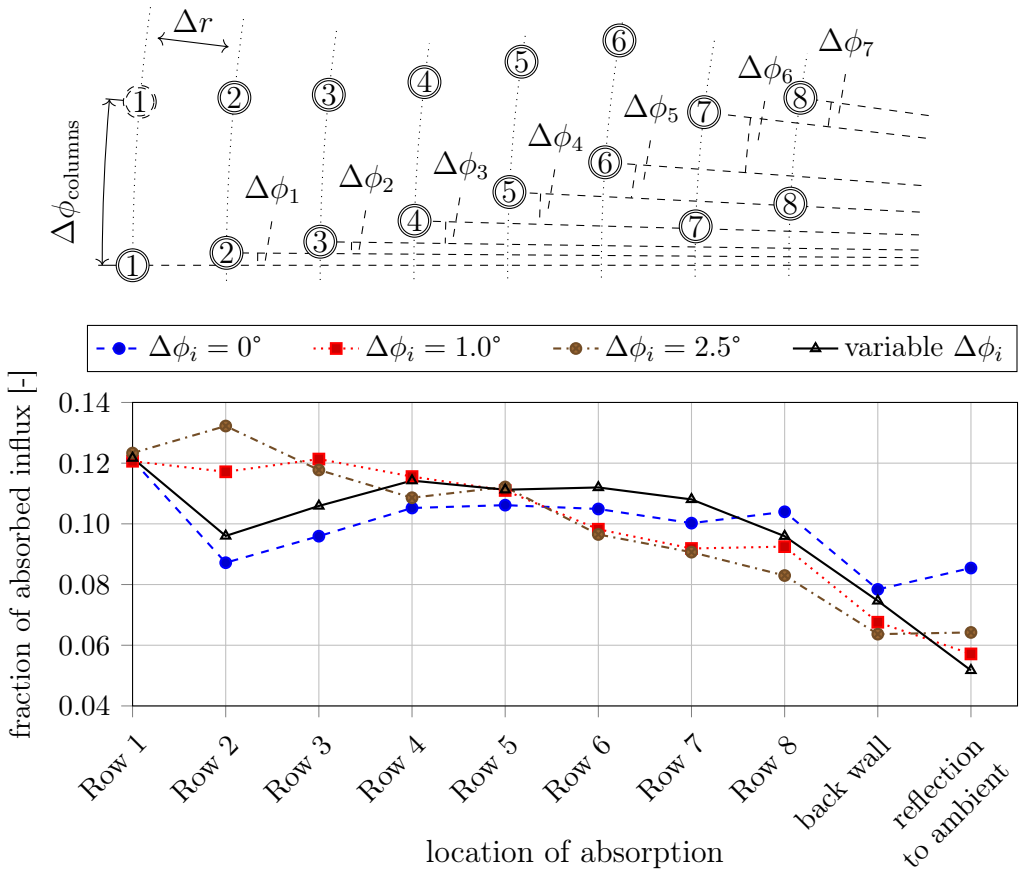

Figure 7.3: Distribution of absorbed incoming flux in the absorber tube rows for constant and variable angular offsets, $\Delta\phi_i$, between the 8 tube rows

cosine-shape on the tube front and almost no impinging radiation at the back for rows 1 and 6–10 is visible. Rows 2–5 experience less influx from their front because they are partially shaded by rows in their respective front. The offset angles between rows in this configuration are $\Delta\phi_{1...9} = [0; 0; 0; 0; 1; 1; 1; 1; 1]°$. Row 10 experiences the highest fraction of influx from its back because of the high reflectivity of the back wall behind it. The large thermal input difference over the tubes' circumference is aspired to be alleviated in the HPAR concept by cooling especially the front of the tubes with the cold NPA stream.

7.3 Internal convection

The main challenges of solar air receivers compared to other receiver technologies arise due to the poor heat transfer characteristics of air. Internal heat transfer

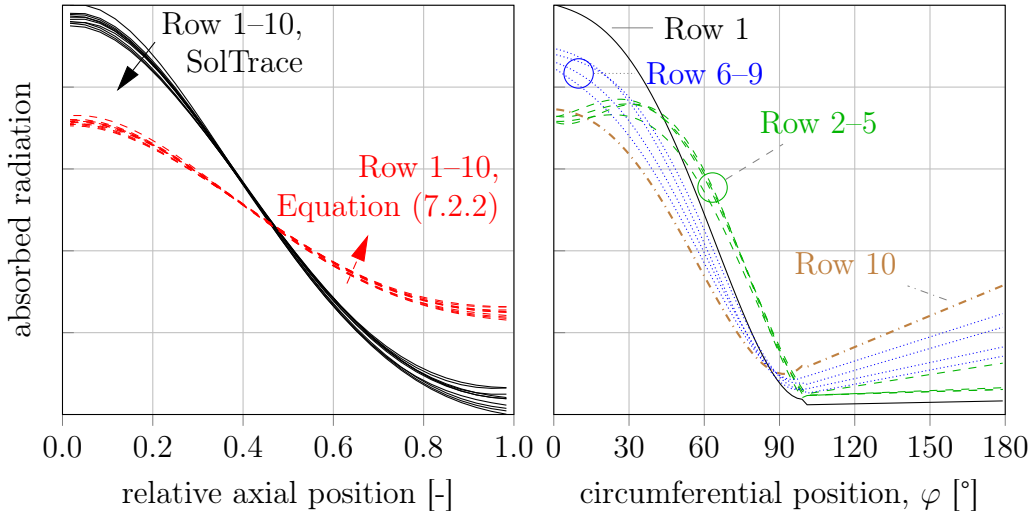

Figure 7.4: Curve fits for (left) axial flux distribution on tubes of all rows based on SolTrace results and according to Equation (7.2.2) from axial tube center (0) to tube end (1) and (right) circumferential distribution with piece-wise threshold at 100°

enhancements have, therefore, commonly been proposed for air receivers (see Section 6.3). A heat transfer model for the internal convection in plain and enhanced absorber tubes needs to be developed to realistically estimate the thermal and flow conditions as part of the overall receiver model.

7.3.1 Plain tube under circumferentially uniform heat flux

The convective heat rate inside a tube, $\dot{Q}_{\text{conv,i}}$, can generally be calculated through Newton's law of cooling

$$\dot{Q}_{\text{conv,i}} = h_{\text{conv,i}}\, A_{\text{tube,i}} \left(T_{\text{tube,i}} - \overline{T}_{\text{PA}}\right). \tag{7.3.1}$$

The difference[2] between mean PA temperature, $\overline{T}_{\text{PA}}$, and tube inner wall temperature, $T_{\text{tube,i}}$, needs to be kept as low as possible to minimize material temperature and thermal losses. The heat transferring surface area of the tube, $A_{\text{tube,i}}$, is practically limited as the number of tubes that are flowed through in series cannot be increased without increasing the cost of the system, the pressure drop and the absorber surface area. Finally, the convective heat transfer coefficient, $h_{\text{conv,i}}$, mainly depends on flow conditions.

[2]To simplify computational solving for tube temperatures, the logarithmic mean has not been used here. It has to be made sure that the temperature increase of the fluid is small compared to the temperature difference between tube and fluid (for example by utilizing short axial sections).

The heat transfer coefficient is derived from the definition of the inner tube wall Nusselt number, Nu_i:

$$h_\mathrm{conv,i} = k_\mathrm{PA}\, Nu_\mathrm{i}/d_\mathrm{i} \tag{7.3.2}$$

with k_PA being the thermal conductivity of air and d_i the inner diameter of the tube. The local Nusselt number for fully turbulent flow inside a tube can be calculated via a modification of Gnielinski's equation (Gnielinski, 2010*a*, Sect. G1.4.1, Eq. 28), which is valid for fully developed flow in the Reynolds numbers range $1 \times 10^4 \leq Re_\mathrm{i} \leq 1 \times 10^6$

$$Nu_{\mathrm{i},x} = \frac{(f_\mathrm{i}/8)\ Re_\mathrm{i}\, Pr_\mathrm{i}}{1 + 12.7\sqrt{f_\mathrm{i}/8}\left(Pr_\mathrm{i}^{2/3} - 1\right)}\left[1 + 1/3\,(d_\mathrm{i}/x)^{2/3}\right]. \tag{7.3.3}$$

This modification includes the effect of flow development at the axial coordinate x from the inlet of the pipe. All fluid parameters including the Prandtl number, Pr_i, are determined for the bulk mean fluid temperature. The Darcy-Weisbach friction factor, f_i, is calculated from the Colebrook equation (Çengel and Ghajar, 2011, Section 8.6)

$$\frac{1}{\sqrt{f_\mathrm{i}}} = -2.0\,\log_{10}\left(\frac{\varepsilon_\mathrm{rough,i}/d_\mathrm{i}}{3.7} + \frac{2.51}{Re_\mathrm{i}\sqrt{f_\mathrm{i}}}\right), \tag{7.3.4}$$

in which $\varepsilon_\mathrm{rough,i} = 0.002\,\mathrm{mm}$ represents the surface roughness of the tube (for a smooth stainless steel tube according to Çengel and Ghajar, 2011, Figure A-20). The pressure drop over the tube length is then given by the definition of f_i

$$\Delta p = f_\mathrm{i}\frac{L}{d_\mathrm{i}}\frac{\rho\,\overline{U}^2}{2} \tag{7.3.5}$$

with the tube (section) length L and the fluid mean velocity $\overline{U}$.

An additional pressure drop for each U-shaped bend between rows is calculated according to Kast *et al.* (2010, Sect. L1.3.7)

$$\Delta p_\mathrm{bend} = \zeta_\mathrm{bend}\frac{\rho_\mathrm{NPA,bend}\,U_\mathrm{bend}^2}{2}. \tag{7.3.6}$$

The fluid density, $\rho_\mathrm{NPA,bend}$, and velocity, U_bend, are determined at the inlet to the bend. The drag coefficient ζ_bend is calculated from a curve fit to Reynolds number-dependent data for a 90°-bend with the appropriate bend radius to tube diameter ratio in Kast *et al.* (2010, Sect. L1.3, Fig. 16)

$$\zeta_{90^\circ} = 257.08\, Re_\mathrm{NPA,bend}^{-0.582}. \tag{7.3.7}$$

Based on Kast *et al.* (2010, Sect. L1.3, Fig. 15), it is estimated that the pressure drop in an 180°-bend is 1.4 times larger than in a 90°-bend

$$\zeta_\mathrm{bend} = 1.4\,\zeta_{90^\circ}. \tag{7.3.8}$$

7.3.2 Circumferentially non-uniform heat flux

In order to account for non-uniform heat fluxes, the previous model of circumferentially uniform heat transfer coefficients and wall temperatures has to be adapted. Circumferentially non-uniform temperature and heat flux profiles can cause varying heat transfer coefficients (mainly due to differences in local fluid temperatures) which influences the temperature profile at the tube wall. If the circumferential temperature profile is calculated with a bulk heat transfer coefficient or Nusselt number, these effects are neglected (Reynolds, 1963). Alternatively, a circumferentially varying Nusselt number can be derived for arbitrary flux profiles.

The in-depth description of the used method and required tabulated data are given by Gärtner *et al.* (1974). The general steps of the approach are the following:

1. The mean heat flux into the fluid over all circumferential sections, j, of an axial section, i, is calculated,

$$\bar{\dot{q}}_{\mathrm{conv,i},i} = \sum_{j}^{N_{\mathrm{circ}}} \dot{q}_{\mathrm{conv,i},i,j}. \tag{7.3.9}$$

2. The relative flux variation from the mean is given by

$$\dot{q}_{\mathrm{conv,i},i,j,\mathrm{rel}} = \left(\dot{q}_{\mathrm{conv,i},i,j} - \bar{\dot{q}}_{\mathrm{conv,i},i}\right) / \bar{\dot{q}}_{\mathrm{conv,i},i}. \tag{7.3.10}$$

3. The relative flux variation over angle φ is expressed as a Fourier series

$$\dot{q}_{\mathrm{conv,i},i,j,\mathrm{rel}} = \sum_{n} \left[a_n \cos(n\,\varphi) + b_n \sin(n\,\varphi)\right], \tag{7.3.11}$$

   wherein n is the order of the series. The constants a_n and b_n to fit the flux profile are approximated with the "Fseries" function for MATLAB[3].

4. The local Nusselt number can finally be calculated with Reynolds and Prandtl number dependent coefficients, G_n, which are given by Gärtner *et al.* (1974, Table 1):

$$Nu_{\mathrm{i},i,j} = \frac{2\,\dot{q}_{\mathrm{conv,i},i,j}/\bar{\dot{q}}_{\mathrm{conv,i},i}}{G_0 + \sum_n G_n \left[a_n \cos(n\,\varphi) + b_n \sin(n\,\varphi)\right]} \tag{7.3.12}$$

The influence of using the described model for a generic case with circumferentially non-uniform flux is depicted in Figure 7.5. The temperature gradient in the tube as well as the maximum tube temperature increase for the enhanced model.

[3] Fseries.m — "Simple real Fourier series approximation" by Matt Tearle , `http://www.mathworks.com/matlabcentral/fileexchange/31013-simple-real-fourier-series-approximation/content/Fseries.m`

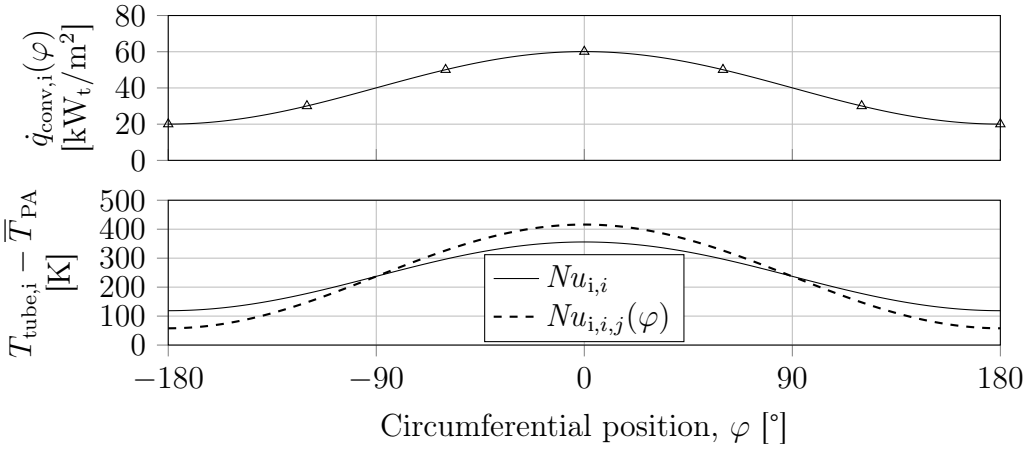

Figure 7.5: (Top) Dictated circumferentially non-uniform heat flux and (bottom) temperature differences between tube wall and fluid neglecting (solid line) and accounting for (dashed line) the non-uniform flux profile ($Re_\mathrm{i} = 30\,000$, $Pr_\mathrm{i} = 0.7$)

For a circumferentially uniform flux, the equation simplifies to $Nu_{\mathrm{i},i} = 2/G_0$. In the developed model, the value given by Gärtner *et al.* for G_0 is replaced with Equation (7.3.3) for enhanced accuracy at the tube inlet so that $G_0 = 2/Nu_{\mathrm{i},x}$.

7.3.3 Internal heat transfer enhancements

As discussed in Section 7.3.1, the required temperature difference between absorber and fluid to transfer a given amount of thermal energy can be lowered by increasing the convective heat transfer coefficient, $h_{\mathrm{conv,i}}$, or the heat transfer surface area. Heat transfer enhancements (HTE) commonly aim at one or both of these options (Siddique *et al.*, 2010).

When implementing HTEs in tubular solar receivers, the positive effect (namely increase of mean heat transfer and possibly more uniform circumferential temperature profile) has to be weighed against the negative (higher cost, pressure drop and potentially material stress).

Chen *et al.* (2001) conducted heat transfer and flow experiments on so-called dimpled tubes, depicted in Figure 7.6. They found the increase in heat transfer coefficient for some enhancements to be greater than the increase in friction coefficient, that is $J = \left(h_{\mathrm{tube,i,HTE}}/h_{\mathrm{tube,i,smooth}}\right) / \left(f_{\mathrm{i,HTE}}/f_{\mathrm{i,smooth}}\right) \geq 1$. For one of the investigated geometries, the calculated value was $J = 1.16$, which they found to be larger than any other HTE technology's. The influence on cost and material strength is expected to be small as a dimpled tube can be manufactured by mechanically deforming a smooth tube.

Due to its advantageous heat transfer and pressure drop characteristics, the design of experimental sample "tube 6", as defined by Chen *et al.* (2001), is modeled as an HTE for the HPAR absorber tubes. The geometrical parameters of this design are $e/d_\mathrm{i} = 0.0362$, $e/p = 0.06$, $e/\phi = 0.1091$ and three dimples

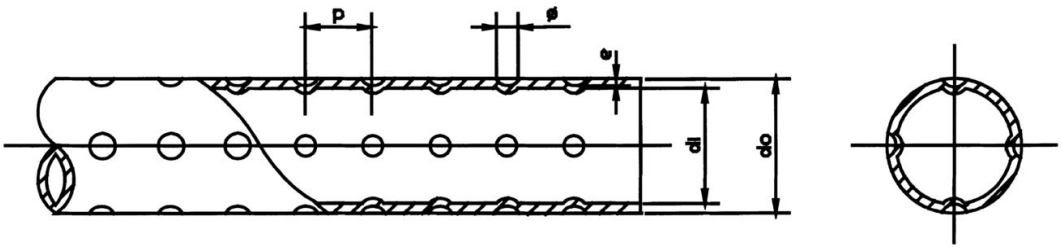

Figure 7.6: Geometry of a dimpled tube with 4 dimples around the circumference (Chen *et al.*, 2001)

around the circumference (compare to Figure 7.6). Based on experimental results, they define coefficients for curve-fits of friction factor and Nusselt number in dependence of the flow Reynolds number

$$f_{\mathrm{i,HTE}} = 1.045 \times 10^{-1} Re_{\mathrm{i}}^{-0.1426}, \tag{7.3.13}$$

$$Nu_{\mathrm{i,HTE}} = 1.460 \times 10^{-2} Re_{\mathrm{i}}^{0.8795}\, Pr_{\mathrm{i}}^{1/3}. \tag{7.3.14}$$

In some simulations, these correlations are used outside of the range at which measurements were conducted ($7.68 \times 10^3 \geq Re_{\mathrm{i}} \geq 5.2 \times 10^4$). If the HTE is found to be a promising option, this will have to be scrutinized.

The applicability of the previously described method for modeling circumferentially non-homogeneous flux distributions (see Section 7.3.3) is unknown. Increased turbulence in a tube employing heat transfer enhancements is expected to lower the negative effect of thermal stratification in tubes with circumferentially non-homogeneous flux. The method by Reynolds (1963) has nevertheless been implemented as a worst case in terms of temperature gradients.

7.4 Tube wall conduction and radiation inside the tube

Conduction in the tube determines the temperature difference between inner and outer tube wall and can decrease the circumferential temperature gradients. Due to the expected high temperatures and circumferential temperature gradients in the tube wall, radiation heat transfer inside the tube needs to be considered.

7.4.1 Conduction through the tube wall

Conduction through the tube wall in axial, radial and circumferential direction is calculated from Fourier's law of heat conduction

$$\dot{Q}_{\mathrm{cond}} = -k_{\mathrm{tube}}\, A \frac{\mathrm{d}T}{\mathrm{d}x}. \tag{7.4.1}$$

Therein, the thermal conductivity of the tube material, k_{tube}, is calculated in dependence of the section's mean material temperature with Equation (A.2.1). The tube ends are assumed to be adiabatic, that is, no energy is conducted to/from the inlet, outlet and U-bends between tubes.

7.4.2 Radiation inside the tubes

The radiation absorbed on the back wall of a tube section (i, j) can be calculated from the sum of the emitted radiation of every other tube segment, $\dot{Q}_{\text{i,emit},\xi,\chi}$, its view factors to the section, $F_{\text{view},\xi,\chi\to i,j}$, and the seconds' absorptance, $\alpha_{\text{i},i,j}$:

$$\dot{Q}_{\text{rad,i,in},i,j} = \alpha_{\text{i},i,j} \sum_{\xi,\chi} F_{\text{view},\xi,\chi\to i,j}\, \dot{Q}_{\text{emit,i},\xi,\chi}. \tag{7.4.2}$$

The absorptance is equal to the emittance (assuming validity of Kirchoff's law for gray bodies) and is set to a constant value of $\alpha_{\text{i}} = \varepsilon_{\text{i}} = 0.85$ (see Appendix A.2). Each section's emitted radiation is calculated from the Stefan-Boltzmann law — see Equation (6.1.4) — to which the reflected radiation is added (modeled as diffuse).

The view factor from each section to every other section was calculated with the ray tracing method of the Surface to Surface model in the computational fluid dynamics (CFD) software ANSYS Fluent V.15.0.0. In that model, the view factors between all cell surfaces are calculated and summed up for all surfaces of one defined area (named selection). For follow-up calculations, the axial and circumferential segment dimensions were chosen at 6.667 mm and 22.5°, respectively. To calculate the view factors, however, a smaller axial cell size of 4.17 mm was chosen while the circumferential discretization was not refined further.

The sum of all view factors from a section to all cells at least three axial sections up- or downstream were found to be less than 0.1 %. Therefore, only three axial sections were modeled. The view factors from a section to all other sections in the same and the two neighboring axial sections are depicted in Figure 7.7.

A mesh-dependency study was conducted for the "Resolution" of the ray tracing simulation. At resolutions above 100, only insignificant changes in the result were found. The computational time required for one such simulation is only a few seconds. The results of selected surfaces' view factors were validated with analytic correlations according to Howell (2010).

7.5 Thermal radiation in the cavity

In solar applications, radiation emitted from heated absorber surfaces is commonly referred to as *thermal* radiation to distinguish it from incoming (concentrated) solar radiation. This terminology has been adopted in this work.

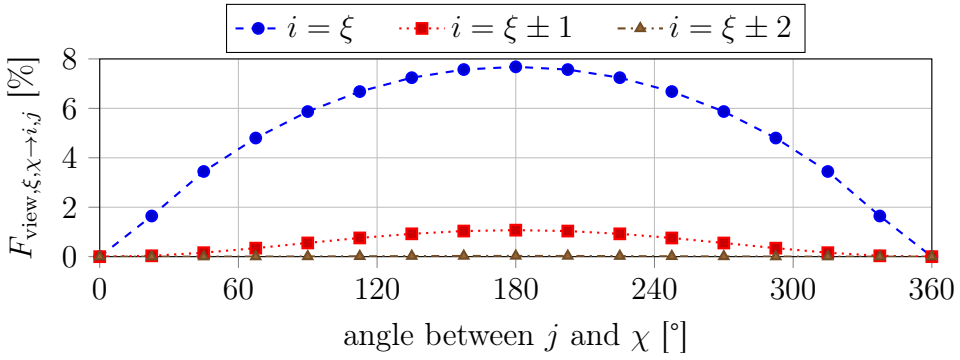

Figure 7.7: View factors from section (ξ, χ) to 16 circumferential, j, and three axial sections, i, inside a tube

As mentioned previously, thermal radiation is commonly the dominant thermal loss mechanism is high-temperature solar receivers. The tube bundle design in the HPAR concept is an attempt to lower losses by absorbing emitted radiation from heated absorber tubes on other tubes' surfaces. The modeling of thermal radiation heat transfer is, therefore, indispensable to evaluate the performance of an HPAR concept receiver.

7.5.1 View factors between tubes, walls and ambient

View factors between tube surfaces are again calculated with Fluent's Surface to Surface ray tracer. To simplify the model of the receiver — and minimize computational time considerably — the receiver is modeled as horizontal — that is, without a tilt and with vertical tubes. Therefore, a single column of tubes can be modeled with the periodic boundary walls reintroducing radiation that leaves the domain through the respective opposite wall. A screenshot of the geometry of the model is shown in Figure 7.8(a). In more detailed upcoming simulations, for example in CFD studies, this can be changed. However, for parametric studies of the tube layout, a horizontal receiver model is deemed sufficient.

Figure 7.8(b) depicts the tube section size in the ray tracing model for determining view factors between these sections, aperture, back wall and top/bottom wall. The domain is cut in two symmetric domains halfway of the axial dimension. The remaining half tubes are discretized into 3 axial segments each, measuring a sixth of the total tube length. Circumferentially, each tube is discretized into 4 segments. In total, for a setup with 10 rows, view factors between $10 \times 3 \times 4 = 120$ tube sections, 10 top/bottom wall sections, the aperture and the back wall are calculated. As each sections has a view factor to every other section and itself, this results in a total number of view factors of $(120 + 10 + 1 + 1)^2 = 17\,424$.

Mesh independence is investigated as for the radiation model for the inside

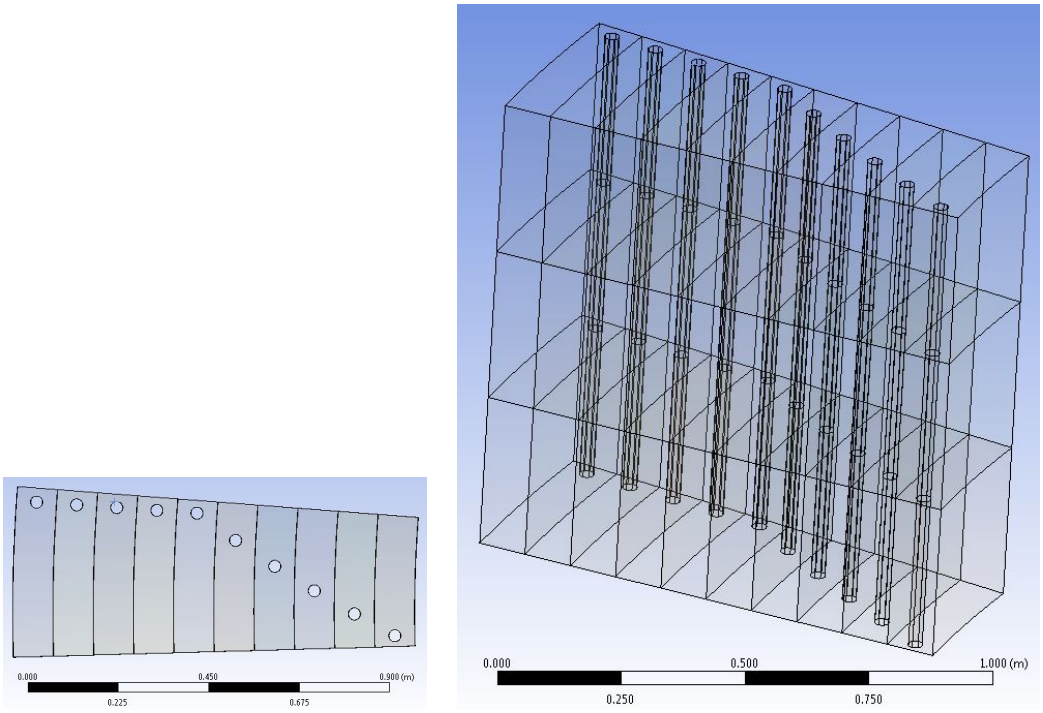

(a) (b)

Figure 7.8: Geometry of a modeled tube arrangement for view factor calculation in Fluent (a) from top showing periodicity and (b) from an angle showing the axial and circumferential cell size (see details in text)

of the tubes in terms of its ray tracing "Resolution". At a resolution of 400, no considerable changes in results were found. Furthermore, the results were verified according to the simplified reciprocity correlation for areas of identical surface areas

$$F_{\text{view},\xi,\chi\rightarrow i,j} = F_{\text{view},i,j\rightarrow\xi,\chi}. \tag{7.5.1}$$

The individual view factors are automatically converted into matrices suitable for the overall receiver heat transfer model by means of a MATLAB code.

The view factors to ambient of all 4 circumferential sections at 2 of the 3 axial positions of all tube rows are shown in Figure 7.9. As expected, the view factors are lower for sections that are (a) in rows deeper inside the receiver cavity, (b) closer to the back of the tube and (c) — to a lesser extend — closer to the axial ends of the tube. The latter is caused by increasing view factors to the top/bottom walls for tube sections that are in closer proximity to them. The top/bottom wall sections' view factors to ambient also show the expected trend.

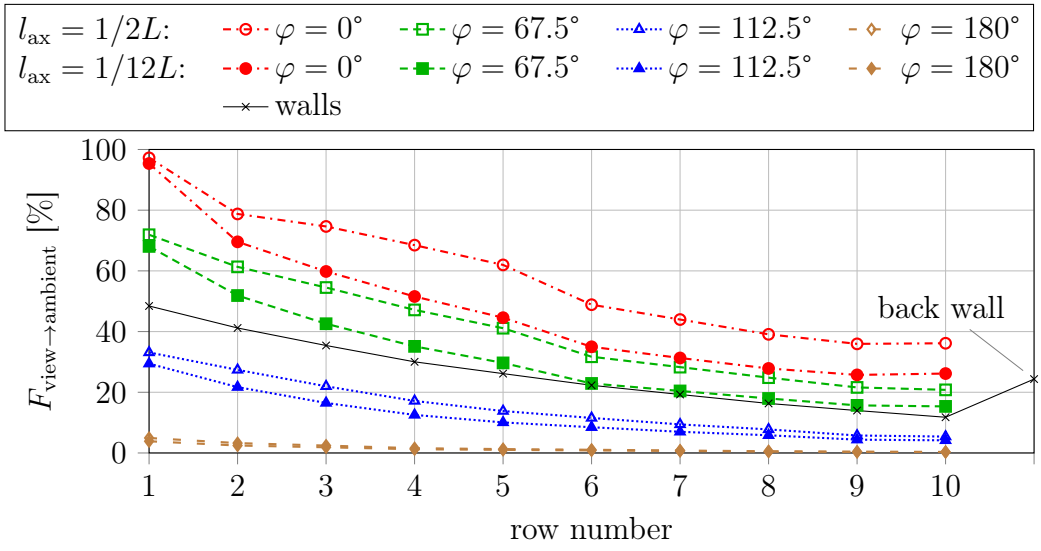

Figure 7.9: View factors to ambient from 4 different circumferential and 2 different axial locations, respectively, of all tube rows as well as from the top, bottom and back wall

7.5.2 Optical properties

The optical properties of the outer tube wall are those of Pyromark 2500 paint on Inconel. Ho *et al.* (2013) calculated the total hemispherical emittance of the paint applied on a steel tube, ε_{Pyro}, and provided a fitted curve for it in the temperature range 100 °C–1000 °C. As Ho *et al.* found the emittance to be in a similar range for Pyromark applied on Inconel tubes, although with a larger variance, a polynomial fit to the curve provided was used in this project's radiation model (see Appendix A.3). The surfaces absorptance for thermal radiation is assumed to be equal to the emittance and independent on the influx angle.

The top/bottom and back wall are all modeled with an absorptance for radiation in the thermal spectrum and total hemispherical emittance of $\alpha_{walls,rad} = \varepsilon_{walls,rad} = 0.50$ according to Ebert *et al.* (2015).

7.6 External convection

External convection from the absorber tubes to the non-pressurized air (NPA) flow is the most complex heat transfer mechanism to model in an HPAR concept receiver. This is because the fluid domain is much larger and more complex than for the internal heat transfer to the PA stream and convection is generally more complex to model than radiation as it depends on microscopic flow phenomena. Due to the size of the flow domain, CFD codes were ruled out as a way of modeling the whole fluid domain in the cavity (or even a

periodic sub-domain). Semi-empirical correlations for the heat transfer between tube bundles and a fluid flowing through them, on the other hand, have been developed and scrutinized for many decades due to their technical relevance, for example in heat exchangers. These, however, commonly do not factor in local heat transfer (inhomogeneous in the circumferential and axial dimension) from tubes of greatly varying temperatures, large distances between tubes (as needed to increase flux penetration) and non-periodic tube arrangements. In this section, a simplified model for this complex heat transfer problem is developed based on semi-empirical correlations from Gnielinski (2010*c*).

7.6.1 Convective heat transfer for a single row of tubes

The heat transfer between a row of tubes and the fluid flowing through it can be calculated in a similar manner as the internal heat transfer of a tube in Equation (7.3.1)

$$\dot{Q}_{\mathrm{conv,o,row}} = \overline{h}_{\mathrm{conv,o,row}}\, A_{\mathrm{tube,o}} \Delta T_{\mathrm{LM,o}}. \tag{7.6.1}$$

Therein, $A_{\mathrm{tube,o}}$ represents the outer surface area of a tube,

$$A_{\mathrm{tube,o}} = L_{\mathrm{tube}}\, \pi / 4\, d^2_{\mathrm{tube,o}} \tag{7.6.2}$$

and $\Delta T_{\mathrm{LM,o}}$, the logarithmic mean temperature difference between the tube and the fluid, is calculated from the NPA flow inlet and outlet temperature to the tube row, $T_{\mathrm{NPA,in}}$ and $T_{\mathrm{NPA,out}}$, respectively

$$\Delta T_{\mathrm{LM,o}} = \frac{(T_{\mathrm{tube,o}} - T_{\mathrm{NPA,in}}) - (T_{\mathrm{tube,o}} - T_{\mathrm{NPA,out}})}{\ln\left[(T_{\mathrm{tube,o}} - T_{\mathrm{NPA,in}}) \,/\, (T_{\mathrm{tube,o}} - T_{\mathrm{NPA,out}})\right]}. \tag{7.6.3}$$

Determining the heat transfer coefficient, $\overline{h}_{\mathrm{conv,o,row}}$, is complicated as its value depends on the geometry of the tube bundle and flow conditions. For a single row of tubes, the flow — and therefore the heat transfer coefficient — is assumed to be identical to the case of a single tube (with outer diameter d_{o}) in free flow (see Gnielinski, 2010*c*, Sect. G7.2)

$$\overline{h}_{\mathrm{conv,o,row}} = 2\, \overline{Nu}_{\mathrm{row}}\, k_{\mathrm{NPA}} / \left(\pi\, d_{\mathrm{o}}\right). \tag{7.6.4}$$

This approach is chosen because of the large distance between tubes to allow for penetration of solar radiation. The overall Nusselt number is calculated from its laminar and turbulent contributions

$$\overline{Nu}_{\mathrm{row}} = 0.3 + \sqrt{\overline{Nu}^2_{\mathrm{lam}} + \overline{Nu}^2_{\mathrm{turb}}}\,, \tag{7.6.5}$$

$$\overline{Nu}_{\mathrm{lam}} = 0.664 \sqrt{Re_{\mathrm{NPA}}} \sqrt[3]{Pr_{\mathrm{NPA}}} \quad \text{and} \tag{7.6.6}$$

$$\overline{Nu}_{\mathrm{turb}} = \frac{0.037 Re^{0.8}_{\mathrm{NPA}} Pr_{\mathrm{NPA}}}{1 + 2.443 Re^{-0.1}_{\mathrm{NPA}} \left(Pr^{2/3}_{\mathrm{NPA}} - 1\right)} \tag{7.6.7}$$

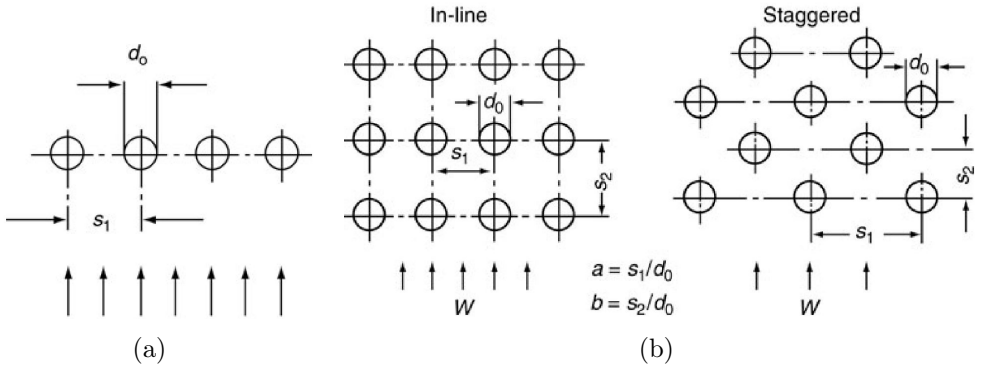

Figure 7.10: Sketches defining pitch ratios a and b for (a) a single-row setup and (b) a tube bundle (Gnielinski, 2010*c*, Sect. G7, Fig. 1 and Fig. 2)

with the Prandtl number of the external flow being calculated as usual, $Pr_{\mathrm{NPA}} = \mu_{\mathrm{NPA}}\, c_{\mathrm{p,NPA}}/k_{\mathrm{NPA}}$, while a correction factor representing the void fraction between the tubes, Ψ, is introduced to the Reynolds number correlation

$$Re_{\mathrm{NPA}} = \frac{\left(\overline{U}_{\mathrm{NPA}}/\Psi\right)\left(\pi/2\, d_{\mathrm{o}}\right)\rho_{\mathrm{NPA}}}{\mu_{\mathrm{NPA}}}. \tag{7.6.8}$$

For a single row of tubes, the void fraction is given through

$$\Psi = 1 - \pi/\left(4a\right) \tag{7.6.9}$$

with the transverse pitch ratio defined as $a = s_1/d_{\mathrm{tube,o}}$ (see Figure 7.10). All fluid parameters are evaluated at the fluid mean temperature between inlet and outlet of the flow $\overline{T}_{\mathrm{NPA}} = \left(T_{\mathrm{NPA,in}} + T_{\mathrm{NPA,out}}\right)/2$ (as described by Gnielinski, 2010*c*, Sect. G7.2).

7.6.2 Convective heat transfer for tube bundle

Based on the heat transfer from a single row of tubes, the average heat transfer from a bundle of tubes to the fluid stream can be calculated. To account for the larger heat transfer coefficient in bundles (due to the increased turbulence) a correction factor, f_{A}, is introduced so that the average Nusselt number over the bundle is

$$\overline{Nu}_{\mathrm{o,bundle}} = f_{\mathrm{A}}\, \overline{Nu}_{\mathrm{row}}. \tag{7.6.10}$$

This arrangement factor, f_{A}, depends on the transverse and longitudinal pitch ratios of the bundle, a and b, respectively, as well as if the arrangement is in-line or staggered (see Figure 7.10, b)

$$f_{\mathrm{A,in\text{-}line}} = 1 + \frac{0.7\left(b/a - 0.3\right)}{\Psi^{1.5}\left(b/a + 0.7\right)^2} \text{ or} \tag{7.6.11}$$

$$f_{\mathrm{A,stag}} = 1 + 2/\left(3b\right). \tag{7.6.12}$$

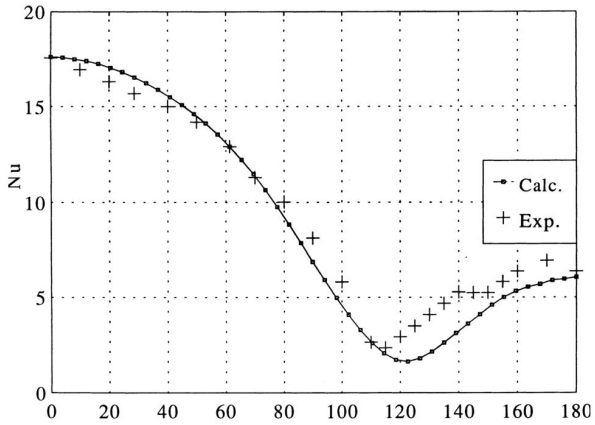

Figure 7.11: Calculated and experimentally derived Nusselt number distribution over circumference (in degree) of tube in cross-flow at $Re = 390$ (Buyruk *et al.*, 1998, Fig. 12)

If the longitudinal pitch ratio, b, is smaller than unity, the void fraction is calculated through

$$\Psi = 1 - \pi / (4ab) \tag{7.6.13}$$

instead of through Equation (7.6.9).

From equations (7.6.11) and (7.6.12) it can be deduced that if the longitudinal pitch, that is the distance between rows of the bundle, becomes large the rows can be treated independently as the heat transfer enhancement through preceding rows is small.

7.6.3 Circumferential changes in heat transfer of flow around a tube

The heat transfer around the circumference of a tube in cross-flow is not constant. The highest value of the local Nusselt number typically occurs at the front of the tube as the boundary layer only starts developing there (see Figure 7.11). The location of the minimum depends on the flow conditions but is commonly not at the back but close to the sides of the tube in flow direction.

The more effective heat transfer in the front of the tube can have a positive effect on the HPAR concept as it can lead to lower temperatures at the most irradiated and exposed surfaces. However, for the developed model a circumferentially homogeneous Nusselt number is assumed as the local flow conditions are unknown. This effect can be implemented at a later stage, likely with a positive effect on the receiver performance.

7.6.4 Developed model

The created model is based on the previously presented correlations, however, Nusselt numbers are calculated for each individual axial section (with the respective tube temperature) instead of for the whole tube bundle. The respective fluid velocity, $\overline{U}_{\mathrm{NPA,row}}$, is calculated from the cross-sectional flow area in each row. As a conservative assumption, the bundles are considered as being in-line because the angular offset between rows is mostly small. After each row, perfect mixing of the outlet air of each section is assumed so that the inlet air to all sections of one row has the identical temperature. This is a optimistic assumption as it does not consider stratification of the flow. However, treating the flow as two- or three-dimensional is not feasible in the present model.

7.6.5 Convection from walls

Convective heat transfer from the top/bottom and back wall sections is expected to be relatively low compared to that from tubes (due to the their higher temperatures). The top/bottom walls are modeled as flat plates in parallel flow according to Çengel and Ghajar (2011, Section 7-2). For laminar flow, which is expected to occur for

$$Re_{\mathrm{NPA,L_{wall}}} = L_{\mathrm{wall}}\,\overline{U}_{\mathrm{NPA}}\,\rho_{\mathrm{NPA}}/\mu_{\mathrm{NPA}} \leq 5 \times 10^5, \tag{7.6.14}$$

the average heat transfer coefficient over the wall length in flow direction, L_{wall}, is calculated through

$$\overline{h}_{\mathrm{NPA},L_{\mathrm{wall}}} = \overline{Nu}_{L_{\mathrm{wall}}}\,k_{\mathrm{NPA}}/L_{\mathrm{wall}} = 0.664 Re^{0.5}_{\mathrm{NPA},L_{\mathrm{wall}}}\,Pr^{1/3}_{\mathrm{NPA}}. \tag{7.6.15}$$

As the geometrical design of the back wall and, therefore, flow conditions along its surface are unknown, no convective heat transfer to or from the NPA stream is modeled at this point in time. This will be reviewed in Section 9.3.

7.7 Merging models

The presented heat transfer models are coupled for each tube and wall section by means of energy balances. The temperature of each tube and wall section, m, is iterated until the respective energy balance equation is satisfied

$$\begin{aligned}&\dot{Q}_{\mathrm{sol,abs},m} + \dot{Q}_{\mathrm{rad,i,in},m} + \dot{Q}_{\mathrm{emit,i},m} + \dot{Q}_{\mathrm{cond},m} \\ &+ \dot{Q}_{\mathrm{conv,PA},m} + \dot{Q}_{\mathrm{conv,NPA},m} + \dot{Q}_{\mathrm{rad,o,in},m} + \dot{Q}_{\mathrm{emit,o},m} = 0.\end{aligned} \tag{7.7.1}$$

Therein, all outgoing heat rates have a negative sign and all incoming ones are positive.

Table 7.2: Dependence of results on axial and circumferential segment size

Parameter	Unit			
axial size	mm	66.7	33.3	66.7
circumferential size	°	22.5	22.5	12.3
$t_{\mathrm{PA,out}}$	°C	762.356	761.957	762.429
η_{t}	%	69.253	69.214	69.271

7.8 Grid independence

For all simulations, the axial and circumferential cell sizes were set to 66.7 mm and 22.5°, respectively. To prove that this resolution is sufficiently fine, simulations for one configuration were additionally conducted with finer meshes in the axial and circumferential dimension, respectively.

The calculated thermal efficiency, η_{t}, and maximum tube temperature, $t_{\mathrm{tube,max}}$, for models with twice the axial and circumferential resolution (segment sizes of 33.3 mm and 12.3°), respectively, are presented in Table 7.2. The changes in these performance indicators are negligible. Note that the resolution of the view factor calculations was not changed.

Chapter 8

Results, variations and findings

The developed receiver model is used in this section to evaluate different configurations. Firstly, a reference case is created and investigated. Based on observations on its performance, different configurations are developed and their performance compared. Finally, recommendations on more fundamental changes to the general design of the HPAR concept receiver are given.

8.1 Reference case

The reference case has the same design as used to generate the plots of Figure 7.4 and Figure 7.9, namely

- 10 rows of tubes with offset angles of $\Delta\phi_{1\ldots9} = [0; 0; 0; 0; 1; 1; 1; 1; 1]^\circ$,
- an angle of $\Delta\phi_{\text{columns}} = 6^\circ$ between tube columns (resulting in 60 tubes per row),
- an identical distance between the rows of $\Delta r = 0.1\,\text{m}$,
- tubes with a length of 2 m, inner and outer diameters of $d_\text{i} = 25\,\text{mm}$ and $d_\text{o} = 30\,\text{mm}$, respectively, and no HTEs,
- the aperture geometry as defined in Section 7.2.3 (45° truncated cone) and
- all rows are flowed through in series.

The input parameters of the simulations and performance of this receiver are described in the following sections.

8.1.1 Input parameters and performance indicators

The most relevant input parameters to reach the defined boundary conditions (800 °C and 534 °C PA and NPA outlet temperature, respectively, as well as a

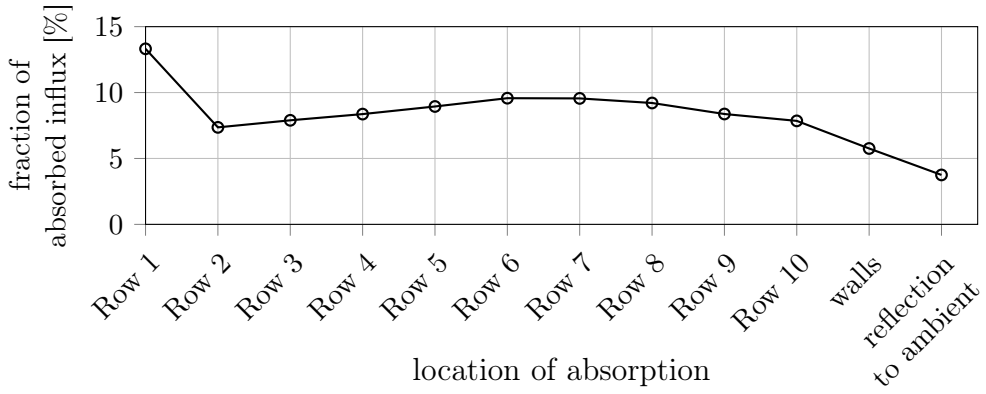

Figure 8.1: Absorption on the tubes and walls as well as reflection losses of the reference receiver design

pressure drop below 100 mbar) for a given receiver geometry are the two mass flow rates and the solar influx on the aperture. The rules to determine these are:

- The solar influx is increased until the maximum tube temperature is reached or until the design PA outlet and the maximum allowable PA pressure drop are reached.
- The PA mass flow rate is adjusted to reach the design outlet temperature or the highest achievable value within the allowable pressure drop range.
- The NPA flow velocity is set so that its outlet temperature reaches the design value.

8.1.2 Performance indicators and observations

The fractions of the incoming solar radiation that is absorbed in each row, by the inner and top/bottom walls and that is reflected out of the receiver are depicted in Figure 8.1 for the defined configuration. Reflection losses are less than 4 % and less than 5.5 % and 0.3 % is absorbed at the inner and top/bottom walls, respectively. The fraction of incoming radiation that is absorbed in the absorber tubes is therefore greater than 90 %. Absorption per row is close to constant except for the front row, which absorbs far more of the incoming radiation than any of the other rows.

As the PA stream flows through all 20 m of tube length, the permissible mass flow rate is low at 0.034 kg/s per column, or 2.1 kg/s for the whole receiver. The development of the fluid's pressure throughout the flow path is shown in Figure 8.2 (top). Due to the low flow velocity, the conductive heat flux into the tube, $\dot{q}_{\mathrm{cond}\rightarrow\mathrm{i}}$, is low and the absorber tubes are not cooled effectively. Especially the first tube experiences a much higher temperature

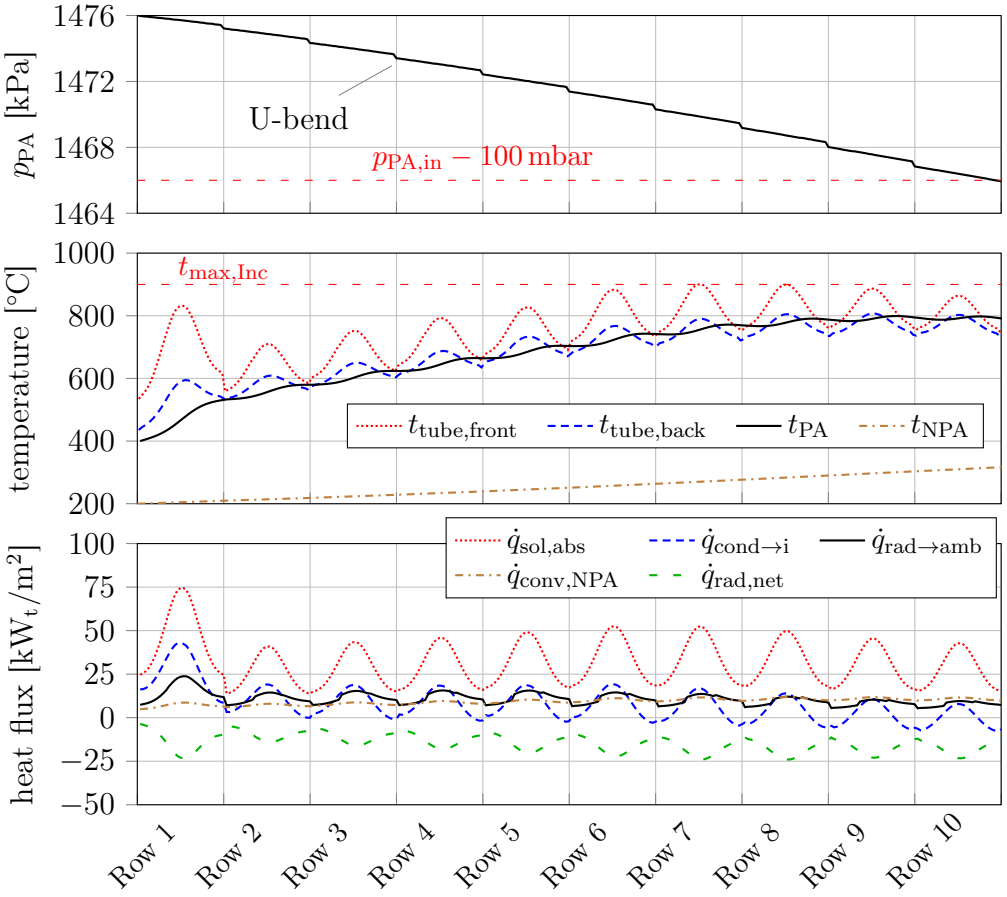

Figure 8.2: Reference case performance: (Top) pressure drop of PA stream, (middle) tube and air temperatures as well as (bottom) circumferential mean heat fluxes at outer wall of tubes over axial flow length of rows

than the contained fluid as well as large circumferential and axial temperature gradients (see Figure 8.2, middle), which also leads to high radiation losses to ambient, $\dot{q}_{rad\to amb}$. This is despite a mean incoming solar flux at the aperture of only $\overline{\dot{q}}_{sol,aper} = 65.7\,kW_t/m^2$, which however results in a *local* absorbed flux of $\dot{q}_{sol,abs} = 217\,kW_t/m^2$ at the front of the axial center of the first tube row (see flux distribution modeling in Section 7.2.4). It is noteworthy, that the volumetric effect (see Section 6.2.1) is achieved as absorbers in the first five rows of the receiver are almost entirely at a lower temperature than the PA outlet stream.

Cooling by convection to the NPA flow is also low, represented by $\dot{q}_{conv,NPA}$ in Figure 8.2 (bottom). The reasons being a low flow inlet velocity, $\overline{U}_{NPA,in} = 0.2\,m/s$, and the poor heat transfer characteristics. In fact, even at this low velocity, the NPA temperature is only increased by approximately 100 K instead of the desired 334 K.

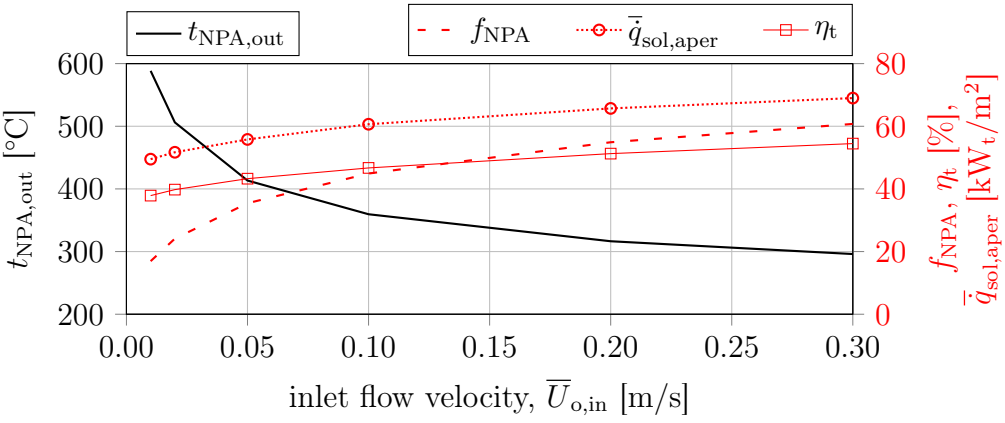

Figure 8.3: Performance under varying NPA flow velocities: NPA outlet temperature, fraction of thermal input to NPA stream, f_{NPA}, receiver influx, $\dot{q}_{\mathrm{sol,in}}$, and receiver thermal efficiency, η_{t}

The effect of NPA flow velocities on the receiver performance is depicted in Figure 8.3. The design NPA outlet temperature can only be reached at inlet flow velocities below 0.02 m/s. However, at these low velocities, the fraction of energy that is transferred to the NPA stream,

$$f_{\mathrm{NPA}} = \dot{Q}_{\mathrm{conv,NPA}} / \dot{Q}_{\mathrm{conv,NPA+PA}}, \tag{8.1.1}$$

is low and the thermal efficiency of the receiver is penalized by the low permitted solar flux. Furthermore, these flow velocities are much lower than typical wind velocities on top of a 50 m-high tower. Wind protection might be necessary to ensure reliable operation of the HPAR system and avoid convective losses.

The design PA outlet temperature is only reached in configurations with $\overline{U}_{\mathrm{NPA,in}} \leq 0.2\,\mathrm{m/s}$. Therefore, the NPA inlet flow velocity is kept at this value in all further designs for comparability. Solutions for increasing the outlet temperature of and heat transfer to the NPA stream are presented in Chapter 9.

For the reference case with $\overline{U}_{\mathrm{NPA,in}} = 0.2\,\mathrm{m/s}$, the fraction of thermal receiver output that is transferred to the NPA stream is $f_{\mathrm{NPA}} = 53.9\,\%$. The thermal efficiency of the PA part of the receiver, that is if the energy input into the NPA stream is considered as a loss, amounts to $\eta_{\mathrm{t}\to\mathrm{PA}} = 54.1\,\%$. These values are compared to other configurations' results in Section 8.3.

In conclusion, the reference design only permits a low solar flux and still results in large temperature gradients, especially in the tubes of the front row. To alleviate this, the effect of different flow paths and implementing HTEs is investigated in Section 8.2. Additionally, the temperature increase in the NPA stream is far from its design value for any relevant flow velocities.

8.2 Internal flow paths and HTEs

One of the limitations of the reference design is the low PA mass flow rate due to the long flow path and the restriction on the maximum pressure drop. An option to shorten the flow path length while maintaining the number of rows (and tube bundle depth) is to split the flow into several parallel streams. The total mass flow rate can therefore be increased without causing a larger pressure drop. Positive side effects are that (a) the heat transfer from the tubes is increased due to higher flow Reynolds numbers and (b) more tube rows are in contact with the coldest inlet air. Both of these effects can lower the tubes' temperatures and therefore the receiver's thermal efficiency. The downside is that the PA has to be heated up on a shorter path length, requiring a larger temperature difference between tubes and air stream.

8.2.1 Two parallel flow paths ("2-path")

The first investigated flow scheme has two parallel paths that include all rows with odd and even numbers, respectively. The rows with the largest view factors to ambient (Row 1 and Row 2) are cooled with the coldest inlet air and, accordingly, the tube temperature in Row 2 is lowered compared to a single path scheme with the same solar influx (see Figure 8.4).

The total PA mass flow rate can be increased to 0.110 kg/s without exceeding the pressure drop limitation, however, at this flow rate the PA outlet temperature drops to 740 °C. The pressure, temperature and heat flux curves are shown in Figure 8.4 for comparison with the Reference design. Due to the increased heat transfer in the tubes, the solar influx can be increased by 34 % and the receiver rating by 77 %. The resulting thermal efficiency of the receiver is 67.5 % (see Table 8.1).

Lowering the PA flow rate to achieve the nominal PA outlet temperature does not show the expected effect. The heat transfer in the tube worsens and the absorber temperature exceeds the allowable range. Therefore, the flux also has to be lowered and the nominal outlet temperature can not be reached with the 2-path setup. This can only be resolved if the heat transfer to the fluid is improved so that the temperature difference between tube and fluid is lowered.

8.2.2 Dimpled tubes

A possibility to lower the temperature difference between tube and fluid is the implementation of internal HTEs. In Section 7.3.3, dimpled tubes were found to have advantageous properties as heat transfer enhanced absorbers. The effect of adding dimpled tubes with the geometry presented in that section to the 2-path configuration is investigated here.

Due to the increased friction factor of the dimpled tube compared to the smooth tube, the PA mass flow rate has to be lowered to 0.104 kg/s. Comparing

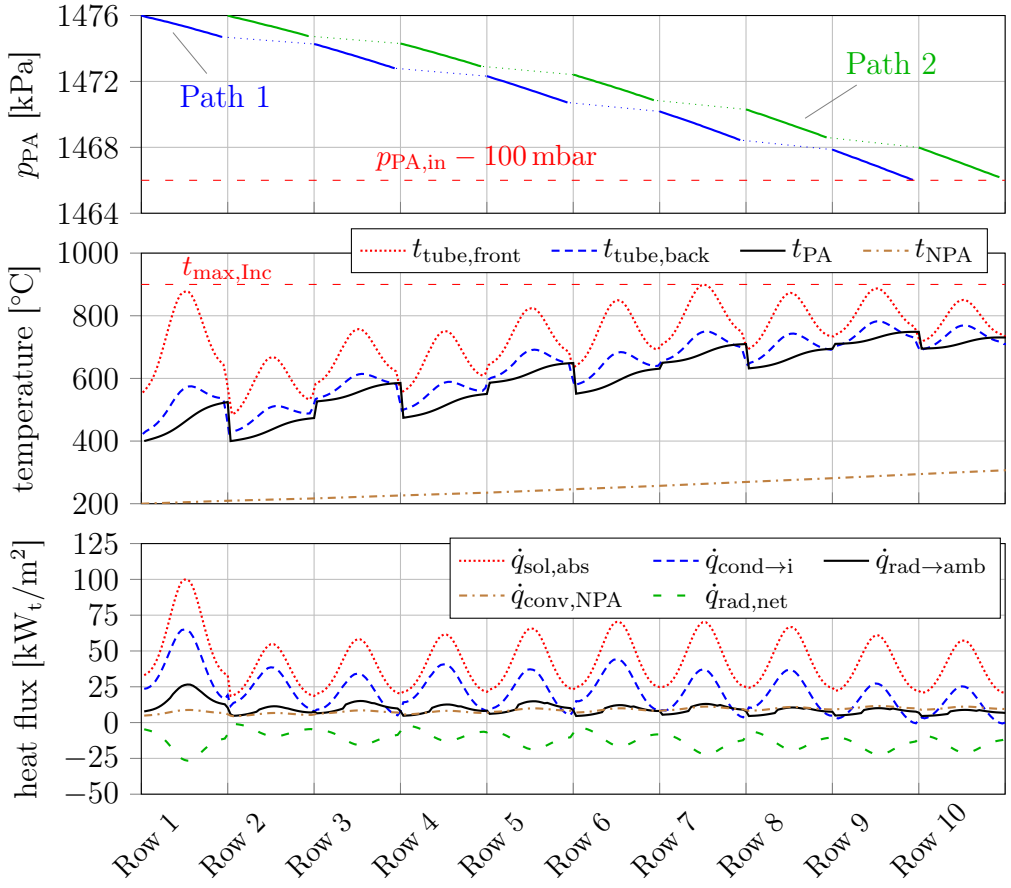

Figure 8.4: 2-path case performance: (Top) pressure drop of PA stream, (middle) tube and air temperatures as well as (bottom) circumferential mean heat fluxes at outer wall of tubes over axial flow length of rows

the temperature and heat flux curves of the dimpled 2-path design in Figure 8.5 with those of the plain 2-path design in Figure 8.4, it stands out that (a) the differences between (minimum and maximum) tube temperatures and flow temperatures are lowered as well as (b) the fraction of incoming solar radiation that can be transferred as thermal energy into the PA stream is increased. The effect on the receiver performance is an increased thermal efficiency (+1.0 %) and rating (+7.1 %) besides the higher PA outlet temperature of 788 °C.

8.2.3 Partial parallel flows (“Triple path”)

The first tube row has particular relevance for the receiver efficiency due to its exposed position which leads to large view factors to ambient (see Figure 7.9). In the configurations simulated so far, the temperature of the first row and thermal radiation losses from it are high. A way of introducing additional

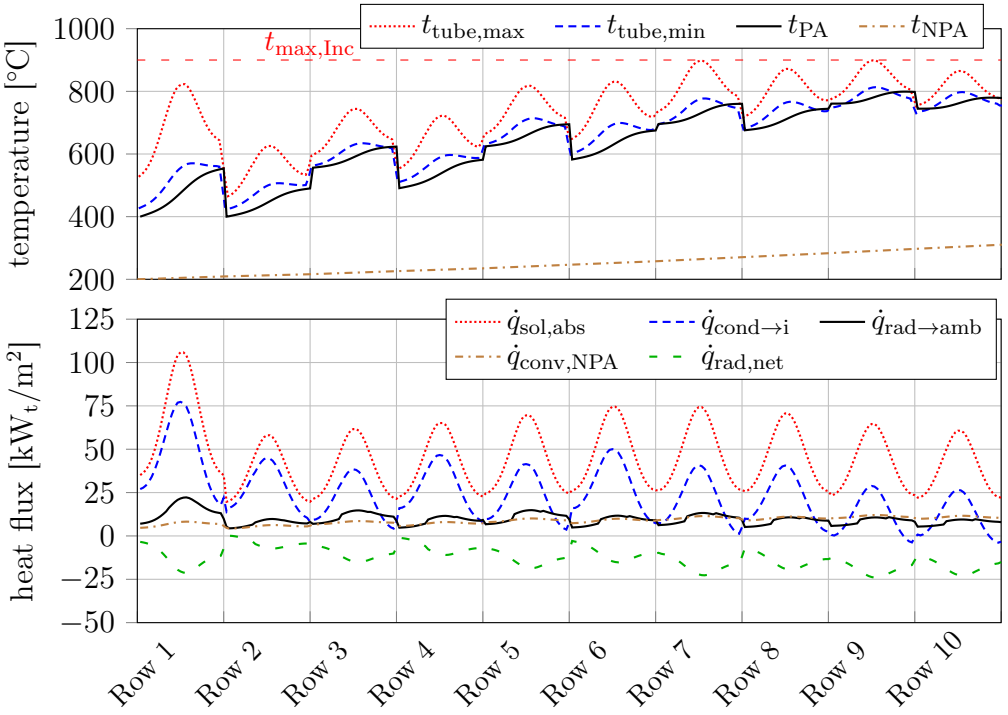

Figure 8.5: 2-path case with dimpled tubes: (Top) tube and air temperatures as well as (bottom) circumferential mean heat fluxes at outer wall of tubes over axial flow length of rows

cooling to this row is to increase the mass flow rate through its tubes. To keep the total pressure drop of the flow paths within the allowable range, the flow in the remaining tubes, however, has to be lowered. This can be achieved by introducing the full inlet flow into the first tube row and splitting it up into several flow paths at its outlet.

For better comparison, a configuration was chosen that permits this concept in a design with 10 tube rows: The full mass flow splits into three equal streams at the outlet of Row 1. Every flow path, therefore, includes 4 tubes. Path 1, for example, flows through rows 1, 2, 5 and 8, Path 2 through rows 1, 3, 6 and 9, etc. While the pressure drop in the first row is large due to the high flow velocity, the total pressure drop of the flow paths allows for a slightly increased total column mass flow rate of 0.114 kg/s (see Figure 8.6, top). The pressure drop of splitting the flow into three branches has not been calculated separately and is, at this stage, assumed equal to that of the modeled U-bend.

The temperature profile in Figure 8.6 (middle) shows the advantage of the high PA mass flow rate in the first tube row: The maximum material temperature as well as the temperature gradients in the axial and circumferential dimension are considerably lowered compared to any of the previous configurations. Thermal radiation losses to ambient from this tube are even

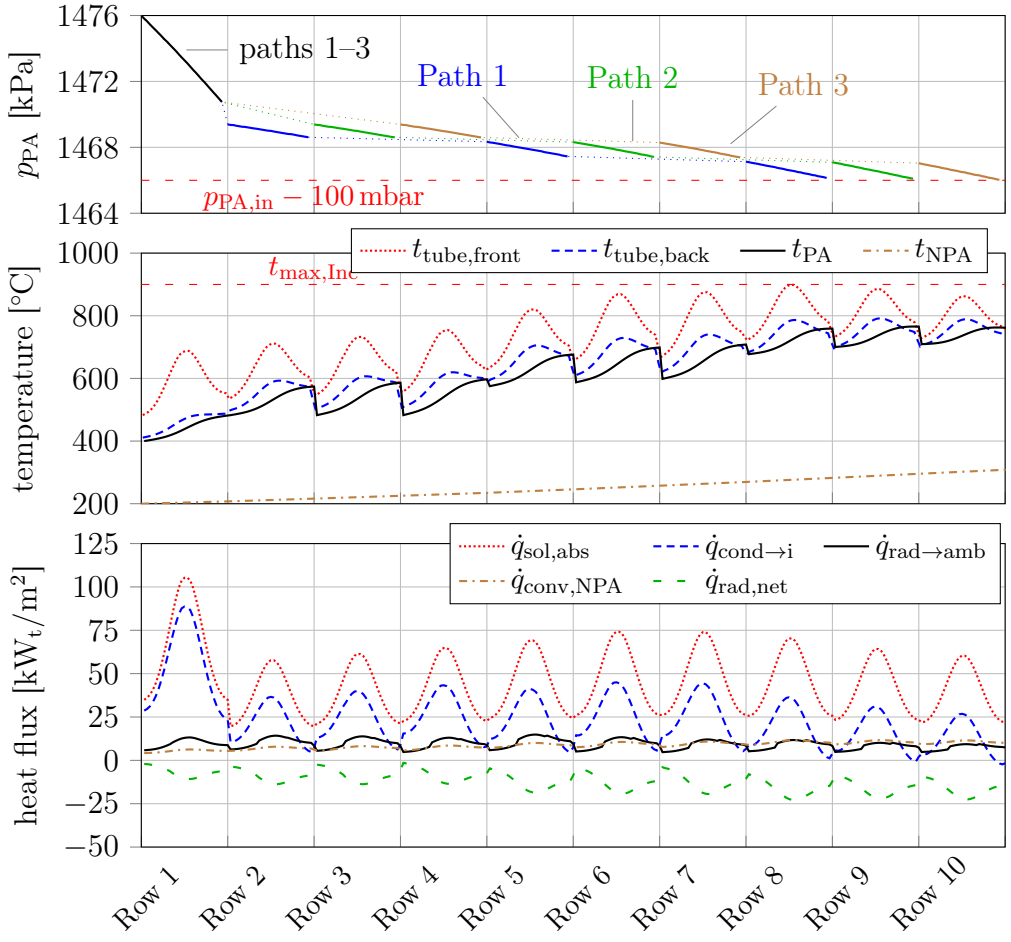

Figure 8.6: Triple path case with dimpled tubes: (Top) pressure drop of PA stream, (middle) tube and air temperatures as well as (bottom) circumferential mean heat fluxes at outer wall of tubes over axial flow length of rows

lower than from Row 2 (see Figure 8.6, bottom), which has an approximately 25 % lower view factor to ambient. This is caused by the effective removal of thermal energy into the PA stream in Row 1. In some of the following rows, however, the difference between absorbed radiation and conductive heat flux into the tube (and therefore the PA stream) is higher than in the dimpled 2-path case.

8.3 Conclusions on basic HPAR concept

The most important performance indicators of the presented configurations are listed in Table 8.1. The calculated thermal efficiency of all configurations with multiple flow paths are of a similar magnitude, almost 40 % greater than

Table 8.1: Performance indicators of configurations with different flow paths (†: dimpled tubes)

Parameter	Unit	Configurations			
		Reference	2-path	2-path†	Triple path†
$\dot{m}_{\mathrm{PA}}$	kg/s	0.0340	0.110	0.104	0.114
$\overline{U}_{\mathrm{NPA,in}}$	m/s	0.200	0.200	0.200	0.200
Δp_{PA}	mbar	100	99.5	100	100
$t_{\mathrm{PA,out}}$	°C	791	740	788	762
$t_{\mathrm{NPA,out}}$	°C	316	307	310	308
$t_{\mathrm{tube,max}}$	°C	901	899	899	899
$\overline{\dot{q}}_{\mathrm{sol,aper}}$	$\mathrm{kW_t/m^2}$	65.7	88.1	93.4	92.9
$\dot{Q}_{\mathrm{t,HPAR}}$	$\mathrm{MW_t}$	1.97	3.47	3.72	3.76
f_{NPA}	%	54.9	28.5	27.5	26.7
$\eta_{\mathrm{t\rightarrow PA}}$	%	23.1	48.3	49.5	50.7
η_{t}	%	51.3	67.5	68.2	69.3
$\eta_{\mathrm{opt+t}}$	%	49.3	65.0	65.6	66.6

that of the reference case. As the geometrical design of all configurations is identical, the optical efficiency is as well. The differences in combined optical and thermal efficiency, $\eta_{\mathrm{opt+t}}$, are therefore solely caused by the differences in thermal efficiency.

Heat transfer enhancement through dimpled tubes brings a further improvement in outlet temperature, thermal efficiency and receiver rating. The Triple path setup renders a lower outlet temperature than the 2-path setup, however, thermal efficiency and rating are marginally higher. Temperature gradients and the maximum tube temperature in Row 1 are considerably lower in the Triple path setup (compare figures 8.5 and 8.6).

Simulations with variations of the basic HPAR concept showed that heating up of the PA stream (close) to the design outlet temperature appears to be possible in a vertical tube bundle design. However, several problems could not be resolved even with adapted flow path layouts and internal heat transfer enhancements:

- Temperature gradients between the front and back of tubes as well as the temperature difference between the tubes and the PA flow are large.
- The maximum allowable material temperature of the tubes is problematic for reaching the design outlet temperature.
- The thermal efficiency (to the PA stream) is too low to be competitive with other tested pressurized air receiver designs.
- The temperature increase in the NPA stream is far below its design value.

The HPAR was, essentially, only simulated as a pressurized air receiver. If the heat transfer to the NPA stream could be increased to achieve its nominal outlet temperature, the issues with high temperatures and temperature gradients in the absorber tubes could additionally be alleviated. In the following chapter, additions to the basic HPAR design to increase the thermal energy input to the NPA stream are proposed.

Chapter 9

Enhanced designs[1]

The heat input to the NPA stream was previously found to be insufficient to implement the developed HPAR receiver into the SUNDISC cycle. In this chapter, three different additions to the concept are proposed as solutions to this shortcoming and their potential is estimated. Detailed thermal modeling, however, is considered out of scope for this project.

9.1 Finned tubes

External HTEs on tubes are commonly implemented in heat exchanger designs. As for internal HTEs, the increase in heat transfer is typically achieved by increasing the involved surface area, maximizing the heat transfer coefficient or both. Finned tubes utilize both and are the most common passive enhancement. In this section, the potential of using circular fins on the outside of the absorber tubes to sufficiently raise the thermal energy input into the NPA stream is investigated. Potential negative effects of the implementation on the system performance are additionally addressed.

9.1.1 Desired external convective heat flux

For evaluating if a HTE is capable of providing the needed enhancement, the desired heat flux is calculated. Based on SUNDISC cycle plant simulations, the fraction of thermal energy to be transferred to the PA stream in the HPAR was previously calculated to be below 38 % (see Section 7.1). While this value depends on numerous assumptions in the modeling, it is used as a benchmark for the desired ratio of heat transfer to the respective streams. Taking into account the differences in inner and outer tube surface areas, the desired mean heat flux of all tube sections to the NPA stream (relative to the outer surface

[1] parts of this section have been submitted for publication (see Heller and Hoffmann, 2016)

area of a plain tube), $\overline{\dot{q}}_{\mathrm{conv,NPA}}$, can be calculated

$$\begin{aligned}
\frac{\dot{Q}_{\mathrm{conv,NPA}}}{\dot{Q}_{\mathrm{conv,PA}}} &= \frac{1-0.38}{0.38} \\
\therefore \dot{Q}_{\mathrm{conv,NPA}} &= \frac{1-0.38}{0.38}\,\dot{Q}_{\mathrm{conv,PA}} = \frac{0.62}{0.38}\,(1-f_{\mathrm{NPA}})\,\dot{Q}_{\mathrm{t,HPAR}} \qquad (9.1.1)\\
&= 1.63 \times 0.733 \times 3.76\,\mathrm{MW_t} = 4.50\,\mathrm{MW_t}
\end{aligned}$$

$$\begin{aligned}
\overline{\dot{q}}_{\mathrm{conv,NPA}} &= \frac{\dot{Q}_{\mathrm{conv,NPA}}}{n_{\mathrm{rows}}\,n_{\mathrm{column}}\,L_{\mathrm{tube}}\,d_{\mathrm{o}}\,\pi} \qquad (9.1.2)\\
&= \frac{4.50\,\mathrm{MW_t}}{10 \times 60 \times 2\,\mathrm{m} \times 30\,\mathrm{mm} \times \pi} = 39.8\,\mathrm{kW_t/m^2}
\end{aligned}$$

The values for the combined thermal rating of the receiver, $\dot{Q}_{\mathrm{t,HPAR}}$, and the fraction of thermal input to the NPA stream, f_{NPA}, are taken from the results for the Triple path setup in Table 8.1.

9.1.2 Potential heat flux and outlet temperature of finned tube bundle

A simple model for heat transfer in finned tube bundles, developed based on correlations given by Schmidt (2010), is presented in Appendix E. In this section, a parametric study is conducted with that model to determine the achievable outlet temperature of and heat flux to the NPA stream flowing through such a bundle. The flux is given relative to the original tube outer surface area, $\dot{q}_{\mathrm{conv,NPA,finned}} = \dot{Q}_{\mathrm{conv,NPA,finned}}/A_{\mathrm{tube,o}}$.

Geometry and temperature assumptions

The spacing between fins and their thickness are set to $s = 5\,\mathrm{mm}$ and $\delta = 1\,\mathrm{mm}$, respectively, while their height is varied in the range $1\,\mathrm{mm} \leq h_{\mathrm{f}} \leq 30\,\mathrm{mm}$ (for the definition of these geometrical parameters, see Appendix E). The NPA inflow temperature and pressure are set to 200 °C and 101.3 kPa, respectively. Simulations are conducted for flow velocities in the range $0.01\,\mathrm{m/s} \leq \overline{U}_{\mathrm{NPA,in}} \leq 1\,\mathrm{m/s}$. Similar to the results of the Triple path case shown in Figure 8.6, the temperature of the tubes is assumed to linearly increase from 600 °C in the first row (200 K above PA inlet temperature) to the maximum allowable material temperature of 900 °C in the last row (with a constant temperature for each tube).

Results

From the results shown in Figure 9.1 (top), it can be deduced that both aims, increasing the bundle outlet temperature to 534 °C and the convective heat flux

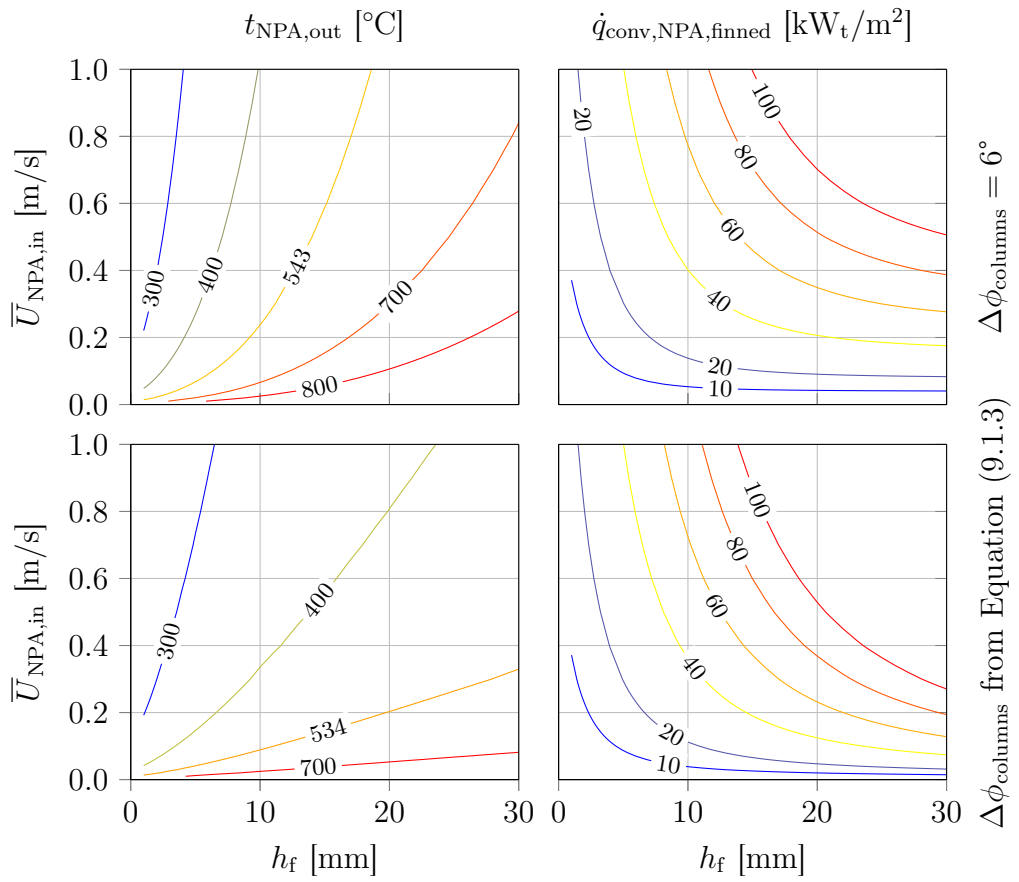

Figure 9.1: Contour plots of (left) outlet temperatures of and (right) convective heat flux to NPA stream of finned tube bundles with (top) fixed angular distance between tubes in each row of 6° and (bottom) with adapted angular distances for constant optical porosity, respectively

to the NPA stream above 40 kW$_\mathrm{t}$/m^2, are achieved for certain combinations of fin heights of more than approximately 12 mm and flow inlet velocities above 0.18 m/s.

Adapted porosity

At the combinations of fin spacing and fin height found necessary to increase the NPA stream outlet temperature considerably, the fraction of solar radiation that passes through between the fins of a tube is expected negligible. A ray tracing simulation in Fluent with a fin height of $h_\mathrm{f} = 20$ mm and an unblocked tube length of $s - \delta = 4$ mm resulted in a view factor from the open aperture between the fins to itself of less than 5 %. The used model, however, does not account for higher absorption of solar radiation per row due to the increased effective diameter of the finned tube. If the magnitude of solar penetration into the depth of the receiver is to be maintained, the tubes in a row have to

be spaced farther apart. In a second study, the optical porosity of the rows was kept at the same value as for the plain tubes by increasing the transversal spacing between the tubes of a row

$$\frac{r_{\text{Row 1}}\ \sin(\Delta\phi_{\text{columns}}) - (d_\text{o} + 2\,h_\text{f})}{r_{\text{Row 1}}\ \sin(\Delta\phi_{\text{columns}})} = \frac{4\,\text{m} \times \sin(6^\circ) - 30\,\text{mm}}{4\,\text{m}\ \sin(6^\circ)} = 92.8\,\%. \tag{9.1.3}$$

The resulting NPA outlet temperature for simulations with the adapted geometry, shown in Figure 9.1 (bottom left), is considerably lower than in the previous configurations, while the heat flux from the remaining tubes increases. At NPA inflow velocities above 0.3 m/s, the outlet temperature is calculated to be below the desired value.[2] Both, flux and outlet temperature boundary conditions are only satisfied in one and the same design if it incorporates fin heights above approximately 17 mm.

For these geometries, the angular distance between tubes of a row increases to at least 12.8° according to Equation (9.1.3). The number of tubes in the receiver, which is directly linked to the thermal rating of the PA stream, would therefore decrease by more than 50 %. Additionally, the distance between the tubes in NPA flow direction, Δr, would have to be increased to maintain a similar absorption behavior and, therefore, the receiver aperture area would increase (given that the structure at the center of the receiver is not adjusted). This will in turn lead to higher radiation losses.

Receiver thermal output estimate

The thermal output of a receiver featuring finned tubes is in the following estimated. The configuration features fins of the smallest diameter that satisfies the demand on outlet temperature of and convective heat flux to the NPA stream. The fin height of this setup is $h_\text{f} = 17\,\text{mm}$, which results in an angular distance between tubes in a row of $\Delta\phi_{\text{columns}} = 12.8^\circ$, according to Equation (9.1.3), or 28 tubes per row. At an NPA inlet flow velocity of $\overline{U}_{\text{NPA,in}} = 0.16\,\text{m/s}$, the stream is heated to 539 °C and the convective heat flux reaches $\overline{\dot{q}}_{\text{conv,NPA}} = 40.4\,\text{kW}_\text{t}/\text{m}^2$.

Assuming that the heat transfer on the tubes' inside is unaffected by the fins, the convective heat transfer to the PA stream is only adjusted by the number of columns (that is, tubes per row) from the result of the Triple path setup in Section 8.2.3

$$\dot{Q}_{\text{conv,PA}} = \dot{Q}_{\text{t,HPAR}}\,(1 - f_{\text{NPA}})\,\frac{n_{\text{columns},12.8^\circ}}{n_{\text{columns},6^\circ}} \tag{9.1.4}$$

$$= 3.76\,\text{MW}_\text{t} \times 0.733 \times 28/60 = 1.29\,\text{MW}_\text{t}. \tag{9.1.5}$$

[2] Note that the inlet flow velocity that was chosen in simulations with plain tubes, $\overline{U}_{\text{NPA,in}} = 0.2\,\text{m/s}$, lies within the range of values for which the design NPA outlet temperature can be reached (see Section 8.1.2).

The thermal energy transferred to the NPA stream is

$$\begin{aligned} \dot{Q}_{\text{conv,NPA}} &= \overline{\dot{q}}_{\text{conv,NPA}}\, n_{\text{rows}}\, n_{\text{columns}}\, A_{\text{tube,o}} \\ &= 40.4\,\text{kW}_\text{t}/\text{m}^2 \times 10 \times 28 \times 0.189\,\text{m}^2 = 2.13\,\text{MW}_\text{t}, \end{aligned} \tag{9.1.6}$$

resulting in a total thermal receiver output of

$$\dot{Q}_{\text{t,HPAR,finned}} = \dot{Q}_{\text{conv,PA}} + \dot{Q}_{\text{conv,NPA}} = 3.42\,\text{MW}_\text{t}. \tag{9.1.7}$$

This is approximately 9 % lower than the total thermal output of the Triple path receiver with plain tubes. Configurations with larger NPA velocities (and fin heights) will render higher ratings but lower shares of PA output.

First observations regarding finned design

It could be shown that the implementation of externally finned absorber tubes has the potential to satisfy the boundary conditions in terms of NPA outlet temperature and receiver thermal ratings. Due to the higher absorption of radiation in rows of finned tubes, however, these tubes have to be spaced farther apart, resulting in a lower thermal output of the PA stream. As the tube temperature distribution cannot be calculated through these simple models, the effect on a receiver's thermal efficiency is not known. The previously developed receiver model is therefore adapted to include a simplified fin model and used to simulate the performance of a receiver with finned absorber tubes.

9.1.3 Simplified finned absorber model

The simplified absorber model is developed to enable predictions of the potential of an HPAR concept receiver with finned absorber tubes, not to accurately model the receiver in detail. The latter would require more sophisticated models mainly of the external convective heat transfer on externally irradiated finned tubes, for example through CFD. However, the computational effort of such models is expected to be prohibitively high.

Assumptions and simplificiations

The geometry of the finned tubes is crucially simplified for all radiation calculations to a tube with the effective outer diameter of the fin, that is $d_{\text{o,HTE}} = d_\text{o} + 2\,h_\text{f}$. This applies to the influx distribution, the determination of view factors between surfaces (both through ray tracing) and to the thermal radiation heat transfer. No micro-cavity effect of the fins could therefore be considered for any radiation heat transfer.

For calculating the emitted radiation from the virtual cylinder of diameter $d_{\text{o,HTE}}$, a constant temperature difference between each fin tip and its root is set. Note, that this temperature does not influence the convective heat

transfer from the finned tube. The chosen approach is conservative and should merely be seen as an estimate on the potential of increasing the convective heat transfer to the NPA stream.

Assumptions in the approach include that (a) all convective heat transfer to the NPA stream occurs at the tube and (b) there is no radiative heat transfer between fins and the tube (all radiation is emitted or absorbed at the virtual cylinder's surface). The only heat input to the fin and tube is therefore absorbed radiation at the tip and via conduction through the fin, respectively. The heat flux from the outer tube surface into the material is estimated at the mean value from the Triple path setup in Section 8.2.3

$$\bar{\dot{q}}_{\mathrm{cond}\to\mathrm{i}} = 22.9\,\mathrm{kW_t/m^2} \tag{9.1.8}$$

and convection is set to the desired value found in Section 9.1.1

$$\bar{\dot{q}}_{\mathrm{conv,NPA}} = 39.8\,\mathrm{kW_t/m^2}. \tag{9.1.9}$$

The heat rate from one fin to the tube is then

$$\begin{aligned} \dot{Q}_{\mathrm{cond,fin}\to\mathrm{tube}} &= \left(\bar{\dot{q}}_{\mathrm{conv,NPA}} + \bar{\dot{q}}_{\mathrm{cond}\to\mathrm{i}}\right) s\,\pi\,d_{\mathrm{o}} \\ &= 62.7\,\mathrm{kW_t/m^2} \times 5\,\mathrm{mm} \times \pi \times 30\,\mathrm{mm} = 29.5\,\mathrm{W_t}. \end{aligned} \tag{9.1.10}$$

The temperature difference between fin tip and root can be derived from the integrated form of Fourier's law of heat conduction in cylindrical coordinates (see Çengel and Ghajar, 2011, Equation 3-37)

$$\begin{aligned} \Delta T_{\mathrm{fin}} &= \frac{\dot{Q}_{\mathrm{cond,fin}\to\mathrm{tube}}}{2\,\pi\delta_{\mathrm{fin}}\,k_{\mathrm{fin}}} \ln\left(d_{\mathrm{o,HTE}}/d_{\mathrm{o}}\right) \\ &= \frac{29.5\,\mathrm{W_t}}{2 \times \pi \times 1\,\mathrm{mm} \times 25\,(\mathrm{W/m\,K})} \ln\left(70\,\mathrm{mm}/30\,\mathrm{mm}\right) = 159\,\mathrm{K}. \end{aligned} \tag{9.1.11}$$

The thermal conductivity of the fin, k_{fin}, had to be estimated because its temperature is unknown (the chosen value is accurate for Inconel at a temperature of approximately 835 °C). Furthermore, the fin height is set to a value of 20 mm. This is slightly larger than as suggested by the tube bundle model in Section 9.1.2 for reaching the design outlet temperature of the NPA stream (≥ 17 mm). Due to the higher flux to the NPA stream from the larger fins, the flexibility in choosing other geometrical and design flow parameters is increased.

To retain a constant open porosity, the chosen fin height would require an angular distance between rows of approximately 14° according to Equation (9.1.3). For simplicity, the original value is doubled to 12° instead. Similarly, the radial distance between rows and the angles between tubes of a row are also doubled to 0.2 m and $\Delta\phi_{1\ldots9} = [0; 0; 0; 0; 2; 2; 2; 2; 2]^\circ$, respectively. The outer aperture area is kept constant so that the receiver is extended towards the central axis of the tower.

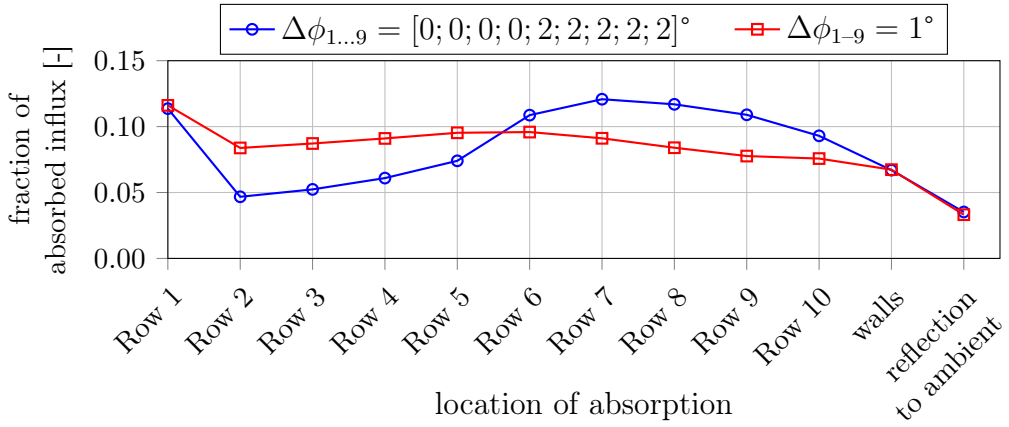

Figure 9.2: Absorption on the tubes and walls as well as reflection losses of the finned receiver design

As this layout results in high absorbed fluxes in rows 6–10 (see Figure 9.2), another configuration was designed for a more homogeneous flux distribution. The results of both are presented in the next section.

The convective heat transfer is calculated according to the model presented in Appendix E. Furthermore, the inflow temperature into each row is constant. This means that perfect mixing between the air in contact with fins and the mostly unheated flow is assumed, which is thought to be optimistic due to the large angular distance between tubes.

Results

The temperature and flux distribution over the tubes' lengths for the first externally finned Triple path design are depicted in Figure 9.3. Compared to the plain tube configurations, the several-fold increase in convective heat transfer to the NPA stream is apparent. At the same time, however, conduction towards the tube's inside — that is, to the PA stream — is much lower. Note that the temperature of the fins was allowed to exceed the nominal maximum temperature of Inconel as they do not have to sustain a pressure difference.

The mean absorbed solar flux in Row 1 and rows 6–9 is considerably higher than in previous configurations despite a lower mean flux on the receiver of $74.2\,\mathrm{kW_t/m^2}$. The reason being that the absorbed solar flux, $\dot{q}_{\mathrm{sol,abs}}$, is calculated relative to the surface area of the original (plain) tube.

As the tube temperature in the first five rows is kept mostly below 600 °C, the radiation losses to ambient are low and the thermal efficiency of the receiver reaches 78.0 % (see Table 9.1). However, due to low temperature increase in the first five rows, neither of the two air streams is heated to its respective design outlet temperature.

In the second configuration, with an angle of $\Delta\phi_i = 1°$ between each row,

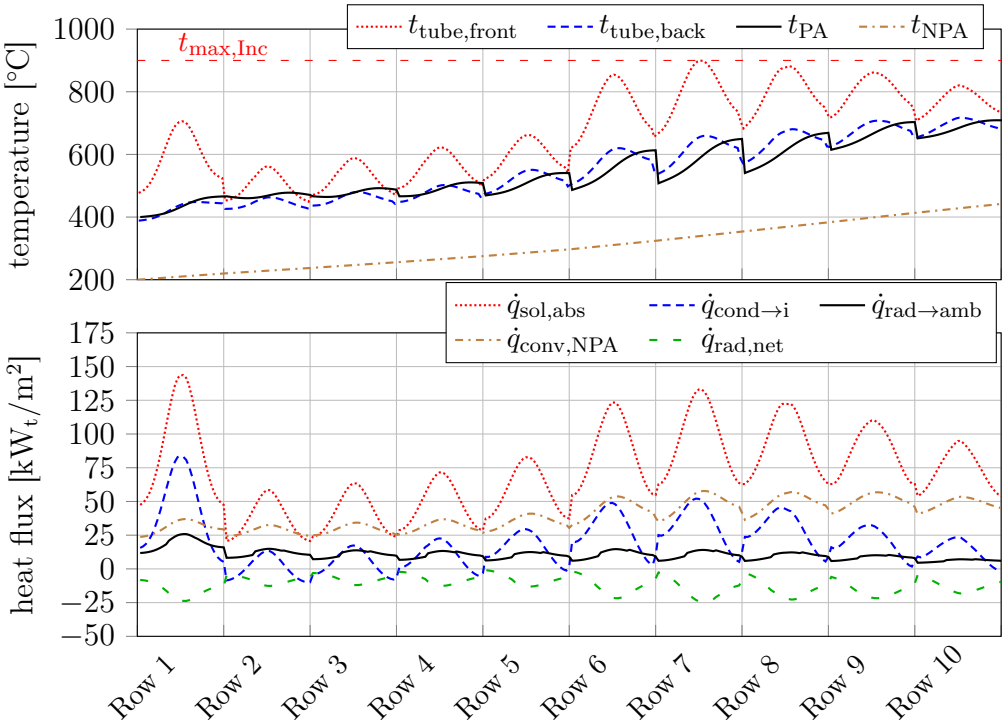

Figure 9.3: Externally finned case with variable $\Delta\phi_\text{i}$: (top) tube and air temperatures as well as (bottom) circumferential mean heat fluxes at outer wall of tubes over axial flow length of rows

Table 9.1: Performance indicators of finned configurations

Parameter	Unit	Configurations		
		Triple path	variable $\Delta\phi_\text{i}$	$\Delta\phi_\text{i} = 1°$
$\dot{m}_\text{PA}$	kg/s	0.114	0.114	0.114
$\overline{U}_\text{NPA,in}$	m/s	0.200	0.200	0.200
Δp_PA	mbar	100.4	96.6	99.8
$t_\text{PA,out}$	°C	762	694	738
$t_\text{NPA,out}$	°C	308	442	479
$t_\text{tube,max}$	°C	899	900	900
$\overline{\dot{q}}_\text{sol,aper}$	kW$_\text{t}$/m^2	92.9	74.2	90.0
$\dot{Q}_\text{t,HPAR}$	MW$_\text{t}$	3.76	3.38	3.91
f_NPA	%	26.7	67.2	67.3
$\eta_{\text{t}\to\text{PA}}$	%	50.7	25.6	24.3
η_t	%	69.3	78.0	74.2
$\eta_\text{opt+t}$	%	66.6	75.1	71.6

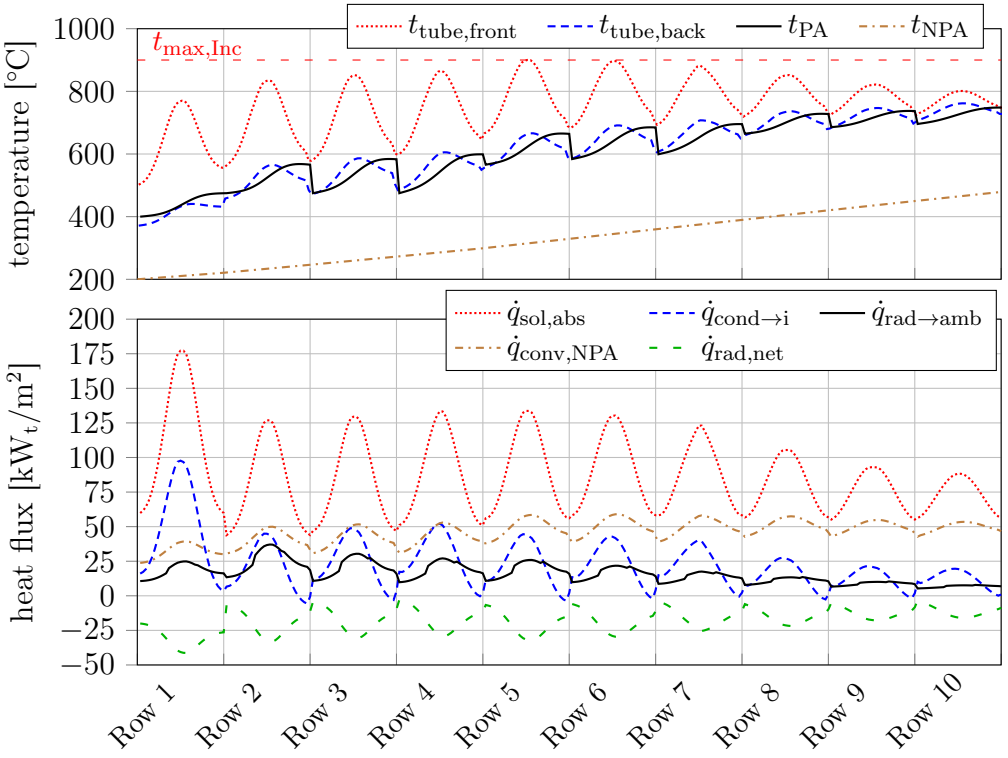

Figure 9.4: Externally finned case with $\Delta\phi_{\text{i}} = 1°$: (Top) tube and air temperatures as well as (bottom) circumferential mean heat fluxes at outer wall of tubes over axial flow length of rows

the outlet temperature of the PA and NPA stream is increased by almost 40 K, respectively, compared to the former design. This is, however, achieved by greatly increased tube temperatures in the outermost tube rows, which results in higher radiation losses to ambient (see Figure 9.4). Radiation emission from all tubes is higher than in any configuration simulated so far. The thermal efficiency is as a result lower than in the previous design (see Table 9.1).

Both modeled configurations do not reach the design outlet temperature of the PA and NPA stream. However, this could be achieved by optimizing the geometry of the receiver and fins. The total thermal receiver rating can be increased due to the improved heat transfer to the NPA stream. The rating of the PA part of the receiver drops significantly due to the reduced number of absorber tubes.

9.1.4 Conclusions on the potential of finned tubes in the HPAR concept

The implementation of externally finned tubes as the absorbers of an HPAR concept receiver was shown to significantly improve the heat transfer to the

NPA stream. In simplified heat transfer simulations, NPA outlet temperatures close to the design value were achieved and the thermal efficiency of the receiver could be raised to 78.0 %, however, at the cost of a lowered rating of the PA subsystem and at a lower PA outlet temperature than previously achieved.

The temperature distribution inside the fins is not physically modeled. The fins are instead assumed to have a constant temperature difference to the respective tube of 159 K, which is though to be very conservative. Including a heat transfer model for the fins is expected to render (a) lowered total emissions of thermal radiation and (b) higher heat transfer to the NPA stream. Reflections of solar and thermal radiation is expected to be lower for a geometrical modeling of the fins instead of the current massive tube model as micro-cavity effects occur.

Perfect mixing of the NPA flow after each tube row is a further assumption in the model that needs to be scrutinized. As the bundle has a large open porosity as well as a low flow speed and some tubes are directly in the wake of rows upstream the NPA flow, inhomogeneous heating of the flow is expected. The heat transfer on these rows' surface would be lower due to the lower temperature difference between flow and tube, which also leads to a lower NPA outlet temperature. These effects will have to be investigated in dedicated flow simulations of the individual configurations.

Finally, neither thermo-mechanical limits nor manufacturability of the fins were considered. While the fins could possibly sustain higher temperatures than the tubes due to the lack of pressure differences, the large temperature differences will incur thermal stresses. Furthermore, problems due to fouling could occur depending on system design.

9.2 Quartz glass elements

Even the highest investigated NPA inlet flow velocities are considerably lower than typical wind velocities on top of a 50 m-high tower. Quartz glass panes have previously been proposed to minimize convective losses of pressurized air receivers, for example in the SOLHYCO project (see Section 6.3.2). Here, the influence of such elements on the absorption of solar radiation, thermal radiation losses and convective heat transfer to the NPA stream is estimated.

9.2.1 Geometry

Depending on the geometry of the quartz elements, they can have several effects: (a) Reduction of convection losses due to wind, (b) reduction of thermal losses through reflection and absorption of exiting thermal radiation (greenhouse effect) and (c) adjustment of flow direction and velocity to enhance the convective heat transfer to the NPA stream. The design of the elements' shape and their positioning includes several variables for which to optimize is not in scope of

this project. Instead, the effect of the most basic configuration, a window with the geometry of a truncated cone in front of the receiver aperture, is modeled and possibilities of further implementations are proposed. In accordance with the design tested by Hertel *et al.* (2016), the thickness of the window was set to 9 mm.

9.2.2 Thermal modeling

The main effect of the described quartz window on incoming solar radiation is that additional reflection losses occur and the optical efficiency of the receiver system decreases. The coating developed by Amsbeck *et al.* (2009) for the non-pressurized window of the SOLHYCO receiver has a solar transmittance of 97 %. Amsbeck *et al.* further calculate the window's absorption of incoming solar radiation to be less than 1 %. In this model, the fraction of flux being absorbed on any of the surfaces of the receiver was therefore reduced by 4 %. The additional reflection losses are assumed to be independent of the angle of incoming radiation and refraction of rays is neglected. As the reflection losses from the original non-window design are below 4 %, re-reflection of these from the quartz window into the receiver is also neglected as it only amounts to approximately $4\,\% \times 3\,\% = 0.12\,\%$ of the incoming flux.

In the thermal spectrum of radiation, transmittance of quartz glass is considerably lower than in the optical spectrum. The spectral transmission, τ_λ, and reflectivity, ρ_λ, of a 9 mm thick non-coated quartz glass are depicted in Figure 9.5 alongside the spectrum of emitted radiation wavelengths for a black body at 800 °C. According to Amsbeck *et al.* (2009, Section 4.1.2, Paragraph 3), "[...] the coating does not influence the optical properties of fused silica for wavelengths above 2.5 μm." Based on Figure 9.5, the reflectivity of thermal radiation from the receiver is estimated at $\rho_\lambda = 6\,\%$.

The window is cooled by natural or mixed convection on its outside and forced convection of the NPA stream on its inside. An accelerated flow from nozzles in the top and bottom wall can be used to enhance the cooling of the window and pre-heating of the NPA stream. However, as the flow conditions are unknown, convective heat transfer from the window is not modeled at this stage. The quartz temperature is, therefore, unknown and radiation emission from the window into the receiver is neglected.

A conservative estimate on the potential of the amount of reintroduced thermal energy *if* thermal emissions from the window were considered can be derived as follows: In the case that the convective heat rate on the inside of the window is equal to that on the outside (which is conservative as the flow on the inside can be optimized for more effective heat transfer, see above) and, furthermore, that all of the emitted radiation from the window to its inside is absorbed, half of the energy absorbed in the quartz would be reintroduced to the receiver.

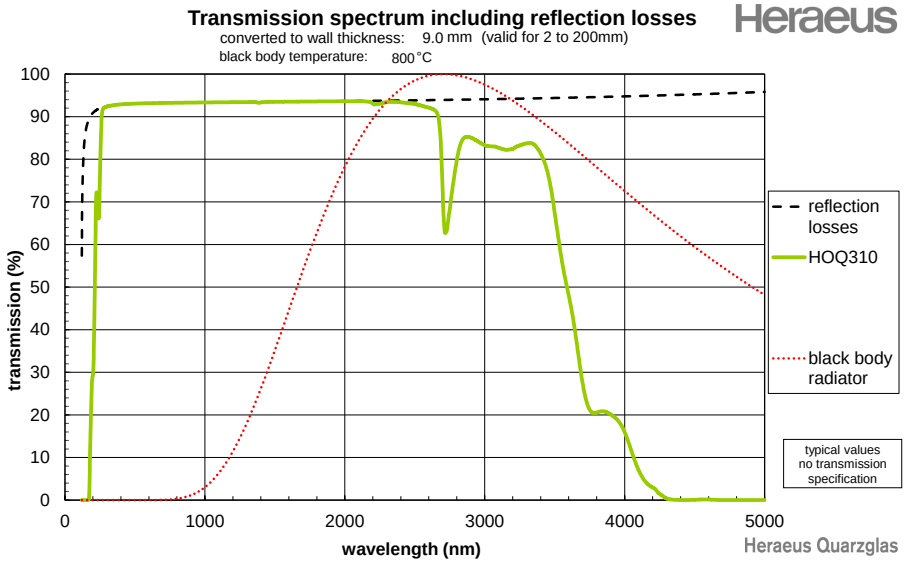

Figure 9.5: Transmissivity and reflectivity of 9 mm-thick HOQ310 "Natural Fused Quartz" as well as black-body emittance profile at 800 °C; generated with the Transmission Calculator v0.81WE by Heraeus Quarzglas (2016)

Absorptivity, α_λ, can be calculated as

$$\alpha_\lambda = 1 - \tau_\lambda - \rho_\lambda. \tag{9.2.1}$$

From Figure 9.5, the absorptivity in the thermal spectrum can then be estimated at 50 %, which means that a quarter of the radiation losses could be recovered. At previously estimated thermal efficiencies in the range of 70 % to 78 %, the relative thermal efficiency increase is between 7 % and 10 %, which exceeds the penalty on the optical efficiency. This is besides the need for wind protection as mentioned previously.

9.2.3 Results

The performance indicators of the Window configuration are presented in Table 9.2. Compared to the previously investigated finned design, the quartz expectedly leads to a slight increase in thermal efficiency of approximately 1 % while the combined thermal and optical efficiency decreases due to the higher reflection losses that require a higher solar influx to achieve the same tube and fluid outlet temperatures. The temperature and heat flux curves are not shown, as they are almost identical to the ones of Figure 9.4.

Table 9.2: Performance indicators of quartz glass-enhanced configurations

Parameter	Unit	Configurations			
		$\Delta\phi_\mathrm{i} = 1°$	Window	$3 \times U_\mathrm{NPA}$	Partial
$\dot{m}_\mathrm{PA}$	kg/s	0.114	0.114	0.114	0.114
$\overline{U}_\mathrm{NPA,in}$	m/s	0.200	0.200	0.200	0.200
Δp_PA	mbar	99.8	99.8	99.2	98.8
$t_\mathrm{PA,out}$	°C	738	739	733	764
$t_\mathrm{NPA,out}$	°C	479	480	589	552
$t_\mathrm{tube,max}$	°C	900	901	900	901
$\overline{\dot{q}}_\mathrm{sol,aper}$	$\mathrm{kW_t/m^2}$	90.0	92.9	111	107.0
$\dot{Q}_\mathrm{t,HPAR}$	$\mathrm{MW_t}$	3.91	3.92	4.98	4.73
f_NPA	%	67.3	67.3	74.7	70.8
$\eta_\mathrm{t\to PA}$	%	24.3	24.6	20.1	23.0
η_t	%	74.2	75.1	79.5	78.7
$\eta_\mathrm{opt+t}$	%	71.6	69.6	73.7	72.9

9.2.4 Quartz elements as flow accelerators

Quartz elements within the tube bundle have the potential to increase the heat transfer to the NPA stream without significantly lowering the penetration of incoming radiation. This can be achieved (a) by accelerating the flow around the absorber tubes through lowering the open porosity and (b) by acting as additional surface areas for heat transfer. The latter, however, requires the absorption of (thermal) radiation which would in turn lower the influx on the backsides of tubes in the front rows. Furthermore, mixing of the air stream after each row of tubes should be improved due to the elements acting as flow barriers in the unheated stream and due to increased turbulence. A sketch of the concept is presented in Figure 9.6.

The accurate prediction of the impact of this enhancement on the receiver performance would require a detailed radiation and convection model for the quartz elements. Here, only the impact on the convective heat transfer from the finned tubes is addressed by increasing the maximum flow velocity in every row of the tube bundle (without changing the mass flow rate).

The results of two configurations with a quartz window and quartz elements

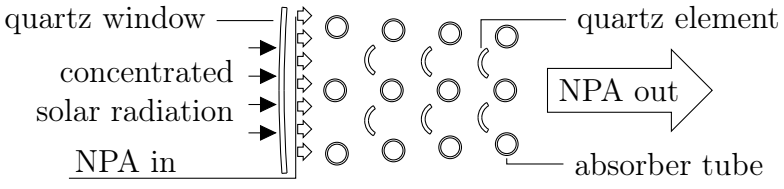

Figure 9.6: Schematic of the concept of quartz elements as flow accelerators

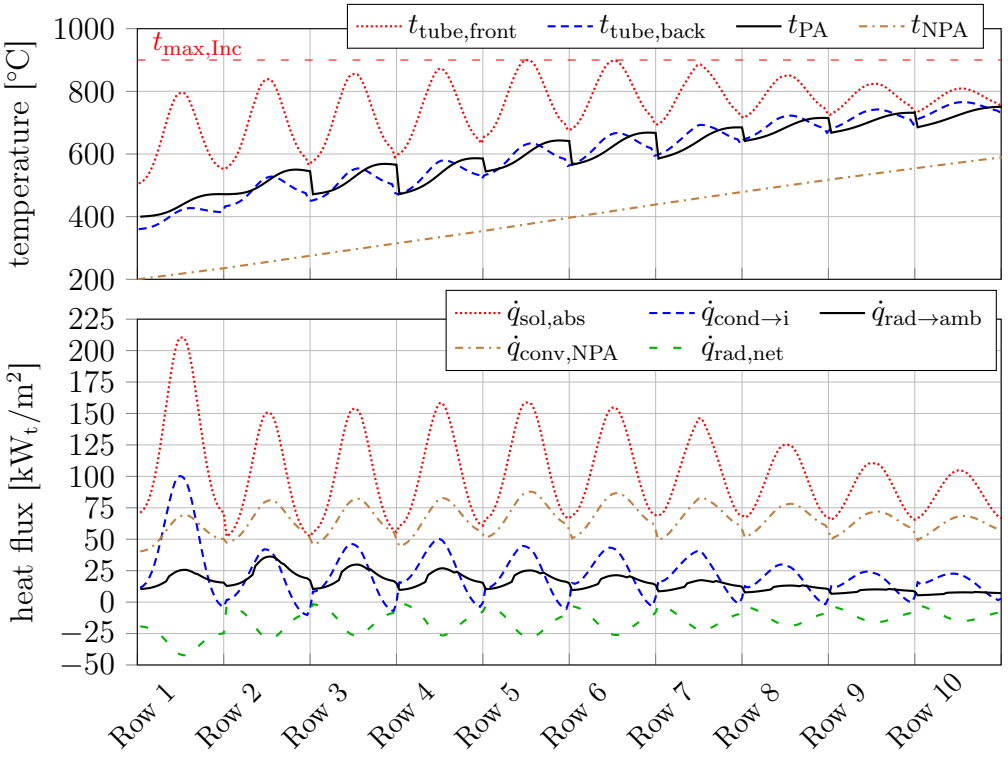

Figure 9.7: Quartz elements: (Top) tube and air temperatures as well as (bottom) circumferential mean heat fluxes at outer wall of tubes over axial flow length of rows

as flow accelerators are presented in Table 9.2. The first design ($3 \times U_{\text{NPA}}$) features the identical geometry as the Window setup, however, assuming flow velocities around the tubes to be thrice as high. Two thirds of the open flow porosity between finned tubes is, therefore, blocked by quartz elements. The changes have a large impact on the NPA stream's outlet temperature, which is increased by 110 K and exceeds the design value. As the heat transfer to the NPA stream is increased, the receiver rating, thermal efficiency and allowable solar influx are also higher than without quartz elements. The PA outlet temperature cannot be increased because the last three rows, which absorb less radiation than the remaining seven, are cooled as effectively as the others (see Figure 9.7) — despite lower temperature differences to the flow — due to the highest NPA flow velocity around them.

To increase the PA outlet temperature, a further configuration (Partial) is modeled in which only the flow around the first seven tubes is accelerated with quartz elements. The temperature and heat flux curves in Figure 9.8 show that the tube temperatures as well as the heating of the PA stream in the last three rows can be increased. However, this is achieved by lowering the heat transfer to the NPA stream. As the view factors to ambient from the depth of the cavity are low, the small penalty in receiver efficiency of this configuration

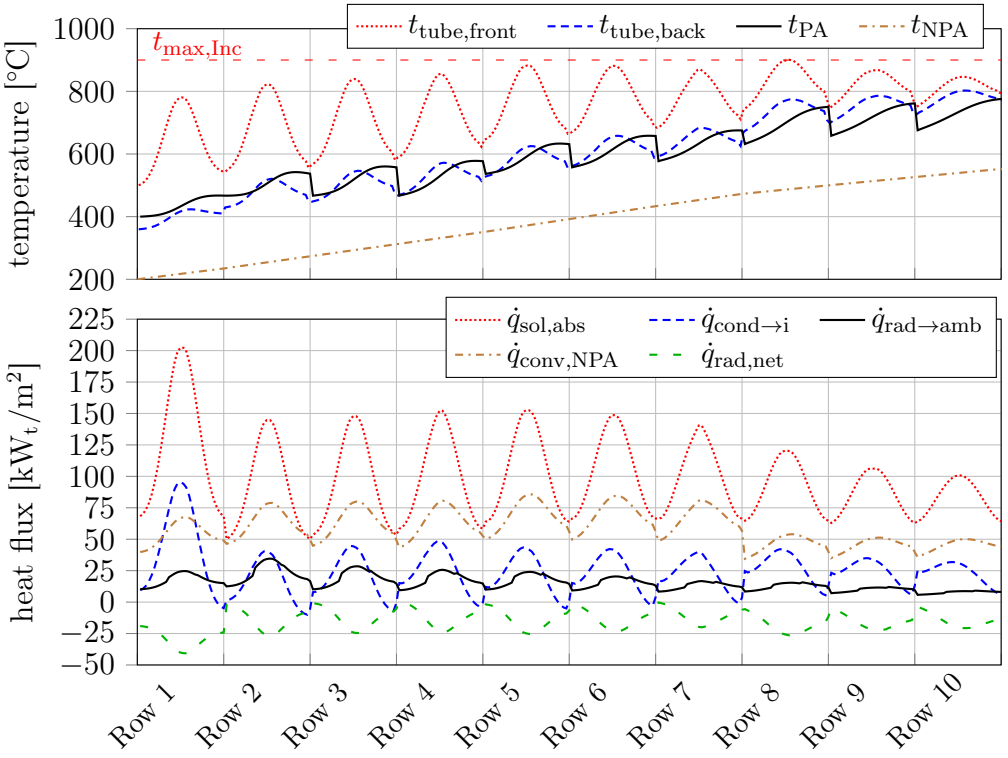

Figure 9.8: Partial quartz elements: (Top) tube and air temperatures as well as (bottom) circumferential mean heat fluxes at outer wall of tubes over axial flow length of rows

(see Table 9.2) is rather caused by the lowered receiver thermal output than by the elevated tube temperature of the last three rows of tubes.

The efficiency and air outlet temperatures of the receiver can be optimized further by adjusting the row geometry as well as the usage of quartz elements and fins. However, for these detailed investigations to be sensible, the previously mentioned improvements to the heat transfer and flow models would have to be implemented.

9.2.5 Part-load performance of receiver with quartz elements

The part-load behavior of the last presented configuration is examined by defining a part-load solar influx fraction, $f_{\text{sol,aper,pl}} = \overline{\dot{q}}_{\text{sol,aper,pl}}/\overline{\dot{q}}_{\text{sol,aper,dp}}$, between 0.3 and 1.1. It was discovered that to keep the PA mass flow rate and outlet temperature constant, the mass flow rate of the NPA stream has to be lowered to a magnitude at which its outlet temperature increases (for $f_{\text{sol,aper,pl}} < 1.0$). Otherwise, too much thermal energy is transferred to the NPA stream and the PA outlet temperature decreases. It is assumed that NPA at the calculated

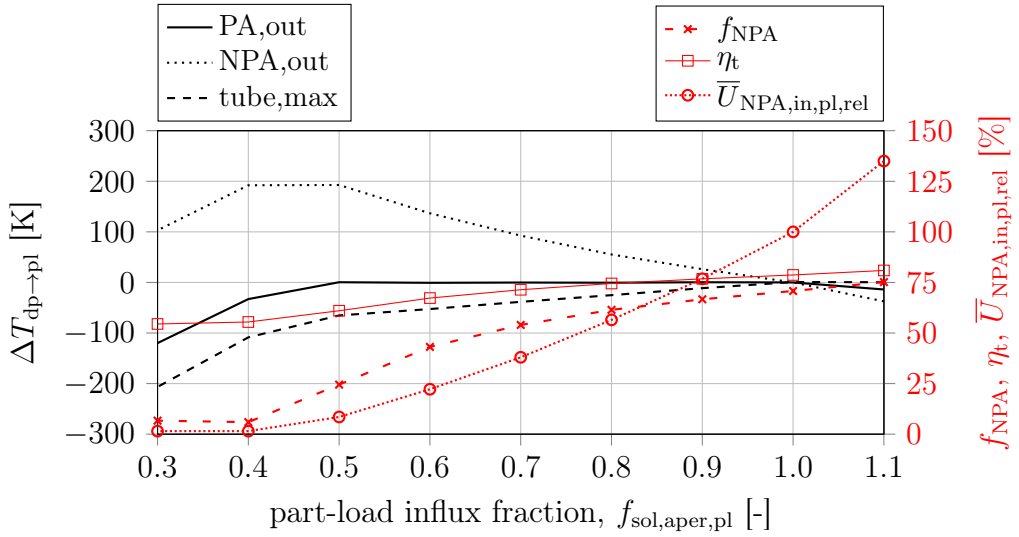

Figure 9.9: Part-load performance of receiver with finned absorber tubes and quartz glass elements; $\Delta T_{dp\to pl}$: temperature difference between design point and part load; $\overline{U}_{NPA,in,pl,rel} = \overline{U}_{NPA,in,pl}/\overline{U}_{NPA,in,dp}$

elevated temperatures can be utilized in the TES or SG, for example by mixing it with ambient air to adjust the charging temperature to the nominal level.

Figure 9.9 depicts the difference in temperature between design point and part load, $\Delta T_{dp\to pl}$, of both streams' outlet and of the maximum value for the tube over the part-load influx fraction. The design-point PA outlet temperature (765 °C as per Table 9.2) can be maintained for $f_{sol,aper,pl} \geq 0.5$. In this range, the maximum tube temperature decreases slightly for lower part-load fractions and the NPA outlet temperature increases strongly.

At $f_{sol,aper,pl} = 0.4$, the part load NPA inlet velocity as a fraction of its design point value, $\overline{U}_{NPA,in,pl,rel} = \overline{U}_{NPA,in,pl}/\overline{U}_{NPA,in,dp}$, reaches almost zero. Less than 6 % of the thermal output is used to heat up this stream and the receiver thermal efficiency drops below 60 %.

For $f_{sol,aper,pl} < 0.5$, the PA stream cannot be heated to its nominal outlet temperature. For these load cases either the turbine runs in part-load, a fuel combustor is used to reach the turbine inlet temperature or the PA stream is closed. In the latter case, the receiver can potentially still be used as a pure NPA receiver or the tubes are solely preheated for times of higher solar influx.

For solar fluxes above the design point value, the NPA flow can be increased to keep the tube temperature below its allowable maximum. Both streams' outlet temperature decreases slightly in this case and the fraction of thermal energy that is transferred to the NPA stream increases.

At lower than design point solar influx, the maximum tube temperature and the temperature gradients along all dimensions of the tube decrease. The temperature profiles at $f_{sol,aper,pl} = 0.5$ are depicted in Figure 9.10. Due to the

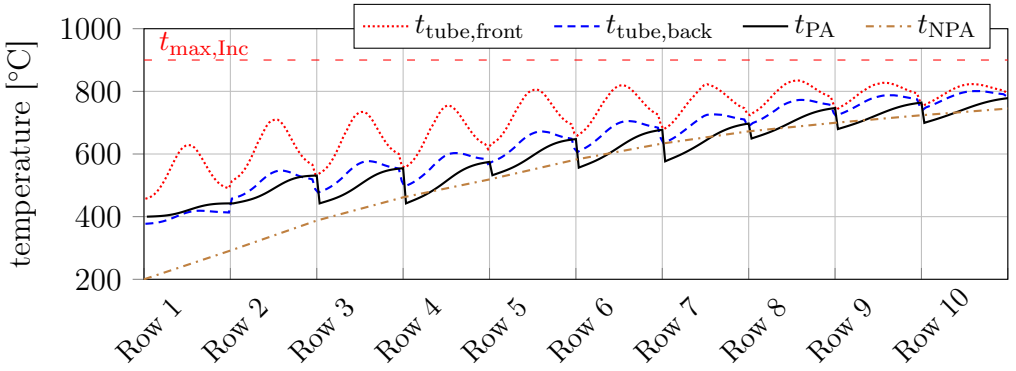

Figure 9.10: Influx part-load of $f_{\text{sol,aper,pl}} = 0.5$: Tube and air temperatures

large temperature gradients at the defined design-point, nominal operation might in practice be at lower influxes (and efficiencies). This will have to be determined based on investigations on stresses in the material.

9.2.6 Conclusions on enhancements to the HPAR through quartz glass

Simulations of HPAR concept configurations with plain and finned absorber tubes have shown that the velocity at which NPA is drawn into the receiver is low compared to that of wind under common conditions. The concept therefore needs to incorporate a mechanism to shield the tube bundle from wind.

A non-pressurized quartz glass window installed in front of the aperture is proposed. While the window introduces additional optical losses in the order of 4 %, the capture of thermal radiation losses is thought to more than compensate for these. As the window absorbs a large share of impinging thermal radiation originating from the receiver, active cooling with return air before it is drawn into the bundle would enable utilizing this thermal energy. The design of the window and the cooling air distribution were not addressed here.

A further application for quartz glass in an HPAR concept receiver is the introduction of quartz elements between the tubes of the bundle to direct the flow towards the hot surfaces, increase its mixing and accelerate it to improve the convective heat transfer. The influence of these inserts on solar radiation penetration and thermal radiation between surfaces was not investigated as this would require to design specific quartz geometries and their locations. The overall effect on efficiency and temperature distribution is, however, expected to be positive as thermal radiation is blocked from exiting the receiver. The effect of increased flow velocities around the tubes — and therefore enhanced convective heat transfer from them — was modeled by tripling their magnitude in the receiver model. As expected, considerably higher outlet temperatures of

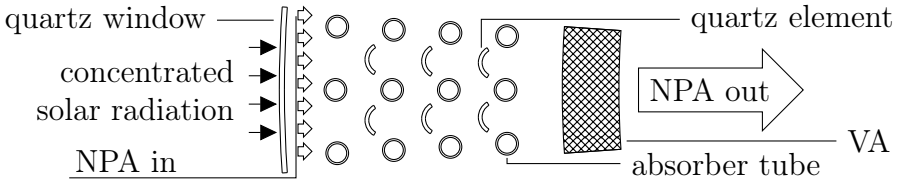

Figure 9.11: Schematic of the receiver concept featuring a volumetric absorber

and heat rates to the NPA stream resulted.

It was shown that the PA stream can be operated at its design outlet temperature and mass flow rate for an incoming solar flux as low as 50 % of its design value. The NPA stream is adjusted to allow for this strategy, however, the stream's outlet temperature increases at part-load. Tube temperatures and temperature gradients are found to be lower at part-load so that lowering the design-point solar influx should be considered to lower thermal stresses in the absorber tubes.

9.3 Volumetric absorber

An alternative to implementing fins on the absorbers to increase the NPA outlet temperature is to only preheat the stream in the tube bundle and use additional dedicated absorber elements to reach the design outlet temperature. These elements are located behind the last tube row so that they (a) have low view factors to ambient and (b) allow for larger open porosities of the tube bundle as radiation that passes it is mostly utilized.

A potential manifestation of this concept is similar to the dual-receiver concept of Buck *et al.* (2006) which was presented in Section 1.2.2. The schematic in Figure 9.11 depict the location of the volumetric absorber in the center of the receiver system, the heating of the ambient air and the absorption of concentrated solar radiation. The major difference between the design by Buck *et al.* and the one that is investigated in this section is the different fluid in the absorber tubes and the associated thermal properties, namely the tube temperatures and sustainable fluxes.

In this section, the developed thermal receiver model is adapted to include the basic modeling of an (open) volumetric absorber instead of the back wall. Performance results of receiver configurations featuring this concept instead of finned tubes are presented.

9.3.1 Thermal model of the volumetric absorber

The thermal model of the volumetric absorber (VA) is based on a bulk optical and thermal efficiency instead of modeling the radiative and convective heat

transfer in detail and determining a mean absorber temperature. Therefore, the model is VA design-independent.

A VA in the center of an HPAR receiver is expected to operate at lower fluxes and temperatures compared to the design specifications of developed open volumetric air receiver technologies (see Section 6.2). The NPA outlet air only needs to be heated to 534 °C while mean air outlet temperature of up to 800 °C were reached, for example, with a HiTRec receiver (see Section 6.2.2). Hoffschmidt *et al.* (2003*b*) measured a combined optical and thermal efficiency of $\eta_{\mathrm{VA,opt+t}} = 81(7)\,\%$ at an air outlet temperature of 550 °C. However, lower cost alternatives to the ceramic HiTRec technology, for example featuring metalic wire mesh absorbers, should be considered.

While low required air outlet temperatures lead to higher thermal efficiencies, elevated air inlet temperatures and low solar fluxes act in the opposite way. The VA inside the HPAR concept receiver will experience low mean solar fluxes because the sustainable mean flux of the tubular absorbers is in the order of only $100\,\mathrm{kW_t/m^2}$. If seen as advantageous and technically feasible, the VA can however be located further towards the central tower axis to take advantage of the geometrical diminution of the cross-sectional area.

At the described temperature and flux levels, the efficiency of the VA is estimated at $\eta_{\mathrm{VA,opt+t}} = 70\,\%$. As this includes all optical losses, the thermal energy that is transferred to the NPA stream is then calculated directly from the sum of all impinging solar or thermal radiation (assuming equal absorptivity for these spectra)

$$\dot{Q}_{\mathrm{VA,conv,NPA}} = \eta_{\mathrm{VA,opt+t}} \left(\dot{Q}_{\mathrm{VA,sol,in}} + \dot{Q}_{\mathrm{VA,rad,in}} \right). \tag{9.3.1}$$

All reflection and emission of radiation from the VA is assumed to be diffuse and combined in one heat rate

$$\dot{Q}_{\mathrm{VA,rad,out}} = (1 - \eta_{\mathrm{VA,opt+t}}) \left(\dot{Q}_{\mathrm{VA,sol,in}} + \dot{Q}_{\mathrm{VA,rad,in}} \right). \tag{9.3.2}$$

9.3.2 Simulations

The first investigated setup is identical in tube bundle geometry to the one used for plain tubes — that is, $\Delta\phi_{1\ldots9} = [0;0;0;0;1;1;1;1;1]^\circ$ and $\Delta\phi_{\mathrm{columns}} = 6^\circ$ — however, a quartz window in front of the aperture and quartz elements in every row of the tube bundle are integrated. The performance indicators of this configuration (VA) are given in Table 9.3 and its temperature and heat flux curves are depicted in Figure 9.12. The parameter f_{VA} represents the fraction of the thermal energy input to the NPA stream that is transferred in the VA.

The receiver with VA does not achieve the desired fluid outlet temperatures without exceeding the allowable tube temperature. The large temperature difference between tube and fluid occurs predominantly in the last five rows of the receiver, which absorb considerably more radiation than rows 2–4. This can

Table 9.3: Performance indicators of configurations with a VA

Parameter	Unit	Configurations		
		Partial	VA	VA-13
$\dot{m}_{\mathrm{PA}}$	kg/s	0.114	0.114	0.105
$\overline{U}_{\mathrm{NPA,in}}$	m/s	0.200	0.200	0.200
Δp_{PA}	mbar	98.8	97.1	99.3
$t_{\mathrm{PA,out}}$	°C	764	715	800
$t_{\mathrm{NPA,out}}$	°C	552	492	534
$t_{\mathrm{tube,max}}$	°C	901	900	888
$\overline{\dot{q}}_{\mathrm{sol,aper}}$	$\mathrm{kW_t/m^2}$	107.0	108	135
$\dot{Q}_{\mathrm{t,HPAR}}$	$\mathrm{MW_t}$	4.73	5.14	5.97
f_{NPA}	%	70.8	53.7	53.0
f_{VA}	%	0	67.7	56.6
$\eta_{\mathrm{t}\rightarrow\mathrm{PA}}$	%	23.0	38.4	36.2
η_{t}	%	78.7	83.0	77.1
$\eta_{\mathrm{opt+t}}$	%	72.9	78.4	73.0

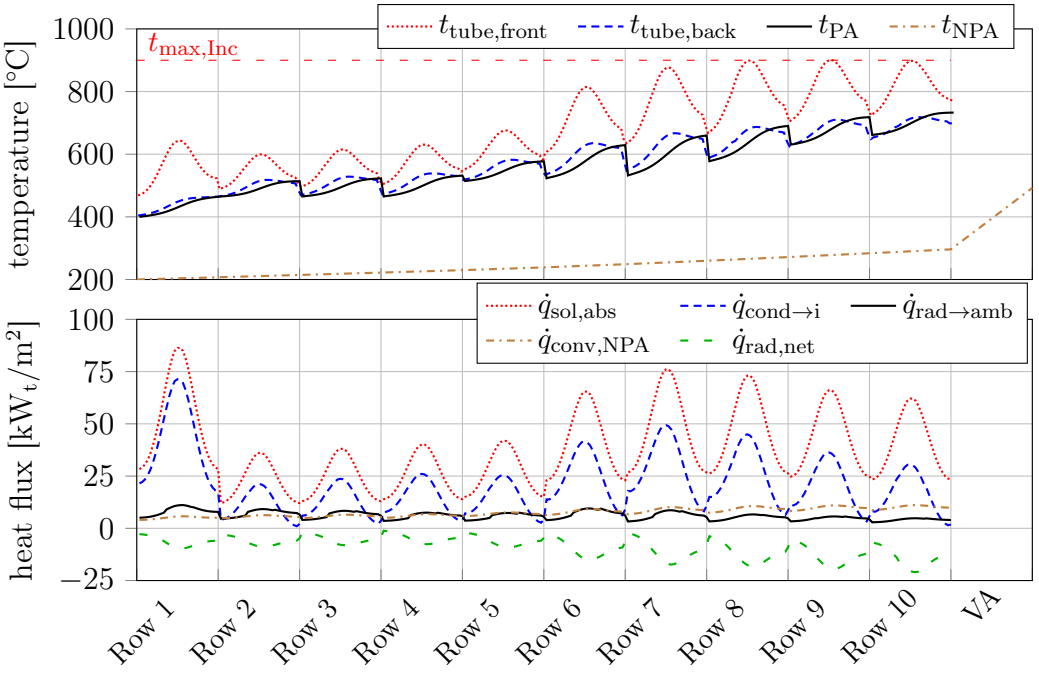

Figure 9.12: Configuration with VA: (Top) tube and air temperatures as well as (bottom) circumferential mean heat fluxes at outer wall of tubes over axial flow length of rows

either be resolved by exposing rows 2–4 to more solar radiation by increasing their angular offset, $\Delta\phi_{1\text{–}4}$, or by exposing the inside rows to less radiation by aligning them behind the previous rows, that is $\Delta\phi_i = 0°$. The former leads to higher radiation losses from rows 2–4 as their temperatures increase. The latter approach lowers the total absorbed radiation in the tube bundle and, therefore, the heat rate to the PA stream.

As an alternative, a tube bundle with a larger number of rows is investigated. The number of rows is set to 13 to allow for a similar flow path scheme as used so far. In the new configuration (VA-13), each path is extended by an additional tube to allow for lower absorbed fluxes and temperature gradients on the tube surfaces. The bundle configuration is in-line, $\Delta\phi_i = 0°$, which is expected to allow for sufficient radiation to reach the VA at the center of the receiver.

The temperatures and their gradients in the tubes are considerably lower than in any of the modeled finned-tube configurations (see Figure 9.13). The tube temperatures in the first seven rows are almost entirely lower than the PA outlet temperature of 800 °C. This is caused by the lower absorbed flux on the outer tube surfaces, while the overall rating of the receiver is high due to the increased number of tubes per row and rows as well as due to the VA, which contributes more than half of the thermal input to the NPA stream. The thermal efficiency of the configuration is calculated to be slightly lower than for the receivers employing finned tubes, however, the combined optical and thermal efficiency is approximately equal. Furthermore, this configuration is the only one that reaches both stream's nominal outlet temperatures.

9.3.3 Part-load performance of receiver with volumetric absorber

The performance of the VA-13 configuration for part-load solar influx fractions between 0.6 and 1.1 is shown in Figure 9.14. It can be seen that both streams' nominal outlet temperature is reached for all simulated load cases (even for $f_{\text{sol,aper,pl}} = 1.1$), while the maximum tube temperature decreases towards lower solar influx.

At $f_{\text{sol,aper,pl}} = 0.6$, the NPA mass flow rate is practically nil. The constant NPA outlet temperature might not be achieved if a more detailed modeling approach for the VA is implemented. The low maximum tube temperatures indicate that either higher outlet temperatures of the streams or a higher mass flow rate of the NPA stream would be possible.

9.3.4 Conclusions on HPAR with volumetric absorber

A volumetric absorber behind the absorber tube bundle, where it has a low view factor to ambient, was proposed to achieve the design NPA outlet temperature.

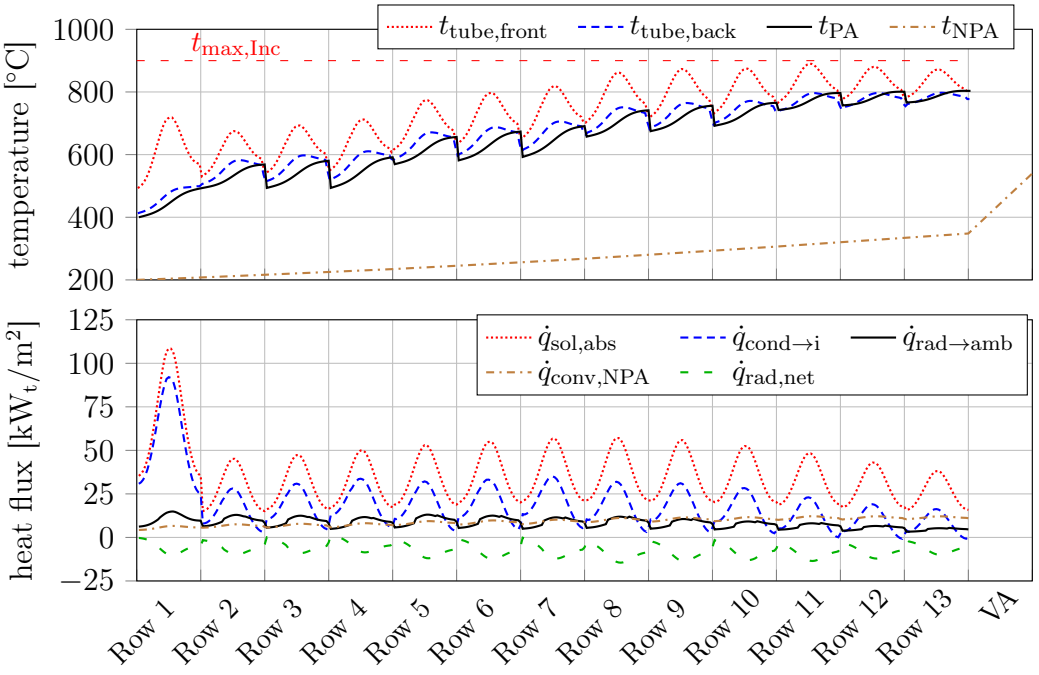

Figure 9.13: Configuration with VA and 13 rows of tubes (VA 13): (Top) tube and air temperatures as well as (bottom) circumferential mean heat fluxes at outer wall of tubes over axial flow length of rows

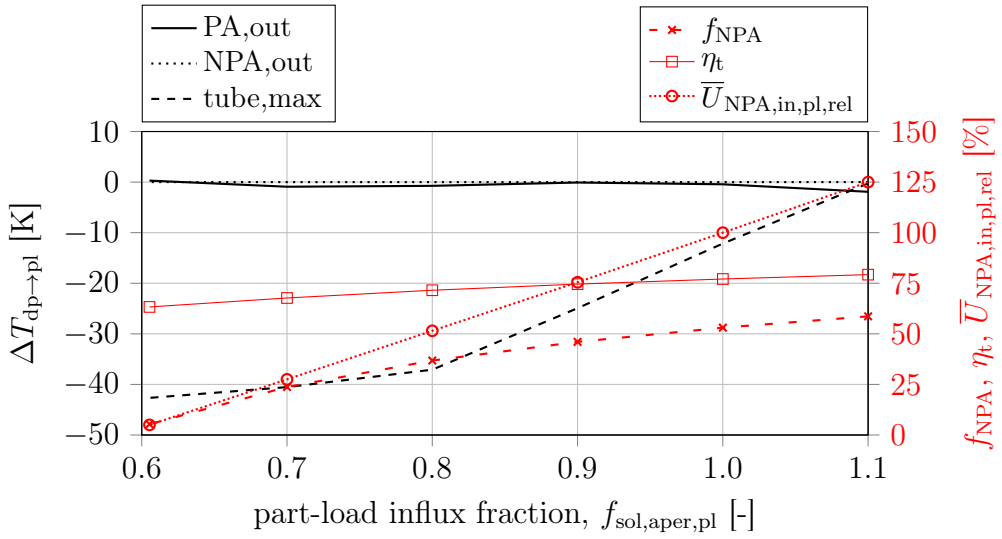

Figure 9.14: Part-load behavior of receiver with VA; $T_{\text{dp}\to\text{pl}}$: temperature difference between design point and part load; $\overline{U}_{\text{NPA,in,pl,rel}} = \overline{U}_{\text{NPA,in,pl}}/\overline{U}_{\text{NPA,in,dp}}$

Due to the large heat transferring surface area in it, the NPA flow velocity can be increased, leading to higher heat fluxes from the absorber tubes.

The VA model that was implemented into the receiver model is based on a constant overall efficiency of the absorber. In spite of being a simple model, it is thought to be sufficient to evaluate the potential of the receiver. For more accurate part-load modeling, a dedicated heat transfer model of the VA would be required.

The enhanced receiver shows a comparatively good performance in terms of achievable outlet and absorber material temperatures, efficiency as well as stable conditions in part-load. However, an additional component is introduced to the system, which leads to increased costs. Due to the low required outlet temperature, it is expected that cost-effective designs and materials can be utilized for the additional absorber.

9.4 Conclusions on enhancements to the HPAR concept

Three enhancements to the basic HPAR concept were presented. They aim at (a) increasing the outlet temperature of the NPA stream, (b) lowering the temperature gradients in the tubes, (c) improving mixing of the NPA stream between rows of the bundle and (d) avoiding excessive convective losses by shielding the receiver from wind. Simulations of enhanced configurations were conducted with simplified heat transfer models to evaluate their potential.

Firstly, externally finned absorber tubes allow for increased convective heat transfer to the NPA stream. This leads to higher allowable fluxes, heating of the NPA stream to design temperature (depending on fin geometry) and higher receiver efficiencies (up to 71.6 % combined optical and thermal efficiency at a PA outlet temperature of 738 °C). However, the greater absorption of incoming radiation per tube row requires larger spacing between tubes in a row and, thus, reduced the thermal energy input to the PA stream. Durability of finned tubes under high temperature gradients needs to be investigated and is expected to be critical.

Secondly, a non-pressurized quartz glass window at the receiver aperture can be implemented in any of the investigated configurations to alleviate wind effects. The combined thermal and optical efficiency of the receivers is expected to benefit from such shield but in order to quantify the effects, more detailed radiation and convection models have to be implemented.

The thermal energy input to the NPA stream can, furthermore, be increased by accelerating the flow velocity through the tube bundle and increasing mixing between rows of tubes. Quartz elements located between the tubes of the bundle show potential for this application. In one such configuration, a combined optical and thermal efficiency of 72.9 % was achieved while even exceeding the

NPA stream's nominal outlet temperature and heating the PA stream to a temperature of 764 °C.

Thirdly, a volumetric absorber behind the absorber tube bundle can be used instead of finned absorber tubes to increase the NPA outlet temperature to its design value. Compared to configurations with finned absorbers, the tubes can be located closer to each other while still achieving sufficient penetration of solar radiation into the depth of the receiver.

One such configuration with 13 rows of absorber tubes was simulated to achieve both streams' nominal outlet temperature at a lower maximum tube temperature and less severe temperature gradients than found in all other designs. The combined optical and thermal efficiency of the receiver was predicted to be 73.2 %. The part-load performance showed a promising behavior with constant outlet temperatures for load fractions between 60 % and 110 %. The validity of the simplified VA model for these operating conditions will have to be verified, though.

The VA introduces an additional component to the receiver assembly, increasing its total cost and complexity. These additional costs will have to be compared to the cost of manufacturing finned tubes of high grade steel.

To sum up, all three investigated enhancements have shown merit to the basic HPAR concept. A quartz glass window is expected to be indispensable for lowering convection losses while its cost and thermal behavior were not modeled. Similarly, quartz glass elements between the tubes of the bundle are expected to greatly improve mixing of the NPA stream and enable directing it onto the highest-temperature surfaces. To calculate the thermal potential of finned absorber tubes, the level of detail of the flow and heat transfer model has to be increased considerably. However, manufacturability and durability of the components are unproven. An additional volumetric absorber, on the other hand — if manufactured in a cost-effective way — seems to simplify operation of a hybrid receiver due to its robust design.

Chapter 10

Conclusions on dual-pressure air receiver system

The SUNDISC cycle requires a pressurized and a non-pressurized air stream to be heated in the receiver system. In other studies, receiver concepts have been proposed and tested for either heating up pressurized or non-pressurized air so that the required system can be a combination of two of these technologies. However, all of the concepts have shortcomings that have so far prohibited their commercial implementation. These are mainly a high cost, low thermal efficiency, negative impact on the plant's optical efficiency or the utilization of fragile materials. The HPAR concept, on the other hand, describes a hybrid receiver capable of (pre-)heating a pressurized and a non-pressurized air stream in one component without necessitating a pressurized window, ceramic absorbers or secondary concentration of solar flux.

A simplified thermal model of a 360° HPAR manifestation was developed to investigate its potential as part of a cascaded hybrid receiver system in the SUNDISC cycle. The desired HPAR outlet temperature of the pressurized and non-pressurized air stream in the chosen setup is 800 °C and 524 °C, respectively. Developed sub-models for all important heat transfer mechanisms include the following: (1) The solar flux distribution on the absorber tubes and the receiver walls from a solar field was modeled via ray tracing. (2) Radiative heat transfer inside the tubes as well as between tubes, receiver walls and ambient is calculated using view factors determined in the Surface to Surface ray tracing model of ANSYS Fluent. (3) Local convective heat transfer inside the tubes is calculated from semi-empirical correlations. (4) Convection to the non-pressurized air stream around the tubes is calculated in a one-dimensional model based on correlations from the VDI Heat Atlas.

Initial studies with these models showed that (a) large solar flux and temperature gradients occur in the tubes' axial and circumferential dimension, (b) the thermal efficiency of the receiver is predicted to be low and (c) the heat transfer to the non-pressurized air stream is far from sufficient to reach its desired outlet temperature for any sensible mass flow rates. Through a

combination of adjusting the flow path of the pressurized air stream through the tube rows and implementing internal heat transfer enhancements (dimpled tubes), the combined optical and thermal efficiency of the receiver could be increased from 49.3 % to 66.6 % and its thermal rating from 1.97 MW_t to 3.76 MW_t. However, the temperature gradients remained high and the insufficient heat transfer to the non-pressurized air stream has to be addressed through fundamental changes in the receiver design.

Externally finned absorber tubes can transfer several-fold higher heat fluxes to the non-pressurized air stream than plain tubes. To estimate the potential of a receiver with finned tubes to reach the defined design parameters, the previously developed model was adjusted to include a one-dimensional model of convective heat transfer from finned tubes to the non-pressurized air stream. For thermal radiation modeling, a mean temperature of the tube-fin assembly is estimated with a conservative approach.

Thermal efficiencies of approximately 74 % were calculated with the model. However, to achieve penetration of concentrated solar radiation into the depth of the receiver, the angular distance between the tubes of each row had to be increased due to the higher absorption in the finned tubes. This leads to lower thermal energy input to the pressurized air stream and potentially lower optical efficiencies. Achieving the design outlet temperatures of both air streams requires tuning of the receiver and fin geometry.

Even configurations with reasonably large fins could only achieve the nominal non-pressurized air flow outlet temperature for mean inflow velocities below 0.3 m/s. To avoid excessive convection losses, a non-pressurized quartz glass window was proposed. The reduction in thermal radiation losses of this window is expected to overcompensate the increased optical losses due to reflections. A dedicated cooling strategy for the window with non-pressurized air before being drawn through the tube bundle can further reduce losses from radiation absorbed in the window.

Additional quartz glass elements in the tube bundle were proposed to increase the flow velocity along the absorber tubes and its mixing (both improving the convective heat transfer). In one configuration with tripled flow velocity along the surfaces of a finned tube bundle, an increase in the receiver's efficiency by 6 %, in the receiver rating by 27 % and in both flows' respective outlet temperature could be achieved. Neither the impact of the elements on radiation heat transfer nor convective heat transfer from them was modeled as this would require the definition of their physical design and location as well as the development of a heat transfer model for the flow around them. The elements are expected to be necessary to achieve mixing of the NPA stream between tube rows. However, as perfect mixing was previously assumed this improvement could not be quantified.

The final investigated enhancement is a volumetric absorber located behind the last row of absorber tubes to reach the nominal outlet temperature of the non-pressurized air stream. In a configuration with 13 rows of plain absorber

tubes and an additional volumetric absorber, the combined solar and thermal efficiency was calculated at approximately the same value as for a receiver with finned tubes. However, the receiver rating could be increased by 28 % and the nominal outlet temperatures were reached. Furthermore, temperatures and temperature gradients in the absorber tubes were considerably lower than for any other design. The thermal model of the volumetric absorber is based on a constant bulk efficiency of 70 %.

Part III

Conclusions

Chapter 11

General conclusions and outlook

A novel CSP cycle, the SUNDISC cycle, is proposed to increase the capacity factor of a combined cycle plant with a solarized gas turbine and packed bed thermal energy storage system. A techno-economical model of this cycle was developed and used for a parametric study to identify sensible plant configurations and quantify their respective performance.

The hourly, steady-state models of the subcomponents are of differing levels of detail with the steam generator, Rankine cycle and receiver models as well as the operating strategy being comparatively basic. Additionally, the available cost data for most components is not up to date and therefore carries large uncertainties.

The simulation results show that compared with a reference combined cycle CSP plant, the SUNDISC cycle plant generates electricity at a 25 % lower levelized cost (0.141 USD/kW_e h) and a more than 75 % higher capacity factor. A plant with larger solar components (solar field, receiver and storage system) and a slightly higher levelized cost of 0.143 USD/kW_e h was simulated to generate electricity at an almost constant rate of 5 MW_e during more than 8200 h per year, which is close to baseload characteristics. A learning-curve scenario predicts a large cost reduction potential of the technology with the levelized cost dropping to less than 0.075 USD by the year 2035.

Given this prospect, the SUNDISC cycle should be developed further and in more detail. The recommended next step is to refine critical subsystems of the existing model. Namely, the steam generator and Rankine cycle should be modeled in detail and include an air-return loop, the receiver systems should consider solar flux distribution and the part-load behavior of all systems should be included. Furthermore, most cost figures are based on old estimates and should be updated. The improved model can then be used to predict the techno-economic performance of such a plant for specific applications and the ones in which it is most cost-competitive.

In Part II of this work, it was investigated if a dual-pressure air receiver system can advantageously be used to preheat the pressurized and heat the non-pressurized air streams of the SUNDSIC cycle in one component of simple

design and at a high efficiency. The considered dual-receiver is a manifestation of the HPAR concept, which describes a metallic tubular receiver in which the absorbers are arranged as a vertical or tilted tube bundle that is cooled by the internal pressurized and the external non-pressurized air streams. The heat transfer mechanisms were modeled via ray tracing (for solar absorption and thermal radiation view factors) as well as using semi-empirical correlations (for internal and external convection). The absorber tubes were discretized in the axial and circumferential dimension while both streams' flow was modeled in one dimension.

Simulations with the combined receiver model showed that the basic HPAR concept cannot heat the two air streams to their respective required outlet temperature without exceeding the material limitations of the absorber tubes. Furthermore, the achieved thermal efficiency of the system is not competitive with existing dedicated pressurized or non-pressurized air receiver technologies and temperature gradients in the tubes were high.

Several evolutions of the system lead to higher thermal efficiencies and receiver ratings but the tube temperature gradients and the non-pressurized air stream's outlet temperature could only be improved with fundamental changes to the receiver design. While these changes (finned tubes, quartz elements and a volumetric absorber) were shown to have potential for enhancing a receiver's performance, more detailed optical, thermal, mechanical and flow modeling is required to confirm these findings.

In conclusion, the HPAR concept does not provide the desired thermal performance in a simple, plain absorber tube design. If a finned absorber design is chosen, questions of manufacturability and mechanical durability have to be addressed in the development process. In case of the additional volumetric absorber, it has to be proven that such a hybrid receiver is cost competitive with a receiver system with two dedicated, decoupled receivers for the two pressure levels.

Appendices

Appendix A

Material properties

In this appendix, the used thermodynamic properties of air, Inconel 601 and Pyromark 2500 are presented. All properties are given in dependency of the absolute temperature, in *kelvin*, of the respective material, T_{air}, T_{Inc} and T_{Pyro}.

A.1 Dry air

Air properties in dependence of temperature for all models are calculated using the equations given in this section. The two ranges of interest are:

1. For the non-pressurized cycle: $p_{\text{air}} = 1\,\text{bar}$ and $0\,°\text{C} < t_{\text{air}} < 550\,°\text{C}$
2. For the gas turbine unit and pressurized air receiver: $1\,\text{bar} < p_{\text{air}} < 20\,\text{bar}$ and $300\,°\text{C} < t_{\text{air}} < 1110\,°\text{C}$

In these ranges, the dynamic viscosity and thermal conductivity are almost independent of pressure, while the specific heat capacity shows some dependency on it mainly for temperatures of less than 300 °C. However, at these low temperatures, the heat capacity only needs to be calculated for air at ambient pressure. A single correlation can therefore be used for each of the respective properties.

The used polynomial fits are created based on data by Wagner *et al.* (2010, Sect. D2.2). As values are only provided up to a maximum temperature of 1000 °C, extrapolation is necessary for the highest temperatures. The trends of the curve fits up to 1110 °C appear sensible (see Figure A.1).

The maximum deviation of all correlations is less than 0.7 % in the given temperature and pressure ranges. This maximum always occurs at the highest pressure and lowest temperature, which is a combination that will not occur in the investigated setup.

Density The air density is calculated from the ideal gas law:

$$\rho_{\text{air}} = \frac{p_{\text{air}}}{R_{\text{air}}\, T_{\text{air}}}. \tag{A.1.1}$$

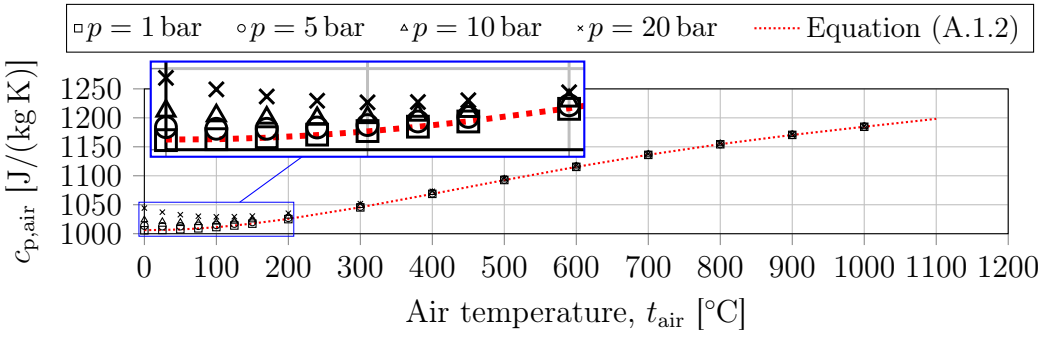

Figure A.1: Specific isobaric heat capacity of air at different pressures (Wagner *et al.*, 2010, Sect. D2.2, Table 8) and polynomial fit

Specific isobaric heat capacity

$$\begin{aligned} c_{\mathrm{p,air}} = \big[&1.0736 \times 10^{3} - 5.4746 \times 10^{-1}(T/\mathrm{K}) \\ &+ 1.3508 \times 10^{-3}(T/\mathrm{K})^{2} - 9.7756 \times 10^{-7}(T/\mathrm{K})^{3} \\ &+ 9.7756 \times 10^{-10}(T/\mathrm{K})^{4}\big]\ \mathrm{J/(kg\,K)} \end{aligned} \tag{A.1.2}$$

Difference in specific enthalpy The equation is derived by symbolic integration of Equation (A.1.2).

$$\begin{aligned} \Delta h_{\mathrm{air}} &= \int_{T_{\mathrm{air},1}}^{T_{\mathrm{air},2}} c_{\mathrm{p,air}} \mathrm{d}T_{\mathrm{air}} \\ &= \big[1.0736 \times 10^{3}(T_{\mathrm{air}}/\mathrm{K}) - 2.7373 \times 10^{-1}(T_{\mathrm{air}}/\mathrm{K})^{2} \\ &\quad + 4.5027 \times 10^{-4}(T_{\mathrm{air}}/\mathrm{K})^{3} - 2.4439 \times 10^{-7}(T_{\mathrm{air}}/\mathrm{K})^{4} \\ &\quad + 4.8404 \times 10^{-11}(T_{\mathrm{air}}/\mathrm{K})^{5}\big]_{T_{\mathrm{air},1}}^{T_{\mathrm{air},2}}\ \mathrm{J/(kg\,K)} \end{aligned} \tag{A.1.3}$$

Thermal conductivity

$$\begin{aligned} k_{\mathrm{air}} = \big[&2.0089 \times 10^{-3} + 9.1072 \times 10^{-5}(T_{\mathrm{air}}/\mathrm{K}) - 3.5465 \times 10^{-8}(T_{\mathrm{air}}/\mathrm{K})^{2} \\ &+ 1.0024 \times 10^{-11}(T_{\mathrm{air}}/\mathrm{K})^{3}\big]\ \mathrm{W/(m\,K)} \end{aligned} \tag{A.1.4}$$

Dynamic viscosity

$$\begin{aligned} \mu_{\mathrm{air}} = \big[&9.7319 \times 10^{-7} + 7.1453 \times 10^{-8}(T_{\mathrm{air}}/\mathrm{K}) - 5.0947 \times 10^{-11}(T_{\mathrm{air}}/\mathrm{K})^{2} \\ &+ 2.8385 \times 10^{-14}(T_{\mathrm{air}}/\mathrm{K})^{3} - 6.5891 \times 10^{-18}(T_{\mathrm{air}}/\mathrm{K})^{4}\big]\ \mathrm{Pa\,s} \end{aligned} \tag{A.1.5}$$

A.2 Inconel 601

The material properties of Inconel needed for the heat transfer model are derived from a document by the Special Metals Corporation (2005).

Density The density of Inconel 601 is assumed to be constant at $8110\,\mathrm{kg/m^3}$.

Thermal conductivity

$$k_{\mathrm{Inc}} = \left[6.3425 + 1.6861 \times 10^{-2}(T_{\mathrm{Inc}}/\mathrm{K})\right] \mathrm{W/(m\,K)} \tag{A.2.1}$$

Specific heat capacity

$$c_{\mathrm{Inc}} = \left[3.6875 \times 10^{2} + 2.6955 \times 10^{-1}(T_{\mathrm{Inc}}/\mathrm{K})\right] \mathrm{J/(kg\,K)} \tag{A.2.2}$$

Emittance No temperature-dependent emittance data for Inconel 601 could be found, however, commonly stated values for oxidized steel are in the range of 0.6 to 0.9 (Greene *et al.*, 2000) with higher values at higher operating temperatures. For the developed models, emittance of steel is only needed for the inside of the absorber tubes, where oxidization and high temperatures are to be expected. Therefore, a rather high value of $\varepsilon_{\mathrm{Inc}} = 0.85$ is estimated irrespective of temperature.

A.3 Pyromark 2500

The optical properties of Pyromark 2500 coating on Inconel tubes are derived from experimental data and calculations by Ho *et al.* (2013).

Solar-weighted total directional absorptance The absorptance of solar radiation is modeled depending on the angle of the incoming ray, θ, according to a curve fit defined by Ho *et al.* (2013, Equation 2 and Table 2) on the basis of measurements

$$\alpha(\theta) = \alpha_{\mathrm{n}} \cos(\theta) \,/\, \cos(0.984\theta)\,. \tag{A.3.1}$$

Therein, α_{n} represents the absorptance of radiation that impinges normal to the absorbing surface. Ho *et al.* measured a value of $\alpha(\theta = 10^{\circ}) = 0.944$ for Pyromark paint on an Inconel tube, from which $\alpha_{\mathrm{n}} = 0.9445$ can be derived.

Total hemispherical emittance The emittance of thermal radiation is presented by Ho *et al.* (2013) as the total hemispherical emittance, that is the integral of emitted radiation at a specific surface temperature, T_{Pyro}. Their results are here fitted with a third order polynomial curve (see Figure A.2)

$$\begin{aligned} \varepsilon_{\mathrm{Pyro}} \;=\; & 5.6333 \times 10^{-1} + 9.3629 \times 10^{-4}\, T_{\mathrm{Pyro}} \\ & -9.2306 \times 10^{-7}\, T_{\mathrm{Pyro}}^{2} + 3.0861 \times 10^{-10}\, T_{\mathrm{Pyro}}^{3}. \end{aligned} \tag{A.3.2}$$

The third order fit was chosen as values calculated with if for temperatures outside the allowed range ($> 900\,^{\circ}\mathrm{C}$) tend to be an overestimate. This is expected to lead to faster simulation convergence opposed to an underestimate.

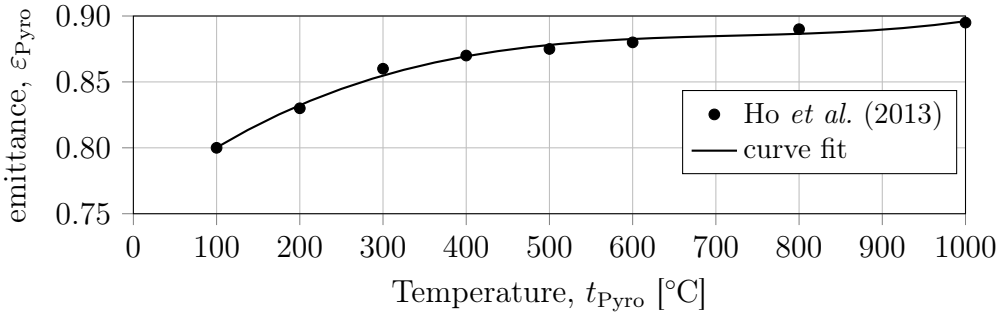

Figure A.2: Total hemispherical emittance over surface temperature for Pyromark 2500 paint as read off Ho *et al.* (2013, Fig. 5) and as modeled (curve fit)

Appendix B

Solar field model in SAM

The solar field model in SAM is used to calculate the cumulative cosine, blocking, shading, spillage and atmospheric attenuation losses of the field. Definitions of these losses and the implemented calculation approaches in SAM are explained by Wagner (2008). In the following sections, the used input parameters for the SAM model of the eSolar heliostat field are stated and its validation is shown.

B.1 Sierra field

The solar field model is in the following developed based on eSolar's Sierra Sun-Tower power plant. The model is validated with experimental and simulation data from literature.

B.1.1 Heliostat properties

Each heliostat consists of a single flat mirror of 1.42 m width and 0.8 m height, giving it a surface area of 1.14 m^2 (Tyner and Pacheco, 2009). The image error of the flat mirrors is given as 1.4 mrad by Schell (2011). Simulations with all investigated field sizes did not show considerably lowered spillage losses when ideally curved mirrors were implemented. The heliostat reflectance, "soiling efficiency" and availability are all set to 1.0 as these effects are added during post-processing in the plant model.

According to Kolb (2011), the heliostat stow wind speed (that is, the speed at which the heliostat has to be defocused and stowed to avoid damage) for large heliostats is in the range of 11 m/s to 18 m/s. For the small, close-to-ground heliostats implemented, that limit could be even higher. The maximum wind speeds in the used weather files for Lancaster, California, and Upington, South Africa, are less than 19 m/s and 13 m/s, respectively. Heliostat stowing has, therefore, been deactivated by setting a large value for the stow wind speed.

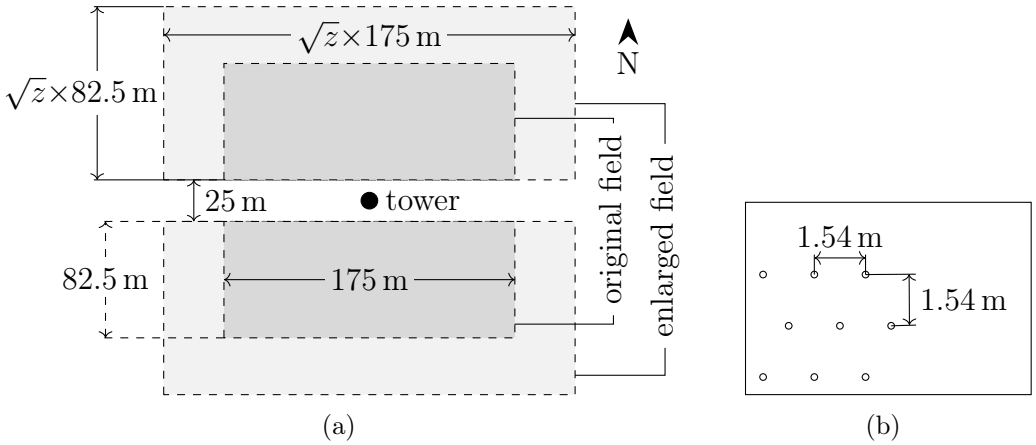

Figure B.1: (a) Layout of modeled solar field and (b) positioning of heliostats' fixed axis based on Sierra SunTower

B.1.2 Field geometry

For the heliostat field layout, one of the fields of the Sierra SunTower fields was attempted to be reproduced from data by Schell (2011). The outer geometry of each of the two subfields is a rectangle with 175 m length in East-West direction and 82.5 m in North-South direction. The two subfields are divided by a tower access road with a width of 25 m, depicted in Figure B.1(a).

It is estimated that the East-West distance between two heliostats in a row is the same as the North-South distance between two rows. Each of these rows is shifted by half the distance between two heliostats from the next row to lower blocking and shading effects — see Figure B.1(b). At a respective spacing distance of 1.54 m, 11 978 heliostats with a total aperture area of 13 607 m^2 are fitted into a double-field. This is 1.7 % smaller than the installed area of 13 836 m^2 stated by Schell (2011), which is assumed to be an acceptable deviation.

B.1.3 Atmospheric attenuation

Atmospheric attenuation, the loss of reflected radiation through scattering by particles, is calculated via an empirical correlation (Wagner, 2008, Eq. 2.6) for clear conditions (visibility = 23 km) for each heliostat

$$\eta_{\text{atm}} = 1 - \left[0.006739 + 0.1046\left(\frac{s}{\text{km}}\right) - 0.0170\left(\frac{s}{\text{km}}\right)^2 + 0.002845\left(\frac{s}{\text{km}}\right)^3\right]. \tag{B.1.1}$$

Therein, s is the distance of the investigated heliostat to the receiver.

The annual average of the attenuation losses of all heliostats amounts to 1.6 % and 3.1 % for the smallest and largest investigated heliostat field, respectively.

B.1.4 Validation

To validate the built SAM model, the annual combined cosine, blocking and shading efficiency, η_{cbs}, is calculated for the Sierra plant and compared to the value of 70.1 %, found by Schell (2011) in ray-tracing simulations. The effect of spillage, which is included in a lump solar field efficiency calculated in SAM, is minimized by lowering the image error to nil. The original Sierra receivers consist of a North-facing and a South-facing cavity with an aperture of approximately 3.6 m width and 2 m height each. However, the used version of SAM only features external cylindrical receivers. The target was, therefore, approximated as a cylinder of 2 m height and 3.6 m diameter. Location and weather information are imported from the TMY3-file for "Lancaster Gen Wm Fox Field" which is included in SAM.

The DNI-weighted annual efficiency is calculated from the SAM-derived data for every hour, i, and the input DNI data, I_{DNI} (see also Gauché *et al.*, 2011):

$$\eta_{\text{cbs,a}} = \frac{\sum_{i=1}^{8760} \eta_{\text{cbs},i}\, I_{\text{DNI},i}}{\sum_{i=1}^{8760} I_{\text{DNI},i}} = 72.3\,\%. \tag{B.1.2}$$

The difference of 3.1 % between this value and the one given by Schell (2011) could be caused by the differing receiver geometries. Heliostats towards the eastern and western edges of the field have a larger target with the cylindrical receiver, possibly resulting in lower blocking and shading losses.

The second value from literature that the SAM model is validated against is the solar field design point efficiency at summer solstice. Tyner and Pacheco (2009) state a heliostat field efficiency (including losses due to availability, mirror reflectivity, cleanliness, cosine, blocking, shading, spillage and atmospheric attenuation) of 78 %. Tyner and Pacheco (p. 3) also state that "Reflector cleanliness of 98 % is routinely achieved." This value is, therefore, used for this validation (only), resulting in the input of the value $\eta_{\text{HS,refl}}\,\eta_{\text{HS,clean}} = 0.95 \times 0.98 = 0.931$ for "Mirror Reflectance and Soiling" in SAM (with $\eta_{\text{HS,refl}}$ from Section 2.1.2). With all remaining values set as described above, the solar field efficiency on 21-Jun at 12:00 p.m. is calculated to be 79.1 %, or 1.5 % higher than given by Tyner and Pacheco. Once again, spillage losses are expected to be under-estimated due to the larger modeled target.

The validation of the model via the annual cosine, blocking and shading efficiency as well as via the design-point solar field efficiency was reasonably successful. Both values are overestimated by less than 4 % with the receiver geometry model seen as a potential source of error. For the technology investigated in this work, a surrounding receiver system of modular subsystems will be employed (instead of two cavities). The SAM model is expected to be more accurate for this setup.

B.2 Solar field size increase

In order to model solar plants with different solar multiples, the field size has to be adjusted to provide the required thermal energy to the receiver. In this section, the changes that are made in the model to realistically model larger solar fields are explained.

B.2.1 Field geometry

The aspect ratio of the subfields and the distance between heliostats stay constant. The North-South dimension as well as the East-West dimension are, therefore, multiplied by the square root of the aperture area increase factor, z (see Figure B.1, a).

B.2.2 Tower height

The tower height, H_{T}, is adjusted with the solar field aperture area. More specifically, the ratio of the distance between the farthest away heliostat and the tower base, $d_{\mathrm{HS,max}}$, to the tower height is kept constant at the value of the Sierra plant

$$H_{\mathrm{T}} = d_{\mathrm{HS,max}} \left[\frac{H_{\mathrm{T}}}{d_{\mathrm{HS,max}}} \right]_{\mathrm{Sierra}} . \tag{B.2.1}$$

The tower heights of the respective modeled solar fields are depicted in Figure 2.3.

B.2.3 Receiver aperture area

The receiver aperture area, A_{Re}, has an influence on the solar field efficiency because a larger target area reduces spillage losses. This is especially relevant when the distance between a heliostat and the receiver becomes large. Therefore, the receiver aperture has to be adjusted for increased solar field sizes.

The appropriate receiver aperture area is calculated as the quotient of its thermal rating, $\dot{Q}_{\mathrm{Re,out,nom}}$, and an assumed nominal specific rating for air receivers, $\dot{q}_{\mathrm{Re,out,nom}}$,

$$A_{\mathrm{Re}} = \frac{\dot{Q}_{\mathrm{Re,out,nom}}}{\dot{q}_{\mathrm{Re,out,nom}}}. \tag{B.2.2}$$

The specific rating is approximated from the full load rating and size of the prototype receiver of the SOLAIR project (Hennecke *et al.*, 2007):

$$\begin{aligned} \dot{q}_{\mathrm{Re,out,nom}} &= \dot{Q}_{\mathrm{Re,out,SOLAIR,nom}} / A_{\mathrm{Re,SOLAIR,nom}} \\ &= 2.5\,\mathrm{MW_t}/6\,\mathrm{m^2} \approx 417\,\mathrm{kW_t/m^2}. \end{aligned} \tag{B.2.3}$$

The design-point (dp) receiver thermal rating is approximated by multiplying the solar field aperture area, A_{SF}, with the incoming radiation, the solar

field efficiency (see Section B.1.4) and the estimated combined thermal and optical efficiency of the receiver system, $\eta_{\mathrm{Re,t+o}}$ (see Hoffschmidt *et al.*, 2003*a*) — all at design point —

$$\dot{Q}_{\mathrm{Re,out,dp}} = A_{\mathrm{SF}} \left[\dot{I}_{\mathrm{DNI}}\, \eta_{\mathrm{SF}}\, \eta_{\mathrm{Re,t+o}}\right]_{\mathrm{dp}} = A_{\mathrm{SF}} \times 950\,\mathrm{W/m^2} \times 0.78 \times 0.76. \quad \text{(B.2.4)}$$

The diameter, D_{Re}, and height, H_{Re}, of the cylindrical receiver are assumed to be equal because it was found that this design results in a higher solar field efficiency than receivers with the same width-to-height ratio as the Sierra SunTower cavity receiver

$$D_{\mathrm{Re}} = H_{\mathrm{Re}} = \sqrt{A_{\mathrm{Re}}/\pi}. \quad \text{(B.2.5)}$$

Other geometries could be preferable but the influence on the solar field efficiency is expected to be small.

Appendix C

Cost adjustment through learning rate[1]

Some of the cost figures used in the economic model of the SUNSPOT and SUNDISC cycle (see Section 2.1.6) are outdated and their current values, especially in real terms, are considerably lower. The specific solar field cost listed in Table 2.3, for example, translates to 193 USD/m^2 when adjusted to the year 2015 while current figures are close to 120 USD/m^2 (Schlaich Bergermann und Partner, 2015). In this section, predictions for current and future component costs are presented.

Technology cost decline is calculated based on the method used in the ATHENE model (Trieb, 2004). The specific cost of a component in the year τ, c_τ, is dependent on its initial cost, c_0, the initially cumulative installed capacity of the technology, P_0, and the cumulative installed capacity in year τ, P_τ

$$c_\tau = c_0 \, (P_\tau / P_0)^{\log PR / \log 2} \, . \tag{C.0.1}$$

The progress ratio of the respective technology, PR, is dependent on its maturity. For example, Trieb (2004, p. 11) states a large progress ratio for a power block, $PR_{\mathrm{PB}} = 0.94$, and a much lower value for TES technology, $PR_{\mathrm{TES}} = 0.88$. This is because power block technology based on steam has been developed at commercial scale for decades while TES technology has only been installed in a few projects. The progress ratios as estimated for the components of this study are presented in Table C.1.

The cumulative capacity of previously installed components of the respective technologies for the years 2005 and 2015 are estimates based on capacities of pilot, demonstration and commercial plants (derived from Ávila-Marín, 2011, Table 2, and Reilly and Kolb, 2001, Table 1-2). The values are given in Table C.1. The specific costs of air receiver components are calculated to have a higher value in 2015 than in 2005 (in nominal terms). Due to the small increase in installed capacity of these technologies, the cost increase due to inflation is

[1] parts of this section are under preparation for publishing (see Heller *et al.*, 2016*a*)

larger than the cost decrease from innovation and operating experience. The generic central receiver components (mainly the solar field) on the other hand, show a considerable drop in specific cost in this period.

As a scenario for the future, it is assumed that from 2015 onward, the global cumulative CSP capacity will have a compound annual growth rate (CAGR) of 18 % (Grobbelaar *et al.*, 2014) from today's 5 GW_e. It is further assumed that half of the new capacity will be installed as central receiver technology, which means a large cost reduction for the affected components' (namely, solar field, tower and control).

The capacity of pressurized and non-pressurized air receiver plants is expected to only grow at the CAGR of 18 % until 2020. Afterwards, these two technologies are assumed to be commercially available and each account for 10 % of the newly installed central receiver capacity. The resulting specific component costs, at an estimated inflation rate of 2 % p.a., are presented in Table C.1. The costs of solar air receiver components only drop significantly once their medium scale roll-out has occurred (post 2020). The specific costs for 2025 are likely optimistic but are shown nonetheless to present a possible future scenario.

Table C.1: Estimated progress ratio, PR, reference cumulative installed capacity, P_τ, and specific cost, c_τ, of components (for cost sources see Section 2.1.6; the specific cost of the tower is the constant multiplier of an exponential correlation depending on tower height; all cost are nominal values)

Component	PR [-]	P_{2005}	P_{2015}	P_{2020}	P_{2025}	Unit	c_{2005}	c_{2015}	c_{2020}	c_{2025}	Unit
TES system	0.95	0	3.0	6.9	510	MW_t	9.50	11.5	11.9	9.59	USD/kW_th
HPRS	0.90	2.2	6.9	16	1300	MW_t	191	194	189	107	USD/kW_t
LPRS	0.90	8.2	18	42	1300	MW_t	125	133	130	85.1	USD/kW_t
Brayton cycle	0.94	2.2	6.9	16	1300	MW_t	519	567	582	434	USD/kW_e
Adaption of GT	0.85	2.2	6.9	16	1300	MW_t	1090	1010	916	362	10^3 USD
Rankine cycle	0.94	8.2	18	42	1300	MW_t	729	821	842	684	USD/kW_e
Solar field	0.90	0.18	3.6	56	190	10^6 m^2	160	123	89.2	81.7	USD/m^2
Tower	0.95	0.18	3.6	56	190	10^6 m^2	484	470	423	426	10^3 USD
Control	0.95	0.18	3.6	56	190	10^6 m^2	605	587	529	533	10^3 USD
Annual O&M	0.97	0.18	3.6	56	190	10^6 m^2	58.6	64.7	63.3	66.2	USD/kW_e

Appendix D

Receiver system pressure drop

In this appendix, the pressure drop of the pressurized air flow path between the compressor outlet and the turbine inlet is investigated for an HPAR concept receiver adapted to the SUNDISC cycle, as presented in Section 6.4.2. The high-temperature receiver (HTRe) model is roughly based on the REFOS volumetric receiver with a pressurized quartz glass window (see Section 6.3.1).

D.1 Flow path and operating parameters

The pressure drop of the components in the flow path between compressor outlet and turbine inlet are calculated employing empirical correlations derived from the VDI Heat Atlas (Kast *et al.*, 2010). The simplified flow path model is based on the diagram in Figure D.1 showing the components for which a pressure drop was calculated. All piping up- and downstream of the HPAR is referred to as "pipes" to simplify differentiation between it and the HPAR's absorber tubes.

The local air density is determined through the ideal gas law. The correlations of the remaining fluid properties are the polynomial fits presented in Appendix A.1. Note that the fits were generated from data for $T_{\text{air}} \leq 1000\,^{\circ}\text{C}$. This is exceeded downstream the HTRe, however, the error is thought to be minor and only linearly influences the value of the Reynolds number and the friction factor.

The main operating parameters, based on Section 7.1, are given in Table D.1. The distances between the receivers and the gas turbine as well as the length of the toroidal manifolds are estimated based on investigations of solar flux absorption in an HPAR manifestation.

In an attempt to minimize the number of variables, the diameters of headers, manifolds and turbine inlet feeder are correlated to the flow velocity so that it stays approximately constant at the (preliminary) design value of 20 m/s. The flow velocity in the HPAR and HTRe is not limited but defined by the number of parallel flow paths and the absorber tube diameter.

1 3 serial Y-junctions splitting the flow into 8 individually controllable streams
2 regulating valve
3 HPAR section header
4 bend
5 HPAR section inlet manifold
6 diverging flow into HPAR branches
7 HPAR absorber tubes
8 converging flow from HPAR branches
9 HPAR outlet manifold
10 T-junction to combine two streams of manifold
11 HTRe header
12 bend
13 HTRe manifold
13 diverging flow into HTRe branches
14 HTRe unit
15 converging flow from HTRe branches
16 HTRe outlet manifold
17 bend
18 turbine inlet pipe
19 bend

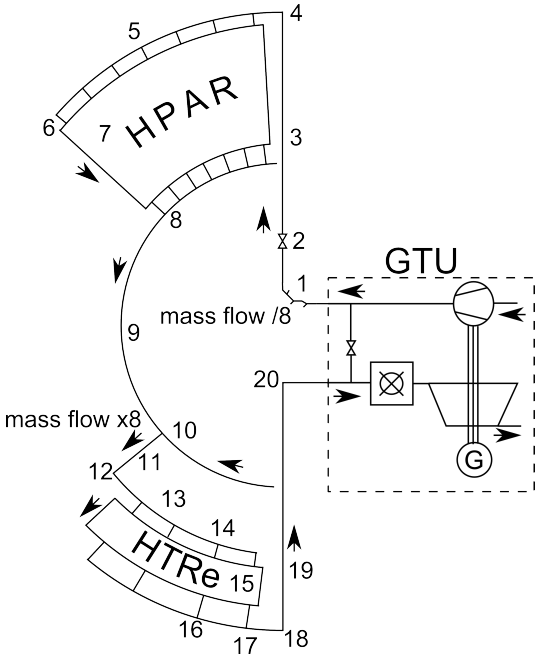

Figure D.1: Simplified flow path

Table D.1: Input operating parameters and dimensions

Parameter	Unit	Value
compressor outlet pressure	Pa	15×10^5
compressor outlet temperature	°C	400
HPAR outlet temperature	°C	800
turbine inlet temperature	°C	1100
air mass flow	kg/s	20.5
absorber tube inner diameter	mm	25.0
roughness of all pipes	mm	0.4
number of parallel flow paths	-	360
HPAR header length	m	4
HPAR inlet manifold radius	m	4
HPAR outlet manifold radius	m	2
HTRe header length	m	2
turbine inlet feeder length	m	2
number of parallel HTRe systems	-	40
pressure drop in HTRe	Pa	1000

The three serial Y-junctions (1) are designed to split the main flow into equal mass flows for each 45° section of the HPAR. At the current stage, there are no regulating valves incorporated for the mass flows in the individual HTRe units.

The magnitude of tube roughness, $\varepsilon_{\text{rough,i}} = 0.2\,\text{mm}$, is the value given in the Heat Atlas (Kast *et al.*, 2010, Sect. L1.2, Table 1) for "uniformly rusted" welded steel pipes. This is thought to be a conservative assumption for the condition of and, thus, pressure drop in the pipes.

D.2 Pressure drop correlations

For each component, the pressure drop, Δp, is calculated in dependence of the flow velocity, U, density, ρ, and a specific drag coefficient, ζ,

$$\Delta p = \zeta \frac{\rho U^2}{2}. \tag{D.2.1}$$

The definition of the drag coefficient differs for each type of component and its magnitude can vary depending on additional parameters, for example, flow Reynolds number or radius of a bend. The correlations and calculations for the types of components as derived from the Heat Atlas and presented in Table D.2. The resulting values for the drag coefficient and the calculated pressure drops with the used respective parameters are given in Table D.3 and the cumulative pressure drop is shown in Figure D.2.

Table D.2: Drag coefficients correlations (Kast *et al.*, 2010); $\varepsilon_{\text{rough,i}}$: tube roughness; A_{branch} and A_{manifold}, cross-sectional flow area of branch and manifold, respectively

Component type			ζ correlation	Section in reference
Y-junction	ζ	=	$f(d_{\text{i}}) = 0.067$	L1.3. Table 1
flow through pipes	$1/\sqrt{\zeta}$	=	$2\log_{10}\left[\frac{2.51}{Re\sqrt{\zeta}} + \frac{\varepsilon_{\text{rough,i}}/d_{\text{i}}}{3.71}\right]$	L1.1.3
regulating valve	ζ	=	$f(d_{\text{i}}) = 1.0$	L1.3. Fig. 21
bend (two-segment 90°-elbow)	ζ	=	0.5, for $Re > 1 \times 10^3$	L1.3. Fig. 16+19
entry from manifold to branches	ζ	=	$f(Re) = 1.1 \ldots 0.27$	L1.3. Fig. 2+3
branches entry to manifold	ζ	=	$(1 - A_{\text{branch}}/A_{\text{manifold}})^2$	L1.3.3
T-junction	ζ	=	$f(d_{\text{i}}) = 1.56$	L1.3. Table 1

Table D.3: Component pressure drops

	Component	d_{i} [mm]	ζ [-]	Δp [Pa]
1	Y-junctions	410...145	0.067	312
2	HPAR header	145	0.0258	1104
3	regulating valve	145	1.0	1554
4	bend	145	0.5	778
5	manifold	145	0.0258	434
6	branch diverge	25	0.55	855
7	HPAR	25		10 000
8	branch converge	25	0.9954	1390
9	manifold	520	0.0188	218
10	T-junction	520	1.56	1502
11	header	520	0.0202	424
12	bend	520	0.5	1929
13	manifold	520	0.0202	1333
13	branch diverge	368	0.27	418
14	HTRe	368		1000
15	branch converge	368	0.9506	712
16	manifold	591	0.0184	147
17	bend	591	0.5	374
18	turbine inlet feeder	591	0.0184	93
19	bend	591	0.5	375
	total			24 953

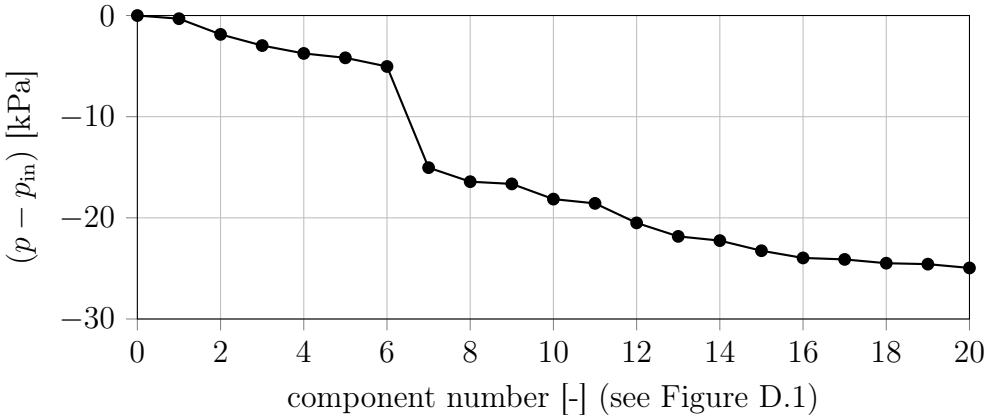

Figure D.2: Differential pressure over flow path

D.3 Results

The chosen receiver system flow path combined with the defined flow velocities generates a pressure drop of 250 mbar from compressor outlet to turbine inlet, which is the maximum allowable for such a system as defined by Uhlig *et al.* (2015). The result was found for an approximate flow velocity of 20 m/s, an estimated pressure drop of 100 mbar for the HPAR absorber and 360 parallel flow paths in the HPAR. The resulting tube diameters of 25 mm for the absorber tubes and between 145 mm and 600 mm in the piping is thought to be reasonable.

To lower the system pressure drop or allow for higher pressure drops in the HPAR system the flow path can be altered or the flow velocity in the main pipes can be decreased. However, the latter can only be achieved by increasing the pipe diameters which induces higher cost. Both options should only be turned to at a later stage in the development of a cascaded receiver system. The maximum allowable pressure drop in the HPAR absorber — measured from the inlet of the first absorbing tube to the outlet of the last one — can, therefore, be defined as 100 mbar until more detailed designs are available.

Appendix E

Finned tube calculations

The heat flux and achievable non-pressurized air (NPA) outlet temperature in a bundle of finned tubes is estimated based on semi-empirical correlations by Schmidt (2010, Sect. M1.1).

E.1 Finned tube bundle heat transfer model

Heat transfer from finned tubes to an external flow can be calculated similar as for plain tubes (compare to Equation 7.6.1)

$$\dot{Q}_{\text{conv,NPA,finned}} = h_{\text{conv,NPA,finned}} \left(A_{\text{tube,o,free}} + \eta_{\text{fins}} A_{\text{fins}}\right) \left(T_{\text{finned}} - \overline{T}_{\text{NPA}}\right). \tag{E.1.1}$$

but with an added fin efficiency factor, η_{fins}, and a differing driving temperature difference (Schmidt, 2010, Sect. M1.1, Eq. 3). A_{fins} represents the surface area of the fins and $A_{\text{tube,o,free}}$ the free outer surface area of the tube, that is the original tube surface area without the area occupied by fins, so that the total surface area of the finned tube is $A_{\text{finned}} = A_{\text{fins}} + A_{\text{tube,o,free}}$.

The fin efficiency is defined as the ratio of the temperature differences from fin to fluid and from tube to fluid, respectively. As the fins in an finned tubular absorber likely have a higher temperature than the tubes, because they absorb most of the radiation, this efficiency would render values above unity. For this model, it is assumed that conduction can alleviate this temperature gradient so that all fins have the identical temperature as their base tube and the fin efficiency is equal to unity (this issue is addressed again in Section 9.1.3).

The Nusselt number, and therefore heat transfer coefficient, for tube bundles is calculated according to Gnielinski (2010*b*). The approach is that for a generic body in cross-flow with the characteristic length $l_{\text{c}} = \pi/2 \sqrt{d_{\text{o}}^2 + h_{\text{f}}^2}$ (see fin geometry parameters in Figure E.1). Equations (7.6.4–7.6.7) are used for calculating the flow Nusselt number from which the convective heat transfer coefficient is calculated

$$h_{\text{conv,NPA,finned}} = Nu_{l_{\text{c}}} k_{\text{NPA}} / l_{\text{c}}. \tag{E.1.2}$$

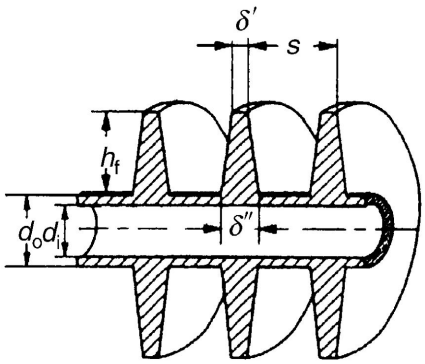

Figure E.1: Sketch defining geometric parameters of circular finned tube (Schmidt, 2010, Sect. M1, Fig. 1); for flat, circular fins $\delta = \delta' = \delta''$

The Nusselt and Reynolds numbers are respective to the characteristic length (see Gnielinski, 2010*b*, Sect. G6.1)

$$Re_{l_c} = \overline{U}_{\mathrm{NPA,sT}}\, l_c\, \rho_{\mathrm{PA}}/\mu_{\mathrm{NPA}}. \tag{E.1.3}$$

The mean inlet flow velocity, $\overline{U}_{\mathrm{PA,in}}$, is corrected for temperature increase and flow cross-section reduction in the bundle

$$\overline{U}_{\mathrm{NPA,sT}} = \overline{U}_{\mathrm{NPA,in}}\, \frac{s_1}{s_1 - D_o}\, \frac{\overline{T}_{\mathrm{NPA}}}{T_{\mathrm{NPA,in}}}. \tag{E.1.4}$$

All fluid properties are evaluated at the flow's mean temperature between inlet and outlet, $\overline{T}_{\mathrm{NPA}} = (T_{\mathrm{NPA,in}} + T_{\mathrm{NPA,out}})/2$. The geometry of an in-line tube bundle is represented by the transversal spacing between tubes of a row, s_1, see also Figure 7.10(a).

The presented method is applied to each individual tube in a representative column of a bundle identical in geometry to the one described in Section 7.1. The rows are treated individually to account for the change in flow cross section towards the center of the cylindrical receiver. Perfect mixing of the fluid after each row is assumed, which increases the heat transfer. At the chosen geometry with five rows in-line with large transversal distances in between, this assumption is likely not accurate. However, to predict the degree of mixing in the bundle, at least two-dimensional modeling of the flow would be necessary.

List of References

Allen, K., Heller, L. and von Backström, T. (2016). Cost Optimum Parameters for Rock Bed Thermal Storage at 550–600 °C: A Parametric Study. *Journal of Solar Energy Engineering*, vol. 138, no. 6.
Available at: http://dx.doi.org/10.1115/1.4034334

Allen, K. and von Backström, T. (2016). Rock bed thermal storage for concentrating solar power: Requirements, concepts, and costs. *Solar Energy (under review)*.

Allen, K., von Backström, T., Kröger, D. and Kisters, A. (2014). Rock bed storage for solar thermal power plants: Rock characteristics, suitability, and availability. *Solar Energy Materials and Solar Cells*, vol. 126, pp. 170–183. ISSN 09270248.
Available at: http://dx.doi.org/10.1023/B:NARR.0000032647.41046.e7

Allen, K.G. (2010). *Performance characteristics of packed bed thermal energy storage for solar thermal power plants*. M.Sc., Stellenbosch University.
Available at: http://hdl.handle.net/10019.1/4329

Allen, K.G. (2014). *Rock bed thermal storage for concentrating solar power plants*. PhD, Stellenbosch University.
Available at: http://hdl.handle.net/10019.1/86521

Allen, K.G., von Backström, T.W. and Kröger, D.G. (2015). Rock bed pressure drop and heat transfer: Simple design correlations. *Solar Energy*, vol. 115, pp. 525–536. ISSN 0038092X.
Available at: http://dx.doi.org/10.1016/j.solener.2015.02.029

Amsbeck, L., Helsch, G., Röger, M. and Uhlig, R. (2009). Development of a Broadband Antireflection Coated Transparent Silica Window for a Solar-Hybrid Microturbine System. In: *Proceedings of SolarPACES 2009*. Berlin, Germany.

Ávila-Marín, A.L. (2011). Volumetric receivers in Solar Thermal Power Plants with Central Receiver System technology: A review. *Solar Energy*, vol. 85, no. 5, pp. 891–910. ISSN 0038-092X.
Available at: http://dx.doi.org/10.1016/j.solener.2011.02.002

Avila-Marin, A.L., Fernandez-Reche, J. and Tellez, F.M. (2013). Evaluation of the potential of central receiver solar power plants: Configuration, optimization and trends. *Applied Energy*, vol. 112, pp. 274–288. ISSN 03062619.
Available at: http://dx.doi.org/10.1016/j.apenergy.2013.05.049

Becker, M., Fend, T., Hoffschmidt, B., Pitz-Paal, R., Reutter, O., Stamatov, V., Steven, M. and Trimis, D. (2006). Theoretical and numerical investigation of flow stability in porous materials applied as volumetric solar receivers. *Solar Energy*, vol. 80, no. 10, pp. 1241–1248. ISSN 0038092X.
Available at: `http://dx.doi.org/10.1016/j.solener.2005.11.006`

Behar, O., Khellaf, A. and Mohammedi, K. (2013). A review of studies on central receiver solar thermal power plants. *Renewable and Sustainable Energy Reviews*, vol. 23, pp. 12–39. ISSN 13640321.
Available at: `http://dx.doi.org/10.1016/j.rser.2013.02.017`

Bellard, D., Ferriere, A., Pra, F. and Couturier, R. (2012). Experimental Characterization of a High-Temperature Pressurized Air Solar Absorber for the PEGASE Project. In: *Proceedings of SolarPACES 2012*. Marrakech, Morocco.

Bode, S.-J. and Gauché, P. (2012). Review of Optical Software for Use in Concentrating Solar Power Systems. In: *Proceedings of SASEC 2012*. Stellenbosch, South Africa.
Available at: `http://sterg.sun.ac.za/wp-content/uploads/2012/06/CSP-061.pdf`

Boyce, M.P. (2006). *Gas turbine engineering handbook*. 3rd edn. Gulf Professional Publishing, Burlington, MA. ISBN 978-0-7506-7846-9.

Buck, R. (2003). Modularer Druck-Receiver für solarunterstützte fossile Gasturbinen- und Kombikraftwerke (REFOS-2) Schlußbericht. Tech. Rep., DLR, Stuttgart.

Buck, R. (2005). Hocheffiziente Solarturm-Technologie (HST) Schlussbericht (excerpt). Tech. Rep., German Aerospace Center (DLR), Stuttgart.

Buck, R. (2016). Personal communication.

Buck, R., Barth, C., Eck, M. and Steinmann, W.-D. (2006). Dual-receiver concept for solar towers. *Solar Energy*, vol. 80, no. 10, pp. 1249–1254. ISSN 0038092X.
Available at: `http://dx.doi.org/10.1016/j.solener.2005.03.014`

Buck, R., Brauning, T., Denk, T., Pfänder, M., Schwarzbözl, P. and Téllez, F.M. (2002). Solar-Hybrid Gas Turbine-based Power Tower Systems (REFOS). *Journal of Solar Energy Engineering*, vol. 124, no. 1, pp. 2–9.
Available at: `http://dx.doi.org/10.1115/1.1445444`

Buyruk, E., Johnson, M. and Owen, I. (1998). Numerical and experimental study of flow and heat transfer around a tube in cross-flow at low Reynolds number. *International Journal of Heat and Fluid Flow*, vol. 19, no. 3, pp. 223–232. ISSN 0142727X.
Available at: `http://dx.doi.org/10.1016/S0142-727X(97)10027-3`

Çengel, Y.A. and Ghajar, A.J. (2011). *Heat and Mass Transfer*. 4th edn. McGraw-Hill, New York. ISBN 978-007-131112-0.

Chen, J., Müller-Steinhagen, H. and Duffy, G.G. (2001). Heat transfer enhancement in dimpled tubes. *Applied Thermal Engineering*, vol. 21, no. 5, pp. 535–547. ISSN 13594311.
Available at: http://dx.doi.org/10.1016/S1359-4311(00)00067-3

Curzon, F.L. and Ahlborn, B. (1975). Efficiency of a Carnot engine at maximum power output. *American Journal of Physics*, vol. 43, no. 1, p. 22. ISSN 00029505.
Available at: http://dx.doi.org/10.1119/1.10023

del Río, A., Korzynietz, R., Brioso, J., Gallas, M., Ordóñez, I., Quero, M. and Díaz, C. (2015). Soltrec — Pressurized Volumetric Solar Air Receiver Technology. *Energy Procedia*, vol. 69, pp. 360–368. ISSN 18766102.
Available at: http://dx.doi.org/10.1016/j.egypro.2015.03.042

Department of Energy (2013). Integrated Resource Plan for Electricity (IRP) 2010-2030.
Available at: http://www.doe-irp.co.za/content/IRP2010_updatea.pdf

Dreißigacker, V., Zunft, S. and Müller-Steinhagen, H. (2013). A thermo-mechanical model of packed-bed storage and experimental validation. *Applied Energy*. ISSN 03062619.
Available at: http://dx.doi.org/10.1016/j.apenergy.2013.03.067

Ebert, M., Arnold, W., Avila-Marin, A., Denk, T., Hertel, J., Jensch, A., Reinalter, W., Schlierbach, A. and Uhlig, R. (2015). Development of Insulation for High Flux Density Receivers. *Energy Procedia*, vol. 69, pp. 369–378. ISSN 18766102.
Available at: http://dx.doi.org/10.1016/j.egypro.2015.03.043

Eck, M., Buck, R. and Wittmann, M. (2006). Dual Receiver Concept for Solar Towers up to 100 MW. *Journal of Solar Energy Engineering*, vol. 128, no. 3, pp. 293–301. ISSN 01996231.
Available at: http://dx.doi.org/10.1115/1.2210501

Fend, T., Schwarzbözl, P., Smirnova, O., Schöllgen, D. and Jakob, C. (2013). Numerical investigation of flow and heat transfer in a volumetric solar receiver. *Renewable Energy*, vol. 60, pp. 655–661. ISSN 09601481.
Available at: http://dx.doi.org/10.1016/j.renene.2013.06.001

Fraidenraich, N., Gordon, J.M. and Tiba, C. (1992). Optimization of gas-turbine combined cycles for solar energy and alternative-fuel power generation. *Solar Energy*, vol. 48, no. 5, pp. 301–307. ISSN 0038092X.
Available at: http://dx.doi.org/10.1016/0038-092X(92)90058-I

Gärtner, D., Johannsen, K. and Ramm, H. (1974). Turbulent heat transfer in a circular tube with circumferentially varying thermal boundary conditions. *International Journal of Heat and Mass Transfer*, vol. 17, no. 9, pp. 1003–1018. ISSN 00179310.
Available at: http://dx.doi.org/10.1016/0017-9310(74)90182-3

Gauché, P., Rudman, J. and Silinga, C. (2015). Feasibility of the WWF Renewable Energy Vision 2030 — South Africa. Tech. Rep., WWF South Africa.
Available at: `http://www.wwf.org.za/media_room/publications/?14461/Feasibility-of-the-WWF-Renewable-Energy-Vision-2030---South-Africa`

Gauché, P., von Backström, T.W. and Brent, A.C. (2011). CSP Modeling Methodology for Macro Decision Making - Emphasis on the Central Receiver Type. In: *Proceedings of SolarPACES 2011*. Granada, Spain.
Available at: `http://blogs.sun.ac.za/sterg/files/2011/08/SolarPACES2011_Gauche_final.pdf`

Gnielinski, V. (2010*a*). *G1 Heat Transfer in Pipe Flow*. Springer Berlin Heidelberg, Berlin, Heidelberg. ISBN 978-3-540-77877-6.
Available at: `http://dx.doi.org/10.1007/978-3-540-77877-6_34`

Gnielinski, V. (2010*b*). *G6 Heat Transfer in Cross-flow Around Single Tubes, Wires, and Profiled Cylinders*. Springer Berlin Heidelberg, Berlin, Heidelberg. ISBN 978-3-540-77877-6.
Available at: `http://dx.doi.org/10.1007/978-3-540-77877-6_39`

Gnielinski, V. (2010*c*). *G7 Heat Transfer in Cross-flow Around Single Rows of Tubes and Through Tube Bundles*. Springer Berlin Heidelberg, Berlin, Heidelberg. ISBN 978-3-540-77877-6.
Available at: `http://dx.doi.org/10.1007/978-3-540-77877-6_40`

Grange, B., Ferrière, A., Bellard, D., Vrinat, M., Couturier, R., Pra, F. and Fan, Y. (2011). Thermal Performances of a High Temperature Air Solar Absorber Based on Compact Heat Exchange Technology. *Journal of Solar Energy Engineering*, vol. 133, no. 3, p. 031004. ISSN 01996231.
Available at: `http://dx.doi.org/10.1115/1.4004356`

Grasse, W. (1991). PHOEBUS - international 30 MWe solar power tower. *Solar Energy Materials*, vol. 24, no. 1-4, pp. 82–94.
Available at: `http://dx.doi.org/10.1016/0165-1633(91)90050-U`

Greene, G.A., Finfrock, C.C. and Irvine, T.F. (2000). Total hemispherical emissivity of oxidized Inconel 718 in the temperature range 300–1000 °C. *Experimental Thermal and Fluid Science*, vol. 22, no. 3-4, pp. 145–153. ISSN 08941777.
Available at: `http://dx.doi.org/10.1016/S0894-1777(00)00021-2`

Grobbelaar, S., Gauché, P. and Brent, A. (2014). Developing a competitive concentrating solar power industry in South Africa: Current gaps and recommended next steps. *Development Southern Africa*, vol. 31, no. 3, pp. 475–493. ISSN 0376-835X.
Available at: `http://dx.doi.org/10.1080/0376835X.2014.891971`

Heller, L., Allen, K.G., Lubkoll, M., Pitot de la Beaujardiere, J.-F.P., Gauché, P. and Hoffmann, J. (2016*a*). The SUNDISC cycle: A direct storage-charging dual-pressure air receiver cycle. *(in preparation)*.

Heller, L. and Gauché, P. (2014). Dual-pressure air receiver cycle for direct storage charging. *Energy Procedia*, vol. 49, pp. 1400–1409. ISSN 18766102.
Available at: http://dx.doi.org/10.1016/j.egypro.2014.03.149

Heller, L. and Hoffmann, J. (2014). Comparison of Different Configurations of a Combined Cycle CSP Plant. In: *Proceedings of SASEC 2014*. Port Elizabeth, South Africa.

Heller, L. and Hoffmann, J. (2016). Enhancements to the Hybrid Pressurized Air Receiver (HPAR) Concept in the SUNDISC Cycle. *AIP Conference Proceedings (under review)*.

Heller, L., Hoffmann, J. and Gauché, P. (2016*b*). The Hybrid Pressurized Air Receiver (HPAR) in the SUNDISC Cycle. *AIP Conference Proceedings*, vol. 1734.
Available at: http://dx.doi.org/10.1063/1.4949071

Heller, P. (2010). Solar-Hybrid Power and Cogeneration Plants. Tech. Rep. 019830, Deutsches Zentrum für Luft- und Raumfahrt e.V.
Available at: http://cordis.europa.eu/documents/documentlibrary/132084181EN8.zip

Hennecke, K., Schwarzbözl, P., Alexopoulos, S., Göttsche, J., Hoffschmidt, B., Beuter, M., Koll, G. and Hartz, T. (2008). Solar power tower Jülich — The first test and demonstration plant for open volumetric receiver technology in Germany. *Proceedings of SolarPACES 2008*, pp. 1–8.

Hennecke, K., Schwarzbözl, P., Hoffschmidt, B., Göttsche, J., Koll, G. and Beuter, M. (2007). The Solar Power Tower Jülich — A solar thermal power plant for test and demonstration of air receiver technology. In: Goswami, D.Y. and Zhao, Y. (eds.), *Proceedings of ISES World Congress 2007*, pp. 1749–1753. Springer Berlin Heidelberg.
Available at: http://dx.doi.org/10.1007/978-3-540-75997-3_358

Heraeus Quarzglas (2016). Transmission Calculator.
Available at: https://www.heraeus.com/en/hqs/fused_silica_quartz_knowledge_base/t_calc/transmission_calculator.aspx

Hertel, J., Uhlig, R., Söhn, M., Schenk, C., Helsch, G. and Bornhöft, H. (2016). Fused silica windows for solar receiver applications. *AIP Conference Proceedings*, vol. 1734, no. 030020.
Available at: http://dx.doi.org/10.1063/1.4949072

Hirsch, T., Ahlbrink, N., Pitz-Paal, R., Teixeira Boura, C., Hoffschmidt, B., Gall, J., Abel, D., Nolte, V., Wirsum, M., Andersson, J. and Diehl, M. (2011). Dynamic Simulation of a Solar Tower System with Open Volumetric Receiver - A review on the VICERP Project. In: *Proceedings of SolarPACES 2011*. Granada, Spain.

Hischier, I., Hess, D., Lipiński, W., Modest, M. and Steinfeld, A. (2009). Heat Transfer Analysis of a Novel Pressurized Air Receiver for Concentrated Solar Power via Combined Cycles. *Journal of Thermal Science and Engineering Applications*,

vol. 1, no. 4, p. 041002. ISSN 19485085.
Available at: http://dx.doi.org/10.1115/1.4001259

Hischier, I., Leumann, P. and Steinfeld, A. (2012). Experimental and Numerical Analyses of a Pressurized Air Receiver for Solar-Driven Gas Turbines. *Journal of Solar Energy Engineering*, vol. 134, no. 2, p. 021003. ISSN 0199-6231.
Available at: http://dx.doi.org/10.1115/1.4005446

Hischier, I., Poživil, P. and Steinfeld, A. (2015). Optical and Thermal Analysis of a Pressurized-Air Receiver Cluster for a 50 MWe Solar Power Tower. *Journal of Solar Energy Engineering*, vol. 137, no. 6, p. 61002. ISSN 0199-6231.
Available at: http://dx.doi.org/10.1115/1.4031210

Ho, C.K. and Iverson, B.D. (2014). Review of high-temperature central receiver designs for concentrating solar power. *Renewable and Sustainable Energy Reviews*, vol. 29, pp. 835–846. ISSN 13640321.
Available at: http://dx.doi.org/10.1016/j.rser.2013.08.099

Ho, C.K., Mahoney, A.R., Ambrosini, A., Bencomo, M., Hall, A. and Lambert, T.N. (2013). Characterization of Pyromark 2500 Paint for High-Temperature Solar Receivers. *Journal of Solar Energy Engineering*, vol. 136, no. 1, p. 014502. ISSN 0199-6231.
Available at: http://dx.doi.org/10.1115/1.4024031

Hoffschmidt, B. (1996). Vergleichende Bewertung verschiedener Konzepte volumetrischer Strahlungsempfänger. Tech. Rep., Deutsches Zentrum für Luft- und Raumfahrt e.V., Köln.

Hoffschmidt, B., Dibowski, G., Beuter, M., Fernandez, V., Téllez, F. and Stobbe, P. (2003*a*). Test Results of a 3 MW Solar Open Volumetric Receiver. In: *Proceedings of ISES Solar World Congress 2003*, vol. 10, pp. 1–8. Göteborg, Sweden.

Hoffschmidt, B., Fernandes, V., Mavroidis, I., Romero, M. and Stobbe, P. (2001). Development of Ceramic Volumetric Receiver Technology. In: *5th Cologne Solar Symposium*. Cologne, Germany.

Hoffschmidt, B., Téllez, F.M., Valverde, A., Fernández, J. and Fernández, V. (2003*b*). Performance Evaluation of the 200-kWth HiTRec-II Open Volumetric Air Receiver. *Journal of Solar Energy Engineering*, vol. 125, no. 1, p. 87. ISSN 01996231.
Available at: http://dx.doi.org/10.1115/1.1530627

Hofmann, A., Schenk, C. and Uhlig, R. (2009). Optical quartz glass windows for high concentrated thermal power plants. In: *Proceedings of SolarPACES 2009*. Berlin, Germany.

Howell, J.R. (2010). *A Catalog of Radiation Heat Transfer Configuration Factors*. 3rd edn. Austin, Texas.

Hughes, P. (1975). *The Design and Predicted Performance of Arlington House*. Ph.D., University of Wisconsin, Madison.
Available at: http://minds.wisconsin.edu/handle/1793/34541

IRENA (2015). Renewable Power Generation Costs in 2014. Tech. Rep., International Renewable Energy Agency.
Available at: http://www.irena.org/DocumentDownloads/Publications/Overview_RenewablePowerGenerationCostsin2012.pdf

Karni, J., Kribus, A., Doron, P., Rubin, R., Fiterman, A. and Sagie, D. (1997). The DIAPR: A high-pressure, high-temperature solar receiver. *Journal of Solar Energy Engineering*, vol. 119, no. 1, pp. 74–78. ISSN 0199-6231.
Available at: http://dx.doi.org/10.1115/1.2871853

Kast, W., (Revised by Hermann Nirschl), Gaddis, E.S., Wirth, K.-E. and Stichlmair, J. (2010). *L1 Pressure Drop in Single Phase Flow*. Springer Berlin Heidelberg, Berlin, Heidelberg. ISBN 978-3-540-77877-6.
Available at: http://dx.doi.org/10.1007/978-3-540-77877-6_70

Kehlhofer, R. (1999). *Combined-cycle gas & steam turbine power plants*. 2nd edn. PennWell, Tulsa. ISBN 0878147365.

Kolb, G.J. (2011). An Evaluation of Possible Next-Generation High-Temperature Molten-Salt Power Towers. Tech. Rep., Sandia National Laboratories, Albuquerque, USA.
Available at: http://prod.sandia.gov/techlib/access-control.cgi/2011/119320.pdf

Kolb, G.J., Ho, C.K., Mancini, T.R. and Gary, J.A. (2011). Power Tower Technology Roadmap and Cost Reduction Plan. Tech. Rep., Sandia National Laboratories, Albuquerque.
Available at: prod.sandia.gov/techlib/access-control.cgi/2011/112419.pdf

Korzynietz, R., Quero, M. and Uhlig, R. (2012). SOLUGAS — Future Solar Hybrid Technology. In: *Proceedings of SolarPACES 2012*. Abengoa Solar, Marrakech, Morocco.

Kretzschmar, H. and Gauché, P. (2012). Hybrid Pressurized Air Receiver for the SUNSPOT Cycle. In: *Proceedings of SASEC 2012*. Stellenbosch, South Africa.
Available at: http://sterg.sun.ac.za/wp-content/uploads/2012/06/CSP-141.pdf

Kribus, A., Doron, P., Rubin, R., Karni, J., Reuven, R., Duchan, S. and Taragan, E. (1999). A Multistage Solar Receiver: The Route to High Temperature. *Solar Energy*, vol. 67, no. 1-3, pp. 3–11. ISSN 0038-092X.
Available at: http://dx.doi.org/10.1016/S0038-092X(00)00056-6

Kribus, A., Doron, P., Rubin, R., Reuven, R., Taragan, E., Duchan, S. and Karni, J. (2001). Performance of the Directly-Irradiated Annular Pressurized Receiver (DIAPR) Operating at 20 Bar and 1,200celsius. *Journal of Solar Energy Engineering*, vol. 123, no. 1, p. 10. ISSN 01996231.
Available at: http://dx.doi.org/10.1115/1.1345844

Kribus, A., Gray, Y., Grijnevich, M., Mittelman, G., Mey, S. and Caliot, C. (2014). The promise and challenge of volumetric absorbers. *Solar Energy*, vol. 110, pp. 463–481. ISSN 0038092X.
Available at: `http://dx.doi.org/10.1016/j.solener.2014.09.035`

Kribus, A., Ries, H. and Spirkl, W. (1996). Inherent Limitations of Volumetric Solar Receivers. *Journal of Solar Energy Engineering*, vol. 118, p. 151. ISSN 01996231.
Available at: `http://dx.doi.org/10.1115/1.2870891`

Kröger, D.G. (2011). SUNSPOT The Stellenbosch University Solar Power Thermodynamic Cycle. Tech. Rep., Stellenbosch University, Stellenbosch.
Available at: `http://blogs.sun.ac.za/sterg/files/2011/05/SUNSPOT-2.pdf`

Laing, D., Bahl, C., Bauer, T., Lehmann, D. and Steinmann, W.-D. (2011). Thermal energy storage for direct steam generation. *Solar Energy*, vol. 85, no. 4, pp. 627–633. ISSN 0038-092X.
Available at: `http://dx.doi.org/10.1016/j.solener.2010.08.015`

Li, K.W. and Priddy, A.P. (1985). *Power plant system design*. 1st edn. John Wiley and Sons, Inc. ISBN 9780471888475.

Lubkoll, M., von Backström, T.W. and Kröger, D.G. (2014). Survey on Pressurized Air Receiver Development. In: *Proceedings of SASEC 2014*. Port Elizabeth, South Africa.

Mallinson, D.H. and Lewis, W.G.E. (1948). The part-load performance of various gas-turbine engine schemes. *Proceedings of the Institution of Mechanical Engineers*, vol. 159, no. 1, pp. 198–219. ISSN 0020-3483.
Available at: `http://dx.doi.org/10.1243/PIME_PROC_1948_159_019_02`

Marcos, M.J., Romero, M. and Palero, S. (2004). Analysis of air return alternatives for CRS-type open volumetric reciever. *Energy*, vol. 29, no. 5-6, pp. 677–686. ISSN 03605442.
Available at: `http://dx.doi.org/10.1016/S0360-5442(03)00176-2`

Muñoz de Escalona, J.M., Sánchez, D., Chacartegui, R. and Sánchez, T. (2012). Part-load analysis of gas turbine & ORC combined cycles. *Applied Thermal Engineering*, vol. 36, no. 0, pp. 63–72. ISSN 1359-4311.
Available at: `http://dx.doi.org/10.1016/j.applthermaleng.2011.11.068`

NREL (2012). SolTrace Optical Modeling Software V. 2012.7.9.
Available at: `http://www.nrel.gov/csp/soltrace/`

Osuna, R., Morillo, R., Cantero, F., Robles, P., Romero, M., Valverde, A., Monterreal, R., Pitz-paal, R., Brakmann, G., Ruiz, V., Silva, M. and Menna, P. (2006). PS10, Construction of a 11MW Solar Thermal Tower Plant in Seville , Spain. In: *Proceedings of SolarPACES 2006*. Seville, Spain.

Pacheco, J.E. (2002). Final Test and Evaluation Results from the Solar Two Project. Tech. Rep., Sandia National Laboratories, Albuquerque.
Available at: `dx.doi.org/10.2172/793226`

Pitot de la Beaujardiere, J.-F.P., Reuter, H.C., Klein, S.A. and Reindl, D.T. (2016). Impact of HRSG characteristics on open volumetric receiver CSP plant performance. *Solar Energy*, vol. 127, pp. 159–174. ISSN 0038092X.
Available at: http://dx.doi.org/10.1016/j.solener.2016.01.030

Pitz-Paal, R., Dersch, J. and Milow, B. (2005). ECOSTAR Roadmap Document. Tech. Rep., DLR.
Available at: http://www.promes.cnrs.fr/uploads/pdfs/ecostar/ECOSTAR.Roadmap.pdf

Quero, M., Korzynietz, R., Ebert, M., Jiménez, A.A., del Río, A. and Brioso, J.A. (2014). Solugas — Operation Experience of the First Solar Hybrid Gas Turbine System at MW Scale. *Energy Procedia*, vol. 49, pp. 1820–1830. ISSN 1876-6102.
Available at: http://dx.doi.org/10.1016/j.egypro.2014.03.193

Reilly, H.E. and Kolb, G.J. (2001). An Evaluation of Molten-Salt Power Towers Including Results of the Solar Two Project. Tech. Rep., Sandia National Laboratories.
Available at: http://www.osti.gov/energycitations/product.biblio.jsp?osti_id=791898

Reynolds, W. (1963). Turbulent heat transfer in a circular tube with variable circumferential heat flux. *International Journal of Heat and Mass Transfer*, vol. 6, no. 6, pp. 445–454. ISSN 00179310.
Available at: http://dx.doi.org/10.1016/0017-9310(63)90119-4

Röger, M., Rickers, C., Uhlig, R., Neumann, F. and Polenzky, C. (2009). Infrared-Reflective Coating on Fused Silica for a Solar High-Temperature Receiver. *Journal of Solar Energy Engineering*, vol. 131, no. 2, p. 021004. ISSN 01996231.
Available at: http://dx.doi.org/10.1115/1.3097270

Romero, M., Buck, R. and Pacheco, J.E. (2002). An Update on Solar Central Receiver Systems, Projects, and Technologies. *Journal of Solar Energy Engineering*, vol. 124, no. 2, p. 98. ISSN 01996231.
Available at: http://dx.doi.org/10.1115/1.1467921

Romero, M., Marcos, M.J., Osuna, R. and Fernández, V. (2000). Design and Implementation plan of a 10 MW Solar Tower Power Plant Based on Volumetric-Air Technology in Seville (Spain). In: *Proceedings of the Solar 2000*, pp. 89–98. Madison, Wisconsin.

Sagara, K. and Nakahara, N. (1991). Thermal performance and pressure drop of rock beds with large storage materials. *Solar Energy*, vol. 47, no. 3, pp. 157–163. ISSN 0038-092X.
Available at: http://dx.doi.org/10.1016/0038-092X(91)90074-7

Schell, S. (2011). Design and evaluation of esolar's heliostat fields. *Solar Energy*, vol. 85, no. 4, pp. 614–619. ISSN 0038092X.
Available at: http://dx.doi.org/10.1016/j.solener.2010.01.008

Schlaich Bergermann und Partner (2015). Point-focusing Solar Energy Technology: Stellio Heliostat confirms unprecedented optical and economic performance. Available at: http://www.sbp.de/fileadmin/sbp.de/Presse/Downloads/150819_Stellio_Heliostat_Press_Release_2.pdf

Schmidt, K.G. (2010). *M1 Heat Transfer to Finned Tubes*. Springer Berlin Heidelberg, Berlin, Heidelberg. ISBN 978-3-540-77877-6. Available at: http://dx.doi.org/10.1007/978-3-540-77877-6_94

Schumann, T.E.W. (1929). Heat transfer: A liquid flowing through a porous prism. *Journal of the Franklin Institute*, vol. 208, no. 3, pp. 405–416. ISSN 0016-0032. Available at: http://dx.doi.org/10.1016/S0016-0032(29)91186-8

Schwarzbözl, P., Buck, R., Sugarmen, C., Ring, A., Marcos Crespo, M.J., Altwegg, P. and Enrile, J. (2006). Solar gas turbine systems: Design, cost and perspectives. *Solar Energy*, vol. 80, no. 10, pp. 1231–1240. ISSN 0038-092X. Available at: http://dx.doi.org/10.1016/j.solener.2005.09.007

Selvam, R.P. and Strasser, M.N. (2012). Development of a Structured Thermocline Thermal Energy Storage System. In: *World Renewable Energy Forum*, pp. 1–17. Denver, CO.

Siddique, M., Khaled, A.-R.A., Abdulhafiz, N.I. and Boukhary, A.Y. (2010). Recent advances in heat transfer enhancements: A review report. *International Journal of Chemical Engineering*, , no. 1. ISSN 1687806X. Available at: http://dx.doi.org/10.1155/2010/106461

SIEMENS AG (2005). SGT-100 Industrial Gas Turbine. Tech. Rep.. Available at: http://www.energy.siemens.com/br/en/fossil-power-generation/gas-turbines/sgt-100.htm

SOLGATE Project Report (2005). Solar hybrid gas turbine electric power system. Tech. Rep., European Commission, Brussels, Belgium. Available at: http://bookshop.europa.eu/en/solgate-solar-hybrid-gas-turbine-electric-power-system-pbKINA21615/downloads/KI-NA-21-615-EN-C/KINA21615ENC_002.pdf?FileName=KINA21615ENC_002.pdf&SKU=KINA21615ENC_PDF&CatalogueNumber=KI-NA-21-615-EN-C

Solúcar (2006). Final Technical Progress Report. Tech. Rep. November 2006. Available at: http://ec.europa.eu/energy/renewables/solar_electricity/doc/2006_ps10.pdf

Special Metals Corporation (2005). Inconel alloy 601. Tech. Rep. 2, Huntington. Available at: www.specialmetals.com/documents/Inconelalloy601.pdf

Trieb, F. (2004). SOKRATES-Projekt Solarthermische Kraftwerkstechnologie für den Schutz des Erdklimas — AP 1.3: Marteinführung und Finanzierungskonzept ATHENE. Tech. Rep., Deutsches Zentrum für Luft- und Raumfahrttechnik (DLR), Stuttgart, Germany.

Available at: http://www.dlr.de/tt/Portaldata/41/Resources/dokumente/institut/system/projects/AP1_3_ATHENE.pdf

Tyner, C.E. and Pacheco, J.E. (2009). eSolar's Power Plant Architecture. In: *Proceedings of SolarPACES 2009*. Berlin, Germany.

Uhlig, R. (2009). Transient Stresses at Metallic Solar Tube Receivers. In: *Proceedings of SolarPACES 2009*. Berlin, Germany.

Uhlig, R., Flesch, R., Gobereit, B., Giuliano, S. and Liedke, P. (2013). Strategies enhancing efficiency of cavity receivers. *Energy Procedia*, vol. 49, pp. 538–550. ISSN 18766102.
Available at: http://dx.doi.org/10.1016/j.egypro.2014.03.058

Uhlig, R., Gobereit, B. and Rheinländer, J. (2015). Advancing Tube Receiver Performance by Using Corrugated Tubes. *Energy Procedia*, vol. 69, pp. 563–572. ISSN 18766102.
Available at: http://dx.doi.org/10.1016/j.egypro.2015.03.065

United States Department of Labor (2016). CPI Inflation Calculator.
Available at: http://www.bls.gov/data/inflation_calculator.htm

U.S. Energy Information Administration (2016). International Energy Outlook 2016. Tech. Rep..
Available at: http://www.eia.gov/forecasts/ieo/

Wagner, M.J. (2008). *Simulation and Predictive Performance Modeling of Utility-Scale Central Receiver System Power Plants*. MSc, University of Wisconsin - Madison.
Available at: http://sel.me.wisc.edu/publications/theses/wagner08.zip

Wagner, W., Kretzschmar, H.-J., Span, R. and Krauss, R. (2010). D2 Properties of Selected Important Pure Substances. In: *VDI Heat Atlas*, pp. 153–300. Springer Berlin Heidelberg, Berlin, Heidelberg.

Wakao, N. and Funazkri, T. (1979). Effect of fluid dispersion coefficients on particle-to-fluid mass transfer coefficients in packed beds. *Chemical Engineering Science*, vol. 33, no. 10, pp. 1375–1384. ISSN 00092509.
Available at: http://dx.doi.org/10.1016/0009-2509(78)85120-3

Waples, D.W. and Waples, J.S. (2004). A review and evaluation of specific heat capacities of rocks, minerals, and subsurface fluids. Part 1: Minerals and nonporous rocks. *Natural Resources Research*, vol. 13, no. 2, pp. 97–122. ISSN 15207439.
Available at: http://dx.doi.org/10.1023/B:NARR.0000032647.41046.e7

Wilson Solarpower (2015). Wilson 247Solar Plant Core Technology.
Available at: http://wilsonsolarpower.com/solutions/corecomponents.html

Zanganeh, G., Pedretti, A., Zavattoni, S.A., Barbato, M.C., Haselbacher, A. and Steinfeld, A. (2013). Design of a 100 MWhth packed-bed thermal energy storage. *Energy Procedia*, vol. 49, pp. 1071–1077. ISSN 18766102.
Available at: http://dx.doi.org/10.1016/j.egypro.2014.03.116

Zunft, S., Hänel, M., Krüger, M., Dreißigacker, V., Göhring, F. and Wahl, E. (2011). Jülich Solar Power Tower - Experimental Evaluation of the Storage Subsystem and Performance Calculation. *Journal of Solar Energy Engineering*, vol. 133, no. 3, p. 031019. ISSN 01996231.
Available at: `http://dx.doi.org/10.1115/1.4004358`